SCIENTIFIC REPORTS
nature research

Check for updates

OPEN

Single-step fabrication and work function engineering of Langmuir-Blodgett assembled few-layer graphene films with Li and Au salts

Ivana R. Milošević[1]✉, Borislav Vasić[1], Aleksandar Matković[2]✉, Jasna Vujin[1], Sonja Aškrabić[3], Markus Kratzer[2], Thomas Griesser[4], Christian Teichert[2] & Radoš Gajić[1]

To implement large-area solution-processed graphene films in low-cost transparent conductor applications, it is necessary to have the control over the work function (WF) of the film. In this study we demonstrate a straightforward single-step chemical approach for modulating the work function of graphene films. In our approach, chemical doping of the film is introduced at the moment of its formation. The films are self-assembled from liquid-phase exfoliated few-layer graphene sheet dispersions by Langmuir-Blodgett technique at the water-air interfaces. To achieve a single-step chemical doping, metal standard solutions are introduced instead of water. Li standard solutions (LiCl, $LiNO_3$, Li_2CO_3) were used as n-dopant, and gold standard solution, $H(AuCl_4)$, as p-dopant. Li based salts decrease the work function, while Au based salts increase the work function of the entire film. The maximal doping in both directions yields a significant range of around 0.7 eV for the work function modulation. In all cases when Li-based salts are introduced, electrical properties of the film deteriorate. Further, lithium nitrate ($LiNO_3$) was selected as the best choice for n-type doping since it provides the largest work function modulation (by 400 meV), and the least influence on the electrical properties of the film.

Graphene, consisting of a single layer carbon arranged in a hexagonal lattice, has attracted extensive interest because of the excellent mechanical and electrical properties associated with its two dimensional structure[1–4]. Chemical vapor deposition (CVD) method has become the most common method for production of large-area graphene films[5]. Still, simple and low-cost methods are needed for mass production especially when considering the cases where high-quality films are not needed for the desired functionality, as in low-power lighting, sensors, transparent heating, and de-icing applications[6]. In that context, liquid-phase exfoliation (LPE) is a perspective way of obtaining large quantities of exfoliated graphite in solution. LPE of graphite results in a dispersion of few-layer graphene sheets (GSs) in the solvent. However, in order to access the full potential of LPE-processed graphene, thin-films needs to be controllably fabricated utilizing techniques capable to introduce self-ordering of GSs[7]. One such example is Langmuir-Blodgett assembly (LBA). Based on surface-tension induced self-assembly of nanoplatelets at the liquid-air interface or the interface of two liquids, LBA is a good method for production of large-scale, highly transparent, thin solution-processed graphene films[8–11].

Excellent electrical conductivity, flexibility and transparency in the visible domain make graphene a natural choice for ultrathin, flexible and transparent electrodes in electronic devices[10,12–19]. Still, a significant work function difference between graphene and frequently employed active layers of photovoltaic and light-emitting diode (LED) devices gives rise to a high contact resistance. Contact resistance can have a significant impact on overall efficiency and performance of the devices[20]. This is of a particular technological relevance considering that any realistic application of graphene based transparent electrode must compete against those based on indium tin

[1]Laboratory for Graphene, other 2D Materials and Ordered Nanostructures of Center for Solid State Physics and New Materials, Institute of Physics, University of Belgrade, Pregrevica 118, 11080, Belgrade, Serbia. [2]Institute of Physics, Montanuniversität Leoben, Franz Josef Str. 18, 8700, Leoben, Austria. [3]Nanostructured Matter Laboratory of Center for Solid State Physics and New Materials, Institute of Physics, University of Belgrade, Pregrevica 118, 11080, Belgrade, Serbia. [4]Institute of Chemistry of Polymeric Materials, Montanuniversität Leoben, Otto-Gloeckel-Straße 2, 8700, Leoben, Austria. ✉e-mail: novovic@ipb.ac.rs; aleksandar.matkovic@unileoben.ac.at

oxide (ITO) or fluorine-doped tin oxide (FTO), which have already gone through decades of interfacial optimization in order to deliver todays' performance[21–23]. Therefore, the understanding of the efficient ways for modulation of the graphene work function is crucial for improving device performances[21,22,24]. In order to enhance the charge injection, the work function of the graphene electrode should be optimized to better match WF of the adjacent layer in order to form an ohmic contact[24].

Recently, the chemical doping has been reported to be an effective method for doping of CVD graphene and tuning its work function by charge transfer between the graphene sheet and metal salts, organic dopants, or metal oxide layers[12,14,21–28]. Such surface charge transfer induced by chemical doping is expected to efficiently control the Fermi level of graphene sheets without introducing substitutional impurities or basal plane reactions, thus, preventing any damage to the carbon networks and not introducing scattering centres that would lower carrier mobility[21]. Kwon *et al.* reported n-type chemical doping of CVD graphene with alkali metal carbonates by soaking in appropriate solutions[23] and alkali metal chlorides by spin-coating of appropriate solutions on the transferred graphene substrates[25]. So far, doping of Langmuir-Blodgett graphene films prepared from LPE dispersions has been done with nitric acid and ozone after the film was formed using the drop-casting method and UV/ozone treatment[9,29]. Chemical doping is especially attractive for LPE-based graphene films since many exposed edges of GSs are expected to enable very efficient functionalization through charge transfer doping. However, the chemical doping with metal salt solutions has not been used to control the work function of LBA graphene films so far. In this work LBA graphene films obtained from LPE dispersion were doped during the process of film formation. Therefore, the formation and doping of the LBA graphene films in our work represent a single-step process. This is a significant improvement compared to previous works where the chemical doping was applied only after the graphene fabrication.

In the present work, we systematically investigated single-step work function modulation (increase and decrease) of the LPE GS films achieved by chemical doping. In particular, using Li standard solutions (LiCl, $LiNO_3$ and Li_2CO_3) as n-dopant, and gold standard solution $H(AuCl_4)$ as p-dopant was investigated. In contrast to previous methods for chemical doping of CVD graphene which can be applied only after the graphene films fabrication, here we described the method for the production and doping of LPE graphene films in a single-step. Single-step work function modulation means doping of the film at the moment of its formation from the LPE graphene dispersion by LBA technique at the air-metal standard solution interface. We have demonstrated tunability of the WF in the range of almost 1 eV, making these metal-salt treated LPE-based graphene electrodes suitable candidates for both electron and hole injection interfaces.

Results and discussion

Morphology of LPE GS films. Fabrication and doping of the GS films is schematically represented in Fig. 1(a): air-metal standard solution interface, introduction of LPE dispersion and formation of the LPE GS film at the interface, scooping of the doped film on the target substrate and finally, obtained doped LPE GS film which is further investigated with different techniques.

Morphology of LPE GS films is depicted in Fig. 1 consisting of both optical (Fig. 1(b1-f1)) and Atomic Force Microscopy (AFM) topographic images (Fig. 1(b2-f2)) for both undoped and metal doped LPE GS films. As can be seen from AFM images, the doping process does not change morphology of LPE films, except that the doped films contain more agglomerates (visible as bright particle-like domains). The following values for the surface roughness were obtained by AFM measurements averaged on ten $50 \times 50\ \mu m^2$ areas: (a) 11.9 ± 1.5 nm for undoped LPE GS film, (b) 11.5 ± 3.5 nm for Li_2CO_3 doped, (c) 13.3 ± 2 nm for $H(AuCl_4)$ doped, (d) 13.7 ± 1.6 nm for LiCl doped, and (e) 13.8 ± 1.2 nm for $LiNO_3$ doped LPE GS films. Therefore, the surface roughness sligtly increases by around 2 nm after the doping, while for Li_2CO_3 doped LPE GS film is practically the same as for the undoped film. Still, optical images recorded on larger scale depict formation of agglomerates in doped films which could degraded their optical (leading to an increased scattering and/or absorption of incoming lights on these clusters) and electrical properties (due to enhanced scattering of charge carriers).

The observed formation of the agglomerates is most likely not an inherent property of the particular metal-salt doping. Overcoming this would likely require further optimization of the LBA process. However, as a benchmark the LBA process in this study was optimized for an undoped film and was left unchanged for all of the metal-salt doped films.

Transmittance measurements. Using the different doping metal standard solution during LBA of graphene films was found to result in different transparency. In the UV region, the transmittance of graphene is dominated by an exciton-shifted van Hove peak in absorption[9,30]. Transmittance at 550 nm was 82% for undoped and 80%, 76%, 74%, 68% for $H(AuCl_4)$, LiCl, $LiNO_3$, Li_2CO_3 doped LPE GS films, respectively (Fig. 2). It can be seen that transmittance decreases for doped LPE GS films. Metal salts decrease the transmittance of the graphene films regardless the type of the present metal (gold or lithium). The degree of the transmittance decrease was related to not only the metal cations but also the anions. Different lithium salts decrease transmittance in different amounts. Transmittance decrease of 14% was the highest for the LPE GS film doped with lithium carbonate (Li_2CO_3). Similar results of the transmittance decrease for metal doped CVD graphene films were obtained in studies of Kwon *et al.*[22,23,25]. Transmittance decrease could be a consequence of the metal particles adsorption and agglomeration on doped films after the solvent evaporation process. Changes in the thickness of LPE GS films with doping could not be excluded because LBA process in this study was optimized for an undoped film and was left unchanged for all of the metal-salt doped films.

Raman measurements. Raman spectra for undoped and $H(AuCl_4)$, LiCl, $LiNO_3$, Li_2CO_3 doped LPE GS films are given in Fig. 3(a). The four basic graphene/graphite peaks D (~1348 cm^{-1}), G (~1579 cm^{-1}), D' (1614

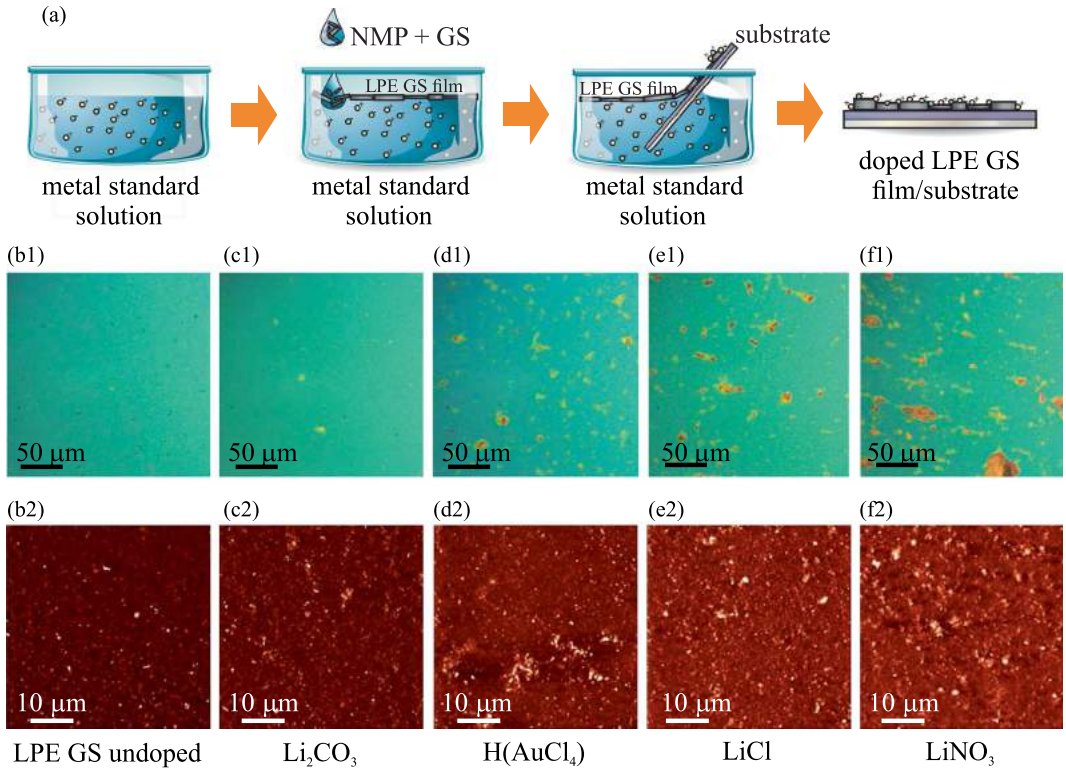

Figure 1. (**a**) Schematic representation of the LPE GS film formation and its doping in the single-step process. (**b1**–**f1**) Optical images are shown in the top row, whereas (**b2**–**f2**) AFM topographic images are shown in the bottom row for the following cases: (**b**) undoped LPE GS film, and (**c**) Li_2CO_3, (**d**) $H(AuCl_4)$, (**e**) LiCl, (**f**) $LiNO_3$ doped LPE GS films. z-scale in all AFM images is 100 nm.

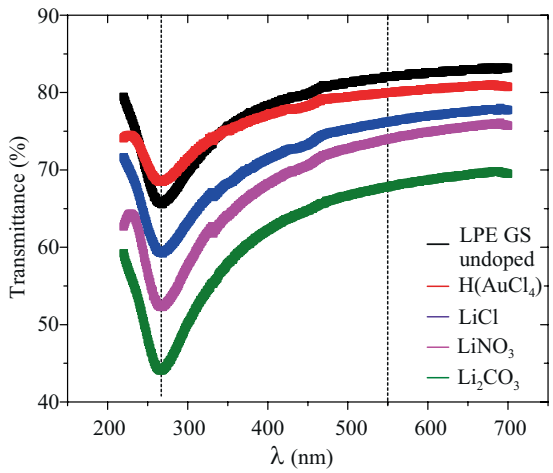

Figure 2. Transmittance spectra of undoped and $H(AuCl_4)$, LiCl, $LiNO_3$, Li_2CO_3 doped LPE GS films.

cm^{-1}) and 2D (2700 cm^{-1}) are observed for all the samples. No significant shifts of any characteristic Raman peaks of graphene were detected after chemical doping (Fig. 3(a)).

The change of the full weight at half-maximum (FWHM) of the Raman modes after doping with metal standard solutions was negligible Fig. 3(b). The only notably change of the Raman spectra was the increase of the intensity ratio of D to G peaks, I(D)/I(G) (Fig. 3(c)). The quantity of defects has been shown to be related to the ratio between the D and G peaks, I(D)/I(G); the larger the ratio, the larger the defect density[31]. We observe increase of the defect density with $H(AuCl_4)$, LiCl, $LiNO_3$, Li_2CO_3 doping in relation to the undoped film and the amount of the increase expressed in percent was 37%, 24%, 29% and 21%, respectively.

All self-assembled films suffer from a large defect density that often leads to a high sheet resistance of deposited film. Therefore, the nature and density of defects in any thin film transparent conductor is important, especially when chemical treatment was used to enhance films' performance. The intensity ratio between the D and

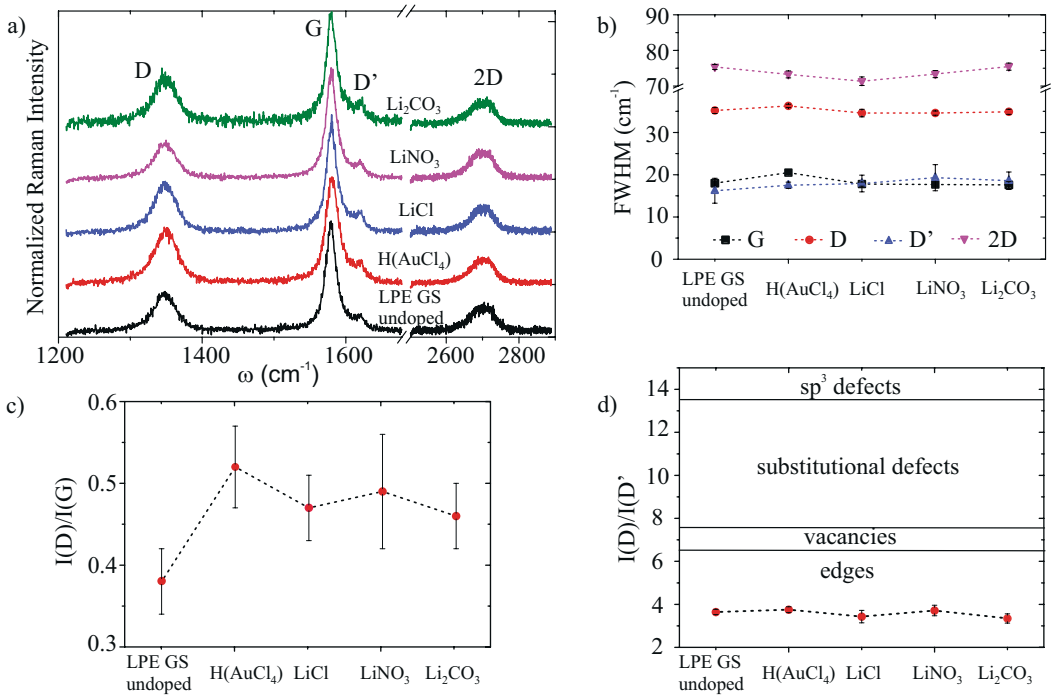

Figure 3. (**a**) Raman spectra of the undoped LPE GS film and films doped with Li and Au salts, (**b**) FWHM of the four basic Raman peaks (**c**)The intensity ratio of D to G peak for different doping metal salts, I(D)/I(G), (**d**) The intensity ratio of D to D' peak, I(D)/I(D'), for different doping metal salts. We refer to peak intensity as the height of the peaks as proposed by Eckmann *et al.*[32].

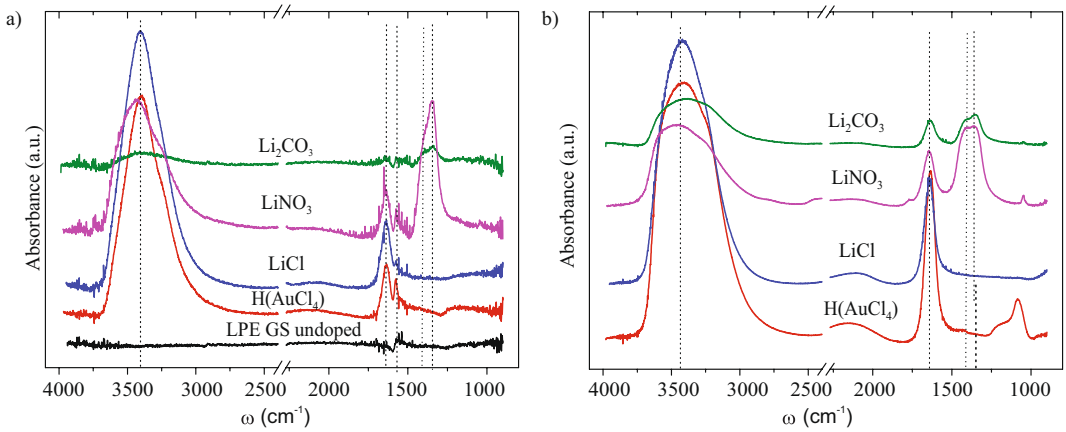

Figure 4. FT-IR spectra of (**a**) undoped and $H(AuCl_4)$, LiCl, $LiNO_3$, Li_2CO_3 LPE GS doped films, (**b**) metal standard solutions (0.1 mg/mL) used for doping processes.

D' peak can be used to get information on the nature of defects in graphene[32,33]. I(D)/I(D') was calculated, and the obtained results were presented in Fig. 3(d). Topological defects (like pentagon-heptagon pairs), boundaries, vacancies, substitutional impurities and sp^3 defects are possible defects in graphene[31]. Studies reporting a ratio of 3.5 for boundaries, 7 for vacancies, 13 for sp^3 and values in-between those for vacancies and sp^3 for substitutional impurities can be found in the literature[31,32,34]. From Fig. 3(d) it can be observed that the D to D' intensity peak ratio is nearly constant in our samples regardless of the doping solution, and the value of the ratio indicates that the edges are the dominant type of defects in our LPE GS films.

Fourier transform infrared absorbance (FT-IR) measurements. FT-IR spectra of undoped and LiCl, $LiNO_3$, Li_2CO_3, $H(AuCl_4)$ doped LPE GS films, as well as FT-IR spectra of corresponding metal standard solutions are shown in Fig. 4.

For the undoped LPE GS film FT-IR spectra is simple. It can be seen only a small peak assignable to C=C skeletal vibration[35–37] of the graphene basal planes at ~1560 cm^{-1}. This peak can also be seen in FT-IR spectra for

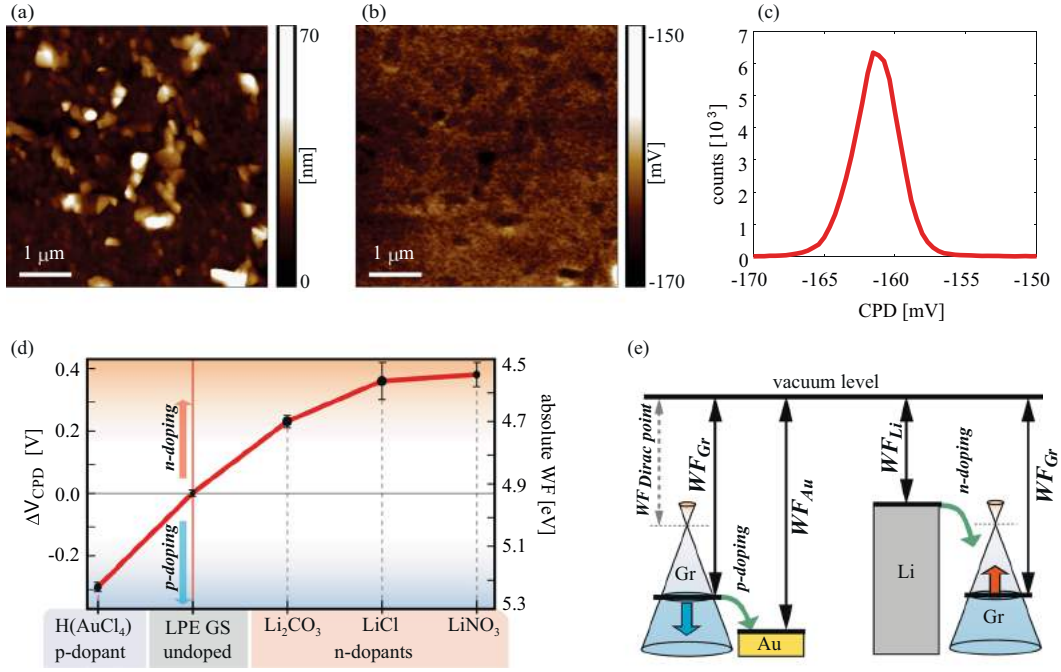

Figure 5. (**a**) AFM topography, (**b**) CPD map measured by KPFM, and (**c**) histogram of (**b**) shown for $H(AuCl_4)$ doped LPE GS film as an example. (**d**) Change in WF for doped LPE GS films for different dopants, in comparison to the undoped LPE GS film. Solid red line in (**d**) is only a guide for the eye. (**e**) Schematic representation of the work functions prior to the interaction (equal vacuum levels) for Au-based salt/graphene and Li-based salt/graphene. The green arrows indicate direction of electron flow showing that in the case of Li (Au) based salts, electrons are transferred to (from) graphene.

all investigated doped films at the same wavenumber indicating that graphene basal planes were not interrupt by doping. The strong peak at around ~3400 cm^{-1} and another, smaller one, near ~1630 cm^{-1} can be seen in all doped LPE GS films (Fig. (4a)) and corresponding metal standard solutions (Fig. (4b)). They are attributed to the water molecules and are assignable to the O-H stretching vibrations (~3400 cm^{-1}) and H-O-H bending mode (~1630 cm^{-1})[38,39]. In the case of FT-IR spectra for LPE GS film doped with $LiNO_3$ the peak at ~1340 cm^{-1} and ~1390 cm^{-1} are assignable to the vibration mode of the NO_3^- ions and asymmetric stretch of O-NO_2, respectively[38,40]. Similar vibration modes can be observed in the case of FT-IR spectra for LPE GS film doped with Li_2CO_3 and can be assigned to the vibration mode of the CO_3^- ions (1340 cm^{-1}) and asymmetric stretch of O-CO_2 (~1390 cm^{-1})[41]. The same vibrational modes could be seen for $LiNO_3$ and Li_2CO_3 standard solutions (Fig. (4b)).

From the observed FT-IR results (Fig. 4(a)) it is clear that additional peaks appear with LPE GS film chemical doping. These additional peaks match with vibrational modes of the anions in solution (Fig. 4(b)). Considering that no new peaks are visible in the given spectra (which would indicate the formation of chemical bonds) the present peaks could be a consequence of the metal salts adsorption to the graphene lattice during the doping. In order to understand Li and Au doping mechanisms XPS measurements were performed and they are presented in separate section.

Work function modulation. Results for the work function dependent on the different metal standard solution used in the LBA process are summarized in Fig. 5. The top row depicts an example with the topography (Fig. 5(a)), corresponding contact potential difference (CPD) map measured by Kelvin probe force Microscopy-KPFM (Fig. 5(b)), and the histogram of the CPD distribution measured on $H(AuCl_4)$ doped graphene film (Fig. 5(c)). The histogram is characterized with a single peak, which is used for the averaging and calculation of the absolute value of work function. The same procedure was done for all considered films. More details about the measurements of CPD and WF calculations are given in Supplementary information in Supplementary Figs. S3-S5. As a result, the values of the absolute work function are presented in Fig. 5(d) for both, doped and undoped LPE GS films. As can be seen, n-doping of graphene films is achieved by Li-based salts, whereas Au-based salt leads to p-doping.

The change of the WF due to the doping can be explained according to the schematic presentation in Fig. 5(e), illustrating that Li (Au) as a lower (higher) work function material compared to GS films. Therefore, presence of Li-based salts into the graphene film results in a reduction of the work function of the entire film. This behavior can be interpreted as an increase in the Fermi level of GSs – compared to the value for the undoped films – indicating predominantly a charge transfer from Li-based salts to graphene (n-doping), as expected when considering that Li has lower WF than graphene (graphite). In contrast to Li-based salts, the Au-based salt shows an opposite trend for the relative change of the work function. This indicates charge transfer from graphene to

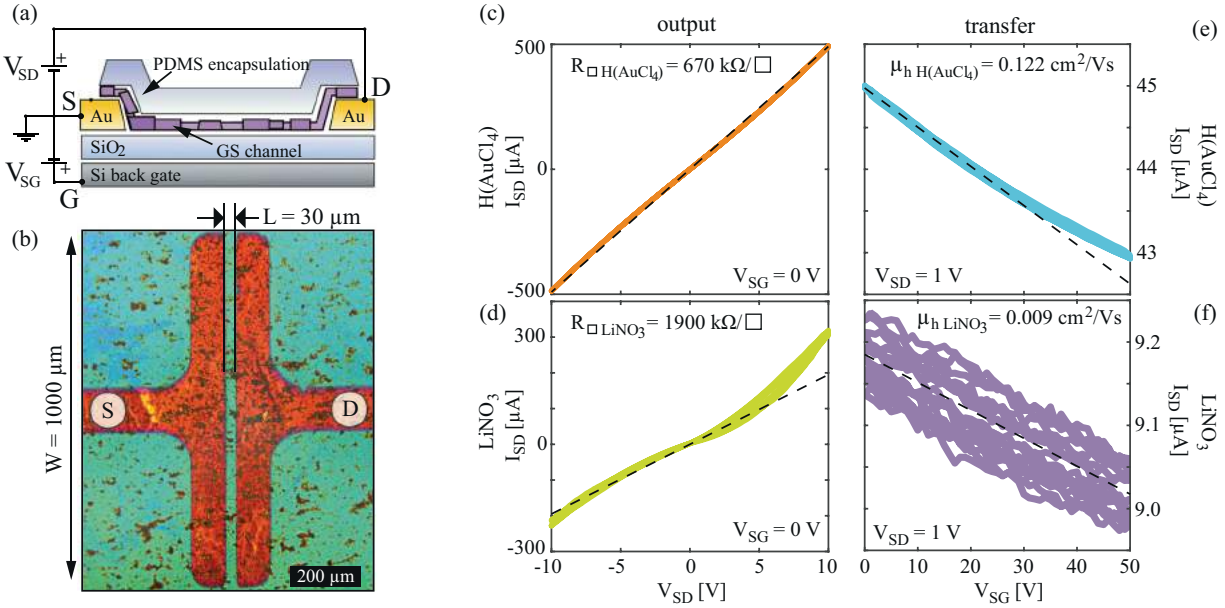

Figure 6. (**a**) Schematic cross-section of the bottom-contacted back-gated FET devices, also indicating electrical connections. (**b**) Optical microscopy image of one of the devices, without PDMS capping (for clarity). LBA GS film covers the entire sample surface. (**c**,**d**) Output curves of $H(AuCl_4)$ and $LiNO_3$ doped samples, and (**e**,**f**) transfer curves of $H(AuCl_4)$ and $LiNO_3$ doped samples, respectively. Dashed lines represent least squares linear fits (to selected regions) that were used to extract sheet resistance and linear mobility.

Au-based salt and a relative reduction of the Fermi level in GSs (p-doping). It is also worth mentioning that poly-crystalline nature of LPE based GS films, large amount of sheet edges and presence of the residual solvent (NMP) results in p-doped films[9], as was also observed in the electrical measurements presented in the following subsection. Therefore, WF values are lower for the LPE-based films by at least 200 meV, than for the pristine exfoliated single-crystals[42]. p-type doping is also reflected on the WF of the reference samples (undoped LPE GS), and therefore on the whole accessible range for the WF modulation by this method. This was also highlighted in Fig. 5(e), where the $WF_{Dirac\ point}$ depicts the case of undoped graphene[42].

According to Fig. 5(d), the maximal doping in both directions is similar, around 0.3–0.4 eV, finally providing a significant range of around 0.7 eV for the work function modulation of LPE GS films. The achieved range was obtained for 0.1 mg/mL concentration of dopants. For smaller concentrations (one order of magnitude lower, 0.01 mg/mL), the observed changes in CPD were in the order of 10 mV. On the other hand, for higher concentrations (for one order of magnitude higher, 1 mg/mL) gave rise to the problems related to the formation of continuous, large-area LPE GS films, and were therefore excluded from this study. The reported shift of the Fermi level is very similar to the other (comparable) systems in the literature. WF values change of 0.3 eV in our experiment (chemical doping by Au ions) are the same order of magnitude as in Kwon *et al.* manuscripts for gold-chloride (WF change of 0.6 eV[21], 0.6 eV[22], 0.4 eV[25]). Compared with Kwon *et al.* alkali carbonate[23] and chloride[25] graphene chemical doping data (0.4 eV and 0.3–0.4 eV, respectively) WF values change for Li in our manuscript (0.2 eV and 0.4 eV) are in the same order of magnitude. Compared with literature data the same effect can be achieved but advantages of our approach is fast and simple solution-based method for one-step fabrication and WF control of large-area graphene films.

Sheet resistance. The schematic cross-section of the devices used for the electrical characterization is shown in Fig. 6(a), also indicating electrical connections. An optical microscopy image for one of the devices without PDMS encapsulation (for clarity) is shown in Fig. 6(b) illustrating source (S) and drain (D) contact geometries. One characteristic set of transport and output curves for $H(AuCl_4)$ and $LiNO_3$ doped film is presented in Fig. 6(c–f). Here linear fits were used to extract sheet resistances and apparent linear hole mobilities. Transfer curves for all four salt-treatments and for the reference LPE GS film are presented in the Supplementary information (Supplementary Fig. S1).

In the cases of a reference (undoped) and $H(AuCl)_4$ doped LPE GS samples, output curves barely deviate from a perfect linear behavior in a rather large bias range, indicating that the contact resistance is negligible in comparison to the channel. This is in contrast to all samples doped with Li-based salts, where a significant deviation from the linear output curves were observed at higher bias, indicating non-negligible contact resistance. This can be attributed to large WF differences with Au bottom contacts in the case of Li-based salt doping of the films. Furthermore, while $H(AuCl_4)$ doping enhances electrical performance of the films, a significant increase of the resistivity and reduction of the mobility was observed in the case of all Li-based salt dopings.

The slope of the transfer curves indicates that holes are the majority carriers for all samples, including both the undoped (reference) and all metal salt doped films. Linear fits to the transfer curves were used to estimate

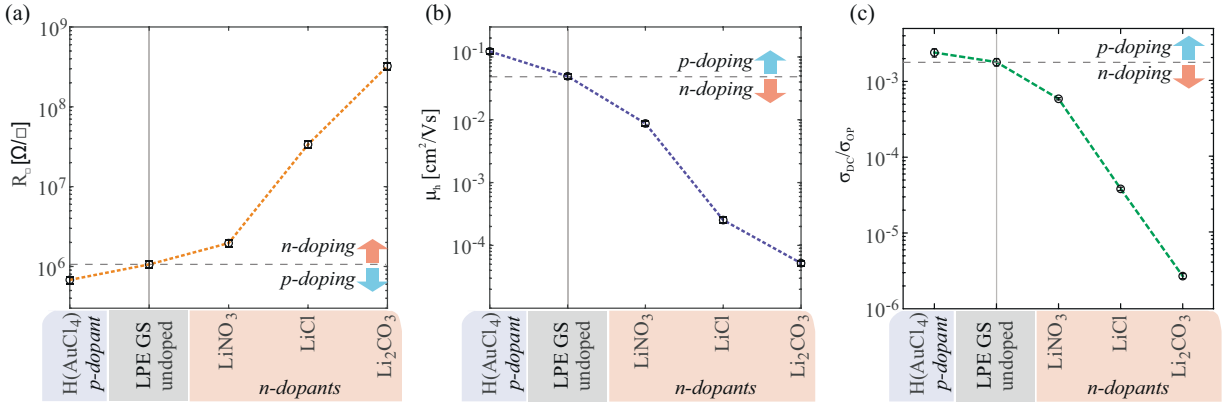

Figure 7. The dependence of the electrical properties of LBA graphene films on the type of metal standard solution based doping; (**a**) sheet resistance, and (**b**) apparent linear hole mobility, and (**c**) direct current conductivity to optical conductivity ratio (σ_{DC}/σ_{OP}). Dashed lines in (**a**–**c**) serve only as a guide for the eye.

apparent hole mobility of the devices. While the type of majority carriers was not affected by the doping, a significant (over one order of magnitude) suppression of the field-effect was observed for Li salt dopings of the films.

Figure 7 summarizes electrical properties obtained for all of the measured devices as a function of the different metal based doping.

The results indicate that anions also play a significant role. In the case of Li-based salts, a large variation of the electrical properties was obtained by the different choice of the anion species. Nonetheless, the experiments point out that metal cations dictate the direction of the WF shift (see Fig. 5), as is apparent in the case of $H(AuCl_4)$ and LiCl where only cation species is varied. Our results of metal based doping of LPE graphene films demonstrate a tradeoff between enhancement of the electrical performance and modulation of the WF. Similar results were obtained for CVD doping with Li and Au salts[23,25]. Of a particular technological relevance is large reduction of the WF of graphene. While many methods for chemical modulation of graphene result in p-type doping[43–46], stable and simple n-type doping is much harder to achieve[47–49]. For an efficient electron injection, a significant reduction of graphene's WF is required. As pointed out by WF measurements and electrical characterization, $LiNO_3$ is the best choice from the tested Li-based salts with respect to both the largest WF reduction (by 400 meV) and least deterioration of the electrical properties of the films with ~2–3 times increase in sheet resistance compared to the reference (undoped LPE GS).

In contrast, doping of LPE GS films by HNO_3 vapor results in an increase of the apparent mobility[9]. However, using a $LiNO_3$ solution reduces the mobility by one order of magnitude. Therefore, Li^+ cations – and not anions – are likely responsible for the deterioration of the electrical properties upon n-doping. An increase of sheet resistance was observed in doping of CVD graphene with alkali metal carbonates and chlorides[23,25]. There, a significant increase in the sheet resistance was related to the combination of carbon atoms and dopant metals because electron donation occurred[23,25]. Also, Chen *et al.* observed that the mobility of the charge carriers decreases with the increase of the potassium doping concentration which they attributed to additional scattering caused by ionized potassium atoms[49,50]. It is most likely that Li^+ cations are acting as scattering centers for the carriers, or provide traps at the boundaries between neighbouring GSs and effectively increase contact resistance between the overlapping GSs.

Finally, considering that the main potential application of these LPE GS films lies in transparent electrodes, direct current conductivity to optical conductivity ratio (σ_{DC}/σ_{OP}) is presented in Fig. 7(c) for all metal standard solution doping cases and for the reference (undoped). σ_{DC}/σ_{OP} is a parameter frequently reported in order to characterize the relative performance of the films in terms of transparency and sheet resistance[11,33,51]. The higher the ratio the better the quality of transparent electrodes[33]. Compared to the changes in the electrical properties (Fig. 7(a)) the changes in the optical properties (Fig. 2) are minor. Therefore, the dependence of the σ_{DC}/σ_{OP} on the type of the metal-ion doping clearly follows the trend set by $1/R_{\square}$.

X-ray Photoemission Spectroscopy (XPS) measurements. In order to understand Au and Li ion doping mechanisms XPS measurements were performed. C 1 s, Au 4 f and Li 1 s core-level XPS spectra are shown in Fig. 8. N 1 s, Cl 2p and O 1 s spectra are presented as Supplementary Fig. S2. The C 1 s peak of undoped and LiCl, $LiNO_3$, Li_2CO_3, $H(AuCl_4)$ doped LPE GS films is shown on Fig. 8(a). The C 1 s peak is deconvoluted using Gaussian profile into 4 components for undoped and doped films: C=C/C–C in aromatic rings (284.5 eV); C–C sp^3 (285.4 eV); C–O (286.6 eV) and C=O (289 eV)[23,52]. In the case of Li_2CO_3 we can see a small additional peak at 289.2–291.0 eV[53] which can be assigned to carbonate. Detected oxygen peak (C=O) is likely due to the residual of NMP and oxygen functionalized edges (C–O) on graphene[54,55]. The C=C/C–C peak was shifted to a lower binding energy by about 0.16, 0.48, 0.10 and 0.83 eV for $H(AuCl_4)$, LiCl, $LiNO_3$ and Li_2CO_3 doping process, respectively. The C=C/C–C peak shifts in present work are a consequence of doping by different metal standard solutions. Kwon *et al.* have shown that degree of doping was related to the electronegativity of the anion in the Au complex where anions with a high electronegativity and high bond strength are adequate for use as a p-type

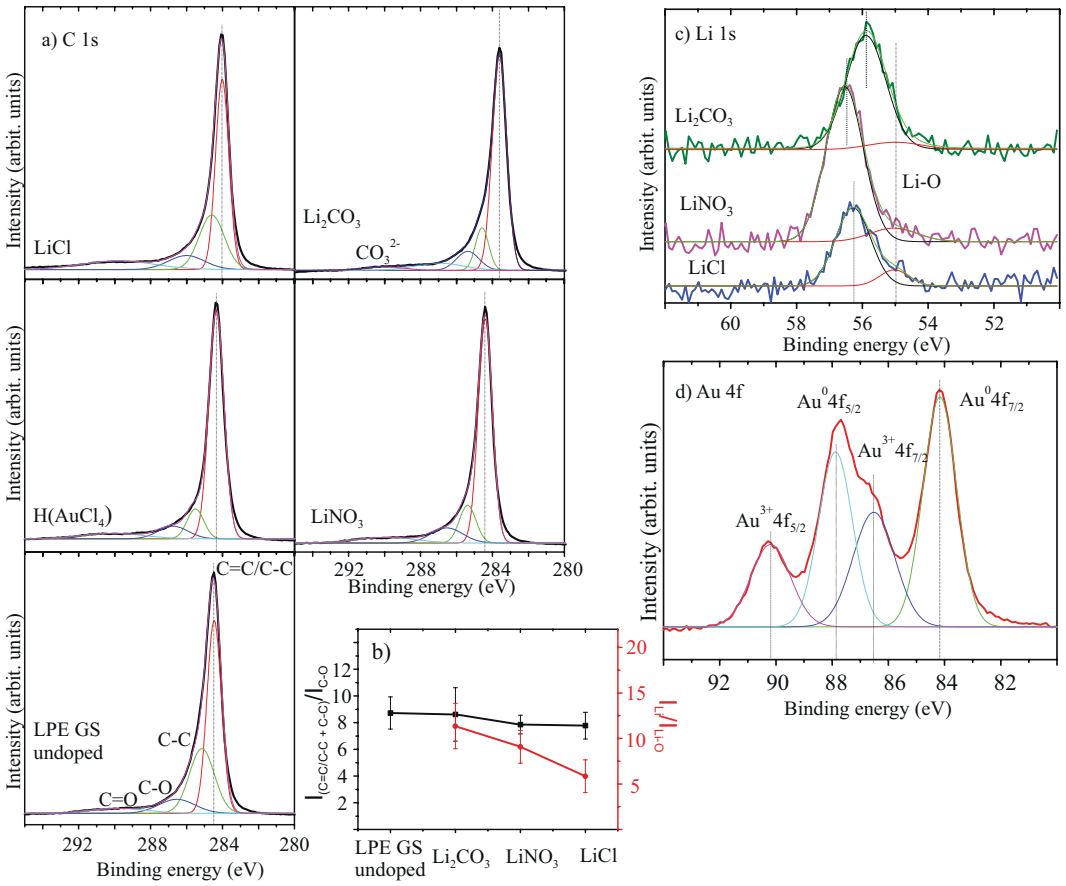

Figure 8. (**a**) XPS C 1 s spectra of undoped and $H(AuCl_4)$, LiCl, $LiNO_3$, Li_2CO_3 doped LPE GS films. C=C/C–C in aromatic rings (284.5 eV); C–C sp^3 (285.4 eV); C–O (286.6 eV) and C=O (289 eV) were considered. For Li_2CO_3 a small additional peak at 289.2–291.0 eV can be assigned to carbonate. (**b**) Peak intensity ratio for the sum of C=C/C-C and C-C peaks intensities, and the intensity of C-O, $I_{(C=C/C-C+C-C)}/I_{(C-O)}$ (black line) and the ratio of Li 1 s intensity from Li salts to Li-O intensity, I_{Li}/I_{Li-O} (red line). (**c**) XPS Li 1 s spectra for different Li compounds and for Li–O. (**d**) The Au 4 f peak in the XPS data of $H(AuCl_4)$.

dopant in graphene[21]. Thus, different shifts of C=C/C–C peak for different metal-salt doping materials could be also a consequence of anions influence on graphene films.

Figure 8(c) show the Li 1 s core-level XPS spectra. Literature values for Li 1 s core-level for different Li compounds are: LiCl (56.2 eV), Li_2CO_3 (55.5 eV) and $LiNO_3$ (55.8 eV)[56] and they correspond well to the values obtained in this work. Li 1 s peak at 55.0 eV is assigned to Li–O bond[57]. Vijayakumar and Jianzhi have shown that lithium ion tends to bind with the oxygen rather than the carbon on graphene surface, and interacts by forming Li-O ionic bond[58]. Also Kwon *et al.* have proposed that C–O–X complexes can be formed during doping treatment and can act as an additional dipole to further reduce the value of WF[23–25,59]. The intensity ratio between sum of the intensities of C=C/C-C and C-C peaks, and the intensity of C-O ($I_{(C=C/C-C+C-C)}/I_{(C-O)}$) is shown in Fig. 8(b). Also, the ratio of Li 1 s intensity from Li salts to Li-O intensity (I_{Li}/I_{Li-O}) can be seen in Fig. 8(b). In both cases, intensity ratios decrease for Li_2CO_3, $LiNO_3$, LiCl, respectively and this implies increased formation of C–O and Li–O bonds. Increased number of Li-O bonds follow the increasing trend of C–O bonds, which is in correlation with the WF change (Fig. (5d)). The above mentioned results strongly suggest that the mechanism of n-type doped LPE GS films with lithium-salts could be explained with formation of Li complexes (C–O–Li).

Figure 8(d) show the Au 4 f peak of gold-chloride doped LPE GS film. The peak is composed of metal (Au^0) and metal ion (Au^{3+}). The peaks at 84.2 eV and 87.9 eV are assigned to neutral Au (Au^0 $4f_{7/2}$ and Au^0 $4f_{5/2}$, respectively), and the peaks at 86.5 eV and 90.2 eV are assigned to Au ion (Au^{3+} $4f_{7/2}$ and Au^{3+} $4f_{5/2}$, respectively). Au ions (Au^{3+}) have positive reduction potential and have tendency to spontaneously accept charges from other materials (graphene) and reduce to Au^0 [21,22,25,60]. Therefore, the mechanism of p-doped LPE GS film can be explained as spontaneous electron transfer from graphene film to Au^{3+}, resulting in depletion of electrons in the graphene networks, thus increasing the WF of doped graphene.

Conclusion

We demonstrate a straightforward single-step method for forming and doping of LPE GS films by metal standard solutions through charge transfer processes. Chemical doping of graphene allows to modulate its WF in a very large range, and therefore potentially enables to use the same electrode material for both, the injection and for the extraction of the electrons. n-doping of graphene films is achieved by Li-based salts, whereas Au-based salt leads

to p-doping. Furthermore, solution-processed graphene films are in particular suited for the chemical modulations, since a large number of the sheet edges opens up many adsorption sites and enhances the doping effects when compared to many other types of graphene.

The morphology of the LPE GS films does not change with the doping process, except that doped films contain agglomerates. FT-IR measurements point out that graphene basal planes stay chemically unchanged with metal doping and the charge transfer process is enabled with adsorption of the metal salts. Li-based salts decrease the WF, while Au-based salts increase the WF of the entire film. The maximal doping in both directions gives a significant range of around 0.7 eV for the work function modulation. Changing the dopant (Au or Li based salts) significantly affects the electrical properties of the films. In the case of the Li-based salts doping of the film, a significant suppression of the field-effect mobility and the increase of the sheet resistance was observed. This indicates that adsorbed Li-anions act as scattering centers for the charges. XPS data indicated that different mechanisms exist in the case of Au and Li doping. For Au ions spontaneous charge transfer occurred from graphene, thus increasing WF. In the case of Li doping, potential adsorption sites are a large number of the sheet edges where C-O bonds are preferential sites for lithium ions and for forming of C-O-Li complexes. In all cases graphene films are p-type, which is in accordance with KPFM measurements. Also, tradeoff between Li complex which reduce the value of WF and anion which increase the value of WF could be a reason of such a doping.

Metal salts charge transfer doping – which happens with this single-step method – provides a facile and effective method to tune the WF of LPE graphene therefore extending the potential use of these materials in low-cost transparent electrode applications.

Methods

Preparation of GS dispersion and doping solutions. A dispersion of GS in N-methyl-2-pyrrolidone (NMP, Sigma Aldrich, product no. 328634) has been used. GS dispersion was prepared from graphite powder (Sigma Aldrich, product no. 332461) of initial concentration 18 mg/mL. The solution was sonicated in a low-power ultrasonic bath for 14 h. The resulting dispersion was centrifuged for 60 min at 3000 rpm immediately after the sonication.

Stock standard solutions used in our work for n-doping are 1 mg/mL LiCl, $LiNO_3$ and Li_2CO_3 and for p-doping is 1 mg/mL gold standard solution (Merck, $H(AuCl_4)$, product no. 170216). Lithium standard solutions were prepared from originated Li salts (LiCl, $LiNO_3$ and Li_2CO_3, Merck, product no. 105679, 105653 and 105680, respectively). By appropriate dilution of the stock solution with deionized water we obtained 0.1 mg/mL metal water solution which is then used in doping process.

Deposition on a substrate and doping of LPE GS films. GS dispersion in NMP was used to fabricate transparent and conductive films by LBA technique at a water-air interface, like in our previous work[9,29,61]. A small amount of GS dispersion was added to the water-air interface and after the film was formed it was slowly scooped onto the target substrate. Applying the same process of fabricating the GS films and using the appropriate metal standard solution instead of water, chemical doping was achieved. As substrates SiO_2/Si wafer were used for electrical and WF measurements, while quartz and CaF_2 substrates were chosen for optical and FT-IR spectroscopy, respectively.

Characterization of undoped and doped LPE GS films. The Morphology of LPE GS films was studied by optical and atomic force microscopy (AFM). Topographic AFM measurements were done by NTEGRA Prima AFM system and NSG01 probes with a typical tip radius of around 10 nm. The surface roughness of LPE GS films was calculated as a root-mean square of the height distribution and averaged on ten $50 \times 50\ \mu m^2$ areas.

Kelvin probe force microscopy (KPFM) – established almost three decades ago[62] and in the meantime frequently applied to graphene[42,63–65] – was employed in order to characterize changes in the electrical surface potential and corresponding Fermi level shifts due to doping. For this purpose, we measured the contact potential difference (CPD) between AFM tip and the sample surface[66] by using Pt covered NSG01/Pt probes with a typical tip curvature radius of 35 nm. In the first pass of KPFM, the sample topography was measured in tapping AFM mode. In the second pass, the probe was lifted by 20 nm, and moved along the trajectory measured in the first pass. Simultaneously, the sum of AC and DC voltage was applied between the sample and the probe. The AC voltage excites AFM probe oscillations during its movement, while the CPD between AFM tip and the sample surface in every point is then equal to the value of variable DC voltage which cancels the AFM probe oscillations. For all samples, the CPD was measured on five $5 \times 5\ \mu m^2$ areas, and then averaged. In order to obtain the absolute value of the work function, the following procedure was applied[42]. The CPD is equal to the work function difference between AFM tip (WF_t) and sample (WF_s), $CPD = WF_t - WF_s$. The calibration of the WF_t was done by a standard procedure consisting of KPFM measurements on a freshly cleaved HOPG with a well known work function of 4.6 eV[42]. Finally, the sample work function was calculated as $WF_s = WF_t$ - CPD, where CPD is measured by KPFM for all, undoped and doped LPE GS films.

The effect of chemical doping on optical properties of LBA GS films was investigated with measurements of optical transmittance, using UV-VIS spectrophotometer (Beckman Coulter DU 720 UV-VIS Spectrophotometer).

Electrical measurements were performed under ambient conditions in a standard field-effect device configuration with Si substrate acting as a back gate electrode, using Keithley 2636 A SYSTEM SourceMeter. Devices were based on bottom-contact gold pads defined by a shadow mask with $L/W = 30\ \mu m/1000\ \mu m$, and SiO_2 as a gate dielectric with thickness of 285 nm. Graphene films were deposited using the same LBA method as described above. The top surface of the devices was encapsulated by polydimethylsiloxane (PDMS) films (GelPak X4) to ensure stable performance and minimize any adsorption/desorption during electrical measurements that could occur from the surroundings (e.g. water vapor). Electrical characterization was performed on several devices of each doping with metal standard solution, and for undoped films as a reference. For each device ten subsequent forward and

backward transfer and output curves were measured, using low sweeping rate (~0.005–1 Hz per point in a voltage sweep) to minimize parasitic capacitance. Sheet resistance and apparent linear field-effect mobility were extracted using fits to output and transfer curves, respectively. For the output measurements source-drain bias was varied in a range between −10 V and +10 V, with the gate electrode grounded. For transfer measurements, the gate voltage was varied between 0 V and 50 V, with source-drain bias at 1 V in all cases except for Li_2CO_3 where due to a very weak field-effect (very low mobility) 10 V bias was used.

The room-temperature micro-Raman spectra of undoped and metal salt doped LPE GS films were collected using Tri Vista 557 triple spectrometer coupled to the liquid nitrogen-cooled CCD detector. Nd:YAG laser line of 532 nm was used for the excitation and 50 magnification objective was used for focusing the beam onto the sample. Low laser power (less than 1 mW) was applied to prevent the thermal degradation of the sample. Each LPE GS film sample was measured at eight different positions.

Fourier transform infrared absorbance spectra (FT-IR spectra) of undoped and metal salt doped LPE GS films were measured over a range of 400–4000 cm^{-1} with Nicolet Nexus 470 FT-IR spectrometer. Standard solutions which were used for the preparation of doped films were measured too and they were prepared by drop casting method on the CaF_2 substrate.

XPS spectra were recorded using a Thermo Scientific instrument (K-Alpha spectrometer, Thermo Fisher Scientific, Waltham, USA) equipped with a monochromatic Al Kα X-ray source (1486.6 eV). High-resolution scans were performed with a pass energy of 50 eV and a step size of 0.1 eV. All analyses were performed at room temperature.

Data availability

The datasets obtained and analysed during the current study that are not included in this article are available from the corresponding authors on reasonable request.

Received: 17 June 2019; Accepted: 28 April 2020;
Published online: 21 May 2020

References

1. Geim, A. K. Graphene: Status and prospects. *Science* **324**, 1530–1534 (2009).
2. Geim, A. K. & Novoselov, K. S. The rise of graphene. *Nat. Mater.* **6**, 183–191 (2007).
3. Novoselov, K. S. *et al*. Room-temperature quantum hall effect in graphene. *Science* **315**, 1379–1379 (2007).
4. Bonaccorso, F., Sun, Z., Hasan, T. & Ferrari, A. C. Graphene photonics and optoelectronics. *Nat. Photonics* **4**, 611–622 (2010).
5. Kwon, K. C., Kim, B. J., Lee, J. L. & Kim, S. Y. Role of ionic chlorine in the thermal degradation of metal chloride-doped graphene sheets. *J. Mater. Chem. C* **1**, 253–259 (2013).
6. Ferrari, A. C. *et al*. Science and technology roadmap for graphene, related two-dimensional crystals, and hybrid systems. *Nanoscale* **7**, 4598–4810 (2015).
7. Backes, C. *et al*. Guidelines for exfoliation, characterization and processing of layered materials produced by liquid exfoliation. *Chem. Mater.* **29**, 243–255 (2017).
8. Li, X. *et al*. Highly conducting graphene sheets and Langmuir-Blodgett films. *Nat. Nanotechnol.* **3**, 538–542 (2008).
9. Matković, A. *et al*. Enhanced sheet conductivity of Langmuir-Blodgett assembled graphene thin films by chemical doping. *2D Mater* **3**, 015002 (2016).
10. Lee, S. K. *et al*. All graphene-based thin film transistors on flexible plastic substrates. *Nano Lett.* **12**, 3472–3476 (2012).
11. Zheng, Q. *et al*. Transparent conductive films consisting of ultralarge graphene sheets produced by Langmuir-Blodgett assembly. *ACS Nano* **5**, 6039–6051 (2011).
12. Park, J. *et al*. Work-function engineering of graphene electrodes by self-assembled monolayers for high-performance organic field-effect transistors. *J. Phys. Chem. Lett.* **2**, 841–845 (2011).
13. Tong, S. W., Wang, Y., Zheng, Y., Ng, M. F. & Loh, K. P. Graphene intermediate layer in tandem organic photovoltaic cells. *Adv. Funct. Mater.* **21**, 4430–4435 (2011).
14. Wang, Y., Tong, S. W., Xu, X. F., Özyilmaz, B. & Loh, K. P. Interface engineering of layer-by-layer stacked graphene anodes for high-performance organic solar cells. *Adv. Mater.* **23**, 1514–1518 (2011).
15. Wu, J. *et al*. Organic light-emitting diodes on solution-processed graphene transparent electrodes. *ACS Nano* **4**, 43–48 (2010).
16. Wang, X., Zhi, L. & Mullen, K. Transparent, conductive graphene electrodes for dye-sensitized solar cells. *Nano Lett.* **8**, 323–327 (2008).
17. Alfano, B. *et al*. Modulating the sensing properties of graphene through an eco-friendly metal-decoration process. *Sensors Actuators, B Chem.* **222**, 1032–1042 (2016).
18. Lynch, P., Khan, U., Harvey, A., Ahmed, I. & Coleman, J. N. Graphene-MoS2 nanosheet composites as electrodes for dye sensitised solar cells. *Mater. Res. Express* **3**, 035007 (2016).
19. Mosciatti, T. *et al*. A multifunctional polymer-graphene thin-film transistor with tunable transport regimes. *ACS Nano* **9**, 2357–2367 (2015).
20. Giubileo, F. & Di Bartolomeo, A. The role of contact resistance in graphene field-effect devices. *Prog. Surf. Sci.* **92**, 143–175 (2017).
21. Kwon, K. C., Kim, B. J., Lee, J. L. & Kim, S. Y. Effect of anions in Au complexes on doping and degradation of graphene. *J. Mater. Chem. C* **1**, 2463–2469 (2013).
22. Kwon, K. C., Choi, K. S. & Kim, S. Y. Increased work function in few-layer graphene sheets via metal chloride doping. *Adv. Funct. Mater.* **22**, 4724–4731 (2012).
23. Kwon, K. C., Choi, K. S., Kim, B. J., Lee, J. L. & Kim, S. Y. Work-function decrease of graphene sheet using alkali metal carbonates. *J. Phys. Chem. C* **116**, 26586–26591 (2012).
24. Huang, J. H., Fang, J. H., Liu, C. C. & Chu, C. W. Effective work function modulation of graphene/carbon nanotube composite films as transparent cathodes for organic optoelectronics. *ACS Nano* **5**, 6262–6271 (2011).
25. Kwon, K. C., Choi, K. S., Kim, C. & Kim, S. Y. Role of metal cations in alkali metal chloride doped graphene. *J. Phys. Chem. C* **118**, 8187–8193 (2014).
26. Wang, X., Xu, J. B., Xie, W. & Du, J. Quantitative analysis of graphene doping by organic molecular charge transfer. *J. Phys. Chem. C* **115**, 7596–7602 (2011).
27. Shin, H. J. *et al*. Control of electronic structure of graphene by various dopants and their effects on a nanogenerator. *J. Am. Chem. Soc.* **132**, 15603–15609 (2010).
28. Shi, Y. *et al*. Work function engineering of graphene electrode via chemical doping. *ACS Nano* **4**, 2689–2694 (2010).

29. Tomašević-Ilić, T. *et al*. Reducing sheet resistance of self-assembled transparent graphene films by defect patching and doping with UV/ozone treatment. *Appl. Surf. Sci.* **458**, 446–453 (2018).
30. Matković, A. *et al*. Spectroscopic imaging ellipsometry and Fano resonance modeling of graphene. *J. Appl. Phys.* **112**, 123523 (2012).
31. Bracamonte, M. V., Lacconi, G. I., Urreta, S. E. & Foa Torres, L. E. F. F. On the nature of defects in liquid-phase exfoliated graphene. *J. Phys. Chem. C* **118**, 15455–15459 (2014).
32. Eckmann, A. *et al*. Probing the nature of defects in graphene by Raman spectroscopy. *Nano Lett.* **12**, 3925–3930 (2012).
33. Rytel, K. *et al*. Ultrasonication-induced sp3 hybridization defects in Langmuir-Schaefer layers of turbostratic graphene. *Phys. Chem. Chem. Phys.* **20**, 12777–12784 (2018).
34. Eckmann, A., Felten, A., Verzhbitskiy, I., Davey, R. & Casiraghi, C. Raman study on defective graphene: Effect of the excitation energy, type, and amount of defects. *Phys. Rev. B - Condens. Matter Mater. Phys.* **88**, 035426 (2013).
35. Drewniak, S. *et al*. Studies of reduced graphene oxide and graphite oxide in the aspect of their possible application in gas sensors. *Sensors* **16**, 103 (2016).
36. Kim, W. J., Basavaraja, C., Thinh, P. X. & Huh, D. S. Structural characterization and DC conductivity of honeycomb-patterned poly(ε-caprolactone)/gold nanoparticle-reduced graphite oxide composite films. *Mater. Lett.* **90**, 14–18 (2013).
37. Ţucureanu, V., Matei, A. & Avram, A. M. FTIR spectroscopy for carbon family study. *Crit. Rev. Anal. Chem.* **46**, 502–520 (2016).
38. Wu, X. *et al*. One-step freezing temperature crystallization of layered rare-earth hydroxide (Ln2(OH)5NO3·nH2O) nanosheets for a wide spectrum of Ln (Ln = Pr-Er, and Y), anion exchange with fluorine and sulfate, and microscopic coordination probed via photoluminescence. *J. Mater. Chem. C* **3**, 3428–3437 (2015).
39. Nakamoto, K. Infrared and Raman Spectra of Inorganic and Coordination Compounds. Part A: Theory and Applications in Inorganic Chemistry; Part B: Application in Coordination, Organometallic, and Bioinorganic Chemistry, 5th Edition (Nakamoto, Kazuo). *John Wiley and Sons* (John Wiley and Sons, 2009).
40. Geng, F. *et al*. New layered rare-earth hydroxides with anion-exchange properties. *Chem. Eur. J.* **14**, 9255–9260 (2008).
41. Lefèvre, G. *In situ* Fourier-transform infrared spectroscopy studies of inorganic ions adsorption on metal oxides and hydroxides. *Adv. Colloid Interface Sci.* **107**, 109–123 (2004).
42. Yu, Y. *et al*. Tuning the graphene work function by electric field effect. *Nano Lett.* **9**, 3430–3434 (2009).
43. Levesque, P. L. *et al*. Probing charge transfer at surfaces using graphene transistors. *Nano Lett.* **11**, 132–137 (2011).
44. Kuruvila, A. *et al*. Organic light emitting diodes with environmentally and thermally stable doped graphene electrodes. *J. Mater. Chem. C* **2**, 6940–6945 (2014).
45. Meyer, J. *et al*. Metal oxide induced charge transfer doping and band alignment of graphene electrodes for efficient organic light emitting diodes. *Sci. Rep* **4**, 5380 (2014).
46. Matković, A. *et al*. Probing charge transfer between molecular semiconductors and graphene. *Sci. Rep* **7**, 9544 (2017).
47. Sanders, S. *et al*. Engineering high charge transfer n-doping of graphene electrodes and its application to organic electronics. *Nanoscale* **7**, 13135–13142 (2015).
48. Han, K. S. *et al*. A non-destructive n-doping method for graphene with precise control of electronic properties via atomic layer deposition. *Nanoscale* **8**, 5000–5005 (2016).
49. Chen, J. H. *et al*. Charged-impurity scattering in graphene. *Nat. Phys.* **4**, 377–381 (2008).
50. Pinto, H. & Markevich, A. Electronic and electrochemical doping of graphene by surface adsorbates. *Beilstein J. Nanotechnol* **5**, 1842–1848 (2014).
51. De, S. & Coleman, J. N. Are there fundamental limitations on the sheet resistance and transmittance of thin graphene films? *ACS Nano* **4**, 2713–2720 (2010).
52. Benayad, A. *et al*. Controlling work function of reduced graphite oxide with Au-ion concentration. *Chem. Phys. Lett.* **475**, 91–95 (2009).
53. López, G. P., Castner, D. G. & Ratner, B. D. XPS O 1s binding energies for polymers containing hydroxyl, ether, ketone and ester groups. *Surf. Interface Anal.* **17**, 267–272 (1991).
54. Hernandez, Y. *et al*. High-yield production of graphene by liquid-phase exfoliation of graphite. *Nat. Nanotechnol* **3**, 563–568 (2008).
55. Kim, H. *et al*. Optoelectronic properties of graphene thin films deposited by a Langmuir-Blodgett assembly. *Nanoscale* **5**, 12365–12374 (2013).
56. Naumkin, A. V., Kraut-Vass, A., Gaarenstroom, S. W. & Powell, C. J. NIST X-ray photoelectron spectroscopy database. Available at: https://srdata.nist.gov/xps/EngElmSrchQuery.aspx?EType=PE&CSOpt=Retri_ex_dat&Elm=Li. (2019).
57. Moulder, J. F., Stickle, W. F., Sobol, P. E. & Bomben, K. D. *Hanbook of X-ray photoelectron spectroscopy. Reference book of standard spectra for indentification and interpretation of XPS data* (Perkin-Elmer Corporation, Physical Electronic division, 1992).
58. Vijayakumar, M. & Jianzhi, H. Exploring the interaction between lithium ion and defective graphene surface using dispersion corrected DFT studies. *ECS Trans* **53**, 23–32 (2013).
59. Pickett, W. E. Negative electron affinity and low work function surface: Cesium on oxygenated diamond (100). *Phys. Rev. Lett.* **73**, 1664–1667 (1994).
60. Syu, J. Y. *et al*. Wide-range work-function tuning of active graphene transparent electrodes via hole doping. *RSC Adv.* **6**, 32746–32756 (2016).
61. Tomašević-Ilić, T. *et al*. Transparent and conductive films from liquid phase exfoliated graphene. *Opt. Quantum Electron.* **48**, 319 (2016).
62. Nonnenmacher, M., O'Boyle, M. P. & Wickramasinghe, H. K. Kelvin probe force microscopy. *Appl. Phys. Lett.* **58**, 2921–2923 (1991).
63. Vasić, B. *et al*. Atomic force microscopy based manipulation of graphene using dynamic plowing lithography. *Nanotechnology* **24**, 015303 (2013).
64. Vasić, B. *et al*. Low-friction, wear-resistant, and electrically homogeneous multilayer graphene grown by chemical vapor deposition on molybdenum. *Appl. Surf. Sci.* **509**, 144792 (2020).
65. Panchal, V., Pearce, R., Yakimova, R., Tzalenchuk, A. & Kazakova, O. Standardization of surface potential measurements of graphene domains. *Sci. Rep* **3**, 2597 (2013).
66. Udum, Y. *et al*. Inverted bulk-heterojunction solar cell with cross-linked hole-blocking layer. *Org. Electron.* **15**, 997–1001 (2014).

Acknowledgements

This work has been supported from the Serbian MPNTR through projects OI 171005, OI 171032, 451-03-02141/2017-09/32 and with support from the Lise Meitner fellowship by Austrian Science Fund (FWF): M 2323-N36. We further acknowledge support by the Austrian Academic Exchange Service (OeAD) via the project SRB 13/2018.

Author contributions

I.M. devised the concept of LPE GS films doping with metal standard solutions in the single-step method. I.M. and J.V. prepared LPE dispersions and fabricated undoped and doped LPE GS films on different substrates. B.V. did AFM and KPFM measurements, A.M. performed electrical measurements, I.M. and J.V. did FTIR measurements, S.A. and I.M. performed Raman measurements and I.M., T.G, M.K., S.A. and J.V. performed and

processed XPS measurements. C.T. and R.G. oversaw the study. I.M., A.M. and B.V. wrote the manuscript. All authors discussed and analysed the results and reviewed the manuscript.

Competing interests

The authors declare no competing interests.

Additional information

Supplementary information is available for this paper at https://doi.org/10.1038/s41598-020-65379-1.

Correspondence and requests for materials should be addressed to I.R.M. or A.M.

Reprints and permissions information is available at www.nature.com/reprints.

Publisher's note Springer Nature remains neutral with regard to jurisdictional claims in published maps and institutional affiliations.

Analyst

ROYAL SOCIETY OF CHEMISTRY

PAPER

View Article Online
View Journal

Cite this: DOI: 10.1039/c9an02518a

Combined Raman and AFM detection of changes in HeLa cervical cancer cells induced by CeO_2 nanoparticles – molecular and morphological perspectives†

Mirjana Miletić,[a] Sonja Aškrabić, *[a] Jan Rüger,[b] Borislav Vasić, [c] Lela Korićanac, [d] Abdullah Saif Mondol,[b] Jan Dellith,[b] Jürgen Popp,[b] Iwan W. Schie[b,e] and Zorana Dohčević-Mitrović[a]

The design of nanoparticles for application in medical diagnostics and therapy requires a thorough understanding of various aspects of nanoparticle–cell interactions. In this work, two unconventional methods for the study of nanoparticle effects on cells, Raman spectroscopy and atomic force microscopy (AFM), were employed to track the molecular and morphological changes that are caused by the interaction between cervical carcinoma-derived HeLa cells and two types of cerium dioxide (CeO_2) nanoparticles, ones with dextran coating and the others with no coating. Multivariate statistical analyses of Raman spectra, such as principal component analysis and partial least squares regression, were applied in order to extract the variations in the vibrational features of cell biomolecules and through them, the changes in biomolecular content and conformation. Both types of nanoparticles induced changes in DNA, lipid and protein contents of the cell and variations of the protein secondary structure, whereas dextran-coated CeO_2 affected the cell-growth rate to a higher extent. Atomic force microscopy showed changes in cell roughness, cell height and nanoparticle effects on surface molecular layers. The method differentiated between the impact of dextran-coated and uncoated CeO_2 nanoparticles with higher precision than performed viability tests. Due to the holistic approach provided by vibrational information on the overall cell content, accompanied by morphological modifications observed by high-resolution microscopy, this methodology offers a wider picture of nanoparticle-induced cell changes, in a label-free single-cell manner.

Received 12th December 2019,
Accepted 24th March 2020

DOI: 10.1039/c9an02518a

rsc.li/analyst

1. Introduction

Nanoparticles (NPs) occupy an important place in the field of biomedicine, having potential in the diagnostics[1,2] and therapy[3–5] of a wide range of diseases. In order to design NPs for targeting a specific cell population and/or specific subcellular compartments, to enhance NP delivery and to achieve an adequate balance between cytotoxic and cytoprotective effects, it is crucial to explore molecular interactions between NPs and cells at different levels.[6] Methods generally used for the investigation of NP–cell interactions are based on a multitude of specific biochemical assays that target one parameter/property per assay and need to employ labels. Screening of the effects of NPs as anticancer agents on the tumor cells *in vitro* is standardly performed using viability/cytotoxicity tests such as trypan blue staining, LDH, SRB, MTT assays and others.[7–10] As mentioned previously, these tests are effect-specific, *i.e.* the trypan blue test dyes the cells only if a membrane is damaged in a way that it becomes permeable, very similar to LDH that detects permeated membranes by measuring the level of lactated hydrogenase released into a culture medium. The SRB test registers the changes in the cell number through the changes in total protein mass and MTT measures the degree of preserved mitochondrial activity. Sometimes changes manifested through a different effect than the one measured by a

[a]Nanostructured Matter Laboratory, Center for Solid State Physics and New Materials, Institute of Physics Belgrade, University of Belgrade, Pregrevica 118, 11080 Belgrade, Serbia. E-mail: sonask@ipb.ac.rs
[b]Leibniz Institute of Photonic Technology, Albert-Einstein-Straße 9, 07745 Jena, Germany
[c]Graphene Laboratory, Center for Solid State Physics and New Materials, Institute of Physics Belgrade, University of Belgrade, Pregrevica 118, 11080 Belgrade, Serbia
[d]Department of Molecular Biology and Endocrinology, Vinča Institute of Nuclear Sciences, University of Belgrade, P.O. Box 522, 11001 Belgrade, Serbia
[e]Department of Medical Engineering and Biotechnology, University of Applied Science Jena, Carl-Zeiss-Promenade 2, 07745 Jena, Germany
†Electronic supplementary information (ESI) available. See DOI: 10.1039/c9an02518a

particular test can remain undetected. For instance, live and metabolically active cells can experience reversible damage of their membranes, while, inversely, dying cells at the initial stages of apoptosis can still have their membranes intact.[7] The most common viability test, trypan blue staining, in these two cases will give false positive or false negative results, respectively. Multiple tests are often needed to detect NP-induced changes and to choose an appropriate approach for the study of the mechanisms behind them most often requires expertise in various analytical techniques. There is a need for methodologies that would enable the extraction of comprehensive data on induced cell changes and detect non-function-specific cellular molecular changes in a single, label-free experiment.

Raman spectroscopy, based on the inelastic scattering of light on molecular vibrations, allows for a label-free and non-destructive way to probe the underlying molecular fingerprint of biological samples.[11] Through the modulations of the corresponding vibrational mode frequencies, linewidths and intensities, characteristics of the transformations of large molecules such as DNA, proteins and lipids can be followed. These changes are of importance because *i.e.* DNA damage can be correlated to cellular processes such as inflammation and oxidative stress,[12] the endocytotic pathway of NP entrance is related to the phospholipid concentration,[13] and the change of the protein secondary structure can mark, for instance, unfolding or aggregation of proteins, or a change in cytoskeleton organization.[14–16] Based on this, Raman spectroscopy represents a tool with potential for fast screening of total biomolecular changes induced in the cells by treatment with NPs and with a possibility of higher sensitivity to the transformations that the cells undergo under the influence of NPs, compared to the tests carried out for the evaluation of individual properties such as cell membrane integrity, protein quantity, mitochondrial activity, *etc*. In the field of biomedical application of NPs, Raman spectroscopy has been mostly employed as an imaging technique for tracing NP intake and subcellular localization.[13,17] Although a few of the studies investigated physiological or pathological changes of the cells induced by drugs and chemicals,[18–21] to our knowledge, there are very few studies that explore the use of Raman spectroscopy for the study of cell changes induced by NPs,[22,23] none of which perform strict multivariate analysis of the entire spectral region of interest for a large number of cells. In addition to the molecular characterization performed by Raman spectroscopy, AFM can be used for the examination of morphology, roughness and composition of particular cell structures, such as cell membrane protrusions, filopodia and lamellipodia, cytoskeleton or sub-membranous cytoplasmatic structures.[24,25] This allows for a more complete and detailed cell morphology investigation and membrane characterization than the one that can be provided by biochemical assays targetting membrane structures.

Among different nanoparticles that have been tested as therapeutic agents, rare-earth oxide CeO_2 NPs are found to be interesting for their therapeutic potential and proposed cell-selective activity: while usually being toxic to cancer cells and sensitizing cancerous tissues to radiotherapy, CeO_2 NPs are often non-toxic to normal healthy cells and even compensate for the negative effects of the radiotherapy on healthy tissues.[26,27] The reason for such a dual activity of CeO_2 NPs lies in their nonstoichiometric nature characterized by the presence of both Ce^{4+} and Ce^{3+} oxidation states and high content of oxygen vacancies. Thus, through oxidation/reduction changes of $Ce^{3+} - Ce^{4+}$, CeO_2 NPs can mediate both oxygen release and intake. Dispersions of powdered CeO_2 NPs in cell medium can be troublesome, which is the case with the majority of oxide nanoparticles, and results in the agglomeration of NPs.[28] Biocompatible coatings such as hydrocarbons, dextran and glucose have been used to coat ceria nanoparticles. By coating with dextran molecules, dispersions of CeO_2 NPs become stable and the controlled application of NPs in cell treatment is enabled.[29] These NPs have been rarely tested as cytotoxic agents[30,31] whereas their interaction with the cells and the influence of the coating on their activity remain unclear. The interaction of CeO_2 NPs with the cells from different cell lines has been evaluated using standard biological assays,[27,32] but their influence on the molecular content and morphology of the cells has not been investigated so far.

In this work, we aimed to investigate the susceptibility of combined Raman and AFM analysis in the detection and discrimination of the effects of two types of oxide NPs of the same crystalline structure and similar composition, but with different coating and redox activities, on HeLa cells, a cervical carcinoma derived cell line. Special attention was dedicated to the analysis of the possible advantages of this methodology over standard biological cytotoxicity assays. The effects of dextran-coated (CD) CeO_2 NPs on HeLa cells were studied for the first time, to our knowledge, and compared to the effect of uncoated CeO_2 NPs. Changes in the vibrational features of intracellular biomolecules induced by NPs were investigated by high-throughput Raman spectroscopy of control cells and two NP-treated cell groups and analyzed by principal component analysis (PCA) and partial least squares regression (PLS). AFM microscopy was used to provide a characterization of NP-induced morphological changes, *i.e.* an increase in the cell roughness, decrease in the cell height and appearance of depressions. The cytotoxicity of CeO_2 NPs was tested *via* trypan blue staining and SRB assay. The combination of Raman spectroscopy and AFM enabled the detection of degrading changes of the nuclear material and cell membrane in the cells induced by both types of NPs. It was shown that group-discriminating spectral modes characteristic of DNA, lipids and proteins experience changes and that the effects of CD NPs are more pronounced compared to those of SPRT NPs. In contrast to the biological cytotoxicity tests, Raman spectroscopy and AFM showed that uncoated CeO_2 NPs also led to a deterioration of cell status. In light of this, our study suggests that Raman spectroscopy, independently or combined with AFM, can be used for the fast and sensitive screening of negative effects that oxide NPs can produce in human cells.

2. Materials and methods

2.1 Nanoparticle synthesis

Two types of CeO_2 NPs were used for the experiments. Uncoated ceria NPs in the powder form, abbreviated in the text as SPRT, were obtained by self-propagating room temperature synthesis, as described in Boskovic *et al.*[33] Dextran-coated NPs (CD in further text) are synthesized in the form of dispersions, based on the synthesis procedure given by Karakoti *et al.*,[29] using ammonia mediated oxidation and dextran T40 for coating.

2.2 Characterization of nanoparticles

The crystalline structure of CeO_2 NPs was investigated by X-ray diffraction (XRD) with a Panalytical X'Pert Pro instrument (PANalytical, Almelo, the Netherlands). Diffraction spectra were recorded in the 2θ interval (20–60)°, with a step size of 0.5°. The X-ray radiation Cu $K\alpha_{1,2}$ line ($K\alpha_1$: transition KLIII; λ = 1.54056 Å) was employed. The Scherrer equation was used for the determination of the crystallite size. TEM (transmission electron microscopy) images were acquired using a JEOL JEM-3010 (300 keV). The average hydrodynamic particle diameter was measured using a Zetasizer Nano ZS90 (Malvern Instruments) apparatus. UV-VIS spectra of NP dispersions were recorded using a Varian Super Scan 3 UV-vis spectrophotometer.

2.3 Cell culture

HeLa cells (ATCC-CCL-2) were grown under standard cell culture conditions (37 °C, 5% CO_2) in DMEM liquid medium with stable glutamine, 3.7 g l^{-1} $NaHCO_3$, and 4.5 g l^{-1} D-glucose (Biochrom AG, Germany) supplemented with 10% fetal calf serum (Merck Millipore, Germany) and 1× penicillin/streptomycin (Sigma Aldrich, Germany). Trypsin/EDTA (0.05%, Biochrom AG, Germany) was employed to detach the cells from the flask, either for passaging, trypan blue assay, Raman imaging or Raman spectroscopy. The seeding density in all cases was 300 000 cells per 25 mm^2 flask or 2000 per well in a 96-well plate.

2.4 Cell treatment with nanoparticles

The cells were treated with NPs 24 hours after seeding in 25 mm^2 flasks (6 batches for CD and 4 batches for SPRT). The starting seeding density, before treatment with NPs, was equal in all batches. CD NPs were added into cell culture medium, to achieve a total concentration of 400 μg ml^{-1}. A stock solution of SPRT NPs has been prepared in sterile deionized water (volume equal to the volume of the applied CD NP solution) and then mixed with cell culture medium in order to reach the final concentration of 400 μg ml^{-1}. Dissolution was aided using an ultrasonic probe system (Bandelin SONOPULS HD 2070), with a power of 15 W, in 3 cycles of 15 s each and 5 s break in between. The medium from the cell flasks was discarded and replaced with the obtained medium with NPs (6 replicates for CD and 4 for SPRT). Proportional volumes of sterile deionized water were added to culture medium in flasks containing control cells. The cells were incubated with NPs for 48 hours, then washed with PBS and detached with trypsin/EDTA. The cells were fixed for 20 min at room temperature in Roti®-Histofix 4% (Roth, Germany), washed twice and re-suspended in PBS. The obtained cell suspensions were used for trypan blue assay, Raman imaging and Raman spectroscopy. In the case of Raman measurements poly-L-lysine was used to immobilize the fixed cells on CaF_2 coverslips. For AFM measurements, the cells were grown on glass coverslips and fixed afterwards in the same manner as described above.

2.5 Trypan blue viability test

Trypan blue at 0.4% (Sigma-Aldrich, Germany) was added to the cell suspension in equal volumes (to obtain a 1 to 2 dilution). Stained and unstained cells were counted within 2–3 minutes using a Neubauer chamber (0.0025 mm^2; Marienfeld, Germany). The percentage of viable (unstained) cells among the total cell population was calculated. Tests were done in 6 replicates for control and CD-treated and in 4 replicates for SPRT-treated cells. The statistical significance of cell number/viability differences between treated and untreated cells was estimated by the one-way ANOVA and *post hoc* Games-Howell test, performed in R.

2.6 Sulforhodamine B assay

The cells were cultured in 96-well plates and treated with NPs (dose and time same as already described). After fixation with trichloroacetic acid, cell cultures were stained for 15 minutes with 0.4% (wt/vol) sulforhodamine B (SRB) (Sigma-Aldrich, Germany) dissolved in 1% acetic acid, according to the procedure given in Skehan *et al.*[9] The unbound dye was removed by four washing steps with 1% acetic acid. SRB which stayed bound to cell proteins was extracted with a 10 mM unbuffered Tris base (Sigma-Aldrich, Germany). The absorbance of the extracted dye solution was measured at 550 nm with a reference wavelength of 690 nm in a microplate reader (Wallac, VICTOR2 1420 Multilabel counter, PerkinElmer, Turku, Finland). The results were presented as the percentage of cell growth determined from the relative ratio between the measured absorbance of the treated sample and absorbance of the control. The assay was performed in 8 replicates for every experimental group. The statistical significance of differences between the treated and untreated cells was estimated by the one-way ANOVA and *post hoc* Games-Howell test, performed in R.

2.7 Raman imaging

Raman imaging was performed on a CRM200 and alpha300 confocal Raman microscope (WITec GmbH, Ulm, Germany). A 785 nm cw diode laser (Toptica Photonics, Gräfelingen, Germany) was used as an excitation source. The laser beam is coupled into the microscope through a single mode optical fiber. The incident laser beam is collimated *via* an achromatic lens and passed through a holographic band pass filter or a dichroic mirror, before it is focused onto the sample through the microscope objective lens. A Nikon Fluor (60×/1.00 NA,

WD = 2.0 mm) water immersion objective was used. The spatial resolution was 0.5 μm, exposure time 0.5 s and a 300 gr mm^{-1} grating was used as a dispersive element. Raman maps of the cells were obtained from focal points in the horizontal plane (*XY*) at different depths and also in the vertical plane (*ZY*), with *XY* being the plane orthogonal to the incident beam direction, and *Z* being the axis parallel to the incident beam direction. Raman spectra were collected from each pixel at different cell depths distanced 1–2.5 μm, and the corresponding maps are made for each plane. The pixel size was 0.5 μm.

2.8 Atomic force microscopy

For AFM measurements, the cells were grown on glass coverslips, treated with NPs and fixed afterwards in the same manner as described above, but without detaching them from the coverslips, and then kept in PBS. Before the experiment they were rinsed twice with water, left to dry at room temperature and then investigated by AFM. AFM measurements of control and treated HeLa cells were performed using an NT-MDT system NTEGRA Prima under ambient conditions (air at the humidity of around 30–40%). Topographic imaging was done in AFM tapping mode, using NSG01 probes from NT-MDT with a typical force constant of 5.1 N m^{-1} and a typical resonant frequency of 150 kHz. Simultaneously with topographic images, the magnitude of AFM cantilever oscillations was recorded as well. In order to make statistical analysis, the AFM measurements were performed on around 15 cells from each group (control, SPRT-treated and CD-treated cells). Two morphological parameters were followed, the cell height and surface roughness. The height was calculated as a maximum height across each cell. The surface roughness was calculated as a root-mean-square deviation of the height distribution of the cell body. Before roughness calculations, all AFM images were flattened by fitting all lines by 2^{nd} order curves.

2.9 Raman spectroscopy

Cell Raman spectra were recorded using a custom-built upright Raman microscopy setup,[34] equipped with a fiber-coupled laser with an excitation wavelength of 532 nm (DPPS, Lasos) and with a power at the sample plane of approximately 50 mW. The excitation light is coupled into a 60× water-immersion objective lens (NA 1.0; Nikon, Japan). The excitation fiber is re-imaged into the sample plane, resulting in a focal spot diameter of approximately 10 μm. The generated Raman signal is collected by the same objective lens and focused using a 60 mm achromatic lens onto the multimodal core, which guides the signal to a spectrometer (IsoPlane160, Princeton Instruments) equipped with a 400 grooves mm^{-1} grating, and detected using a charge-coupled device (CCD) (PIXIS-400BReXcelon; Princeton Instruments). A spectral resolution of 9 cm^{-1} was achieved and spectra were obtained in the interval (400–3300) cm^{-1}. For all experimental groups of cells, *i.e.* control, SPRT-treated, and CD-treated, Raman spectra were recorded and analyzed from 200–250 cells per cell group and the whole experiment was done in duplicate.

2.10 Spectral preprocessing and multivariate data analysis

The processing of Raman spectra was performed in the R environment, using the hyperSpec package. The spectra of a calibration lamp (KOSI, USA) and powdered 4-acetamidophenol (Sigma-Aldrich) were used for intensity and wavenumber calibration, respectively. The spectra were corrected for spectral contributions from water by extended multiplicative scatter correction (EMSC), which is implemented in the cbmodels package.[35,36] The known component spectra of water and cells were used. The spectra obtained entirely from the CaF_2 substrate were excluded from the dataset by k-means clustering. The remaining spectra were normalized relative to the area of spectral ranges of interest (400–1800) cm^{-1} and (2800–3200) cm^{-1}. In order to avoid the influence of CeO_2 mode at 453 cm^{-1}, the spectra were cut below 700 cm^{-1} and used for further analysis. Principal component analysis (PCA) was performed using the prcomp function implemented in R. PLS-LDA analysis was performed in R using widekernelpls.fit and lda functions.

3. Results and discussion

3.1 Characterization of nanoparticles

Two different kinds of CeO_2 NPs were synthesized: uncoated SPRT particles, in nano-powder form, and coated with T40 dextran, CD, in dispersive form. Their crystalline structure and crystallite size were obtained from the analysis of X-ray diffraction patterns. XRD confirmed the fluorite $Fm\bar{3}m$ crystalline structure of CeO_2 both in SPRT and CD NPs. Due to very small sizes of the crystallites, both, the SPRT and CD XRD spectra exhibited broad CeO_2 peaks, Fig. 1(a). The CD spectra, however, had a lower intensity due to much lower sampling mass. The crystallite size calculated from the Scherrer formula was 4 nm for SPRT and 3.5 nm for CD NPs (Table 1).

It is known from previous studies that SPRT NPs have a larger grain size than crystallite size, their average grain size deduced from modeling Raman F_{2g} mode and low-frequency modes is 8–10 nm (ref. 37) and according to the AFM image from Fig. S1(a)† their grain size takes a range of values below ~20 nm. The size of the grains of CD NPs was deduced from transmission electron microscopy, Fig. 1(b). TEM micrographs showed an average grain size of 3–4 nm and confirmed the stability of CD dispersion, with no aggregates and agglomerates observed. In addition to XRD, UV-VIS absorbance measurements of CD and SPRT CeO_2 NPs have been performed, confirming that both types of NPs are CeO_2. The UV-VIS spectra are presented in Fig. S2 of the ESI.† The hydrodynamic radius of NPs obtained by DLS measurements emphasized better stability of CD NPs in water dispersion, compared to SPRT, represented by almost 20 times lower average hydrodynamic radius (Table 1). The results indicate that no aggregates are formed by CD NPs. DLS analysis demonstrated the tendency of SPRT NPs to form agglomerates, and for this reason, an ultrasonic probe system was used for the preparation of SPRT dispersions later in the study. The TEM

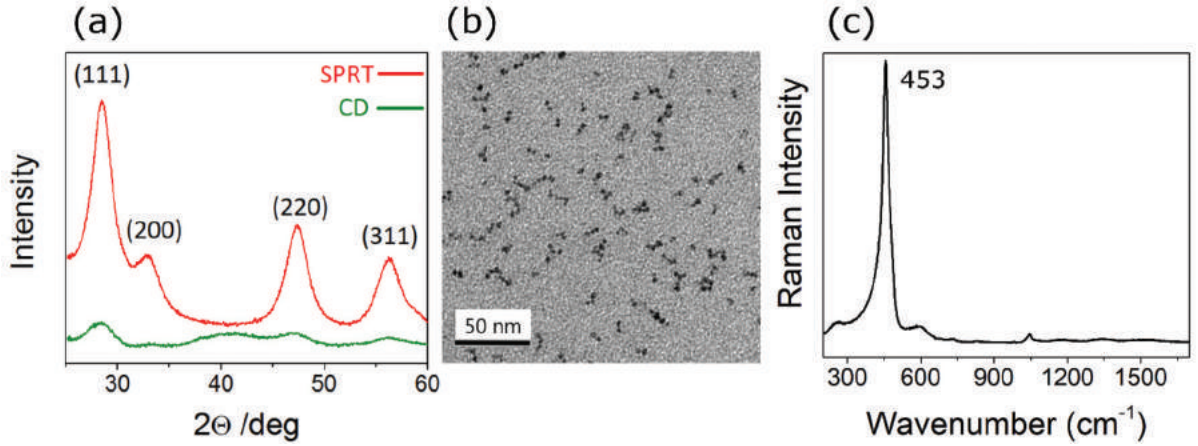

Fig. 1 Characterization of NPs: (a) XRD pattern of SPRT (red) and CD (green) CeO_2 NPs. (b) TEM of CD CeO_2 NPs. (c) Raman spectrum of SPRT CeO_2, showing the characteristic band at 453 cm^{-1}.

Table 1 Crystallite size and average hydrodynamic radius of CeO_2 NPs

	Crystallite size (XRD)	Hydrodynamic radius (DLS)
SPRT (uncoated CeO_2 NPs)	4 nm	849 nm
CD (coated CeO_2 NPs)	3.5 nm	47 nm

image of SPRT NPs in Fig. S1(b)† shows one such agglomerate. Finally, a Raman spectrum of SPRT NPs showed a characteristic CeO_2 Raman F_{2g} mode at 453 cm^{-1}, Fig. 1(c). The Raman mode of CeO_2 was not observed in the spectra of CD NPs, due to the low concentration of small-sized CeO_2 NPs in the dispersion and their very small grain size.

3.2 Cell growth and viability assays

In order to estimate the cell growth changes induced by NPs, both cells attached and cells detached from the flask surface, *i.e.* floating in cell medium, have been counted after incubation with NPs. The results showed an unequivocally significant decrease in cell growth (cell number), following treatment with CD NPs, with $P < 0.01$, Fig. 2(a).

There was, however, a significantly increased number of detached cells for samples treated with these NPs, on average 23% of the total cell number, Fig. 2(g). Considering the detached cells, the total cell number was still significantly lower compared to the control, Fig. 2(b). It can be concluded that CD NPs reduced the growth rate of HeLa cells *in vitro* by five times, presenting around 18% of untreated cell growth. The average cell growth after SPRT NP treatment was also decreased compared to the control (64%), Fig. 2(a) and (b), yet statistically insufficient to confirm the effects of SPRT NPs. A decrease in the growth of CD-treated cells was also evident by simple microscopic observations during experiments, Fig. 2(c) and (d).

To confirm the observed changes in cell growth, a sulforhodamine B (SRB) assay has been used. The test is based on the ability of SRB to bind to proteins' amino acid residues in the cells. The measured absorption of the protein-binding dye is considered to be a measure of cell growth. The results of the SRB assay are shown in Fig. 2(e). The mean growth of control cells is taken as full growth, *i.e.* 100%, whereas the growth of the treated cells was normalized to the mean of control.

The SRB assay was performed in eight batches per three sample groups (one control and two treated), showing a significant decrease of the CD-treated cell growth rate compared to control cells, with $p < 0.05$. It appeared to be reduced on average to 46% regarding the control. Statistical significance for the growth decrease of SPRT-treated cells was below a threshold p value, though a decreasing trend was noticed. The results of SRB growth tests are therefore in accordance with the results obtained by simple cell counting, showing inhibitory effects of CD NPs on HeLa cell growth.

The cell viability was assayed by trypan blue staining, which was chosen because it gives the ratio of the number of dead cells and the number of total cells in the same sample, whereas the majority of viability tests, which are mostly based on colorimetric or fluorescence detection of different reagents, actually normalize the number of dead cells in one sample to the total number of cells in another (control) sample.[8,10] Cell viability tests performed by trypan blue staining are summarized in Fig. 2(f). Although some slightly decreasing trend of the viability of treated cells (especially SPRT-treated cells) can be observed, one-way analysis of variance did not confirm its statistical significance and in conclusion, neither type of CeO_2 NPs influence the cell viability.

Effects of doses of 40 μg ml^{-1} and 100 μg ml^{-1} NPs, as well as exposure times of 24 h and 72 h, are also studied by the SRB test which preceded the tests described above and the results are presented in the ESI (Fig. S3 and S4†). In those experiments, treatment with 400 μg ml^{-1} NPs and exposure of 48 h was chosen as optimal for use in further AFM and Raman experiments.

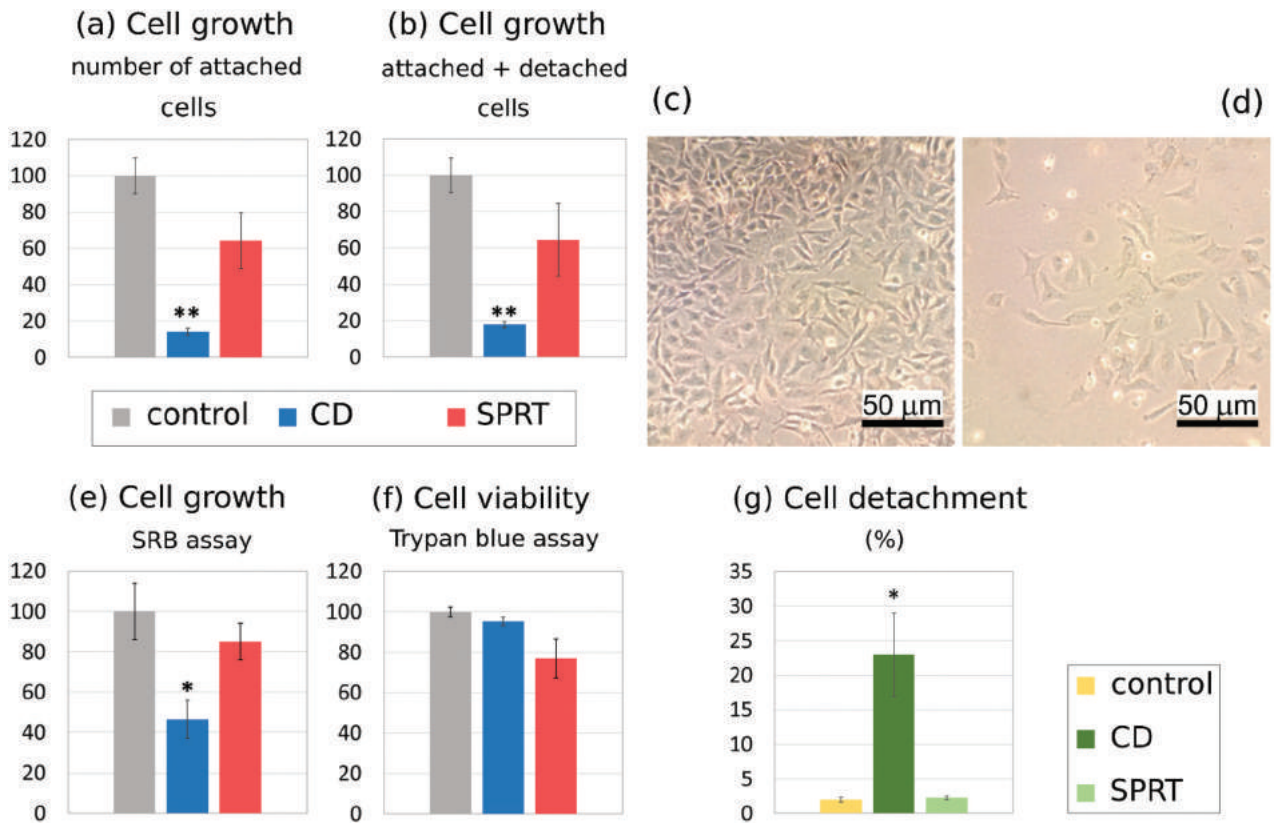

Fig. 2 Results of viability/growth assays. Data presented as mean ± standard error. Statistical significance legend: $*P < 0.05$, $**P < 0.01$, *vs.* control group. (a), (b), (f) and (g) number of replicates $N = 6/6/4$, for untreated/CD-treated/SPRT-treated cells, respectively. (e) $N = 8$, for every group. (a), (b), (e) and (f) Mean of control group is given as 100%, while values for treated groups are expressed related to the mean of control. Statistical significance estimated by one-way ANOVA. (g) Data expressed as the percentage of total number of cells in culture. Statistical significance estimated by one-way non-parametric ANOVA. (c) Microscopy image of control cells. (d) Microscopy image of CD-treated cells. Scale bar on images (c) and (d) is approximate and reflects an order of magnitude.

3.3 Raman imaging

Raman imaging was used to confirm the intracellular localization of SPRT NPs. Due to the small size and surface stability of CD NPs, their Raman signal was too weak to be detected not only in the cells but in the CD NP solution as well. In contrast, SPRT NPs form large aggregates, which results in a strong Raman peak at ~453 cm^{-1} in the spectra of treated cells. Raman maps were reconstructed based on the intensity mapping of the integrated peak area of the Raman mode at 453 cm^{-1}, Fig. 3(a). Fig. 3(b) shows maps obtained according to the Raman intensity in another region of the same spectra, between 1400 and 1500 cm^{-1}. This region is chosen due to a strong signal of characteristic cell Raman features (CH_2 and CH_3 deformation vibrations in proteins and lipids[38]).

At all measured depths, both modes of cell molecules and NPs are present in the Raman spectra. Bright spots on the maps in Fig. 3(a) correspond to dark spots in Fig. 3(b), *i.e.* where the NP mode is more pronounced, the intensity of cell modes is reduced. Considering the confocality of the system, it appears that the NPs are distributed throughout the cytoplasm, and are not only located at the surface of the cell membrane. The Raman images obtained in the vertical plane perpendicular to the previous planes and marked as the *ZY* plane, Fig. 3(c) and (d), confirm the intracellular localization of SPRT NPs. It should be noted that similar Raman maps were made for multiple cells, all showing the presence of NPs throughout the cell.

3.4 Atomic force microscopy (AFM)

The AFM images of control and treated HeLa cells are depicted in Fig. 4. The top, middle and bottom rows display images of control: Fig. 4(a–d), CD-treated: Fig. 4(e–h) and SPRT-treated cells: Fig. 4(i–l), respectively. Going from left to right, the first and the second columns show two-dimensional (2D), Fig. 4(a), (e), and (i), and three-dimensional (3D), Fig. 4(b), (f), and (j), topographic images, respectively. As can be seen, the control cell is characterized with a well-defined nucleus and nucleolus, cell edges and lamellipodia. The surface of the cell is rather smooth, especially on the nucleus. On the other hand, the surface of the cell treated with CD NPs is rough, with pronounced depressions. The nucleus is not well differentiated from the rest of the cell. Several nucleoli are visible, but some of them seem to be fragmented. Finally, the nucleus and nucleoli of the cell treated with SPRT

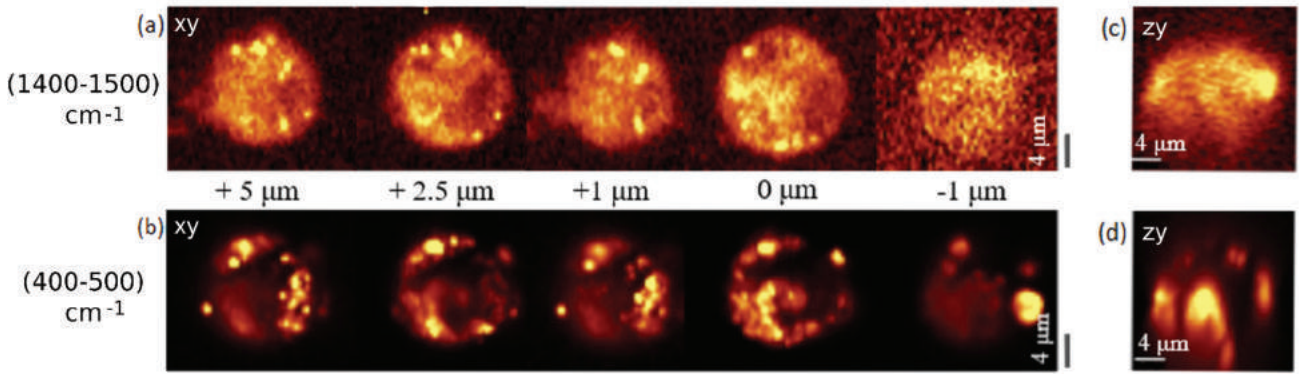

Fig. 3 Raman images of HeLa cells treated with SPRT CeO_2 NPs. (a) and (b) measured in the *XY* plane, (c) and (d) in the *ZY* plane. (a) and (c) made according to the intensity of cell Raman modes in the interval (1400–1500) cm^{-1}. (b) and (d) made according to the integral intensity of NP Raman mode in the range (400–500) cm^{-1}.

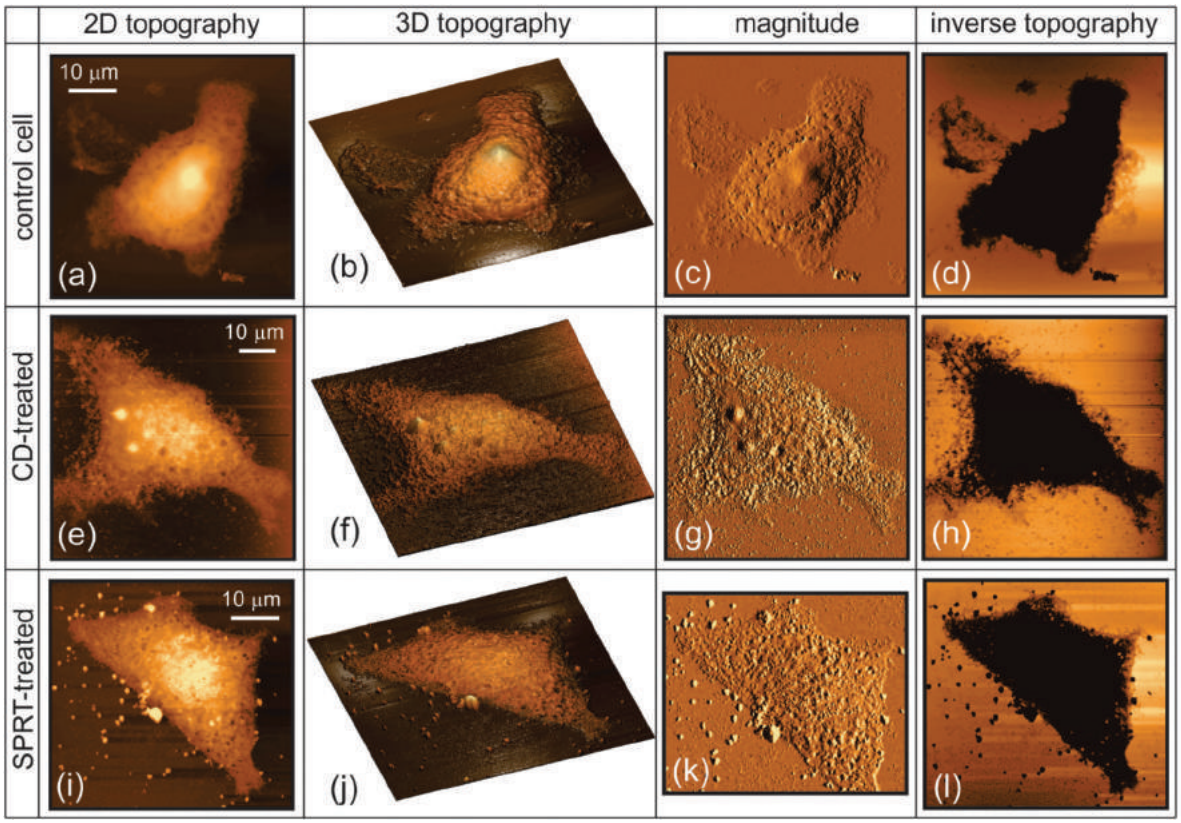

Fig. 4 AFM images of HeLa cells: control (top row), CD-treated (middle row), and SPRT-treated cells (bottom row). The first and the second column (going from the left) show 2D (a, e and i) and 3D (b, f and j) topographical images. The third column shows the AFM magnitude signal (c, g and k). 2D topographical images with inverted contrast emphasizing cell borders are depicted in (d, h and l). Height scales: (a) 1000 nm, (e) and (i) 700 nm.

NPs cannot be recognized and differentiated from the rest of the cell. The cell surface is characterized with large corrugations and many clusters of adsorbed NPs. The visibility of the adsorbed NP clusters is one of the main difference compared to the cells treated with smaller CD NPs, where NPs are hardly visible since they probably penetrated inside cells. The high-resolution AFM images of cell membranes are given in Fig. S5 of the ESI,† showing the appearance of local depressions, 50–100 nm in diameter, in the membranes of treated cells.

The third column of Fig. 4 contains AFM magnitude images, Fig. 4(c), (g), and (k). The magnitude signal is a kind of an error signal with respect to the predefined set-point in AFM tapping mode imaging. Therefore, smooth variations of the magnitude signal across the control cell in Fig. 4(c), especially across the nucleus, indicate a uniform cell surface

without pronounced wrinkles. On the other hand, the magnitude images of the cells treated with NPs in Fig. 4(g) and (k) are very noisy due to the corrugated cell surface. The magnitude image in Fig. 4(c) also shows well defined lamellipodia in the case of the control cell. In order to single out and better emphasize cell edges and lamellipodia, the inverse topographic images in Fig. 4(d), (h), and (l) are given in the most right column. As can be seen, edges of the control cell contain an abundant network of cell brushes. They are fragmented in the cell treated with CD NPs. On the other hand, the cell brushes are rarely seen along the edge of the SPRT-treated cell. The images with the AFM magnitude signal and inverse topography show that there are many small agglomerates around the treated cells which probably originate from the fragmentation of the cell edges and lamellipodia or from NPs, in the case of SPRT NPs.

Fig. 5(a) and (b) present changes of two main morphological parameters, cell height and surface roughness, respectively, due to treatment with NPs. As can be seen, the height of treated cells is decreased in comparison to control cells, and the change is slightly more pronounced for the cells treated with SPRT NPs. As confirmed by the one-way ANOVA test, this change is statistically significant for both types of CeO_2 NPs compared to control, but there is no statistically significant difference between the heights of CD- and SPRT-treated cells. The roughness of CD-treated cells increased to around 13 nm compared to 8 nm measured on the control cells. Increased roughness is a result of many depressions on the cell surface produced by interaction with NPs. The roughness of cells treated with SPRT NPs is not considered due to big adsorbed clusters of NPs, which prevent correct roughness calculation. According to topographic images of control and treated cells, it can be deduced that NPs lead to partial cell damage. This is mainly represented by a decreased height and volume of treated cells, increased surface roughness/corrugations, and not well defined cell elements, such as nucleus, nucleolus, lamellipodia and cell brushes. Overall cell shapes seem to be not influenced by the treatment with NPs, but mainly determined by a local adhesion of cells to the substrate.

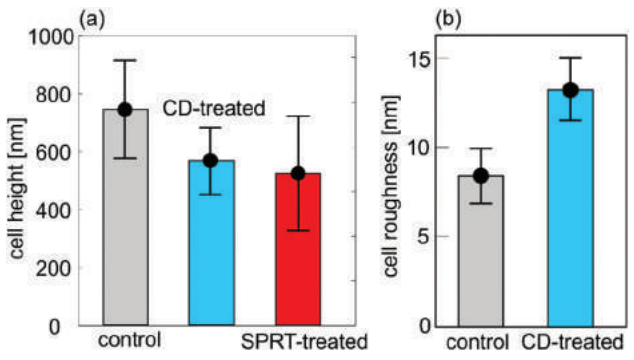

Fig. 5 Morphological changes due to the treatment with NPs: (a) cell height and (b) surface roughness. Roughness of SPRT-treated cells is not considered due to big adsorbed clusters of NPs which prevent correct roughness calculation.

3.5 Raman spectroscopy

The obtained Raman spectra from single cells were analyzed in order to correlate spectral feature changes with NP-induced biomolecular changes. In Fig. 6, the Raman spectra of HeLa cells treated with SPRT NPs, the cells treated with CD NPs and untreated (control) cells are presented as mean ± standard deviation, in the spectral range (700–1800) cm^{-1} and (2800–3200) cm^{-1}. These are the regions where the majority of biomolecules' vibrational peaks are positioned. The obtained Raman spectra were analyzed by PCA, an unsupervised multivariate method used to extract the spectral features, which captures the variance of the analyzed group of spectra. PCA represents the spectra by a linear combination of new, mutually orthogonal vectors, *i.e.* PC loading vectors, which can be multiplied by the corresponding coefficients, PC scores, to reconstruct the original spectra. The first PC loading vector (PC1) carries the largest variance of the entire spectral dataset (control, SPRT-treated and CD-treated, altogether). The amount of variance that PC loading vectors carry decreases with an increasing order of PC loadings and the maximum order is equal to the number of all the Raman spectra subjected to PCA analysis. Generally, for the analysis it is sufficient to use the first few PC components as higher PCs usually absorb more noise.

Local extrema in a PC loading vector can be interpreted as a relative increase/decrease of the intensity of certain vibrational modes. If a PC loading vector contains a maximum at a certain wavenumber and the PC score sign of a spectrum is positive, it suggests that the intensity of the vibrational mode at that particular wavenumber has increased. If, however a PC score sign of the spectrum is negative, the intensity of the particular vibrational mode decreases in this spectrum. Fig. 7 shows PC

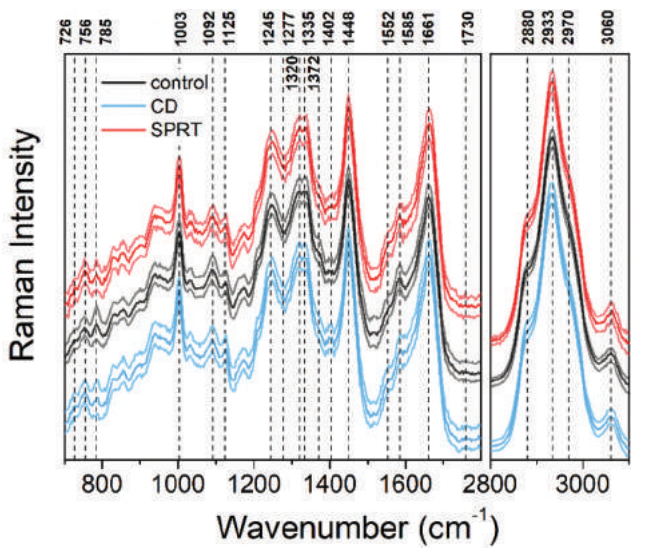

Fig. 6 Raman spectra of control (black), SPRT-treated (red) and CD-treated (blue) cells, presented as mean ± standard deviation. Raman intensity in a high-wavenumber region was rescaled with a factor of 1/3 for presentation purpose.

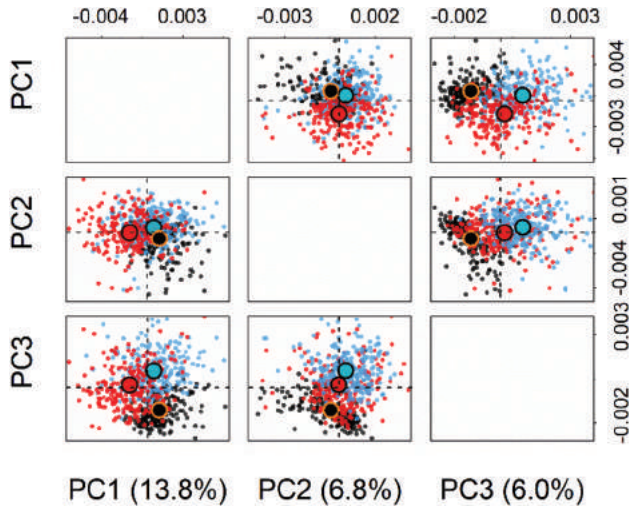

Fig. 7 Score plots of principal component analysis (PCA). Score plots comparing Raman spectra of control (black), SPRT-treated (red) and CD-treated (blue) HeLa cells. Centroids are marked with large bordered circles where circle core colors match the score plot colors of individual groups.

score plots for the first three components, whereas Fig. 8 shows the first three loading vectors (PC1, PC2, PC3) in comparison with two difference spectra (D1/D2), obtained as the difference in control mean spectrum and NP-treated cell mean spectrum (SPRT/CD respectively). According to the PC scores shown in Fig. 7, the PC1 component that carries 13.8% of the total spectral variance separates best SPRT-treated cell spectra from control cell spectra. The PC3 component accounting for 6.0% of spectral variance separates best CD-treated cell spectra from control cell spectra. Since we aim to find the changes between three groups of cells, we choose to analyze the PC1 and PC3 components that separate best the spectra of the three studied cell groups, as presented in Fig. 8. Afterward, these features are related to the molecular changes in the cells induced by SPRT and CD NPs. Score values of the second principal component, PC2, Fig. 7, do not show observable separation between three studied groups of cells and are not analyzed in further text.

The Raman modes present in measured spectra and their assignment to particular biomolecular vibrations are listed in Table 2. In Fig. S6 from the ESI† first three PC loadings in the range (700–1800) cm^{-1} are shown for better clarity.

In the low-wavenumber region (700–1800 cm^{-1}), the PC1 loading does not exhibit particularly prominent features. Still, several peaks can be distinguished. That is the case with a positive peak at 785 cm^{-1}, negative extrema at 1003 cm^{-1} and 1670 cm^{-1}, and few peaks in the region from 1300 to 1515 cm^{-1}. The Raman mode positioned at 785 cm^{-1} is a

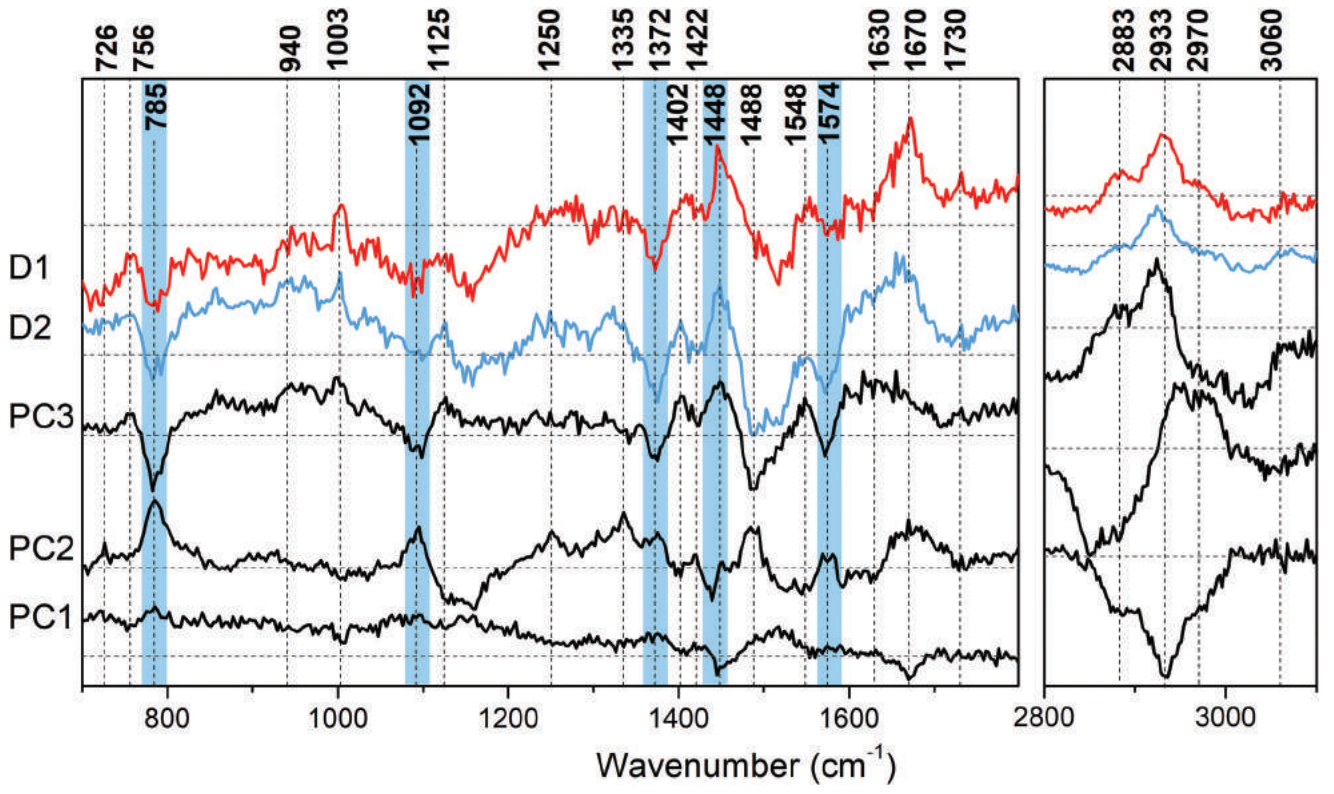

Fig. 8 First three loading spectra (PC1–PC3, from bottom to top), exhibiting Raman spectral differences between cells treated with two types of CeO_2 NPs and untreated (control) cells. Difference spectra (D1, D2), obtained by subtracting the mean spectrum of control cells from the mean spectra of NP-treated cells, are shown at the top of the plot (blue for CD-treated cells, red for SPRT-treated cells). Most prominent modes assigned to nucleic acids are marked with blue shading.

Table 2 Raman modes in the measured cell spectra and their possible assignations

Mean spectra	PC1	PC2	PC3	
Raman bands (cm^{-1})				Related macromolecule
726	720	726		Nucleic acids
756	756	756	756	Tryptophan
785	785	785	785	Nucleic acids
830/853				Tyrosine
940			940	Proteins
1003	1003	1003	1003	Phenylalanine
1092	1092	1092	1092	Nucleic acids
1125	1125	1125	1125	Lipids, proteins
1245		1250		Amide III
1277				Amide III
1320				Proteins, nucleic acids
1335		1335		Proteins, nucleic acids
1372	1372	1372	1372	Nucleic acids
1402	1402	1402	1402	Proteins
	1422	1420	1422	Nucleic acids
1448	1448		1448	Proteins, lipids
		1488	1488	Nucleic acids
1552		1552	1548	Tryptophan
1585		1574	1574	Nucleic acids
	1630	1630	1630	Amide I
1661	1670	1670		Amide I
1730		1730	1730	Lipids
2880	2883		2883	Proteins, lipids
2933	2933		2924	Proteins, lipids
2970				Lipids
3060		3060	3060	Proteins, lipids

typical marker of nucleic acids (ring breathing mode in DNA and RNA bases[39]). Along with less prominent peaks at 726 cm^{-1} and 1092 cm^{-1}, also positive in PC1 loading, as well as the ring-breathing DNA mode at 1372 cm^{-1} and deoxyribose mode at 1422 cm^{-1}, it indicates a decrease in nucleic acid content in SPRT-treated cells (due to negative PC1 scores), when compared to control cells.[39–41] The protein and lipid signals in a Raman spectrum cannot be clearly distinguished, sharing often the same spectral frequencies. Nevertheless, these modes in the PC1 loading spectrum are negative, indicating an increase in total protein and lipid content in SPRT-treated cells. Protein modes at 756 cm^{-1} and 1003 cm^{-1} are assigned to aromatic amino acids, tryptophan and phenylalanine, respectively,[42,43] while the mode at 1402 cm^{-1} (ref. 44) arises from protein methyl groups. The prominent mode at 1670 cm^{-1} represents the amide I band. Its precise spectral position depends on the type of protein secondary structure. Modes at 1448 cm^{-1} and 1125 cm^{-1} could arise from both proteins and lipids.[42,45] Those peaks are, as mentioned above, negative in PC1 loading, having greater contribution in the SPRT-treated cell spectra.

Although the high-wavenumber region of PC1 loading exhibits only a few peaks, those are very pronounced. It therefore demonstrates large differences in this spectral region between groups of cells and seems to be the most important discriminating feature for SPRT-treated cells. Modes in this region originate from protein and lipid vibrations. Although individual contributions of proteins and lipids cannot be clearly distinguished, it was established in the literature that the CH_2 stretching vibration at 2851 cm^{-1} is more of lipid character and that the symmetric CH_3 stretching vibration at 2928 cm^{-1} is more of protein character.[46] Since negative peaks positioned at 2883 cm^{-1} and 2933 cm^{-1} were observed in PC1 loading, this region indicates a higher global lipid and protein content in SPRT-treated cells, which is in accordance with the lower wavenumber region data.

As previously said, PC3 represents spectral changes that help to separate the spectra of CD-treated cells from those of control cells. Score values for PC3 are positive for CD-treated cells and negative for control cells. When it comes to SPRT-treated cells, it can be observed that roughly one half of cell spectra have negative and the other half have positive values of PC3 scores. In accordance with that, the positive peaks in PC3 loading denote a relative increase in the corresponding molecules in CD-treated cells. Contrary to PC1 loading, PC3 loading is more similar to D2, the difference spectrum of CD-treated cells.

Most prominent bands in the PC3 loading are those assigned to nucleic acids. That group consists of already mentioned 785 cm^{-1} mode along with modes at 1092 cm^{-1}, 1488 cm^{-1} and 1574 cm^{-1}.[42,47–49] A negative sign of these peaks in PC3 loading leads to the conclusion that CD-treated cells carry the smallest DNA content, while SPRT-treated cells also have smaller DNA content compared to control, but larger compared to CD-treated cells. Slightly less prominent negative peaks at 1372 cm^{-1} and 1422 cm^{-1} can also be assigned to nucleic acid vibrations.[40] The decreased DNA content is, therefore, the main characteristic of CD-treated HeLa cells.

Except nucleic acid Raman modes, PC3 loading contains two positive peaks: at 1402 cm^{-1}, assigned to proteins, and at 1448 cm^{-1}, assigned to proteins and lipids. The feature at 1730 cm^{-1} cannot be definitely included into the analysis due to its very low intensity, but it should be mentioned that the mode at this position represents a typical lipid spectral marker, while the peak at 1125 cm^{-1} can arise both from lipids and proteins.[42,44,45] The increased lipid content is, therefore, a discriminating feature also for CD-treated cells (not only SPRT-treated, shown by PC1).

More protein Raman modes in PC3 loading are represented with positive peaks at 756 cm^{-1}, 1003 cm^{-1} and 1630 cm^{-1}. The first two originate from aromatic amino acids, tryptophan and phenylalanine,[43] respectively, while the feature at 1630 cm^{-1} belongs to the amide I band. The amide I band in protein Raman spectra can be observed as a broad peak covering frequencies from 1600 cm^{-1} to 1690 cm^{-1}, approximately.[50] It has been used for studies of the protein secondary structure,[42] being highly sensitive to changes in the molecular geometry and hydrogen binding of peptide groups. In both difference spectra as well as in PC1 and PC3 loadings a feature at ~1670 cm^{-1} is present, which can be related to the relative increase of the protein content. In PC3 loading, as well as in CD-cell difference spectrum, a low-wavenumber wing of the amide I band, centered around 1630 cm^{-1}, is more pronounced than in PC1 loading and SPRT-treated cell difference spectrum. This indicates changes in the protein secondary

structure specific for the cells treated with CD NPs. However, this spectral region also contains some water vibration modes[51] which were subtracted during spectra preprocessing, but some artifacts due to this can appear.

A similar conclusion about the increase of total protein and lipid content in NP-treated cells can be derived analyzing the high-wavenumber region of PC3 loading. All modes in this region, at 2883 cm^{-1}, 2924 cm^{-1} and 3060 cm^{-1}, can be assigned to proteins and lipids, though the band at 2883 cm^{-1} is more of lipid character, while the one at 2924 cm^{-1} is more of protein character mode.[46,52] It should be noticed that the peak at 2924 cm^{-1} in PC3 loading is shifted when compared to the 2933 cm^{-1} peak in the original mean cell spectra, as well as compared with the corresponding peak in the PC1 loading spectrum.

To summarize, PC3 indicates a decrease in nucleic acid and an increase in protein and lipid content of NP-treated cells, with observable differences in the relative ratio of features in the amide I band region for SPRT- and CD-treated cell spectra, suggesting changes in the protein secondary structure for the latter.

Contrary to the expectations that uncoated NPs affect the cells more strongly than coated NPs, due to their free surface accessible to the cell molecules, the results from conventional biological assays and Raman measurements lead to the conclusion that dextran-coated CD NPs had a higher impact on cells. The reason for that could be found in the stability *i.e.* the size of NPs. Coated CD NPs, being smaller in size (3–4 nm), can affect the cells more successfully than large aggregates of uncoated SPRT NPs, as the coated particles pass through cell structures more easily. Our AFM measurements showed that a portion of SPRT NPs rest on the cell surface, in the form of large clusters, which interferes with the AFM characterization of the cell membrane surface. However, the Raman imaging results indicate that at least part of the SPRT NPs passes the cell membrane and are located within the cytoplasm and possibly other cell organelles, except the nucleus. Still, the level of activity of those intracellular NP aggregates is lower than the activity of CD NPs, as has been shown by the SRB assay. In order to ensure that the observed changes in the growth of CD-treated cells are caused by CeO_2 and not by dextran itself, we tested for potential interfering effects of a dextran solution on cell culture. A 48 hour treatment with the aqueous dextran solution of the concentration equal to the one used in NP synthesis showed no effect on the growth of cell culture. We thereby confirmed that the effect is due to ceria solely and that dextran itself does not affect the growth, viability and detaching of the cells from the surface.

Conventional biological assays showed that effects of NPs were represented mainly by cell growth inhibition, *i.e.* by a decrease of the overall cell number in treated cell samples. Based on the literature data, most typical Raman spectral markers for reduced cell growth are changes in nucleic acids' Raman modes. In our experiments, the most pronounced differences between the treated and control Raman spectra are also nucleic acids' peaks, indicating the reduced quantity of cell nucleic acids and/or nuclear condensation level. An increase in the overall quantity of proteins and lipids in NP-treated cells points out the effects caused primarily by CD NPs. This could be associated with the enlargement of the overall cell membranous area, due to vacuolization processes, often following NP internalization in the cell.[53]

AFM showed the depletion of lamellipodia and increased levels of cell surface corrugation, as well as poorly defined nuclei borders and partly fragmented nucleoli, in NP-treated cells compared to control cells. Those features are already studied as potential mechanical biomarkers for monitoring antitumor drug effects.[54] It has been shown that the surface roughness of HeLa cells is increased after treatment with some antitumor drugs, which act as proliferation inhibitors.[55] Protein-related changes represented by the features in the amide I band region in the cell Raman spectra could be related to the reorganization of cytoskeletal elements and membrane proteins, causing cell surface modulations.

It was shown that nanoceria interfere with the cytoskeletal organization of neural stem cells.[15] It was also observed that

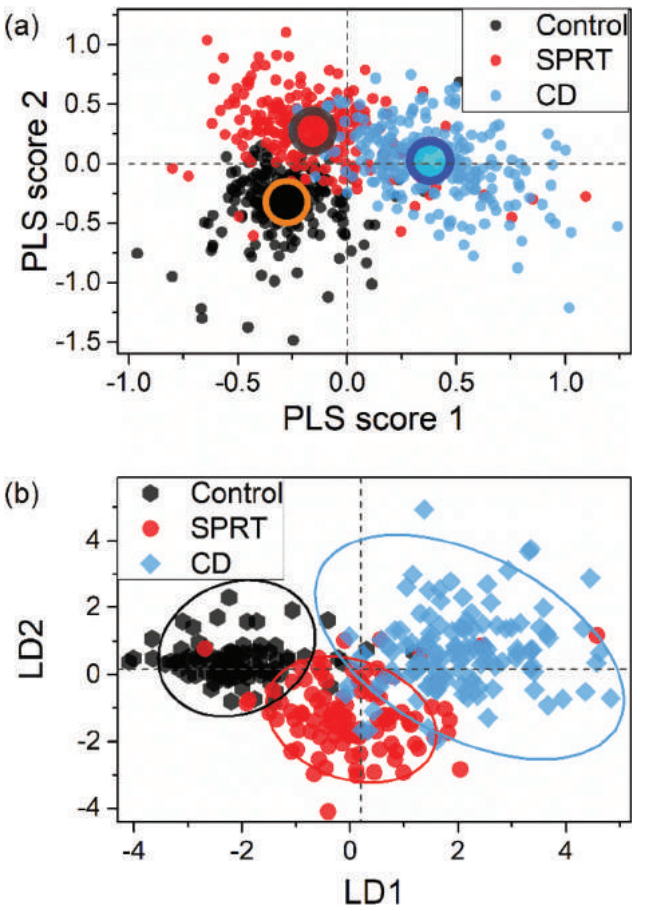

Fig. 9 (a) PLS score plot of first two components. Black dots represent control cells, red SPRT-treated cells and blue dots CD-treated cells, centroids are marked with large bordered circles where circle core colors match the score plot colors of individual groups. (b) LDA projections on LD1 and LD2 for a tested set of spectra. Black hexagons represent control cells, red circles SPRT-treated cells and blue rhombuses CD-treated cells.

gold NPs inhibit the polymerization of cytoskeletal protein tubulin, inducing amide bands' shifts.[14] These NPs induce cell cycle arrest and apoptosis of human lung and breast cancer cells, as shown in the same study. In our experiments, CeO_2 NPs affected the cells by decreasing the cell growth, that could be a consequence of apoptosis or cell cycle arrest.

3.6 Classification of the cells treated with nanoparticles

Partial least squares regression (PLS) analysis is, unlike PCA, a supervised multivariate method and takes into account prior knowledge on the group association of spectra. It is used to decompose the spectral variance in such a way that it optimally separates the spectra from different groups of samples. PLS analysis was performed on all three groups of spectra. PLS scores spanning the space of first two PLS components are shown in Fig. 9(a). A PLS-LDA model was built using a share of total spectral dataset and then tested on the remaining spectra. Linear discriminant analysis (LDA) using first five PLS components was trained on random 360 spectra (training set), 120 from each cell group, and the model was tested on the remaining spectra from the total of 683.

LD1/LD2 scores for the tested spectra are shown in Fig. 9(b) demonstrating good separation and enabling good prediction for spectra membership in each of three groups. The sensitivity of the LDA prediction was 88% and specificity was 92%. The quality of spectra separation shows a potential for the method application in the separation of cells of the same type treated with different kinds of NPs.

4. Conclusions

AFM and Raman spectroscopy were used to study the morphological and molecular changes of HeLa cells exposed to dextran-coated (CD) CeO_2 NPs and uncoated (SPRT) CeO_2 NPs. AFM showed degrading changes of the cell membrane and lamellipodia and an increase of surface roughness in the treated cells. Raman spectroscopy showed that coated CD NPs have a higher impact on HeLa cells, observed through the decrease of DNA content and the increase of the lipid/protein content. Furthermore, modifications in the spectral region characteristic of the protein secondary structure, induced by coated CD NPs, were detected in their Raman spectra. These changes could be connected with cytoskeleton reorganization, causing morphological modifications of the cell surface.

Based on the results of this study, single-cell Raman spectroscopy performed fast and on a large number of cells has potential for quick screening of cell DNA content changes resulting from NP exposure. Raman analysis demonstrated that the two types of ceria NPs both affect DNA, while standard biological assays had been able to confirm only the effects of CD NPs. The formation of lipid structures and the modification of cell proteins can sometimes signal the mechanism of the NP–cell interaction, and these changes are also observable by Raman spectroscopy, as demonstrated in this work. The AFM investigation of surface cell properties combined with Raman spectral fingerprinting of surface molecular structures might be used to extract information on the effect of NPs on the cell–cell and the cell–environment communication. In general, the results obtained by Raman spectroscopy provide guidelines for a more detailed characterization of NP–cell interactions. Finally, multivariate PLS-LDA modeling marked the potential of Raman spectroscopy for the classification of the cells of the same origin in different physiological statuses caused by NPs.

Conflicts of interest

There are no conflicts to declare.

Acknowledgements

This work was supported by the Serbian Ministry of Education, Science and Technological Development (SMESTD) under projects OI 171032, OI 171005 and III 41027, Institute of Physics Belgrade through the grant of SMESTD and German Academic Exchange Service through DAAD project no. 91676974. B. V. acknowledges the support of "Pokreni se za nauku – Startup for science" grant. The authors acknowledge the Leibniz Institute of Age Research – Fritz Lipmann Institute Jena providing access to TEM and to Franka Jahn and Branko Matović for TEM images of nanoparticles. M. M. and S. A. wish to thank Natalie Töpfer, Vera Dugandžić, Novica Paunović and Dimitrije Stepanenko for helpful discussions.

References

1 X. Huang, R. O'Connor and E. A. Kwizera, *Nanotheranostics*, 2017, **1**, 80–102.
2 H. Jo, J. Her and C. Ban, *Biosens. Bioelectron.*, 2015, **71**, 129–136.
3 K. Kalimuthu, B.-C. Lubin, A. Bazylevich, G. Gellerman, O. Shpilberg, G. Luboshits and M. A. Firer, *J. Nanobiotechnol.*, 2018, **16**, 34.
4 S. S. Lucky, K. C. Soo and Y. Zhang, *Chem. Rev.*, 2015, **115**, 1990–2042.
5 O. Lushchak, A. Zayachkivska and A. Vaiserman, *Oxid. Med. Cell. Longevity*, 2018, **2018**, 9.
6 A. Gallud, K. Kloditz, J. Ytterberg, N. Ostberg, S. Katayama, T. Skoog, V. Gogvadze, Y. Z. Chen, D. Xue, S. Moya, J. Ruiz, D. Astruc, R. Zubarev, J. Kere and B. Fadeel, *Sci. Rep.*, 2019, **9**, 4366.
7 M. Wunsch, R. Caspell, S. Kuerten, P. Lehmann and S. Sundararaman, *Cells*, 2015, **4**, 40–55.
8 P. Kumar, A. Nagarajan and P. D. Uchil, *Cold Spring Harb. Protoc.*, 2018, **2018**, 465–468.
9 P. Skehan, R. Storeng, D. Scudiero, A. Monks, J. McMahon, D. Vistica, J. T. Warren, H. Bokesch, S. Kenney and M. R. Boyd, *J. Natl. Cancer Inst.*, 1990, **82**, 1107–1112.

10 T. L. Riss, R. A. Moravec, A. L. Niles, S. Duellman, H. A. Benink, T. J. Worzella and L. Minor, in *Assay Guidance Manual*, ed. G. S. Sittampalam, A. Grossman, K. Brimacombe, M. Arkin, D. Auld, C. Austin, J. Baell, B. Bejcek, J. M. M. Caaveiro, T. D. Y. Chung, N. P. Coussens, J. L. Dahlin, V. Devanaryan, T. L. Foley, M. Glicksman, M. D. Hall, J. V. Haas, S. R. J. Hoare, J. Inglese, P. W. Iversen, S. D. Kahl, S. C. Kales, S. Kirshner, M. Lal-Nag, Z. Li, J. McGee, O. McManus, T. Riss, O. J. Trask Jr., J. R. Weidner, M. J. Wildey, M. Xia and X. Xu, Eli Lilly & Company and the National Center for Advancing Translational Sciences, Bethesda (MD), 2004, https://www.ncbi.nlm.nih.gov/books/NBK144065/.
11 D. W. Shipp, F. Sinjab and I. Notingher, *Adv. Opt. Photonics*, 2017, **9**, 315–428.
12 T. A. J. de Souza, T. L. Rocha and L. P. Franchi, *Adv. Exp. Med. Biol.*, 2018, **1048**, 215–226.
13 M. P. Harvanova, J. Jiravova, J. Malohlava, K. B. Tomankova, D. Jirova and H. Kolarova, *Int. J. Pharm.*, 2017, **528**, 280–286.
14 D. Choudhury, P. L. Xavier, K. Chaudhari, R. John, A. K. Dasgupta, T. Pradeep and G. Chakrabarti, *Nanoscale*, 2013, **5**, 4476–4489.
15 A. R. Gliga, K. Edoff, F. Caputo, T. Källman, H. Blom, H. L. Karlsson, L. Ghibelli, E. Traversa, S. Ceccatelli and B. Fadeel, *Sci. Rep.*, 2017, **7**, 9284.
16 R. Parveen, T. N. Shamsi and S. Fatima, *Int. J. Biol. Macromol.*, 2017, **94**, 386–395.
17 L. Ahlinder, B. Ekstrand-Hammarström, P. Geladi and L. Österlund, *Biophys. J.*, 2013, **105**, 310–319.
18 E. Brauchle, S. Thude, S. Y. Brucker and K. Schenke-Layland, *Sci. Rep.*, 2014, **4**, 4698.
19 A. S. Mondol, N. Töpfer, J. Rüger, U. Neugebauer, J. Popp and I. W. Schie, *Sci. Rep.*, 2019, **9**, 12653.
20 A. Pliss, A. N. Kuzmin, A. V. Kachynski and P. N. Prasad, *Biophys. J.*, 2010, **99**, 3483–3491.
21 I. W. Schie, L. Alber, A. L. Gryshuk and J. W. Chan, *Analyst*, 2014, **139**, 2726–2733.
22 E. Fazio, A. Speciale, S. Spadaro, M. Bonsignore, F. Cimino, M. Cristani, D. Trombetta, A. Saija and F. Neri, *Colloids Surf., B*, 2018, **170**, 233–241.
23 M. Lasalvia, G. Perna and V. Capozzi, *Sensors*, 2019, **19**, 2418.
24 F. Braet, C. Seynaeve, R. De Zanger and E. Wisse, *J. Microsc.*, 2001, **190**, 328–338.
25 H. A. McNally, B. Rajwa, J. Sturgis and J. P. Robinson, *J. Neurosci. Methods*, 2005, **142**, 177–184.
26 G.-M. Lyu, Y.-J. Wang, X. Huang, H.-Y. Zhang, L.-D. Sun, Y.-J. Liu and C.-H. Yan, *Nanoscale*, 2016, **8**, 7923–7932.
27 S. Rajeshkumar and P. Naik, *Biotechnol. Rep.*, 2018, **17**, 1–5.
28 L. Benameur, M. Auffan, M. Cassien, W. Liu, M. Culcasi, H. Rahmouni, P. Stocker, V. Tassistro, J.-Y. Bottero, J. Rose, A. Botta and S. Pietri, *Nanotoxicology*, 2014, **9**, 696–705.
29 A. S. Karakoti, S. V. N. T. Kuchibhatla, K. S. Babu and S. Seal, *J. Phys. Chem. C*, 2007, **111**, 17232–17240.
30 E. Alpaslan, H. Yazici, N. H. Golshan, K. S. Ziemer and T. J. Webster, *ACS Biomater. Sci. Eng.*, 2015, **1**, 1096–1103.
31 J. M. Perez, A. Asati, S. Nath and C. Kaittanis, *Small*, 2008, **4**, 552–556.
32 S. Mittal and A. K. Pandey, *BioMed Res. Int.*, 2014, **2014**, 891934.
33 S. Boskovic, D. Djurovic, Z. Dohcevic-Mitrovic, Z. Popovic, M. Zinkevich and F. Aldinger, *J. Power Sources*, 2005, **145**, 237–242.
34 I. W. Schie, J. Rüger, A. S. Mondol, A. Ramoji, U. Neugebauer, C. Krafft and J. Popp, *Anal. Chem.*, 2018, **90**, 2023–2030.
35 E. Cordero, F. Korinth, C. Stiebing, C. Krafft, I. Schie and J. Popp, *Sensors*, 2017, **17**, 1724.
36 C. Stiebing, I. W. Schie, F. Knorr, M. Schmitt, N. Keijzer, R. Kleemann, I. J. Jahn, M. Jahn, A. J. Kiliaan, L. Ginner, A. Lichtenegger, W. Drexler, R. A. Leitgeb and J. Popp, *Neurophotonics*, 2019, **6**, 1–9.
37 R. Kostić, S. Aškrabić, Z. Dohčević-Mitrović and Z. V. Popović, *Appl. Phys. A*, 2007, **90**, 679–683.
38 C. Matthäus, T. Chernenko, J. A. Newmark, C. M. Warner and M. Diem, *Biophys. J.*, 2007, **93**, 668–673.
39 J. W. Chan, D. S. Taylor, T. Zwerdling, S. M. Lane, K. Ihara and T. Huser, *Biophys. J.*, 2006, **90**, 648–656.
40 A. J. Ruiz-Chica, M. A. Medina, F. Sánchez-Jiménez and F. J. Ramírez, *J. Raman Spectrosc.*, 2004, **35**, 93–100.
41 I. W. Schie and T. Huser, in *Comprehensive Physiology*, ed. R. Terjung, American Physiological Society, 2013, vol. 3, pp. 941–956.
42 Z. Movasaghi, S. Rehman and I. U. Rehman, *Appl. Spectrosc. Rev.*, 2007, **42**, 493–541.
43 N. Stone, C. Kendall, N. Shepherd, P. Crow and H. Barr, *J. Raman Spectrosc.*, 2002, **33**, 564–573.
44 R. K. Dukor, in *Handbook of Vibrational Spectroscopy*, ed. J. M. Chalmers and P. R. Griffiths, John Wiley & Sons, Ltd., 2006, pp. 3335–3361, DOI: 10.1002/0470027320.s8107.
45 K. Czamara, K. Majzner, M. Z. Pacia, K. Kochan, A. Kaczor and M. Baranska, *J. Raman Spectrosc.*, 2015, **46**, 4–20.
46 N. J. Kline and P. J. Treado, *J. Raman Spectrosc.*, 1997, **28**, 119–124.
47 I. Notingher, I. Bisson, J. M. Polak and L. L. Hench, *Vib. Spectrosc.*, 2004, **35**, 199–203.
48 V. V. Pully, A. T. M. Lenferink and C. Otto, *J. Raman Spectrosc.*, 2011, **42**, 167–173.
49 N. Stone, C. Kendall, J. Smith, P. Crow and H. Barr, *Faraday Discuss.*, 2004, **126**, 141–157.
50 A. Rygula, K. Majzner, K. M. Marzec, A. Kaczor, M. Pilarczyk and M. Baranska, *J. Raman Spectrosc.*, 2013, **44**, 1061–1076.
51 D. M. Carey and G. M. Korenowski, *J. Chem. Phys.*, 1998, **108**, 2669–2675.
52 K. Czamara, K. Majzner, A. Selmi, M. Baranska, Y. Ozaki and A. Kaczor, *Sci. Rep.*, 2017, **7**, 40889.
53 D. Septiadi, F. Crippa, T. L. Moore, B. Rothen-Rutishauser and A. Petri-Fink, *Adv. Mater.*, 2018, **30**, e1704463.
54 X. Yun, M. Tang, Z. Yang, J. J. Wilksch, P. Xiu, H. Gao, F. Zhang and H. Wang, *RSC Adv.*, 2017, **7**, 43764–43771.
55 K. S. Kim, C. H. Cho, E. K. Park, M.-H. Jung, K.-S. Yoon and H.-K. Park, *PLoS One*, 2012, **7**, e30066.

Processing and Application of Ceramics 14 [2] (2020) 102–112
https://doi.org/10.2298/PAC2002102D

Influence of oxygen vacancy defects and cobalt doping on optical, electronic and photocatalytic properties of ultrafine $SnO_{2-\delta}$ nanocrystals

Zorana D. Dohčević-Mitrović[1,*], Vinicius D. Araújo[2], Marko Radović[3], Sonja Aškrabić[1], Guilherme R. Costa[4], Maria Ines B. Bernardi[4], Dejan M. Djokić[1], Bojan Stojadinović[1], Marko G. Nikolić[5]

[1]*Nanostructured Matter Laboratory, Institute of Physics Belgrade, University of Belgrade, Pregrevica 118, 11080 Belgrade, Serbia*
[2]*NanoA-UACSA, Universidade Federal Rural de Pernambuco, UFRPE, Cabo de Santo Agostinho, PE, Brazil*
[3]*University of Novi Sad, Group for Nano and Microelectronics, Biosense Institute, Novi Sad, Serbia*
[4]*Instituto de Física de São Carlos, Universidade de São Paulo, USP, 13560-970, São Carlos – SP, Brasil*
[5]*Institute of Physics Belgrade, University of Belgrade, P.O. Box 68, Pregrevica 118, 11080 Belgrade, Serbia*

Received 12 November 2019; Received in revised form 21 February 2020; Accepted 15 March 2020

Abstract

Ultrafine pure and cobalt doped $SnO_{2-\delta}$ nanocrystals ($Sn_{1-x}Co_xO_{2-\delta}$, $0 \leq x \leq 0.05$) were synthesized by microwave-assisted hydrothermal method. The as-prepared nanocrystals have single phase tetragonal rutile structure. With increase of Co content ($x > 0.01$), Co entered into SnO_2 lattice in mixed Co^{2+}/Co^{3+} state. Pronounced blue shift of the band gap with cobalt doping originated from the combined effect of quantum confinement and Burnstain-Moss shift. Raman and photoluminescence study revealed oxygen deficient structure of $SnO_{2-\delta}$ for which the prevalent defects are in the form of in-plane oxygen vacancies. Co-doping induced decrease of in-plane oxygen vacancy concentration and luminescence quenching. $SnO_{2-\delta}$ exhibited significantly better photocatalytic activity under UV light irradiation, than Co-doped samples due to better UV light absorption and increased concentration of in-plane oxygen vacancies which, as shallow donors, enable better electron-hole separation and faster charge transport.

Keywords: *SnO_2 nanopowders, wet-chemical synthesis, defects, optical properties, photocatalysis*

I. Introduction

Tin oxide (SnO_2) is an n-type semiconductor with large band gap (3.6 eV) at room temperature. Because of its unique electronic, optical and electrochemical properties, SnO_2 is widely used in dye-sensitized solar cells, transparent conductive electrodes, solid state sensors, lithium-ion batteries and catalysis [1–7]. During the past decade, SnO_2 nanostructures have become one of the most important oxide nanostructures due to their exceptional properties and potential applications which are strongly influenced by size effects and morphology [8].

In the past decade various efforts were devoted to the synthesis of SnO_2 nanostructures with controlled size and morphology. SnO_2 nanostructures like thin films, nanobelts, nanotubes or nanowires, nanodisks and nanocrystals have been prepared using different methods, such as carbothermal reduction process, hydrothermal and solvothermal, chemical vapour condensation, laser ablation, sol-gel and molten salt techniques [9–18]. However, for most of these methods relatively high temperatures are required during the synthesis process and the samples are usually subjected to additional thermal treatment in order to achieve good crystallinity. In recent years hydrothermal approaches appeared to be widely applied as SnO_2 nanostructures can be obtained with different morphologies and tunable size at mild temperatures [8,19]. Microwave-assisted hydrothermal

*Corresponding author: tel: +381 113713024,
e-mail: *zordoh@ipb.ac.rs*

synthesis (MAH) became a very promising method for obtaining size and morphology controllable oxide nanostructures due to the unique advantages, such as fast heating rate and uniform heating without superheating of the solvent, which results in small particle size, narrow size distribution and high purity of the obtained nanopowders. Therefore, MAH appeared to be very convenient method for obtaining ultrafine SnO_2 nanopowders [19,20].

SnO_2 nanostructures are generally less studied as potential photocatalysts compared to TiO_2 and ZnO, despite its crystalline structure being similar to TiO_2 and good properties such as high photochemical stability, non-toxic nature, strong oxidizing power, and low-cost [21]. In order to improve the photocatalytic efficiency of SnO2, selective doping with metal ions, transition metals (gold, manganese, silver and iron) and rare–earth elements (Ce, Sm, Gd) was performed and well presented in the review paper by Al-Hamdi *et al.* [21]. Among the transition metals, cobalt is rarely applied as dopant. In fact, there are only few papers dedicated to potential applicability of Co-doped SnO_2 nanostructures as photocatalysts [22–24], but none of them investigated the synergic influence of defective nature and Co-doping on photocatalytic properties of very fine SnO_2 nanocrystals. It is well known that photocatalytic efficiency of metal oxide nanostructures can be influenced by the presence of intrinsic defects such as oxygen vacancies [25–28]. The presence of oxygen vacancies strongly influences the charge recombination process and the band gap structure. Namely, oxygen vacancies introduce the defect levels (near conduction or valence band) inside the gap and behave as trapping centres for photogenerated carriers preventing the fast recombination. Besides, oxygen vacancies can facilitate the transferring of charge carriers to adsorbed species (OH^- or water molecules and dissolved oxygen present on the surface of the catalyst) and enhance the formation of reactive radicals which are responsible for improved photocatalytic activity of oxide nanostructures [26,27]. Moreover, the formation of defect states inside the gap reduces the band gap and extends the absorption to visible light [25,27]. The prominent intrinsic defects in SnO_2 nanostructures are oxygen vacancies as well, which form donor/acceptor states inside the SnO_2 gap, influencing its electronic structure and making it conductive [4]. As oxygen vacancies play a critical role in many new physical phenomena, it is important to investigate associated changes in the optical and electronic properties of pure and Co-doped SnO_2 nanomaterials which can have a strong impact on photocatalytic activity of these materials.

In the work presented here, ultrafine, nonstoichiometric pristine and Co-doped $SnO_{2-\delta}$ nanopowders were synthesized via simple and cost effective microwave-assisted hydrothermal method. This paper intends to explore how defective structure and Co-doping provoke changes of optical and electronic properties of $SnO_{2-\delta}$ nanocrystals influencing the photocatalytic performances.

II. Experimental procedure

2.1. Materials preparation

$Sn_{1-x}Co_xO_{2-\delta}$ (where x = 0, 1, 3 and 5 mol%) nanopowders were synthesized by microwave-assisted hydrothermal method using $SnCl_4 \cdot 5\,H_2O$ (98%, Aldrich), $CoCl_2 \cdot 6\,H_2O$, NaOH and HCl as starting precursors. Initially, 1 ml of hydrochloric acid was added to 10 ml of distilled water at 50 °C resulting in a solution with pH between 0 and 1. Next, 17.529 g of $SnCl_4 \cdot 5\,H_2O$ was added and the mixed solution was homogenized under stirring with simultaneous increasing of the water amount to approximately 50 ml. In a case of the doped samples, 0.119 g, 0.357 g and 0.595 g of $CoCl_2 \cdot 6\,H_2O$ were added to obtain 1, 3 and 5 mol% Co-doped samples, respectively. NaOH was added dropwise under vigorous stirring until the pH of the solution was adjusted to 8. The mixed solution was placed in a 110 ml sealed Teflon autoclave and subjected to microwave heating, applying 2.45 GHz of microwave radiation at a maximum power of 800 W. The as-prepared solution was heated at 140 °C for 10 min using heating rate of 14 °C/min and then air-cooled to room temperature. The as-prepared undoped and Co-doped $SnO_{2-\delta}$ nanopowders were submitted to dialysis in order to be separated from the solution and then dried at 80 °C for 12 h.

2.2. Materials characterization

The crystalline structure and average crystallite size of the $Sn_{1-x}Co_xO_{2-\delta}$ samples were evaluated using X-ray diffraction (XRD) measurements. The measurements were carried out using an automatic X-ray diffractometer (Rigaku, Rotaflex RU200B) with CuKα radiation (50 kV, 100 mA, λ = 1.5405 Å) in a θ–2θ configuration using a graphite monochromator. The 2θ scanning range was between 20 and 70°, with a step size of 0.02°. Microstructural analysis was made by transmission electron microscopy (TEM) FEI Titan 60-300 operating at voltages between 60 and 300 kV, using a field emission gun (FEG) with an objective lens (Super Twin) and a corrector that allows resolution of 0.08 nm.

Micro-Raman scattering measurements were performed at room temperature in the backscattering configuration on Tri Vista 557 Raman system equipped with a nitrogen-cooled CCD detector, using 532 nm laser line of optically pumped semiconductor laser (Coherent Verdi G) as an excitation source. UV-visible diffuse reflectance spectra were acquired with a Cary 5G spectrophotometer in the 200–800 nm range. Diffuse reflectance spectra were transformed into the absorbance spectra by the Kubelka-Munk method. The ellipsometric measurements were performed using high resolution variable angle spectroscopic ellipsometer (SOPRA GES5E-IRSE) of the rotating polarizer type. The data

were collected at room temperature in the UV-Vis spectral range with a resolution of 0.02 eV, for the incidence angle of 70°. Photoluminescence emission measurements were performed at room temperature using Spex Fluorolog spectrofluorometer with C31034 cooled photomultiplier under Xenon lamp excitation at 380 nm.

2.3. Photocatalytic experiments

The photocatalytic activity of the $Sn_{1-x}Co_xO_{2-\delta}$ samples, for the degradation of methylene blue (MB) as model pollutant, was tested under UV illumination. The different samples with the same photocatalyst amount (150 mg/l) were immersed in 20 ml of an aqueous solution of methylene blue (5.0 mg/l). The beakers were placed in a photo-reactor at controlled temperature (15 °C), under magnetic stirring, and were illuminated by six 15 W UV lamps (TUV Philips, maximum intensity at 254 nm). The solution was placed in the dark for 60 min to reach the adsorption/desorption equilibrium before UV light exposure. Blank experiment without UV irradiation demonstrated no adsorption of MB dye on the surface of the $Sn_{1-x}Co_xO_{2-\delta}$ samples. The photocatalytic experiments were conducted at the natural pH = 6 of MB dye. At regular time intervals 2 ml aliquots were taken, centrifuged to remove any catalyst particles and the concentration of the dye was determined by UV-Vis absorption spectrophotometer (Shimadzu-UV-1601 PC) monitoring the variation of absorbance at 663 nm.

The formation of hydroxyl radicals ($OH^{\bullet}$) on the surface of the $SnO_{2-\delta}$ sample under the UV light illumination was examined by photoluminescence (PL) technique using terephthalic acid (TA) as a probe molecule. The detailed experimental procedure was described in reference [29]. TA is known to react with $OH^{\bullet}$ radicals induced on the photocatalyst's surface where it produces highly fluorescent 2-hydroxyterephthalic acid which shows an intense PL peak at around 425 nm. The intensity of this peak is proportional to the amount of $OH^{\bullet}$ radicals [30,31] produced in the photocatalytic process. The changes of the 425 nm PL peak intensity were measured at room temperature using 315 nm excitation.

III. Results and discussion

3.1. Crystal structure and morphology

Figure 1a shows XRD patterns of the $Sn_{1-x}Co_xO_{2-\delta}$ ($0 \le x \le 0.05$) nanopowders, whereas the Rietveld refined XRD spectra of the $SnO_{2-\delta}$ and $Sn_{0.95}Co_{0.05}O_{2-\delta}$ samples are presented in Figs. 1b and 1c. The XRD patterns of all the samples revealed single phase tetragonal structure (cassiterite phase). The XRD peaks at 26.6, 33.8, 51.9 and 65.8° can be assigned to (110), (101), (211) and (301) planes, which are in good agreement with literature data (ICDS № 9163). No secondary phases like Co oxides, Co clusters or other tin oxide phases were observed. Moreover, broad diffraction peaks of low intensities compared to those of bulk SnO_2, point to low crystallinity and small crystallite size of the SnO_2 nanoparticles.

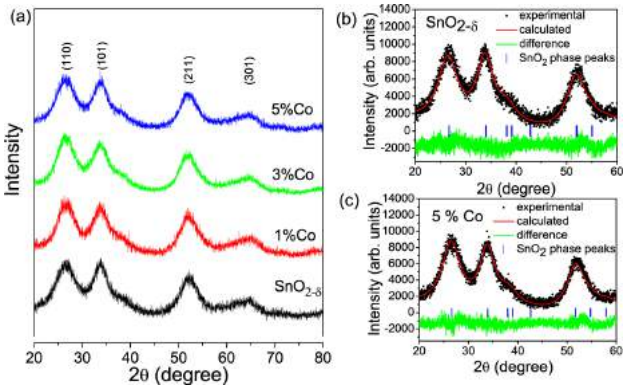

Figure 1. XRD patterns of $Sn_{1-x}Co_xO_{2-\delta}$ nanocrystals ($0 \le x \le 0.05$) indexed to tetragonal rutile structure of SnO_2 (a), Rietveld refined XRD spectra of $SnO_{2-\delta}$ (b) and $Sn_{0.95}Co_{0.05}O_{2-\delta}$ (c) nanoparticles

The average lattice parameters and unit cell volume obtained from the Rietveld refinement data are given in Table 1. These results showed an expansion of the SnO_2 unit cell with increasing cobalt content up to 5%. This variation originates from the substitution of smaller Sn^{4+} cations (0.83 Å) with larger Co^{2+} cations in high spin state (0.89 Å) [32]. The slight shrinkage of the unit cell observed for the 5% Co-doped sample can be related to the presence of increased amount of smaller Co^{3+} cations (*ls*: 0.68 Å or *hs*: 0.75 Å). The average crystallite size (D) of the $Sn_{1-x}Co_xO_{2-\delta}$ nanocrystals was calculated with the Scherrer formula using the 110 reflection and their values are reported in Table 1. Obviously, the mean crystallite sizes of the undoped and Co-doped samples are less than Bohr exciton radius (2.7 nm for SnO_2) [33] and with increased Co-doping the crystallite size of the $Sn_{1-x}Co_xO_{2-\delta}$ nanocrystals decreases. Such a trend implies that Co-doping has an inhibiting effect on the crystal growth. This inhibiting effect of Co on the crystal grains growth was already confirmed in the work of Babu *et al.* [34].

TEM images of the undoped and Co-doped $SnO_{2-\delta}$ samples are presented in Fig. 2. TEM images revealed

Table 1. Lattice parameters (a, c), unit cell volume (V) and average crystallite size (D) of the $Sn_{1-x}Co_xO_{2-\delta}$ nanocrystals

Sample	$a = b$ [Å]	c [Å]	V [Å^3]	D [nm]
$SnO_{2-\delta}$	4.722 ± 0.002	3.180 ± 0.003	70.905	2.5
$Sn_{0.99}Co_{0.01}O_{2-\delta}$	4.747 ± 0.002	3.201 ± 0.003	72.131	2.4
$Sn_{0.97}Co_{0.03}O_{2-\delta}$	4.759 ± 0.002	3.206 ± 0.002	72.609	2.3
$Sn_{0.95}Co_{0.05}O_{2-\delta}$	4.744 ± 0.002	3.186 ± 0.002	71.703	2.2

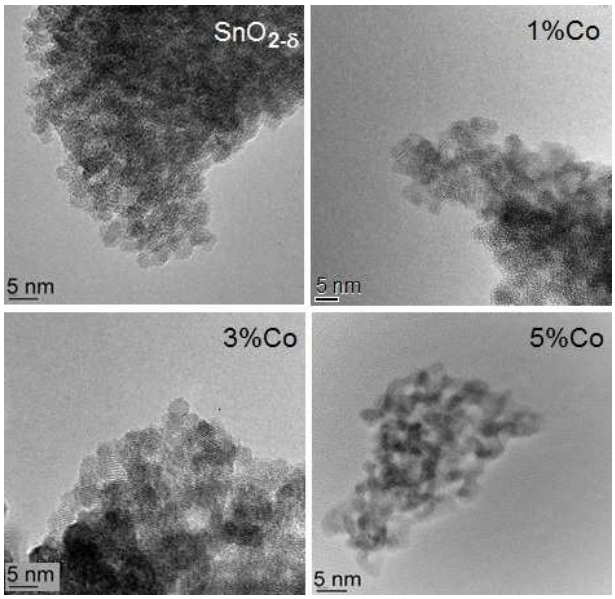

Figure 2. TEM images of $Sn_{1-x}Co_xO_{2-\delta}$ ($0 \le x \le 0.05$) nanoparticles

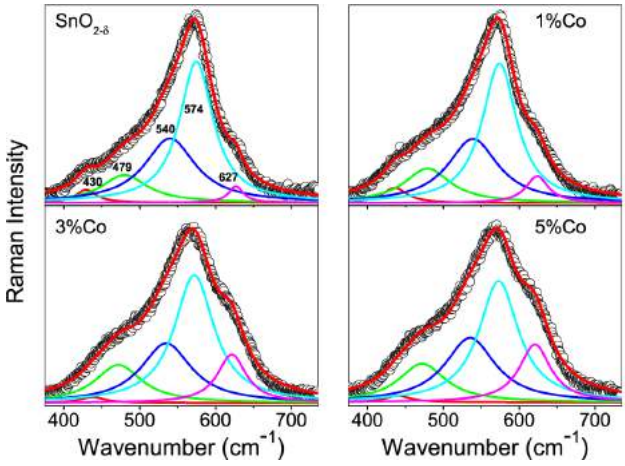

Figure 3. Deconvoluted room-temperature Raman spectra of $Sn_{1-x}Co_xO_{2-\delta}$ nanoparticles

that the undoped $SnO_{2-\delta}$ sample is composed of single crystalline nanoparticles of very small size and quasi-spherical shape. The morphology of the $Sn_{1-x}Co_xO_{2-\delta}$ nanoparticles remained the same with Co-doping. The particles are of spherical shape with the size less than 3 nm, which is in good agreement with the results obtained from XRD data. The observed agglomeration of the $Sn_{1-x}Co_xO_{2-\delta}$ nanoparticles can be ascribed to small crystallite sizes.

3.2. Raman analysis

SnO_2 tetragonal rutile crystalline structure (space group $P4_2/mnm$) has four active Raman modes (non-degenerate A_{1g}, B_{1g}, B_{2g} modes, and a doubly degenerated E_g mode), two active infrared modes (A_{2u} and E_u) and two silent modes (A_{2g}, B_{1u}) [35]. The positions of A_{1g}, B_{1g}, B_{2g} and E_g Raman modes in SnO_2 single crystal under ambient conditions are 634, 123, 776 and 475 cm^{-1}, respectively, and the A_{1g} and E_g modes are of much higher intensity compared to B_{1g} and B_{2g} modes [35].

The Raman spectra of nanocrystalline, non-stoichiometric $SnO_{2-\delta}$ are modified in comparison with single-crystal or polycrystalline SnO_2, because Raman spectroscopy is more sensitive to intrinsic defects and confinement effect than conventional XRD technique. Namely, the position, bandwidth and intensity of Raman modes are size dependent, i.e. Raman modes are broadened, of lower intensity and shifted towards lower or higher energies depending on phonon dispersion curves. Besides, new modes of defect origin can appear [36,37]. The room temperature Raman spectra of the $Sn_{1-x}Co_xO_{2-\delta}$ nanocrystals are presented in Fig. 3 and they are deconvoluted using Lorentzian profiles (full lines in Fig. 3).

In the Raman spectrum of the pure $SnO_{2-\delta}$, the most prominent mode is located at ~574 cm^{-1}. This mode is characteristic for non-stoichiometric $SnO_{2-\delta}$ and it is not present in the Raman spectra of SnO_2 single-crystal [35]. Density functional calculations performed by Liu *et al.* [38] have shown that this mode arises from in-plane oxygen vacancies (V_{Oin}) in the surface region of $SnO_{2-\delta}$ nanoparticles, intensity of which is proportional to their concentration. In very fine nanoparticles this mode has the highest intensity due to the increased concentration of oxygen vacancies. Raman mode at ~627 cm^{-1} can be ascribed to the A_{1g} mode of rutile SnO_2 structure. This mode is of lower intensity, broadened and shifted to lower wave numbers compared to the bulk counterpart, due to the phonon confinement effect [37]. As the crystallite size of the undoped $SnO_{2-\delta}$ is smaller than the Bohr exciton radius, the size effect can be very pronounced in this sample. Another broad Raman mode at ~479 cm^{-1} is assigned to E_g mode and it is shifted to higher wavenumbers with size decrease of $SnO_{2-\delta}$ nanocrystals [37]. Besides these modes, additional modes at around 430 and 540 cm^{-1} appear. These new modes are usually seen in very fine SnO_2 nanoparticles [37–39], nanotubes [40] or nanoribbons [41] because of the increased degree of local disorder, i.e. loss in long-range order due to the large number of lattice vacant positions, especially at the surface of nanoparticles. These modes are of high intensity in small nanoparticles and disappear with particle size increase. According to some literature data, due to the relaxation of the selection rules in nanostructured SnO_2, the mode at 540 cm^{-1} is assigned to the Raman forbidden mode (B_{1u}) [40,41], whereas the new mode at around 430 cm^{-1} can be assigned to the oxygen vacancy clusters (V_C) [39]. The A_{1g} and E_g modes exhibited redshift and broadening with Co-doping. The redshift and broadening of these modes are expected with substitution of Sn^{4+} ions with larger Co^{2+} ions and decreased crystallite size due to the phonon confinement effect. The positions and intensities of the A_{1g}, E_g and oxygen vacancy related modes (V_{Oin} and V_C) are presented in Fig. 4. As it can be seen from Fig. 4, the intensity of A_{1g} mode increases with increased Co concentration, whereas the intensity of E_g

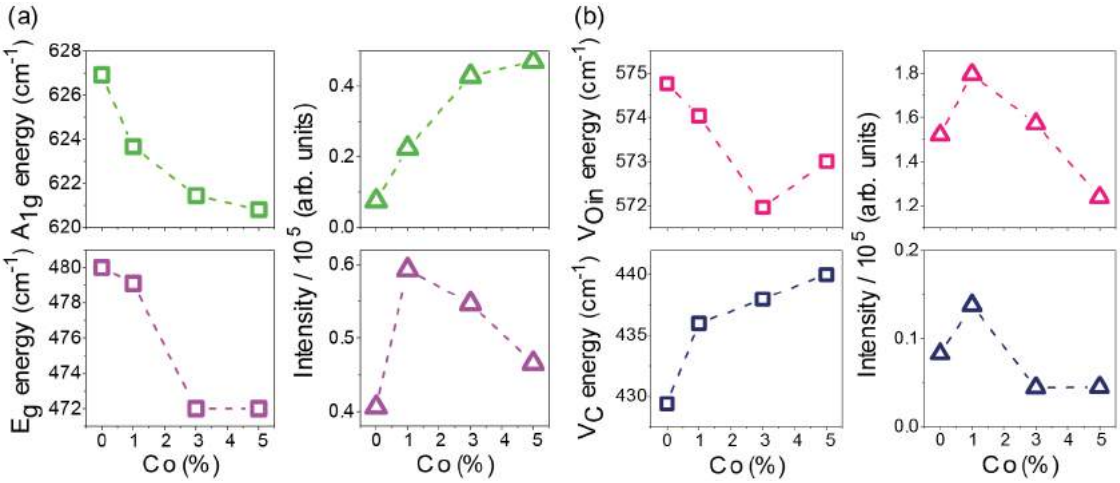

Figure 4. Positions and intensities of A_{1g} and E_g (a) and vacancy (V_{Oin} and V_C) (b) Raman modes

mode is higher in the Co-doped samples compared to the undoped $SnO_{2-\delta}$. The E_g mode intensity slightly decreased in samples doped with higher Co content, as a consequence of lattice distortion and reduction in lattice space symmetry. The position of the Raman mode ascribed to in-plane oxygen vacancies (574 cm^{-1}) did not change significantly, whereas the Raman mode related to vacancy clusters (430 cm^{-1}) shifts to higher energies with Co-doping. The intensity of both modes decreased in the $Sn_{0.97}Co_{0.03}O_{2-\delta}$ sample and this trend is more evident for the $Sn_{0.95}Co_{0.05}O_{2-\delta}$ sample. The intensity reduction of oxygen vacancy related modes in these samples implies that the concentration of oxygen vacancies decreased. The decrease of the oxygen vacancy concentration is expected if the part of Co cations were in Co^{3+} state or if some Co cations were interstitially incorporated in $SnO_{2-\delta}$ lattice [33,42].

In order to see if Co cations substituted Sn^{4+} in Co^{2+} state or the part of them was in Co^{3+} state, UV-Vis absorption measurements were performed and the absorption spectra of the $Sn_{1-x}Co_xO_{2-\delta}$ samples are presented in Fig. 5. In the UV range, the absorption spectrum of $SnO_{2-\delta}$ displays a strong absorption due to

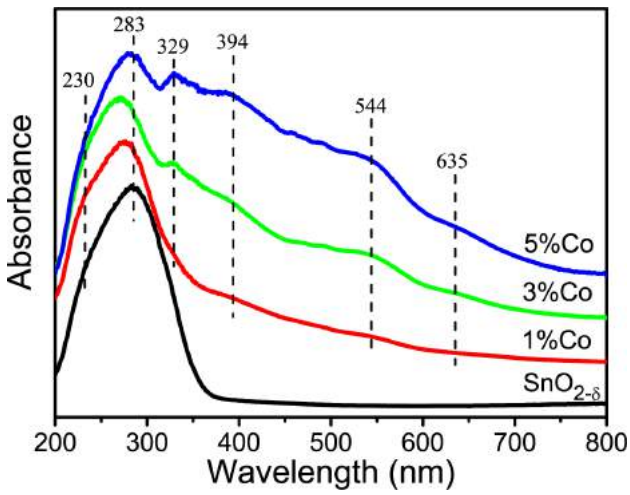

Figure 5. UV-Vis spectra of $Sn_{1-x}Co_xO_{2-\delta}$ nanoparticles

the SnO_2 interband transition. Two peaks at 230 and 283 nm are superimposed giving the broad band which might correspond to the surface Sn^{4+} species and to the $Sn^{4+} \rightarrow Sn^{2+}$ intervalence charge transfer, respectively [43]. In Co-doped samples the broad band is shifted to lower wavelength implying the band gap increase with Co-doping. In the absorption spectra of the $Sn_{0.97}Co_{0.03}O_{2-\delta}$ and $Sn_{0.95}Co_{0.05}O_{2-\delta}$ samples, new bands appear. The band around 329 nm can be assigned to the partial change of oxidation state of Co^{2+} to Co^{3+} [44], whereas the broad band around 400 nm can be ascribed to $^1A_{1g} \xrightarrow{\nu_2} {}^1T_{2g}$ transition of low spin Co^{3+} ions in octahedral environment [45]. The intensity of these bands increased in the $Sn_{0.95}Co_{0.05}O_{2-\delta}$ sample pointing to the increased concentration of Co^{3+} ions. The bands around 544 and 635 nm can be related to $^4A_2(F) \xrightarrow{\nu_2} {}^4T_1(P)$ transition of tetrahedral Co^{2+} species [45]. Therefore, from the absorption spectra of the $Sn_{0.97}Co_{0.03}O_{2-\delta}$ and $Sn_{0.95}Co_{0.05}O_{2-\delta}$ samples it can be deduced that part of Co cations entered into SnO_2 lattice in Co^{3+} state, concentration of which increased with the increased dopant content. This result supports the finding obtained from the refined XRD spectrum of the $Sn_{0.95}Co_{0.05}O_{2-\delta}$ sample, since the shrinkage of the unit cell was ascribed to the increased amount of Co^{3+} cations.

Our conclusions derived from absorption measurements are well-supported by recently published work of Roy *et al.* [46] concerning Co-doped SnO_2 nanocrystals. From the XPS study, Roy *et al.* [46] confirmed the mixed valence nature of Co ions in the host lattice and they have found that the relative concentration of Co^{3+} exceeds that of Co^{2+} with the increase of dopant content. This study also showed that Co incorporation into SnO_2 leads to the reduction of oxygen vacancies which is consistent with our Raman study.

3.3. Optical and electronic properties

The investigation of complex dielectric function by spectroscopic ellipsometry offers an insight into the

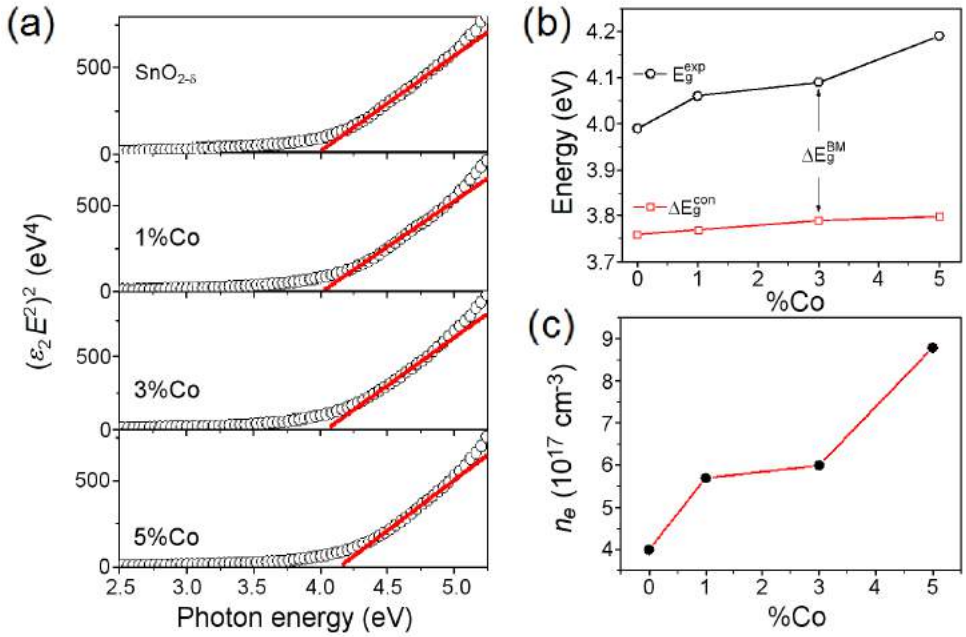

Figure 6. Determination of the direct band gap for $Sn_{1-x}Co_xO_{2-\delta}$ nanoparticles using Tauc law(a); variation of the band gap energy obtained from ellipsometric measurements (E_g^{exp}) and from quantum confinement model (ΔE_g^{con}) (b) and concentration of charge carriers n_e for $Sn_{1-x}Co_xO_{2-\delta}$ samples (c)

most important optical properties of the nanomaterials, such as, optical band gap, interband and intraband transitions, defect electronic states. The imaginary part of dielectric function is directly related to the electronic density of states and in a case of nanopowders it can be deduced from the ellipsometric measurements by applying two-phase model approximation (in our case: $SnO_{2-\delta}$ nanocrystals/air). In order to investigate the optical band gap behaviour and the influence of Co dopant on the absorption edge in $SnO_{2-\delta}$ nanocrystals we applied the Tauc model for direct band gap transition [47], knowing that SnO_2 is a direct band gap material [48]. In this case general expression for $\varepsilon_2(E)$ is:

$$(\varepsilon_2 \cdot E^2)^2 = a(E - E_g) \tag{1}$$

where E is the photon energy, E_g is the band gap and a is the constant related to the density of states for the conduction band. The Tauc plots of the $Sn_{1-x}Co_xO_{2-\delta}$ samples obtained from ellipsometric measurements are presented in Fig. 6a. Linear extrapolation to zero absorption (straight lines in Fig. 6a) gives the band gap energy values of the $Sn_{1-x}Co_xO_{2-\delta}$ samples.

In Fig. 6b, the dependence of the band gap energy (from Fig. 6a) on dopant content for the $Sn_{1-x}Co_xO_{2-\delta}$ samples is represented with open circles. It is obvious that Co-doping induces an increase of the E_g. Also, it is important to notice that all investigated samples have the band gap values higher than that for bulk SnO_2. Such changes in electronic properties of SnO_2 nanomaterials can be a consequence of the quantum confinement effect. This effect causes an increase of the band gap value due to the stronger localization of electronic states inside the volume of nanocrystals. The band gap energy shift, caused by this effect, can be calculated according to the following relation [49]:

$$\Delta E_g^{con} = E_g + \frac{\hbar^2 \pi^2}{2\mu \cdot D^2} \tag{2}$$

where E_g is the band gap value for the bulk SnO_2 (3.6 eV), D is the crystallite radius and μ is the reduced effective mass of the electron-hole pair. From the XRD results it was obtained that the average crystallite size of the undoped $SnO_{2-\delta}$ nanocrystals is lower than Bohr exciton radius, and that it has a tendency of further decrease with Co-doping. Therefore, it is reasonable to take into account the quantum confinement effect in order to properly analyse the band gap behaviour of the $Sn_{1-x}Co_xO_{2-\delta}$ samples. Taking the D values from Table 1 and knowing that $\mu = 0.38m_0$ [48], the band gap values (ΔE_g^{con}) that arise from the quantum confinement effect were calculated using Eq. 2. The ΔE_g^{con} values are presented in Fig. 6b with open squares. Comparing the ΔE_g^{con} values with E_g^{exp} ones it is obvious that observed band gap increase of the $Sn_{1-x}Co_xO_{2-\delta}$ samples cannot be ascribed only to the quantum confinement effect.

Another effect that can cause a shift of optical absorption edge to higher energies is the Burstein-Moss effect, which becomes more relevant in doped semiconductors (like transparent conducting oxides) with high charge carrier concentration. The Burstein-Moss effect is already registered in doped SnO_2 thin films [50,51]. According to this effect, the widening of the optical gap is caused by metallic doping and increase of carrier density which leads to the filling of empty semiconductor electronic states in the vicinity of Fermi level and its shift to higher energies. Assuming parabolic bands and

spherical Fermi surface the band gap shift due to the Burstein-Moss effect can be calculated by simple relation [4]:

$$\Delta E_g^{BM} = \frac{h^2}{2\mu}\left(3\pi^2 \cdot n_e\right)^{2/3} \quad (3)$$

where h is Planck constant, μ is the reduced effective mass and n_e is the carrier concentration.

Additional charge, i.e. increased charge carrier density in pure and doped $SnO_{2-\delta}$ nanocrystals, can originate from the donor type defects like oxygen vacancies and Co-dopants. Raman spectra have already evidenced defective structure of $SnO_{2-\delta}$, whereas Co^{2+} dopants bring additional charge when substituting Sn^{4+} ions. Hence, the observed increase of the E_g from Fig. 6b can be ascribed to the Burstein-Moss shift (ΔE_g^{BM}). Combining Eqs. 2 and 3 it is possible to estimate the concentration of charge carriers (n_e) in the $Sn_{1-x}Co_xO_{2-\delta}$ samples and the obtained values are presented in Fig. 6c. These calculated values are in good agreement with literature data for SnO_2 thin films [52]. As can be seen from Fig. 6c, doping of $SnO_{2-\delta}$ nanocrystals with Co ions causes an increase of the charge carriers concentration and shift of the optical absorption edge toward UV region, making the investigated material more conductive and at the same time more transparent.

It is well known that large number of defects, such as oxygen vacancies or vacancy clusters, can be formed at the SnO_2 nanoparticles surface and subsurface [21]. Intrinsic oxygen vacancies can be of three types: in-plane (V_{Oin}), bridging (V_{OB}) and subbridging (V_{OSB}) vacancies [36,38]. These vacancies can be in different charge states, i.e. vacancies which trap one, two or none electrons, so called F^+, F^0 and F^{++} centres, and they can form defect levels inside the $SnO_{2-\delta}$ gap [53]. Among the optical spectroscopy methods, photoluminescence (PL) spectroscopy is convenient method to investigate the defect structure of the pure and Co-doped $SnO_{2-\delta}$ samples.

Room temperature PL spectra of the $SnO_{2-\delta}$, $Sn_{0.99}Co_{0.01}O_{2-\delta}$ and $Sn_{0.95}Co_{0.05}O_{2-\delta}$ samples using a wavelength of 380 nm for excitation are presented in Fig. 7a. The PL spectrum of $SnO_{2-\delta}$ is deconvoluted into four Gaussian peaks centred at 510, 575, 470 and 446 nm (inset of Fig. 7a). In the deconvoluted PL spectrum of the undoped $SnO_{2-\delta}$ two bands dominate: broad intense band centred at around 510 nm and another band of lower intensity at around 575 nm. Since the excitation and emissions are both lower than the band gap of $SnO_{2-\delta}$, neither of these PL bands can be ascribed to the recombination of the Sn 4p conduction electrons with a holes from a O 2p band. The broad green luminescence around 510 nm is already seen in SnO_2 thin films [10] and nanoparticles [36] and it was attributed to the in-plane oxygen vacancy defects [36]. Therefore, the strong PL peak at 510 nm (2.45 eV) is ascribed to V_{Oin} defects. This finding is in accordance with corresponding Raman spectrum in which the most prominent Raman mode originates from in-plane oxygen vacancies. Another PL band at 575 nm (2.15 eV) can be ascribed to the isolated bridging oxygen vacancy defects, i.e. singly ionized F^+ defects [53]. The PL bands around 470 and 440 nm were seen in SnO_2 nanopowders [54]. These PL bands obtained with similar excitation line as in our case were ascribed to have excitonic origin [54]. It is well known that excitonic bands are formed near the band edge and they are usually of much narrower bandwidth than PL bands which originate from defect structures. As the band gap of the $SnO_{2-\delta}$ sample is around 4 eV, it can be concluded that PL bands at 446 and 470 nm lie deeper in the gap. Hence, it is unlikely that these two bands originate from some excitonic states. Performing density functional calculation for defective $SnO_{2-\delta}$ nanocrystals, Liu *et al.* [38] have shown that PL peaks at 446 and 470 nm originate from the subbridging oxygen vacancies, V_{OSB}. Schematic model for different relaxation processes in the $SnO_{2-\delta}$ nanocrystals is presented in Fig. 7b.

Co-doping induced complete reduction of PL intensity. Even the smallest percent of Co-doping (see Fig. 7a) almost completely quenched the luminescence. By integrating the spectra of the $Sn_{1-x}Co_xO_{2-\delta}$ samples from Fig. 7a, the areas within the boundary of emission were calculated for both undoped and doped samples in order to compare the quantum efficiencies. As the spectra were recorded under the identical excitation/absorption

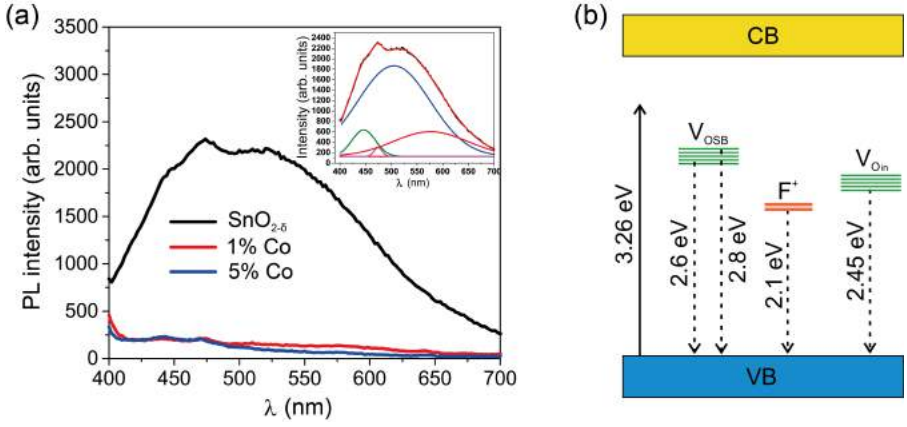

Figure 7. Room-temperature PL spectra of $Sn_{1-x}Co_xO_{2-\delta}$ nanoparticles (a) and the schematic of relaxation mechanism (b)

conditions, the drop in quantum yield value was estimated to be nearly 93%, which evidently implies that cobalt doping drastically quenches the photoluminescence of $SnO_{2-\delta}$. It has been already demonstrated that Co ions act as luminescence quenchers for metal oxides like TiO_2 or ZnO, decreasing the intensity of PL emission by forming the large number of nonradiative centres [55,56]. Therefore, it can be inferred that Co-doping of the $SnO_{2-\delta}$ nanocrystals increases the nonradiative recombination processes.

3.4. Photocatalytic performances

The degradation of MB under the UV light in the presence of the $Sn_{1-x}Co_xO_{2-\delta}$ samples is shown in Fig. 8a. The blank experiment in the absence of the catalyst (black curve) displayed almost no photocatalytic degradation of MB under UV irradiation. The $SnO_{2-\delta}$ nanoparticles exhibited high photocatalytic activity as the degradation of MB was completed after 6 h. The

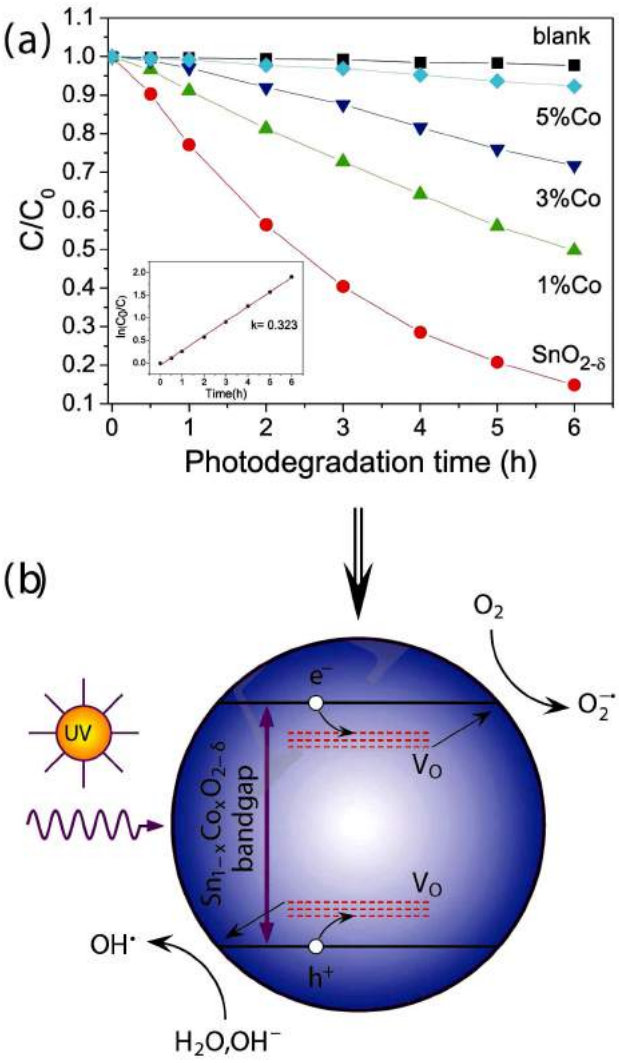

Figure 8. Photocatalytic degradation of MB in the presence of $Sn_{1-x}Co_xO_{2-\delta}$ samples (inset: pseudo first-order reaction kinetics of $SnO_{2-\delta}$ sample) (a) and illustration of proposed photodegradation mechanism under UV light illumination (b)

photocatalytic efficiency of the $SnO_{2-\delta}$ nanoparticles is much better than the ones of bulk SnO_2 [53] and is comparable to other reported works on SnO_2 nanoparticles [24,57]. Photoinduced degradation of MB was significantly slower in the presence of Co-doped samples. After 6 h, the MB degradation of 50% was obtained in the presence of the $Sn_{0.99}Co_{0.01}O_{2-\delta}$ catalyst, whereas significant decrease of photocatalytic activity was registered for the $Sn_{0.97}Co_{0.03}O_{2-\delta}$ and $Sn_{0.95}Co_{0.05}O_{2-\delta}$ samples. The obtained results are in accordance with the solitary work of Entradas *et al.* [22] who showed that increased Co-doping resulted in the decreased photocatalytic activity of SnO_2. The experimental kinetic data for $SnO_{2-\delta}$ catalyst were fitted to the rate equation of a pseudo first-order reaction $\ln(C/C_0) = kt$, where k is the rate constant and C_0 and C are the initial dye concentration and that at time t. The reaction kinetics for the $SnO_{2-\delta}$ catalyst (inset of Fig. 8a) follows the first order and the reaction rate constant estimated from the slope of the linear fit is $0.323\ h^{-1}$. The degradation process of MB is initiated when the electron-hole pairs are formed on the $SnO_{2-\delta}$ surface under the UV irradiation. Photogenerated electrons and holes, if not recombined, can migrate to the catalyst surface and react with adsorbed oxygen, water molecules or hydroxyl anions generating hydroxyl ($OH^\bullet$), superoxide ($O_2^{\bullet-}$) or ($HO_2^\bullet$) radicals. These reactions can be presented by Eq. 4–8:

$$SnO_2 + h\nu \longrightarrow SnO_2(e_{cb}^- + h_{vb}^+) \quad (4)$$

$$e_{cb}^- + O_{2ads} \longrightarrow O_2^{\bullet-} \quad (5)$$

$$h_{vb}^+ + H_2O \longrightarrow H^+ + OH^\bullet \quad (6)$$

$$h_{vb}^+ + OH^- \longrightarrow OH^\bullet \quad (7)$$

$$O_2^{\bullet-} + H^+ \longrightarrow HO_2^\bullet \quad (8)$$

The photocatalytic efficiency of semiconductors like SnO_2 can be enhanced by introducing lattice defects such as oxygen vacancies because these defects can be active sites on the photocatalyst surface and delay the recombination of photogenerated electrons and holes [21,58]. The as-prepared $SnO_{2-\delta}$ nanopowders are very much oxygen deficient as confirmed by Raman results. The oxygen vacancies can form defect states inside the gap influencing the electronic structure of $SnO_{2-\delta}$ nanoparticles, as already seen from PL spectrum. By applying complementary techniques such as ultraviolet photoelectron spectroscopy and ion-scattering spectroscopy, Cox *et al.* [59] analysed oxygen vacancy electronic states on the SnO_2 surface and they showed that in-plane oxygen vacancies V_{Oin} form defect electronic states inside the SnO_2 gap near the conduction band behaving like F^+ centre donor states. Bridging/subbridging oxygen vacancies form states near the valence band [59] playing the role of hole acceptors. These donor/acceptor states can serve as carrier traps for electrons and holes ensuring better charge separation efficiency and suppression of *e-h* recombination process. Besides, doubly ionized (F^{++}) or singly ionized (F^+)

in-plane or subbridging vacancies formed at the surface of the catalyst facilitate charge transfer to adsorption species like H_2O or O_2, forming reactive radicals responsible for dye degradation. The holes, h^+_{vb}, trapped by oxygen vacancies at the nanoparticle surface react with adsorbed H_2O or OH^- groups to form $OH^\bullet$ radicals (Eqs. 6 and 7). Besides, electrons, e^-_{cb}, can be trapped by surface F^{++} vacancies which convert to F^+. Molecular oxygen adsorbed on the $SnO_{2-\delta}$ surface can capture electrons located on F^+ states [58] to form $O_2^{\bullet-}$ radicals:

$$e^-_{cb} + F^{++} \longrightarrow F^+ \quad (9)$$

$$F^+ + O_2 \longrightarrow O_2^{\bullet-} + F^{++} \quad (10)$$

Therefore, it is reasonable to assume that in-plane and subbridging/bridging oxygen vacancies in different charge states play significant role in enhancing the photocatalytic efficiency of $SnO_{2-\delta}$. The proposed mechanism of photodegradation process is presented in Fig. 8b.

Among the reactive radicals, $OH^\bullet$ radicals are considered to be the most important oxidative agent in photocatalytic reactions on metal-oxide nanostructures. They have one of the highest oxidation potentials among the oxidizing species (2.8 V) and can rapidly attack pollutants on the semiconductor surface. These radicals are considered as non-selective oxidizing species, since they can oxidize almost all electron rich organic molecules because of its electrophilic nature. $OH^\bullet$ radicals are usually formed by the reaction between the holes and OH^- or water molecules present on the surface of the catalyst (Eqs. 6 and 7). The formation of $OH^\bullet$ radicals on the surface of UV-illuminated $SnO_{2-\delta}$ was tested by performing the experiment with terephthalic acid, described in detail in section 2.3. The concentration of $OH^\bullet$ radicals was estimated from the intensity change of the PL peak attributed to 2-hydroxyterephtalic acid which is known to be proportional to the amount of $OH^\bullet$ radicals formed [30,31]. Figure 9 showed that intensity of PL peak at around 430 nm gradually increased with the prolonged irradiation time pointing to the higher formation rate of hydroxyl radicals. This result indicates that increased formation of $OH^\bullet$ radicals has a great effect on the photocatalytic activity of $SnO_{2-\delta}$. Further investigations will be directed to the estimation of the optimal SnO_2 concentration and the influence of solution pH on the SnO_2 photocatalytic properties. In that sense, more detailed mechanism study needs to be performed.

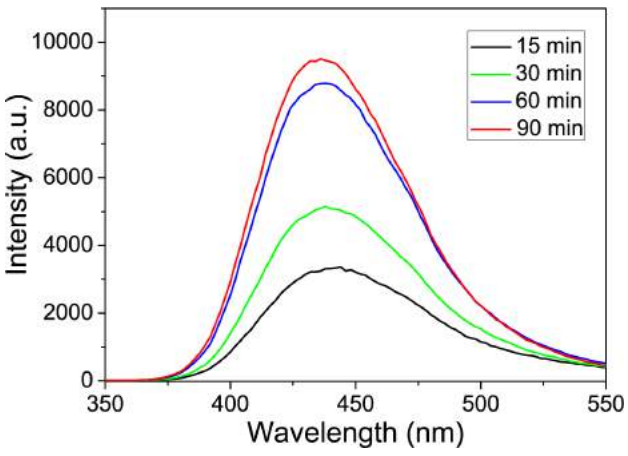

Figure 9. PL intensity change of 430 nm peak observed during UV illumination of $SnO_{2-\delta}$ sample in the solution of terephthalic acid and recorded at different time

With Co-doping the photocatalytic performances of $SnO_{2-\delta}$ were deteriorated. The reasons can be found in increased number of nonradiative centres with increasing cobalt concentration which act as trapping centres, immobilizing the fast transfer of photo-generated electrons to the nanoparticle surface. However, one of the main reasons can be found in the decreased concentration of oxygen vacancies which promotes the charge separation enhancing at the same time the photocatalytic activity. Also, the increased band gap of the Co-doped samples decreases the number of photons with sufficient energy to initiate photocatalytic processes, i.e. less UV energy is absorbed.

IV. Conclusions

Single phase ultrafine $Sn_{1-x}Co_xO_{2-\delta}$ nanocrystals, of a tetragonal (cassiterite-type) crystal structure, were prepared using a simple microwave-assisted hydrothermal synthesis at low temperature without the addition of any surfactant. Rietveld refinement of the XRD data showed that Co cations entered substitutionally into $SnO_{2-\delta}$ lattice and the unit cell volume increased up to $x = 0.05$. The slight shrinkage of the unit cell of the $Sn_{0.95}Co_{0.05}O_{2-\delta}$ sample was ascribed to the increased amount of Co^{3+} cations. The average crystallite size of the $SnO_{2-\delta}$ nanocrystals was less than Bohr exciton radius and it was found to decrease with increasing Co-doping level. UV-Vis absorption measurements confirmed that Co cations entered into the $SnO_{2-\delta}$ lattice in mixed valence state for higher dopant content ($x > 0.01$) and the concentration of Co^{3+} cations increased in the $Sn_{0.95}Co_{0.05}O_{2-\delta}$ sample. Raman spectra revealed oxygen deficient structure of the $SnO_{2-\delta}$ nanocrystals, whereas the oxygen vacancy concentration decreased with increased Co-doping. Further, Co-doping brought significant changes in the optical and electronic properties of tin oxide. $SnO_{2-\delta}$ nanocrystals exhibited blue shift of the band gap energy, compared to the bulk counterpart, due to the combined phonon confinement and the Burstein-Moss effects. The optical band gap energy increased with increasing Co concentration. The luminescence process in $SnO_{2-\delta}$ nanocrystals mainly originated from oxygen vacancy related defects and it was completely quenched in the Co-doped nanocrystals due to the increased nonradiative recombination processes. The oxygen-deficient $SnO_{2-\delta}$ was efficient for the light-induced degradation of methylene blue. Enhanced photocatalytic activity of $SnO_{2-\delta}$ can be ascribed to the

oxygen vacancies-assisted better charge separation and faster charge transport to adsorbed species. On the other hand, deteriorated photocatalytic performances of Co-doped $SnO_{2-\delta}$ nanopowders can be ascribed to the decreased oxygen vacancy concentration and less amount of absorbed UV light because of the band gap widening.

Acknowledgement: The authors acknowledge funding by the Institute of Physics Belgrade, through the grant by the Serbian Ministry of Education, Science and Technological Development. V.D. Araújo and M.I.B. Bernardi wish to thank Brazilian agencies FAPESP, FACEPE and CNPq for financial support.

References

1. H. Park, S. Alhammadi, K. Bouras, G. Schmerber, F. Gérald, D. Aziz, S. Abdelilah, J. Chan-Wook, P. Chinho, K. Woo Kyoung, "Nd-doped SnO_2 and ZnO for application in Cu(InGa)Se_2 solar cells", *Sci. Adv. Mater.*, **9** (2017) 2114–2120.
2. J. Lee, N.H. Kim, Y.S. Park, "Characteristics of SnO_2:Sb films as transparent conductive electrodes of flexible inverted organic solar cells", *J. Nanosci. Nanotechnol.*, **16** (2016) 4973–4977.
3. Y. Chen, J. Lu, S. Wen, L. Lu, J. Xue, "Synthesis of SnO_2/MoS_2 composites with different component ratios and their applications as lithium ion battery anodes", *J. Mater. Chem. A*, **2** (2014) 17857–17866.
4. M. Batzill, U. Diebold, "The surface and materials science of tin oxide", *Prog. Surf. Sci.*, **79** (2005) 47–154.
5. K. Singh, R. Malakar, R. Narzary, K. Priyanka, M. Biplob, "Hydrogen sensing properties of pure and composites of ZnO and SnO_2 particles: Understanding sensing mechanism", *Sens. Lett.*, **15** (2017) 771–778.
6. Z. Zhao, B. Wang, J. Ma, W. Zhan, L. Wang, Y. Guo, Y. Guo, G. Lu, "Catalytic combustion of methane over Pd/SnO_2 catalysts", *Chinese J. Catal.*, **38** (2017) 1322–1329.
7. J.T. Wiswall, M.S. Wooldridge, H.G. Im, "An experimental investigation of catalytic oxidation of propane using temperature controlled Pt, Pd, SnO_2, and 90% SnO_2–10% Pt catalysts", *Catal. Sci. Technol.*, **3** (2013) 618–625.
8. J.S. Chen, X.W.D. Lou, "SnO_2-based nanomaterials: synthesis and application in lithium-Ion batteries", *Small*, **9** (2013) 1877–1893.
9. M.O. Orlandi, A.J. Ramirez, E.R. Leite, E. Longo, "Morphological evolution of tin oxide nanobelts after phase transition", *Cryst. Growth Des.*, **8** (2008) 1067–1072.
10. J. Jeong, S.-P. Choi, C.I. Chang, D.C. Shin, J.S. Park, B.-T. Lee, Y.-J. Park, H.-J. Song, "Photoluminescence properties of SnO_2 thin films grown by thermal CVD", *Solid State Commun.*, **127** (2003) 595–597.
11. Y. Wang, M.H. Wu, Z. Jiao, J.Y. Lee, "One-dimensional SnO_2 nanostructures: facile morphology tuning and lithium storage properties", *Nanotechnology*, **20** (2009) 345704.
12. Z.R. Dai, Z.W. Pan, Z.L. Wang, "Growth and structure evolution of novel tin oxide diskettes", *J. Am. Chem. Soc.*, **124** (2002) 8673–8680.
13. X. Li, Q. Yu, C. Yu, Y. Huang, R. Li, J. Wang, F. Guo, Y. Zhang, S. Gao, L. Zhao, "Zinc-doped SnO_2 nanocrystals as photoanode materials for highly efficient dye-sensitized solar cells", *J. Mater. Chem. A*, **3** (2015) 8076–8082.
14. Y. Liu, F. Yang, X. Yang, "Size-controlled synthesis and characterization of quantum-size SnO_2 nanocrystallites by a solvothermal route", *Colloid Surf. A*, **312** (2008) 219–225.
15. Y.K. Liu, C.L. Zheng, W.Z. Wang, Y.J. Zhan, G.H. Wang, "Production of SnO_2 nanorods by redox reaction", *J. Cryst. Growth*, **233** (2001) 8–12.
16. J.Q. Hu, Y. Bando, Q.L. Liu, D. Golberg, "Laser-ablation growth and optical properties of wide and long single-crystal SnO_2 ribbons", *Adv. Funct. Mater.*, **13** (2003) 493–496.
17. H.Q. Cao, X.Q. Qiu, Y. Liang, L. Zhang, M.J. Zhao, Q.M. Zhu, "Sol-gel template synthesis and photoluminescence of n- and p-type semiconductor oxide nanowires", *Chem. Phys. Chem.*, **7** (2006) 497–501.
18. Y.K. Liu , C.L. Zheng , W.Z. Wang , C.R. Yin , G.H. Wang, "Synthesis and characterization of rutile SnO_2 nanorods", *Adv. Mater.*, **13** (2001) 1883–1887.
19. D. Chen, S. Huang, R. Huang, Q. Zhang, T.-T. Lee, E. Cheng, Z. Hu, Z. Chen, "Highlights on advances in SnO_2 quantum dots: insights into synthesis strategies, modifications and applications", *Mater. Res. Lett.*, **6** (2018) 462–488.
20. P.G. Mendes, M.L. Moreira, S.M. Tebcherani, M.O. Orlandi, J. Andrés, M.S. Li, N. Diaz-Mora. J.A. Varela. E. Longo, "SnO_2 nanocrystals synthesized by microwave-assisted hydrothermal method: towards a relationship between structural and optical properties", *J. Nanopart. Res.*, **14** (2012) 750–13.
21. A.M. Al-Hamdi, U. Rinner, M. Sillanpää, "Tin dioxide as a photocatalyst for water treatment: A review", *Process Saf. Environ.*, **107** (2017) 190–205.
22. T. Entradas, J.F. Cabrita, S. Dalui, M.R. Nunes, O.C. Monteiro, A.J. Silvestre, "Synthesis of sub-5 nm Co-doped SnO_2 nanoparticles and their structural, microstructural, optical and photocatalytic properties", *Mater. Chem. Phys.*, **147** (2014) 563–571.
23. R. Mani, K. Vivekanandan, K. Vallalperuman, "Synthesis of pure and cobalt (Co) doped SnO_2 nanoparticles and its structural, optical and photocatalytic properties", *J. Mater. Sci. Mater. Electron.*, **28** (2017) 4396–4402.
24. D. Chandran, L.S. Nair, S. Balachandran, K. Rajendra Babu, M. Deepa, "Structural, optical, photocatalytic, and antimicrobial activities of cobalt-doped tin oxide nanoparticles", *J. Sol-Gel Sci. Technol.*, **76** (2015) 582–591.
25. Y. Cao, L. Huang, Y. Bai, K. Jermsittiparsert, R. Hosseinzadeh, H. Rasoulnezhad, G. Hosseinzadeh, "Synergic effect of oxygen vacancy defect and shape on the photocatalytic performance of nanostructured TiO_2 coating", *Polyhedron*, **175** (2020) 114214.
26. X. Xu, X. Ding, X. Yang, P. Wang, S. Li, Z. Lu, H. Chen, "Oxygen vacancy boosted photocatalytic decomposition of ciprofloxacin over Bi_2MoO_6: Oxygen vacancy engineering, biotoxicity evaluation and mechanism study", *J. Hazar. Mater.*, **364** (2019) 691–699.
27. Q. Zhang, X. Zhao, L. Duan, H. Shen, R. Liu, "Controlling oxygen vacancies and enhanced visible light photocatalysis of CeO_2/ZnO nanocomposites", *J. Photoch. Photobio. A*, **392** (2020) 112156.
28. B. Matovic, J. Lukovic, B. Stojadinović, S. Aškrabić, A. Zarubica, B. Babic, Z. Dohčević-Mitrović, "Influence of Mg doping on structural, optical and photocatalytic performances of ceria nanopowders", *Process. Appl. Ceram.*,

11 (2017) 304–310.
29. Z. Dohčević-Mitrović, S. Stojadinović, L. Lozzi, S. Aškrabić, M. Rosić, N. Tomić, N. Paunović, S. Lazović, M.G. Nikolić, S. Santucci, "WO_3/TiO_2 composite coatings: Structural, optical and photocatalytic properties", *Mater. Res. Bull.*, **83** (2016) 217–224.
30. T.M. Su, Z.L. Liu, Y. Liang, Z.Z. Qin, J. Liu, Y.Q. Huang, "Preparation of PbYO composite photocatalysts for degradation of methyl orange under visible-light irradiation", *Catal. Comm.*, **18** (2012) 93–97.
31. K. Ishibashi, A. Fujishima, T. Watanabe, K. Hashimoto, "Detection of active oxidative species in TiO_2 photocatalysis using the fluorescence technique", *Electrochem. Commun.*, **2** (2000) 207–210.
32. D. Menzel, A. Awada, H. Dierke, J. Schoenes, F. Ludwig, M. Schilling, "Free-carrier compensation in ferromagnetic ion-implanted SnO_2:Co", *J. Appl. Phys.*, **103** (2008) 07D106.
33. E.J.H. Lee, C. Ribeiro, T.R. Giraldi, E. Longo, E.R. Leite, J.A. Varela, "Photoluminescence in quantum-confined SnO_2 nanocrystals: Evidence of free exciton decay", *Appl. Phys. Lett.*, **84** (2004) 1745–1747.
34. B. Babu, Ch.V. Reddy, J. Shim, R.V.S.S.N. Ravikumar, J. Park, "Effect of cobalt concentration on morphology of Co-doped SnO_2 nanostructures synthesized by solution combustion method", *J. Mater. Sci. Mater. Electron.*, **27** (2016) 5197–5203.
35. P.S. Peercy, B. Morosin, "Pressure and temperature dependences of the Raman-active phonons in SnO_2", *Phys. Rev. B*, **7** (1973) 2779–2786.
36. V. Bonu, A. Das, S. Amirthapandian, S. Dhara, A.K. Tyagi, "Photoluminescence of oxygen vacancies and hydroxyl group surface functionalized SnO_2 nanoparticles", *Phys. Chem. Chem. Phys.*, **17** (2015) 9794–9801.
37. A. Diéguez, A. Romano-Rodríguez, A. Vilà, J.R. Morante, "The complete Raman spectrum of nanometric SnO_2 particles", *J. Appl. Phys.*, **90** (2001) 1550–1557.
38. L.Z. Liu, J.K. Xu, X.L. Wu, T.H. Li, J.C. Shen, P.K. Chu, "Optical identification of oxygen vacancy types in SnO_2 nanocrystals", *Appl. Phys. Lett.*, **102** (2013) 031916.
39. K.N. Yu, Y. Xiong, Y. Liu, C. Xiong, "Microstructural change of nano-SnO_2 grain assemblages with the annealing temperature", *Phys. Rev. B*, **55** (1997) 2666–2671.
40. Y. Liu, M. Liu, "Growth of aligned square-shaped SnO_2 tube arrays", *Adv. Funct. Mater.*, **15** (2005) 57–62.
41. F. Wang, X. Zhou, J. Zhou, T.-K. Sham, Z. Ding, "Observation of single tin dioxide nanoribbons by confocal Raman microspectroscopy", *J. Phys. Chem. C*, **111** (2007) 18839–18843.
42. C. Van Komen, A. Thurber, K.M. Reddy, J. Hays, A. Punnoose, "Structure-magnetic property relationship in transition metal (M = V, Cr, Mn, Fe, Co, Ni) doped SnO_2 nanoparticles", *J. Appl. Phys.*, **103** (2008) 07D141.
43. D.A. Popescu, J.-M. Herrmann, A. Ensuque, F. Bozon-Verduraz, "Nanosized tin dioxide: Spectroscopic (UV-VIS, NIR, EPR) and electrical conductivity studies", *Phys. Chem. Chem. Phys.*, **3** (2001) 2522–2530.
44. I. Rossetti, B. Bonelli, G. Ramis, E. Bahadori, R. Nasi, A. Aronne, S. Esposito, "New insights into the role of the synthesis procedure on the performance of Co-based catalysts for ethanol steam reforming", *Top. Catal.*, **61** (2018) 734–1745.
45. Y. Brik, M. Kacimi, M. Ziyad, F. Bozon-Verduraz, "Titania-supported cobalt and cobalt-phosphorus catalysts: Characterization and performances in ehane oxidative dehydrogenation", *J. Catal.*, **202** (2001) 118–128.
46. S. Roy, A.G. Joshi, S. Chatterjee, A.K. Ghosh, "Local symmetry breaking in SnO_2 nanocrystals with cobalt doping and its effect on optical properties", *Nanoscale*, **10** (2018) 10664–10682.
47. A.S. Ferlauto, G.M. Ferreira, J.M. Pearce, C.R. Wronski, R.W. Collins, X. Deng, G. Ganguly, "Analytical model for the optical functions of amorphous semiconductors from the near-infrared to ultraviolet: Applications in thin film photovoltaics", *J. Appl. Phys.*, **92** (2002) 2424–2436.
48. P.D. Borges, L.M.R. Scolfaro, H.W. Leite Alves, E.F. da Silva Jr., "DFT study of the electronic, vibrational, and optical properties of SnO_2", *Theor. Chem. Acc.*, **126** (2010) 39–44.
49. L. Brus, "Electronic wave functions in semiconductor clusters: experiment and theory", *J. Phys. Chem.*, **90** (1986) 2555–2560.
50. S. Dalui, S. Rout, A.J. Silvestre, G. Lavareda, L.C.J. Pereira, P. Brogueira, O. Conde, "Structural, electrical and magnetic studies of Co:SnO_2 and (Co,Mo):SnO_2 films prepared by pulsed laser deposition", *Appl. Surf. Sci.*, **278** (2013) 127–131.
51. H.S. So, J.-W. Park, D.H. Jung, K.H. Ko, H. Lee, "Optical properties of amorphous and crystalline Sb-doped SnO_2 thin films studied with spectroscopic ellipsometry: Optical gap energy and effective mass", *J. Appl. Phys.*, **118** (2015) 085303.
52. A. Oprea, E. Moretton, N. Bârsan, W.J. Becker, J. Wöllenstein, U. Weimar, "Conduction model of SnO_2 thin films based on conductance and Hall effect measurements", *J. Appl. Phys.*, **100** (2006) 033716.
53. A. Kar, M.A. Stroscio, M. Dutta, J. Kumari, M. Meyyappan, "Growth and properties of tin oxide nanowires and the effect of annealing conditions", *Semicond. Sci. Technol.*, **25** (2010) 024012.
54. I.I. Gontia, M. Baibarac, I. Baltog, "Photoluminescence and Raman studies on tin dioxide powder and tin dioxide/single-walled carbon-nanotube composites", *Phys. Status Solidi B*, **248** (2011) 1494–1498.
55. B. Choudhury, A. Choudhury, "Luminescence characteristics of cobalt doped TiO_2 nanoparticles", *J. Lumin.*, **132** (2012) 178–184.
56. S. Yamamoto, "Photoluminescence quenching in cobalt doped ZnO nanocrystals", *J. Appl. Phys.*, **111** (2012) 094310.
57. S.P. Kim, M.Y. Choi, H.C. Choi, "Photocatalytic activity of SnO_2 nanoparticles in methylene blue degradation", *Mater. Res. Bull.*, **74** (2016) 85–89.
58. X. Pan, M.-Q. Yang, X. Fu, N. Zhang, Y.-J. Xu, "Defective TiO_2 with oxygen vacancies: synthesis, properties and photocatalytic applications", *Nanoscale*, **5** (2013) 3601–3614.
59. D.F. Cox, T.B. Fryberger, S. Semancik, "Oxygen vacancies and defect electronic states on the SnO_2(110)-1 × 1", *Phys. Rev. B*, **38** (1988) 2072–2083.

Applied Surface Science 513 (2020) 145822

Contents lists available at ScienceDirect

Applied Surface Science

journal homepage: www.elsevier.com/locate/apsusc

Full Length Article

Local electrical properties and charging/discharging of CdSe/CdS core-shell nanoplatelets

Borislav Vasić[a,*], Sonja Aškrabić[b], Milka M. Jakovljević[a], Mikhail Artemyev[c]

[a] Graphene Laboratory of Center for Solid State Physics and New Materials, Institute of Physics Belgrade, University of Belgrade, Pregrevica 118, 11080 Belgrade, Serbia
[b] Nanostructured Matter Laboratory of Center for Solid State Physics and New Materials, Institute of Physics Belgrade, University of Belgrade, Pregrevica 118, 11080 Belgrade, Serbia
[c] Research Institute for Physical Chemical Problems of the Belarusian State University, Minsk 220006, Belarus

ARTICLE INFO

Keywords:
CdSe/CdS nanoplatelets
Local electrical properties
Atomic force microscopy

ABSTRACT

Quantum confinement in two-dimensional semiconductor nanoplateletes (NPLs) is determined by their thickness which can be precisely controlled during the synthesis. As a result, NPLs have a very narrow luminescence spectrum and they can provide light sources with very high color purity. Switchable light sources needed for a wide range of applications require the dynamic control of the luminescence. One efficient approach for this purpose is direct charge injection into NPLs. In order to study charging/discharging processes and local electrical properties of CdSe/CdS core-shell NPLs as the model system, here we employed electrical methods based on atomic force microscopy (AFM). Simple and efficient procedures for "write/read/erase" operations are presented: charges are written by a biased AFM tip in contact with the NPLs, their charge state is read by Kelvin probe force or electric force microscopy, whereas injected charges are erased by inversely biased AFM tip. The amount of injected charges is well controlled by a magnitude, polarity and duration of the applied bias voltage, whereas the rate of subsequent spontaneous charge relaxation is dominantly determined by ambient humidity.

1. Introduction

Optoelectronic applications of colloidal semiconductor nanocrystals (NCs) in light-emitting diodes (LEDs) [1] and solar cells [2] are based on their size-tunable electronic and optical properties [3,4]. Due to quantum confinement, discrete energy levels which determine the electronic band gap and optical transitions can be precisely controlled by modifying the size and shape of semiconductor NCs. As a result, they are characterized with a narrow and tunable emission spectrum covering a broad range from ultraviolet, through visible to near-infrared region [1,5–7]. At the same time, relatively simple, cost-effective, flexible and environment-friendly fabrication methods of colloidal chemistry, compatible with various assembling techniques, provide large-area structures needed for applications [8,9].

Although the optoelectronic properties of semiconductor NCs are most relevant for applications, electrostatic properties play a significant role as well, since the charge occupation of discrete electronic states determines the strength and rates of optical transitions [10,11]. Therefore, charging can be an efficient method for the switching of luminescence in semiconductor NCs. This property is very interesting from practical point of view and such dynamic control significantly extends the scope of NCS' applicability. In this context, the most suitable control methods are the electrical ones, such as direct charge injection [12–14], doping [15,16], electric-field control [17–19], or incorporation into LED devices [1,5–7].

Electrical properties of semiconductor NCs are commonly investigated at macro-scale, on large ensembles of nanostructures [20,21]. On the other hand, atomic force microscopy (AFM) based methods enable local studies with a high spatial resolution reaching the single-nanoparticle level. As a result, these methods could provide additional information about local transport properties [22–24] and electronic band structure [25,26]. In addition, AFM based methods are very efficient for the local charging of semiconductor NCs and modulation of their photoluminescence [27] and electrical properties [28], or for the demonstration of inverse effects, where an external light induces local charges in semiconductor NCs leading to photoionization [10,11,29,30] or charge separation [31–33].

Recently, two-dimensional (2D) nanoplatelets (NPLs), a new class of colloidal semiconductor NCs, have attracted a lot of attention because the quantum confinement is determined by NPL thickness [34–37]. Since the thickness can be controlled more precisely than the geometry (size and shape) of standard three-dimensional NCs such as quantum

* Corresponding author.
E-mail address: bvasic@ipb.ac.rs (B. Vasić).

https://doi.org/10.1016/j.apsusc.2020.145822
Received 3 December 2019; Received in revised form 21 January 2020; Accepted 16 February 2020
Available online 20 February 2020
0169-4332/

dots, 2D NPLs provide more narrow emission and light sources with improved color purity. Although, the luminescence control of 2D NPLs by electrical methods has been demonstrated recently [38–40], their electrostatic properties at nanoscale and their control by direct charge injection have been still unexplored.

In this paper, we use AFM based electrical methods, Kelvin probe force microscopy (KPFM) and electric force microscopy (EFM), in order to study local electrical properties of 2D CdSe/CdS core-shell NPLs. They were selected as the model system due to enhanced spontaneous emission and lasing compared to the core-only NPLs [41,42]. We show that charging/discharging of NPLs can be well controlled by a magnitude, polarity and duration of the bias voltage applied by the AFM tip. The paper is organized in the following way. After the initial morphological analysis in Section 3.1, the results for the local electrical surface potential of the NPLs are presented in Section 3.2. Write operation or local charging of the NPLs by the AFM tip as a function of the tip bias voltage and hold time is demonstrated in Section 3.3. KPFM and EFM methods are employed for the read operation and characterization of charged NPLs. The time relaxation of injected charges is studied in Section 3.4 by successive KPFM measurements. Finally, in Section 3.5, a simple AFM based method for the erase operation and fast discharging is illustrated.

2. Material and methods

2.1. Sample preparation

Core-shell CdSe/CdS NPLs having 4.5 ML CdSe core and 3 ML CdS shell, with ca. 20 nm × 30 nm lateral size, were synthesized according to a published procedure [43–45]. These NPLs, being hydrophobic, were functionalized with mercaptoacetic acid (MAA) and thereby negatively charged. After the treatment with MAA, NPLs were rinsed with isopropanol and dispersed in water. Commercial highly n-doped Si wafer with 85 nm thick SiO_2 film on the top was treated in aminopropyl trietoxy silane (APTS) dissolved in toluene, in order to positively charge SiO_2. After being left in solution for 20 min, the substrate was rinsed with toluene. In the next step, the colloidal solution of negatively charged CdSe/CdS NPLs was dropcast onto the wafer covered with ATS and left for 20 min in order to allow for electrostatic self-assembly to occur. After 20 min the substrate was rinsed and 2D layer of close-packed core-shell NPLs on SiO_2 surface was obtained. According to the preparation procedure, the investigated sample can be considered as a film consisting of CdSe/CdS NPLs functionalized with MAA and thin layer of APTS polyelectrolyte underneath. Hereafter it will be called CdSe/CdS film.

2.2. AFM measurements

In order to investigate morphology and local electrical properties of CdSe NPLs, we employed NTEGRA Prima AFM system. Basic topographic imaging was performed in tapping AFM mode. AFM phase and magnitude signals were recorded simultaneously with the topography in order to resolve shape and edges of NPLs with a better resolution. The phase signal corresponds to the phase lag of the AFM cantilever, while the magnitude signal represents the oscillation amplitude of the AFM cantilever.

Local electrical properties were characterized by two-pass techniques, EFM and KPFM. AFM probes NSG01/Pt from NT-MDT with Pt coating were used. In both EFM and KPFM, topography was measured in the first pass by AFM tapping mode. Then, the AFM probe was lifted by 20 nm and the scanning was performed along the same topographic line measured in the first pass. During the second pass in EFM, DC voltage was applied between the AFM probe and the sample while the probe was excited mechanically. The measured EFM signal in the second pass corresponds to the phase lag of the AFM cantilever which is proportional to the gradient of the normal electric force. In order to avoid any confusion with the AFM phase measured during basic topographic imaging, this signal will be hereafter called EFM phase.

On the other hand, during the second pass in KPFM, a sum of AC and variable DC voltage was applied between the AFM probe and sample. The AC voltage excited oscillations of the AFM probe, while the value of the variable DC voltage which canceled these oscillations was equal to the electrical surface potential or to the contact potential difference (CPD) between the probe and sample. The CPD is equal to the work function difference between the tip and sample, WF_{tip} and WF_s, respectively. The absolute value of the sample work function WF_s was calculated as $WF_s = WF_{tip} - CPD$, where the work function of Pt coated AFM tips were calibrated using HOPG as a reference [46].

In order to interpret EFM measurements and the interaction between biased AFM tip and the sample, i.e. whether this interaction is attractive or repulsive, and in order to determine the polarity of charges injected into the sample, the phase signal was adjusted prior to EFM measurements in the following way. By varying the phase of the piezo-driver, the initial AFM phase was set to 90° at the mechanical resonance of employed AFM cantilever, with a decreasing phase across the resonance (with a negative slope). Taking into account that the attractive (repulsive) AFM tip-sample interaction shifts the resonance to lower (higher) frequencies, the attractive (repulsive) interaction is characterized by a decrease (increase) of the phase shift in the considered case.

AFM methods for local charging and subsequent charge detection [47] have been well developed in recent years for semiconductor NCs [27,28], organic nanostructures [48,49], carbon nanotubes [50], 2D materials [51–53] and even biological nanostructures [54]. In this study, the local charging was performed according to the following procedure. After the initial electrical characterization carried out in either KPFM or EFM mode, the AFM system was switched into contact mode, the AFM tip approached to the sample surface, and DC voltage in the range ± 10 V was applied to the AFM tip. The hold time (defined as a time during the bias voltage was applied) was varied from several seconds up to several minutes. After that, the probe was lifted, the voltages were turned off, and the system was switched back into one of the targeted electrical modes in order to characterize changes in electrical properties induced by the injected charges.

3. Results and discussion

3.1. Morphology

Transmission electron microscopy (TEM) image of CdSe/CdS NPLs is given in Fig. 1(a). As can be seen, the NPLs are randomly oriented and typically more elongated in one direction having approximately a rectangular shape with the size of several tenths of nanometers. Although TEM provides the best spatial resolution, AFM enables simpler and faster morphological characterization. 2D and three-dimensional (3D) topographic images of CdSe/CdS film obtained by AFM are depicted in Fig. 1(b) and (c), respectively. Film thickness of 4.7 ± 1.5 nm was determined as an average value of the height distribution while the deviation was calculated as an average roughness. The autocorrelation image is given in Fig. 1(d). The dominant feature is the bright circular domain in the middle. Since the autocorrelation image is approximately isotropic, NPLs do not have any preferential orientation in the plane. Due to the convolution with the AFM tip, NPLs look like rounded grains in topographic images. Therefore, in the grain-size analysis, they were approximated with circular plates. The histogram of their size distribution is displayed in Fig. 1(d). As can be seen, the average NPL radius is around 15 nm, implying that a typical NPL can be represented by a thin disc with a diameter of around 30 nm.

The AFM phase and magnitude signals are displayed in Fig. 1(e) and (f), respectively. As can be seen, boundaries between adjacent NPLs are better resolved whereas the contrast between the NPLs and underlying substrate is more pronounced due to generally higher sensitivity of

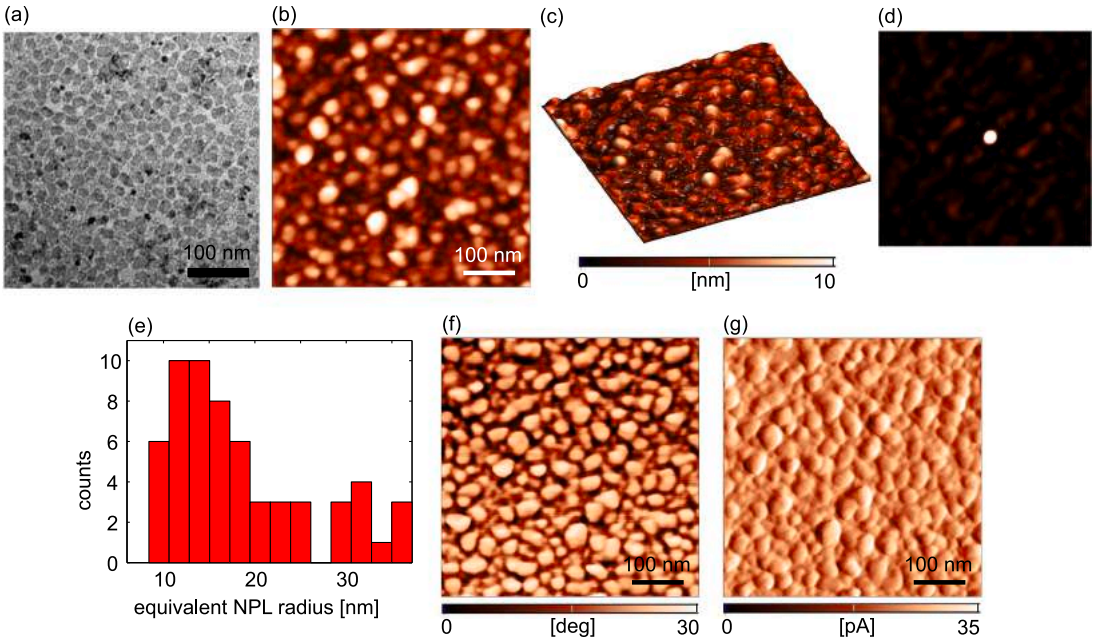

Fig. 1. Morphology of CdSe NPLs: (a) TEM image, (b) 2D and (c) 3D topographic image, (d) autocorrelation image, (e) histogram of the equivalent NPL radius, (f) AFM phase and (g) AFM magnitude image.

phase and magnitude signals to NPL edges. Therefore, these AFM modes provide a high spatial resolution for the imaging of 2D NPLs similar to TEM.

3.2. Electrical surface potential

Topography and CPD map of CdSe/CdS film measured by KPFM are presented in Fig. 2(a) and (b), respectively. The histogram of the CPD map is depicted in Fig. 2(c). It is characterized with a single and narrow peak with the average CPD of 817 ± 7 mV. Taking into account measurements on five different $2 \times 2\ \mu m^2$ areas, the average CPD is 800 ± 25 mV, demonstrating that CdSe/CdS NPLs have uniform surface potential. The absolute value of the work function of CdSe/CdS film was found to be 4.13 ± 0.04 V (after the calibration of the Pt coated AFM tip) which is in good agreement with literature data [55].

Although KPFM is a convenient technique which directly gives CPD as a result, the spatial resolution limited to 20–30 nm does not allow resolving of individual NPLs. In order to overcome this limitation, EFM was employed instead. The EFM phase signal is proportional to gradient of the electric force in the normal direction. As a result, although EFM and KPFM share similar experimental setups, the EFM phase calculated as a spatial derivative is much more sensitive to spatial variations of surface electrical properties. Topography and EFM phase map of CdSe/CdS film are given in Fig. 3(a) and (b), respectively. As can be seen, individual NPLs are clearly resolved in both topographic and EFM image. Most of NPLs have similar EFM contrast. Still, the EFM phase signal is correlated with the topography, which implies that bigger topographic features, which correspond to clusters of several NPLs (appeared during sample preparation), give more pronounced EFM phase contrast.

In order to obtain quantitative information from EFM measurements, the EFM imaging was performed as a function of the EFM bias voltage in the range ± 10 V. For every bias voltage, an average EFM phase shift of CdSe/CdS NPLs was determined. The results of these measurements are summarized in Fig. 3(c) showing a parabolic dependence of the EFM phase on the EFM tip voltage. The experimental data were fitted by the following function [48,53,54]

$$\Phi_{EFM} = C_1(V_{EFM} - V_{sp})^2 + C_2(V_{EFM} - V_{sp}) + \Phi_0, \quad (1)$$

where V_{EFM} is the EFM voltage applied on the AFM probe in the second pass of EFM imaging, V_{sp} is the electrical surface potential which corresponds to the CPD measured by KPFM, whereas C_1, C_2, and Φ_0 are additional fitting constants. The first term in Eq. (1) corresponds to the capacitive tip-sample interaction, whereas the second term represents the Coulombic interaction between biased AFM probe and localized charges at the sample surface [48,53,54].

The fitting curve is presented in Fig. 3(c) by the solid line, the dashed line shows the contribution of the parabolic function (the

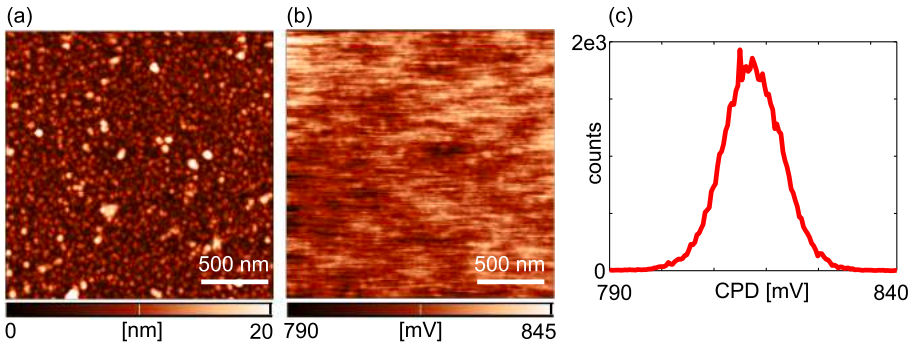

Fig. 2. (a) Topography and (b) CPD measured by KPFM. (c) Histogram of the CPD distribution.

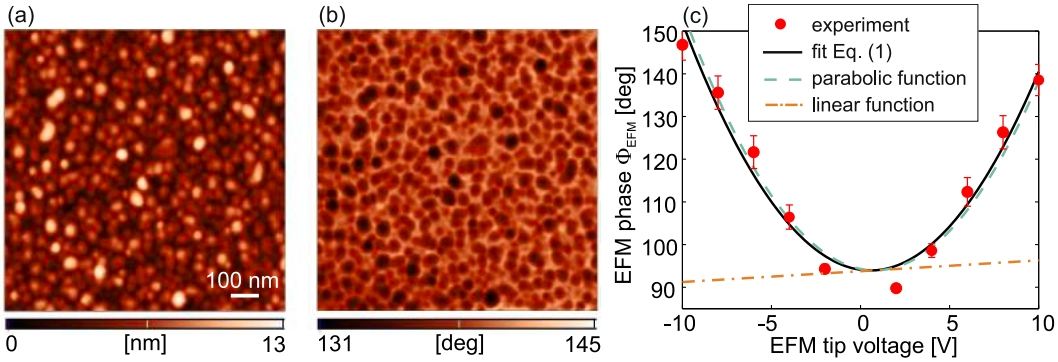

Fig. 3. (a) AFM topographic and (b) EFM phase image. The EFM voltage in the second pass was − 8 V. (c) An average EFM phase of CdSe/CdS NPLs as a function of EFM voltage in the second pass. Dots stand for experimentally measured values, the solid line is fit to Eq. (1), whereas the dashed and dashed-dotted lines stand for the contribution of the parabolic and linear term from Eq. (1), respectively. Every dot represents the EFM phase obtained by the averaging of all NPLs within one scan area of 1 × 1 μm^2 for a given EFM voltage.

capacitive interaction), whereas the dashed-dotted line represents the linear function (Coulombic interaction) from Eq. (1). The local electrical surface potential V_{sp} of CdSe/CdS film obtained from the fit is 0.795 ± 0.025 V. V_{sp} corresponds to the EFM voltage where the EFM phase curve reaches the minimum Φ_0. This is exactly the voltage by which the EFM phase curve is shifted along the voltage axis. The fitting procedure gives non-zero and positive coefficient C_2 meaning that Coulombic interaction has a certain contribution in the measured EFM phase shift. As can be seen in Fig. 3(c), for the positive (negative) voltage difference $V_{EFM} - V_{sp} > 0$ ($V_{EFM} - V_{sp} < 0$), Coulombic interaction leads to a higher (lower) EFM phase shift represented as a change between the solid and dashed line. According to the phase convention explained in Section 2.2, an attractive (repulsive) interaction is characterized by a decrease (increase) of the phase shift. Therefore, in the considered case, the electrical interaction is repulsive (attractive) for positive (negative) voltage difference $V_{EFM} - V_{sp}$ meaning that as-deposited NPLs are slightly positively charged. This is inconsistent with the preparation procedure where NPLs were negatively charged. However, after the deposition, the NPLs inevitably come into the contact with oxygen from air which is well known as p-type dopant for metal chalcogenide quantum dots [56]. Similar p-doping after the exposure to air and the reaction with oxygen was observed for other 2D system such as graphene [57] and thin organic films [48]. Therefore, positive charging of as-deposited NPLs most probably originates from the doping by ambient oxygen. According to the results presented in Fig. 3, EFM allows for a high-resolution electrical imaging of CdSe/CdS films at the single-nanoparticle level. At the same time, electrical surface potential and properties of the electrical interaction can be determined with the same spatial resolution, but an additional processing and fitting of experimentally measured data are necessary.

3.3. Local charging

Results for the electrical surface potential and EFM phase measured after the local charging of CdSe/CdS film at a single point are presented in Fig. 4. The KPFM map measured after the charging at the central point, for the bias voltage $V_{ch} = -8$ V and hold time $T_{ch} = 30$ s is depicted in Fig. 4(a). The cross section of the CPD map along the dashed line is given in Fig. 4(b) showing a significant drop in CPD around the charging point of around ΔCPD ≈ 200 mV (ΔCPD was calculated as a difference between CPD of uncharged (CPD_0) and charged areas (CPD_{ch})). The EFM phase maps after the local charging at a negative bias voltage are depicted in Fig. 4(c) for a positive (top) and negative (bottom) EFM voltage. EFM phase profiles along the dashed lines are given in Fig. 4(d). As can be seen, the EFM phase contrast is reversed upon changing the polarity of the EFM voltage which proves Coulombic tip-sample interaction.

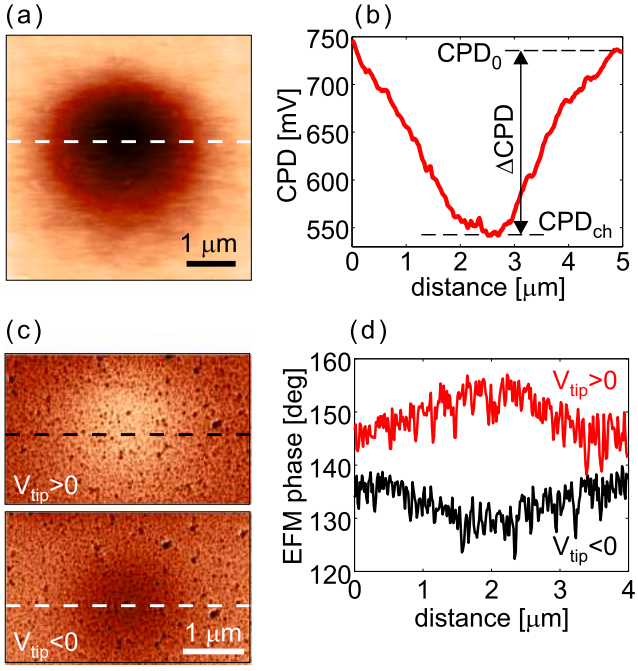

Fig. 4. Electrical characterization after the local charging at the bias voltage $V_{ch} = -8$ V and for the hold time $T_{ch} = 30$ s: (a) CPD map measured by KPFM, and (b) the cross section of the CPD along the dashed line in part (a), (c) EFM phase maps for positive (top) and negative EFM voltage (bottom), and (d) cross sections along the dashed lines in (c).

The EFM phase grows up for the positive EFM voltage when the electrical tip-sample interaction is repulsive. On the other hand, the EFM phase falls down for the negative EFM voltage when the interaction is attractive. Therefore, the sample is locally positively charged, although the charging was performed at a negative bias voltage. This is in accordance with KPFM measurements which indicate a local decrease of Fermi level. According to these results, the mechanism of local charging is not based on charge injection by a biased AFM tip, but on the polarization of the sample surface. This means that negatively biased AFM tip does not inject negative charges, but polarizes the surrounding medium and attracts positive charges.

While the CPD map measured after the charging in Fig. 4(b) consists of a rather smooth potential dip, EFM phase profiles consist of a smooth dip/rise (depending on the bias voltage during the charging) and of superimposed oscillating phase. The oscillating part corresponds to individual NPLs which become either brighter (top EFM image in Fig. 4(c)) or darker (bottom EFM image in Fig. 4(c)) than surrounding

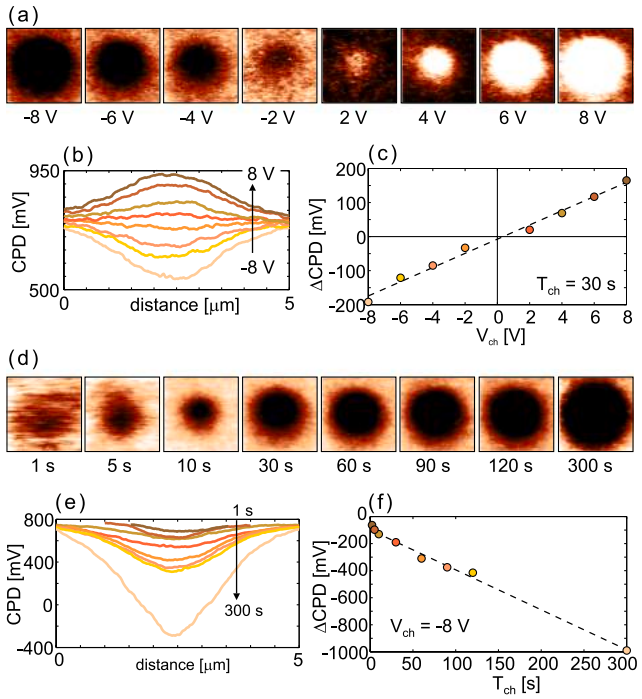

Fig. 5. Change of CPD as a function of bias voltage during the local charging: (a) CPD maps measured by KPFM after the charging for bias voltages in the range ± 8 V for the fixed hold time T_{ch} = 30 s (the scan size is 5 × 5 μm^2 whereas the CPD scale is 700 − 770 mV (760 − 810 mV) for the negative (positive) bias voltages), (b) CPD profiles extracted from the maps in part (a), and (c) ΔCPD (calculated from the profiles in part (b) for the central points) as a function of the bias voltage with a linear fit represented by the dashed line. Change of CPD as a function of the hold time during the local charging: (d) CPD maps measured by KPFM after the charging for the hold time in the range 1 − 300 s and at the fixed bias voltage V_{ch} = −8 V (the scan size is 5 × 5 μm^2 whereas the CPD scale is 630 − 760 mV), (e) CPD profiles from the maps in part (d), and (f) ΔCPD (calculated from the profiles in part (e) for the central points) as a function of the hold time with a linear fit represented by the dashed line.

and uncharged NPLs. The modified EFM phase of NPLs after the charging indicates that charge storage can be detected in individual NPLs.

In order to test the influence of the voltage V_{ch} applied during the charge injection, electrical surface potential was measured by KPFM after the charging for V_{ch} in the range ± 8 V and for the fixed hold time T_{ch} = 30 s. Corresponding CPD maps and profiles are depicted in Fig. 5(a) and (b), respectively. As can be seen, the charged areas have a circular shape with a diameter increasing with $|V_{ch}|$ and reaching around 5 μm for the highest voltage. These areas behave like potential wells while their depth increases with $|V_{ch}|$. Change of the CPD between charged and uncharged areas, ΔCPD, as a function of V_{ch} is plotted in Fig. 5(c). ΔCPD can be fitted with a linear curve represented by the dashed line. For the chosen range of V_{ch}, ΔCPD changes almost linearly in the range ≈ ±200 mV.

Similar study was carried out in order to test the influence of the hold time in the range 1 − 300 s, while keeping constant the voltage during charging (V_{ch} = −8V). CPD maps measured after the charging are shown in Fig. 5(d). The central black circle becomes wider and darker with increasing T_{ch}, reaching around 5 μm in a diameter for the longest hold time. CPD profiles are given in Fig. 5(e) showing potential wells whose depth increases with T_{ch}. The change of the CPD between charged and uncharged areas, ΔCPD, as a function of T_{ch} = 30 s is depicted in Fig. 5(f). Dashed line stands for a fit to the experimentally measured points. By omitting two starting points and going from T_{ch} = 10 s, ΔCPD grows practically linearly with T_{ch} up to − 1000 mV.

Injected charges are trapped in CdSe/CdS film, in CdSe/CdS NPLs and/or in the underneath polyelectrolyte layer, whereas they can be stored at the surface of underlying silicon-dioxide as well. The considered system can be approximated as a plane capacitor. The bottom electrode is silicon, the top electrode consists of CdSe/CdS film and top charged layer of silicon-dioxide, whereas the rest of the silicon-dioxide layer acts as a dielectric. Surface density of injected charges can be approximately calculated according to the following expression $\sigma = \varepsilon_0 \varepsilon_r / t_d \cdot \Delta CPD$, where ΔCPD is change in CPD due to charging, ε_0 is the vacuum permittivity, whereas ε_r and t_d are the permittivity and thickness of a dielectric layer between the NPLs and silicon layer. According to results from Fig. 5, the following relations hold, $\Delta CPD = \alpha_V V_{ch}$ and $\Delta CPD = \alpha_T T_{ch}$, where α_V and α_T are the slopes of the linear fits in Fig. 5(b) and (d), respectively. Surface charge density can be then represented as , where $C_s = \varepsilon_0 \varepsilon_r / t_d$ is the capacitance per area. Therefore, although density of charges injected just into NPLs can not be determined, according to the last formula, density of injected charges can be simply controlled and adjusted by V_{ch} and T_{ch}.

3.4. Time relaxation of injected charges

Time relaxation of injected charges was studied by successive KPFM mapping after the initial charging. The KPFM mapping was maintained until the complete charge relaxation characterized by a nearly flat CPD map. The consecutive CPD maps measured by KPFM are presented in Fig. 6(a) and (d) for the charging by a positive and negative bias voltage, respectively. Corresponding CPD profiles are given in Fig. 6(b)

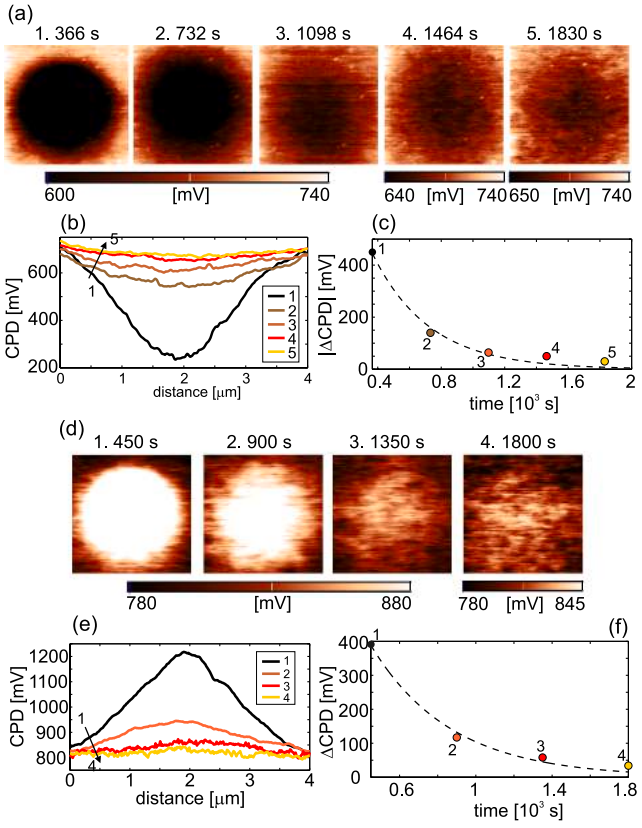

Fig. 6. Time relaxation of the charges injected by applying − 8 V for 60 s: (a) successive CPD maps measured by KPFM before almost complete relaxation (the scan size is 4 × 4 μm^2), (b) CPD profiles, and (c) change of the —CPD— as a function of time. Time relaxation of the charges injected by applying 8 V for 120 s: (d) successive CPD maps measured by KPFM (the scan size is 4 × 4 μm^2), (e) CPD profiles, and (f) change of the CPD as a function of time. Dashed lines in parts (c) and (f) stand for the exponential fits to the experimentally determined points. Time difference between adjacent points is equal to the time needed for one complete KPFM scan which is 366 s for the case in parts (a–c), and 450 s for the case in parts (d–f).

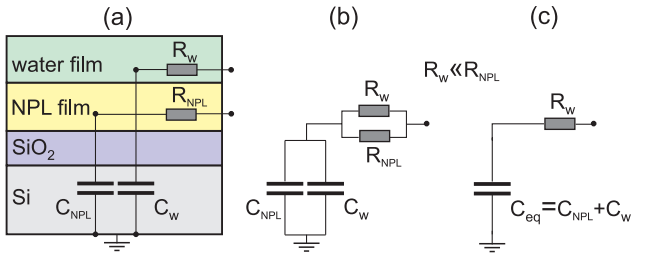

Fig. 7. Physical models for the time relaxation: (a), (b) the equivalent electrical scheme, and (c) a simplified scheme taking into account that the water-layer resistance R_w is much smaller than the in-plane resistance R_{NPL} of the CdSe/CdS film consisting of CdSe/CdS NPLs functionalized with MAA and a thin layer of APTS polyelectrolyte underneath.

and (e), whereas the change of CPD as a function of time is given in Fig. 6(c) and (f), respectively. The absolute value |ΔCPD| was fitted by an exponential function $\Delta CPD_0 \cdot \exp(-t/\tau)$, where t is time, τ stands for the time constant of the relaxation process, whereas ΔCPD_0 is the absolute value of ΔCPD at the initial moment (the moment when the first KPFM scan was finished). According to the fitting results, the time relaxation constants are 418 s and 358 s for positive and negative V_{ch}, respectively, therefore, around 6 − 7 min.

The relaxation rates strongly depend on humidity. At ambient conditions, the sample surface is covered by a thin water layer acting as an additional conducting channel through which injected charges flow away [51]. Simple physical model of the considered system is depicted in Fig. 7(a). As can be seen, there are two films at the top of the silicon-dioxide: the first one is the CdSe/CdS film which consists of CdSe/CdS NPLs functionalized with MAA and a thin layer of APTS polyelectrolyte underneath, whereas the second film is a water layer. Both films have corresponding capacitances with respect to the grounded silicon substrate, C_{NPL} and C_w, respectively. Since the charge transport through the films is lateral, they are modeled by two resistors, R_{NPL} and R_w. Equivalent electrical scheme is given in Fig. 7(b). It is a series circuit between two parallel capacitances, C_{NPL} and C_w, and resistances, R_{NPL} and R_w.

The lateral current through CdSe/CdS film measured by conductive AFM (C-AFM) was zero which indicated a very high resistance R_{NPL}. In order to study charge relaxation in such high-resistance films, KPFM was employed instead [22]. At high humidities above 50%, discharge was very fast (much faster than several minutes needed for one KPFM scan) and it was not possible to observe any charging. Obviously, in this case the water film resistance R_w is very low. On the other hand, the charge relaxation measurements presented in Fig. 6 were done at a lower humidity of around 30%. As a result, the water film resistance R_w is increased, while discharge process is prolonged and can be followed by KPFM. According to the previous analysis, the water layer resistance R_w is much lower than the resistance of CdSe/CdS film, R_{NPL}. Therefore, R_{NPL} can be then omitted, whereas a simplified electrical scheme is given in Fig. 7(c). The time constant of the RC circuit is $\tau = R_w C_{eq}$, where $C_{eq} = C_{NPL} + C_w$. As a result, the relaxation time depends dominantly on the water film resistance R_w, which falls down at increased humidity thus making the relaxation and discharging very fast.

3.5. "Write/read/erase" operations

In addition to charge injection by a biased AFM tip or "writing" operation and KPFM/EFM measurements aimed for "reading" operation, a full control of the charge density requires an efficient mechanism for fast charge erasing in order to avoid long process of spontaneous relaxation discussed in the previous section. In order to erase or nullify charges, it is necessary to ground the sample or to inject charges of opposite polarity during a certain hold time. Such procedure is illustrated in Fig. 8(a). The first CPD map was recorded after charging at

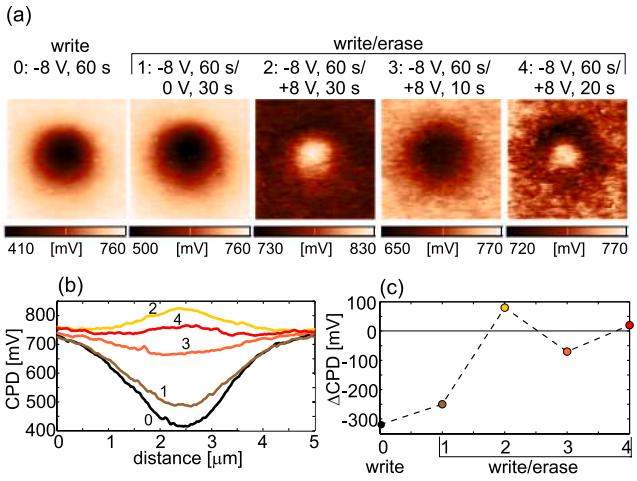

Fig. 8. Write/erase operation: (a) CPD maps measured by KPFM after (0) the writing operation only (charge injection at the negative bias voltage), and (1–4) several trials for the writing and subsequent erasing of injected charges with different combinations of the positive bias voltages and hold times, (b) CPD profiles extracted from the maps in part (a), and (c) change of the CPD for all five cases in part (a). The dashed line is a guide to eye. The scan size of CPD maps is 5 × 5μm^2.

− 8 V for 60 s. The next four CPD maps represent trials aiming to nullify the injected charges in the following way: by subsequent grounding the film for 30 s and by charging the film at the positive voltage of 8V for three different hold times 30 s, 10 s and 20 s. CPD profiles are presented in Fig. 8(b) whereas the evolution of ΔCPD is shown in Fig. 8(c). The writing operation at − 8 V for 60 s generates a potential well with a depth of around 300 mV. Erasing operation should flatten the potential as much as possible and give zero ΔCPD. In this respect, the erasing operation 4 gives the best performance.

4. Conclusion

In a summary, the initial work function of CdSe/CdS film of around 4 eV can be locally modified by the charging with a biased AFM probe. Such "write" operation generated 2D, circular potential wells, with a diameter of several microns and a depth of several hundreds of milivolts. Since the silicon-dioxide and the polyelectrolyte layer beneath NPL can also trap charges, it was not possible to determine the exact density of charges stored in NPLs only. Still, it was shown that the magnitude, polarity and duration of applied bias voltage very efficiently controlled the depth and diameter of the induced potential wells. Therefore, it is reasonable to expect that a proper combination of these control parameters would give a desired charge density in NPLs. "Read" operation was based on KPFM and EFM methods. While the first one gave CPD and work function of NPLs directly as an output, EFM had a better spatial resolution which allowed the electrical imaging of single NPLs. The rate of the spontaneous charge relaxation was dictated by environmental humidity. At the humidity of around 30%, the time relaxation constant was around 5 min, whereas at higher humidities injected charges could not be detected by KPFM/EFM due to very fast discharging through a water adlayer on NPLs. In order to avoid the spontaneous relaxation, trapped charges can be nullified and erased by inversely polarized AFM tip. Presented procedures for "write/read/erase" operations provide efficient means for dynamic control of a charge state of CdSe/CdS NPLs, while further experiments should explore capability of these procedures for the luminescence control.

Declaration of Competing Interest

There are no conflict of interest in this work.

Acknowledgements

This work was supported by the Ministry of Education, Science, and Technological Development of the Republic of Serbia through projects OI171005, OI171032, and III45018. M.A. acknowledges partial financial support from CHEMREAGENTS program and BRFFI grant X18CORG-001. We thank A. Prudnikau, A. Antanovich and A. Mikhailov for help with samples preparation.

References

[1] Y. Shirasaki, G.J. Supran, M.G. Bawendi, V. Bulović, Emergence of colloidal quantum-dot light-emitting technologies, Nat. Photon. 7 (2012) 13.
[2] P.V. Kamat, Quantum dot solar cells. Semiconductor nanocrystals as light harvesters, J. Phys. Chem. C 112 (2008) 18737–18753.
[3] A.P. Alivisatos, Perspectives on the physical chemistry of semiconductor nanocrystals, J. Phys. Chem. 100 (1996) 13226–13239.
[4] A.M. Smith, S. Nie, Semiconductor nanocrystals: structure, properties, and band gap engineering, Acc. Chem. Res. 43 (2010) 190–200.
[5] V.L. Colvin, M.C. Schlamp, A.P. Alivisatos, Light-emitting diodes made from cadmium selenide nanocrystals and a semiconducting polymer, Nature 370 (1994) 354–357.
[6] S. Coe, W.-K. Woo, M. Bawendi, V. Bulović, Electroluminescence from single monolayers of nanocrystals in molecular organic devices, Nature 420 (2002) 800–803.
[7] A.H. Mueller, M.A. Petruska, M. Achermann, D.J. Werder, E.A. Akhadov, D.D. Koleske, M.A. Hoffbauer, V.I. Klimov, Multicolor light-emitting diodes based on semiconductor nanocrystals encapsulated in GaN charge injection layers, Nano Lett. 5 (2005) 1039–1044.
[8] V. Lesnyak, N. Gaponik, A. Eychmüller, Colloidal semiconductor nanocrystals: the aqueous approach, Chem. Soc. Rev. 42 (2013) 2905–2929.
[9] J. Chang, E.R. Waclawik, Colloidal semiconductor nanocrystals: controlled synthesis and surface chemistry in organic media, RSC Adv. 4 (2014) 23505–23527.
[10] T.D. Krauss, L.E. Brus, Charge, polarizability, and photoionization of single semiconductor nanocrystals, Phys. Rev. Lett. 83 (1999) 4840–4843.
[11] T.D. Krauss, S. O'Brien, L.E. Brus, Charge and photoionization properties of single semiconductor nanocrystals, J. Phys. Chem. B 105 (2001) 1725–1733.
[12] C. Wang, M. Shim, P. Guyot-Sionnest, Electrochromic nanocrystal quantum dots, Science 291 (2001) 2390–2392.
[13] W.-K. Woo, K.T. Shimizu, M.V. Jarosz, R.G. Neuhauser, C.A. Leatherdale, M.A. Rubner, M.G. Bawendi, Reversible charging of CdSe nanocrystals in a simple solid-state device, Adv. Mater. 14 (2002) 1068–1071.
[14] P.P. Jha, P. Guyot-Sionnest, Photoluminescence switching of charged quantum dot films, J. Phys. Chem. C 111 (2007) 15440–15445.
[15] M. Shim, P. Guyot-Sionnest, n-type colloidal semiconductor nanocrystals, Nature 407 (2000) 981–983.
[16] D. Mocatta, G. Cohen, J. Schattner, O. Millo, E. Rabani, U. Banin, Heavily doped semiconductor nanocrystal quantum dots, Science 332 (2011) 77–81.
[17] E. Rothenberg, M. Kazes, E. Shaviv, U. Banin, Electric field induced switching of the fluorescence of single semiconductor quantum rods, Nano Lett. 5 (2005) 1581–1586.
[18] S.-J. Park, S. Link, W.L. Miller, A. Gesquiere, P.F. Barbara, Effect of electric field on the photoluminescence intensity of single CdSe nanocrystals, Chem. Phys. 341 (2007) 169–174.
[19] F. Vietmeyer, T. Tchelidze, V. Tsou, B. Janko, M. Kuno, Electric field-induced emission enhancement and modulation in individual CdSe nanowires, ACS Nano 6 (2012) 9133–9140.
[20] N.Y. Morgan, C.A. Leatherdale, M. Drndić, M.V. Jarosz, M.A. Kastner, M. Bawendi, Electronic transport in films of colloidal CdSe nanocrystals, Phys. Rev. B 66 (2002) 075339.
[21] D.S. Ginger, N.C. Greenham, Charge injection and transport in films of CdSe nanocrystals, J. Appl. Phys. 87 (2000) 1361–1368.
[22] M. Drndić, R. Markov, M.V. Jarosz, M.G. Bawendi, M.A. Kastner, N. Markovic, M. Tinkham, Imaging the charge transport in arrays of CdSe nanocrystals, Appl. Phys. Lett. 83 (2003) 4008–4010.
[23] D. Toker, I. Balberg, O. Zelaya-Angel, E. Savir, O. Millo, Size-dependent local conductance properties of CdSe nanocrystal ensembles, Phys. Rev. B 73 (2006) 045317.
[24] R.K. Singha, S. Manna, R. Bar, S. Das, S.K. Ray, Surface potential, charging and local current transport of individual Ge quantum dots grown by molecular beam epitaxy, Appl. Surf. Sci. 407 (2017) 418–426.
[25] B. Alperson, S. Cohen, I. Rubinstein, G. Hodes, Room-temperature conductance spectroscopy of CdSe quantum dots using a modified scanning force microscope, Phys. Rev. B 52 (1995) R17017–R17020.
[26] I. Tanaka, E. Kawasaki, O. Ohtsuki, K. Uno, M. Hara, H. Asami, I. Kamiya, Conductive-tip atomic force microscopy of CdSe colloidal nanodots, Surf. Sci. 532–535 (2003) 801–805.
[27] S. Schäfer, Z. Wang, T. Kipp, A. Mews, Fluorescence modulation of single CdSe nanowires by charge injection through the tip of an atomic-force microscope, Phys. Rev. Lett. 107 (2011) 137403.
[28] S.V. Kondratenko, V.S. Lysenko, Y.N. Kozyrev, M. Kratzer, D.P. Storozhuk, S.A. Iliash, C. Czibula, C. Teichert, Local charge trapping in Ge nanoclusters detected by Kelvin probe force microscopy, Appl. Surf. Sci. 389 (2016) 783–789.
[29] O. Cherniavskaya, L. Chen, L. Brus, Imaging the photoionization of individual CdSe/CdS core-shell nanocrystals on n- and p-type silicon substrates with thin oxides, J. Phys. Chem. B 108 (2004) 4946–4961.
[30] S. Li, M.L. Steigerwald, L.E. Brus, Surface states in the photoionization of high-quality CdSe core/shell nanocrystals, ACS Nano 3 (2009) 1267–1273.
[31] R. Costi, G. Cohen, A. Salant, E. Rabani, U. Banin, Electrostatic force microscopy study of single Au-CdSe hybrid nanodumbbells: evidence for light-induced charge separation, Nano Lett. 9 (2009) 2031–2039.
[32] S. Schäfer, Z. Wang, R. Zierold, T. Kipp, A. Mews, Laser-induced charge separation in CdSe nanowires, Nano Lett. 11 (2011) 2672–2677.
[33] S. Schäfer, A. Reich, Z. Wang, T. Kipp, A. Mews, Charge separation in CdSe/CdTe hetero-nanowires measured by electrostatic force microscopy, Appl. Phys. Lett. 100 (2012) 022110.
[34] S. Ithurria, M.D. Tessier, B. Mahler, R.P.S.M. Lobo, B. Dubertret, A.L. Efros, Colloidal nanoplatelets with two-dimensional electronic structure, Nat. Mater. 10 (2011) 936.
[35] B. Mahler, B. Nadal, C. Bouet, G. Patriarche, B. Dubertret, Core/shell colloidal semiconductor nanoplatelets, J. Am. Chem. Soc. 134 (2012) 18591–18598.
[36] A.W. Achtstein, A. Schliwa, A. Prudnikau, M. Hardzei, M.V. Artemyev, C. Thomsen, U. Woggon, Electronic structure and exciton-phonon interaction in two-dimensional colloidal CdSe nanosheets, Nano Lett. 12 (2012) 3151–3157.
[37] A.V. Antanovich, A.V. Prudnikau, D. Melnikau, Y.P. Rakovich, A. Chuvilin, U. Woggon, A.W. Achtstein, M.V. Artemyev, Colloidal synthesis and optical properties of type-II CdSe-CdTe and inverted CdTe-CdSe core-wing heteronanoplatelets, Nanoscale 7 (2015) 8084–8092.
[38] Z. Chen, B. Nadal, B. Mahler, H. Aubin, B. Dubertret, Quasi-2D colloidal semiconductor nanoplatelets for narrow electroluminescence, Adv. Funct. Mater. 24 (2014) 295–302.
[39] F. Fan, P. Kanjanaboos, M. Saravanapavanantham, E. Beauregard, G. Ingram, E. Yassitepe, M.M. Adachi, O. Voznyy, A.K. Johnston, G. Walters, G.-H. Kim, Z.-H. Lu, E.H. Sargent, Colloidal $CdSe_{1-x}S_x$ nanoplatelets with narrow and continuously-tunable electroluminescence, Nano Lett. 15 (2015) 4611–4615.
[40] A.G. Vitukhnovsky, V.S. Lebedev, A.S. Selyukov, A.A. Vashchenko, R.B. Vasiliev, M.S. Sokolikova, Electroluminescence from colloidal semiconductor CdSe nanoplatelets in hybrid organic–inorganic light emitting diode, Chem. Phys. Lett. 619 (2015) 185–188.
[41] C. She, I. Fedin, D.S. Dolzhnikov, A. Demortière, R.D. Schaller, M. Pelton, D.V. Talapin, Low-threshold stimulated emission using colloidal quantum wells, Nano Lett. 14 (2014) 2772–2777.
[42] B. Guzelturk, Y. Kelestemur, M. Olutas, S. Delikanli, H.V. Demir, Amplified spontaneous emission and lasing in colloidal nanoplatelets, ACS Nano 8 (2014) 6599–6605.
[43] G.H.V. Bertrand, A. Polovitsyn, S. Christodoulou, A.H. Khan, I. Moreels, Shape control of zincblende CdSe nanoplatelets, Chem. Commun. 52 (2016) 11975–11978.
[44] S. Ithurria, D.V. Talapin, Colloidal atomic layer deposition (c-ALD) using self-limiting reactions at nanocrystal surface coupled to phase transfer between polar and nonpolar media, J. Am. Chem. Soc 134 (2012) 18585–18590.
[45] A. Antanovich, A. Prudnikau, M. Artemyev, Optical Properties of Semiconductor Colloidal Quantum Wells, in: A. Maffucci, S.A. Maksimenko (Eds.), Fundamental and Applied Nano-Electromagnetics, Springer, Netherlands, 2016, p. 220.
[46] Y.-J. Yu, Y. Zhao, S. Ryu, L.E. Brus, K.S. Kim, P. Kim, Tuning the graphene work function by electric field effect, Nano Lett. 9 (2009) 3430–3434.
[47] F. Marchi, R. Dianoux, H.J.H. Smilde, P. Mur, F. Comin, J. Chevrier, Characterisation of trapped electric charge carriers behaviour at nanometer scale by electrostatic force microscopy, J. Electrostat. 66 (2008) 538–547.
[48] T. Heim, K. Lmimouni, D. Vuillaume, Ambipolar charge injection and transport in a single pentacene monolayer island, Nano Lett. 4 (2004) 2145–2150.
[49] O.J. Dautel, M. Robitzer, J.-C. Flores, D. Tondelier, F. Serein-Spirau, J.-P. Lère-Porte, D. Guérin, S. Lenfant, M. Tillard, D. Vuillaume, J.J.E. Moreau, Electroactive Nanorods and Nanorings Designed by Supramolecular Association of π-conjugated, Oligomers, Chem.: Eur. J. 14 (2008) 4201–4213.
[50] M. Zdrojek, T. Mélin, H. Diesinger, D. Stiévenard, W. Gebicki, L. Adamowicz, Charging and discharging processes of carbon nanotubes probed by electrostatic force microscopy, J. Appl. Phys. 100 (2006) 114326.
[51] A. Verdaguer, M. Cardellach, J.J. Segura, G.M. Sacha, J. Moser, M. Zdrojek, A. Bachtold, J. Fraxedas, Charging and discharging of graphene in ambient conditions studied with scanning probe microscopy, Appl. Phys. Lett. 94 (2009) 233105.
[52] B. Vasić, M. Kratzer, A. Matković, A. Nevosad, U. Ralević, D. Jovanović, C. Ganser, C. Teichert, R. Gajić, Atomic force microscopy based manipulation of graphene using dynamic plowing lithography, Nanotechnology 24 (2012) 015303.
[53] S.E. Yalcin, C. Galande, R. Kappera, H. Yamaguchi, U. Martinez, K.A. Velizhanin, S.K. Doorn, A.M. Dattelbaum, M. Chhowalla, P.M. Ajayan, G. Gupta, A.D. Mohite, Direct imaging of charge transport in progressively reduced graphene oxide using electrostatic force microscopy, ACS Nano 9 (2015) 2981–2988.
[54] N.S. Malvankar, S.E. Yalcin, M.T. Tuominen, D.R. Lovley, Visualization of charge propagation along individual pili proteins using ambient electrostatic force microscopy, Nat. Nanotech. 9 (2014) 1012.
[55] B. Mahler, L. Guillemot, L. Bossard-Giannesini, S. Ithurria, D. Pierucci, A. Ouerghi, G. Patriarche, R. Benbalagh, E. Lacaze, F. Rochet, E. Lhuillier, Metallic functionalization of CdSe 2D nanoplatelets and its impact on electronic transport, J. Phys. Chem. C 120 (2016) 12351–12361.
[56] A. Stavrinadis, G. Konstantatos, Strategies for the controlled electronic doping of colloidal quantum dot solids, ChemPhysChem 17 (2016) 632–644.
[57] S. Ryu, L. Liu, S. Berciaud, Y.-J. Yu, H. Liu, P. Kim, G.W. Flynn, L.E. Brus, Atmospheric oxygen binding and hole doping in deformed graphene on a SiO_2 Substrate, Nano Lett. 10 (2010) 4944–4951.

PCCP

PAPER

Cite this: *Phys. Chem. Chem. Phys.*, 2017, **19**, 31756

Nitrate-assisted photocatalytic efficiency of defective Eu-doped $Pr(OH)_3$ nanostructures†

S. Aškrabić,*[a] V. D. Araújo,[b] M. Passacantando,[c] M. I. B. Bernardi,[d] N. Tomić,[a] B. Dojčinović,[e] D. Manojlović,[f] B. Čalija,[g] M. Miletić[a] and Z. D. Dohčević-Mitrović*[a]

$Pr(OH)_3$ one-dimensional nanostructures are a less studied member of lanthanide hydroxide nanostructures, which recently demonstrated an excellent adsorption capacity for organic pollutant removal from wastewater. In this study, $Pr_{1-x}Eu_x(OH)_3$ (x = 0, 0.01, 0.03, and 0.05) defective nanostructures were synthesized by a facile and scalable microwave-assisted hydrothermal method using KOH as an alkaline metal precursor. The phase and surface composition, morphology, vibrational, electronic and optical properties of the as-prepared samples were characterized by X-ray diffraction (XRD), X-ray photoelectron spectroscopy (XPS), inductively coupled plasma optical emission spectrometry (ICP-OES), transmission electron microscopy (TEM), field emission scanning electron microscopy (FE-SEM), Raman, infrared (IR), photoluminescence (PL), and diffuse reflectance spectroscopy (DRS). It was deduced that the incorporation of Eu^{3+} ions promoted the formation of oxygen vacancies in the already defective $Pr(OH)_3$, subsequently changing the $Pr(OH)_3$ nanorod morphology. The presence of KNO_3 phase was registered in the Eu-doped samples. The oxygen-deficient Eu-doped $Pr(OH)_3$ nanostructures displayed an improved photocatalytic activity in the removal of reactive orange (RO16) dye under UV-vis light irradiation. An enhanced photocatalytic activity of the Eu-doped $Pr(OH)_3$ nanostructures was caused by the synergetic effect of oxygen vacancies and Eu^{3+} (NO_3^-) ions present on the $Pr(OH)_3$ surface, the charge separation efficiency and the formation of the reactive radicals. In addition, the 3% Eu-doped sample exhibited very good adsorptive properties due to different morphology and higher electrostatic attraction with the anionic dye. $Pr_{1-x}Eu_x(OH)_3$ nanostructures with the possibility of tuning their adsorption/photocatalytic properties present a great potential for wastewater treatment.

Received 12th May 2017,
Accepted 6th November 2017

DOI: 10.1039/c7cp06440c

rsc.li/pccp

Introduction

Nanocrystalline rare earth hydroxides have started to draw attention in the recent years because they are relatively facile to synthesize and usually do not require high-temperature annealing. As all rare earth compounds, lanthanide hydroxides display an interesting catalytic, optical, magnetic and adsorptive properties.[1–5] They also represent a straightforward approach for obtaining rare earth oxides since these hydroxides can be transformed to the corresponding oxides by annealing at higher temperatures. Rare earth hydroxides in the form of one-dimensional nanostructures were synthesized by different methods such as precipitation, hydrothermal or microemulsion method or electrodeposition.[2–9] It is known that lanthanide hydroxides most often crystallize into one-dimensional (1D) structures, such as nanorods, nanobundles or nanobelts. These 1D porous structures have the potential for applications in water pollutant removal since their dimensionality makes them much more accessible to the pollutant molecules. Moreover, it is expected that the abundance of –OH groups (inherent in these materials) can have a significant impact on their photocatalytic and adsorptive properties. As the 1D nanostructures are expected to have a better surface activity if the total surface

[a] *Center for Solid State Physics and New Materials, Institute of Physics Belgrade, University of Belgrade, Pregrevica 118, 11080 Belgrade, Serbia. E-mail: sonask@ipb.ac.rs, zordoh@ipb.ac.rs*
[b] *Unidade Acadêmica do Cabo de Santo Agostinho, Universidade Federal Rural de Pernambuco, Cabo do Santo Agostinho, PE, Brazil*
[c] *Department of Physical and Chemical Sciences, University of L'Aquila, Via Vetoio, 67100 Coppito L'Aquila, Italy*
[d] *Instituto de Física de São Carlos, Universidade de São Paulo, São Carlos, SP, Brazil*
[e] *Center of Chemistry, Institute of Chemistry, Technology and Metallurgy, University of Belgrade, Njegoševa 12, 11000 Belgrade, Serbia*
[f] *Faculty of Chemistry, University of Belgrade, Studentski trg 12-16, 11000 Belgrade, Serbia*
[g] *Faculty of Pharmacy, University of Belgrade, Vojvode Stepe 450, 11221 Belgrade, Serbia*

† Electronic supplementary information (ESI) available. See DOI: 10.1039/c7cp06440c

to volume ratio is higher, it is of interest to obtain nanorods/nanowires with a high length-to-diameter ratio. The 1D geometry (the aspect ratio of longer to shorter dimension) can be tuned in the hydrothermal synthesis process by changing the molar ratios of $[OH^-]/[Ln^{3+}]$, where OH^- ions originate from the hydroxide precursor and Ln^{3+} ions from lanthanide salt or oxide, but this ratio is also dependent on the choice of alkaline metal hydroxide. In the case of $Eu(OH)_3$, it was shown that with increasing ratio of $[OH^-]/[Eu^{3+}]$, the aspect ratio of the 1D nanostructures decreased when NaOH was used,[4] but increased when KOH was used.[10]

Among nanocrystalline lanthanide hydroxides, the electrochemically prepared 1D $Pr(OH)_3$ nanostructures were shown to possess the excellent adsorptive properties regarding the dye removal from water.[6,7] Electrodeposition was also used to produce the 1D $Pr(OH)_3$ nanostructures that demonstrated good adsorption of phosphates.[8] Furthermore, the 1D porous $Pr(OH)_3$ nanowire bundles synthesized by a template-free electrochemical deposition method demonstrated good ferromagnetic properties.[2] In addition, the toxicity studies of the porous $Pr(OH)_3$ nanostructures demonstrated their great potential as the environmentally friendly adsorbent materials.[7]

There are only a few papers dedicated to the investigation of the 1D $Pr(OH)_3$ nanostructures[2,6–9] and a majority of them concerned the adsorptive properties of this material. To the best of our knowledge, the photocatalytic properties of pure or doped $Pr(OH)_3$ have not been investigated up till date. This is probably due to the relatively large band gap of these materials (4.7 eV) and their consequent insufficient efficiency in the absorption of the solar radiation. However, a recent study by Dong *et al.*[3] showed that oxygen vacancies can create the electronic states within the band gap of $La(OH)_3$ nanorods, extending their photoresponse range and making them very efficient photocatalysts. In addition, doping of $La(OH)_3$ nanorods with lanthanides, Ln^{3+}, drastically improved their photocatalytic activity; Eu^{3+} was one of the dopants that produced the best results in this direction.[11]

In this study, $Pr(OH)_3$ nanorods and $Pr_{1-x}Eu_x(OH)_3$ (x = 0.01, 0.03, and 0.05) nanostructures were obtained by a microwave-assisted hydrothermal method. We demonstrated that Eu doping influences the changes in the $Pr(OH)_3$ morphology, the adsorption affinity, and can substantially increase the photocatalytic activity of $Pr(OH)_3$ nanorods towards the dye degradation. In addition, the doping changes the content of oxygen vacancies, which, together with synthesis-introduced nitrates and morphology, determine whether the resulting nanostructures are dominantly photocatalysts or adsorbents. The facile and scalable synthesis, the high photocatalytic activity of Eu-doped $Pr(OH)_3$ nanostructures and the possibility of tuning the ratio of their adsorptive/photocatalytic activity present a great potential for their application in the efficient and cost-effective pollutant removal.

Experimental

Preparation of pure and Eu-doped $Pr(OH)_3$ nanostructures

$Pr_{1-x}Eu_x(OH)_3$ (x = 0, 0.01, 0.03, and 0.05) nanostructures were prepared by the microwave-assisted hydrothermal method from the precursor oxides, Pr_6O_{11} and Eu_2O_3. The synthesis procedure included the following steps: first, the precursors were dissolved in aqueous HNO_3; subsequently, 0.02 mol of the dissolved Pr- and Eu-precursors (0, 1%, 3% and 5% at. Eu) were added into 50 mL of distilled water. Following this, 50 mL of a 10 M KOH solution was added rapidly under vigorous stirring. KOH was chosen as a precursor for the hydrothermal synthesis of pure and doped $Pr(OH)_3$ nanorods in this study, as it has been shown that it enhances the formation of 1D nanorods with a higher ratio of length to diameter.[10] The mixed solution was placed in a 110 mL Teflon autoclave (filling 90% of its volume), which was sealed and placed in a microwave-assisted hydrothermal system; 2.45 GHz of microwave radiation was applied at a maximum power of 800 W. The temperature was measured with a temperature sensor (type K thermocouple) inserted into the vessel. Each of the as-prepared solutions was subjected to the microwave hydrothermal synthesis and heated to a temperature of 140 °C for 10 min. The products were then air-cooled to room temperature. The as-obtained precipitate powder was washed several times with distilled water and isopropyl alcohol and then dried on a hot plate at 60 °C for 24 h.

Characterization

The powder X-ray diffraction (XRD) characterization was performed using a Shimadzu diffractometer (Model XRD-7000, CuKα radiation (λ = 1.54 Å), 40 kV and 30 mA). The scanning range was between 5 and 120° (2θ) with a step size of 0.02° and a step time of 5.0 s. The Rietveld analysis was performed using the Rietveld refinement program GSAS.[12] A pseudo-Voigt profile function was used. The specific surface area (S_{BET}) was estimated from the N_2 adsorption/desorption isotherms at liquid nitrogen temperature following the multipoint BET procedure using a Micromeritics ASAP 2000. The determination of the concentrations of europium in the doped samples was performed by inductively coupled plasma optical emission spectrometry (ICP-OES) using an iCAP 6500 Duo ICP (Thermo Fisher Scientific, Cambridge, UK) spectrometer and RACID86 charge injector device (CID) detector with iTEVA operational software. The quantification of europium in the solutions was performed at the following emission wavelength: Eu II 381.967 nm. The morphology of the nanostructures was characterized by transmission electron microscopy (TEM) and field emission scanning electron microscopy (FE-SEM). The TEM characterization was conducted on a Philips CM 300 microscope operating at 300 kV. The SEM measurements were carried out on a Tescan MIRA3 field emission gun at 10–20 kV under high vacuum. The SEM working distance was between 3.3 and 4 mm. The room-temperature micro-Raman spectra of $Pr_{1-x}Eu_x(OH)_3$ nanostructures were excited using solid state Nd:YAG laser line of 514 nm. Low laser power (~2 mW) was applied to prevent the thermal degradation of the sample. Tri Vista 557 triple spectrometer coupled to the nitrogen-cooled CCD detector was employed for the spectra collection at room temperature. X-ray photoelectron spectroscopy (XPS) measurements were performed using the PHI ESCA system equipped with a non-monochromatic Al X-ray source (1486.6 eV) with a hemispherical analyzer. The infrared transmission spectra (IR) were obtained on a Thermo

Nicolet 6700 Fourier transform infrared spectrophotometer at room temperature. Diffuse reflectance spectra (DRS) were acquired using a Specord M40 Carl Zeiss spectrometer. The room-temperature PL measurements were performed on a Spex Fluorolog spectrofluorometer using a 340 nm excitation wavelength.

Photodegradation tests

The photocatalytic activity of $Pr_{1-x}Eu_x(OH)_3$ nanostructures under UV light irradiation was evaluated by monitoring the decomposition of reactive orange (RO16) as a model pollutant. The batch-type experiments were performed in an open thermostated cell (at 25 °C) equipped with a water circulating jacket to maintain the solution at room temperature. A mercury lamp (125 W) was used as a light source. The initial concentration of RO16 in an aqueous suspension was 50 mg L^{-1} and the working volume was 25 mL. Before the photocatalytic experiment, the cell was kept in dark for 60 min in order to achieve the adsorption–desorption equilibrium. At regular time intervals, the aliquots were taken and the dye concentration was monitored by measuring the variation of the intensity of absorption peak at λ_{max} = 494 nm using a Varian Super Scan 3 UV-vis spectrophotometer. The photocatalytic experiments were conducted at the natural pH of the RO16 dye (pH = 4.7). In order to detect the formation of the photogenerated hydroxyl radicals ($OH^{\bullet}$), the photoluminescence (PL) measurements were performed using terephthalic acid, which is known to react with $OH^{\bullet}$ radicals and produce highly fluorescent 2-hydroxyterephthalic acid. The experiment was conducted at ambient temperature and the photocatalyst was placed in an open thermostated cell filled with 20 mL of 5×10^{-4} mol L^{-1} terephthalic acid in a diluted NaOH aqueous solution with a concentration of 2×10^{-3} mol L^{-1}. A UV light source was used and a sampling was performed after 5, 10, and 15 min. The PL spectra of the reaction solution, using an excitation wavelength of 315 nm, were measured on a Spex Fluorolog spectrofluorometer system following the changes of the PL peak at 425 nm, at which the 2-hydroxyterephthalic acid exhibits an intense PL peak.

Results and discussion

The structural characterization of the obtained $Pr_{1-x}Eu_x(OH)_3$ (x = 0, 0.01, 0.03, and 0.05) nanostructures was performed using XRD analysis and the diffraction patterns are shown in Fig. 1. All diffraction peaks of the as-synthesized samples can be perfectly indexed to the hexagonal $P6_3/m$ space group (ICSD No. 200487 or JCPDS No. 83-2304).[13] The secondary peaks (marked with (*) in Fig. 1) at 23.5°, 33.9° and 43.7° were detected in the Eu-doped samples and ascribed to KNO_3 that was formed from the precursors.[14] The lattice parameters (a and c) and oxygen occupancy factor (O_{occup}) calculated from the Rietveld refinement and the quality factors (R_{exp} and R_{Bragg}) of the refinement are summarized in Table 1.

The lattice parameters slightly decreased with Eu doping due to the substitution of the larger Pr^{3+} ion (radii = 1.179 Å) by the smaller Eu^{3+} ion (radii = 1.12 Å)[15] except for the 3% Eu-doped sample. The decrease in O_{occup} with Eu doping signifies an increase in oxygen vacancy content. From Table 1, it can be seen that the 3% Eu-doped sample has the smallest O_{occup}, *i.e.*, the highest content of oxygen vacancies, the presence of which can be responsible for the observed lattice expansion in this sample.[16] In Table 1, the BET specific surface area and the density of the as-synthesized samples are also presented. Clearly, the specific surface area (S_{BET}) decreased in the doped samples compared to that of the pure hydroxide and was the lowest in the 3% Eu-doped sample.

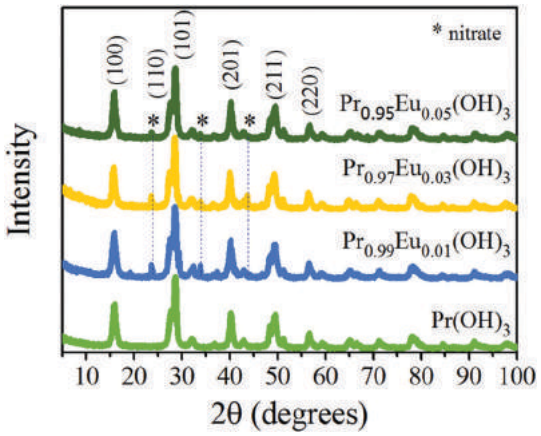

Fig. 1 XRD patterns obtained for $Pr_{1-x}Eu_x(OH)_3$ nanostructures ($0 \leq x \leq 0.05$). The positions of the diffraction peaks assigned to KNO_3 are marked with asterisks.

Table 1 Specific surface area (S_{BET}), lattice parameters (a) and (c), oxygen occupancy factor (O_{occup}), and density (ρ) of $Pr_{1-x}Eu_x(OH)_3$ nanostructures

Sample	S_{BET} (m^2 g^{-1})	a^a (Å)	c^a (Å)	$O_{occup}{}^a$	ρ^a (g cm^{-3})	R_{exp} (%)	R_{Bragg} (%)
$Pr(OH)_3$	130.52	6.453(4)	3.769(9)	0.84(8)	4.45	11.6	6.0
1% Eu	83.24	6.453(4)	3.768(9)	0.80(2)	4.39	12.6	7.0
3% Eu	63.05	6.461(1)	3.769(0)	0.66(6)	4.22	13.0	8.5
5% Eu	82.77	6.449(0)	3.763(4)	0.74(5)	4.34	11.9	6.0

[a] Calculated *via* the Rietveld refinement.

The type of dopant and its incorporation influence the properties of the obtained materials to a great extent. Therefore, it is important to determine precisely the amount of the incorporated Eu in $Pr_{1-x}Eu_x(OH)_3$ ($0.01 \leq x \leq 0.05$) nanopowders. In that sense, the ICP analysis was performed and the results reveal that the content of the incorporated Eu is slightly lower than its nominal content for each doped sample (see Table 2).

The morphology of pure and Eu-doped nanostructures was characterized by TEM and FE-SEM. Fig. 2 shows the TEM images of pure and Eu-doped $Pr(OH)_3$ nanostructures, while the SEM images are shown in Fig. S1 in the ESI.† Pure $Pr(OH)_3$ dominantly consists of well-dispersed nanorods with diameters ranging between 5 and 10 nm (Fig. 2(a)). With the increase of the Eu dopant content, the morphology of the obtained nanomaterials changed and besides nanorods, the increasing presence of irregularly shaped grains that do not have the nanorod morphology was also observed. This can be explained

Table 2 Measured Eu content of $Pr_{1-x}Eu_x(OH)_3$ nanostructures by ICP-OES

Sample	Theoretical Eu content (mg g^{-1})	Measured Eu content (mg g^{-1})	Atomic concentration (%)
$Pr_{0.99}Eu_{0.01}(OH)_3$	7.91	6.45	0.82
$Pr_{0.97}Eu_{0.03}(OH)_3$	23.72	20.50	2.59
$Pr_{0.95}Eu_{0.05}(OH)_3$	39.48	32.64	4.13

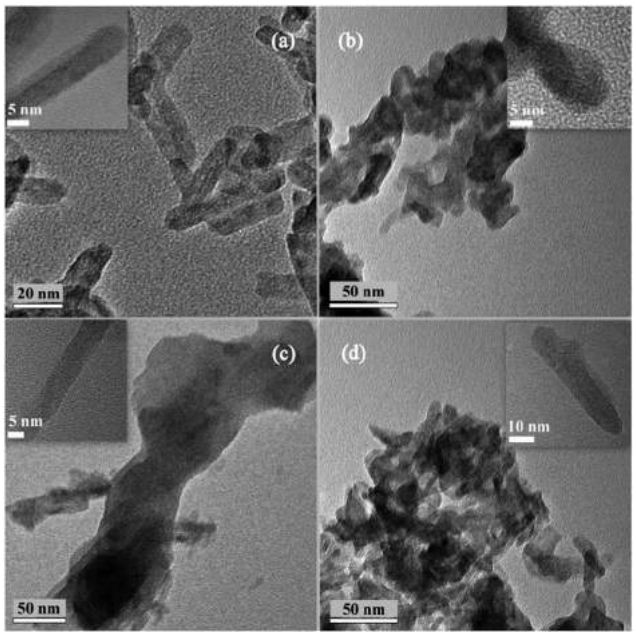

Fig. 2 TEM images of (a) $Pr(OH)_3$, (b) $Pr_{0.99}Eu_{0.01}(OH)_3$, (c) $Pr_{0.97}Eu_{0.03}(OH)_3$, and (d) $Pr_{0.95}Eu_{0.05}(OH)_3$ nanostructures. The insets are the magnified images of individual nanorods.

by the known fact that the dopant atoms can change the crystallization directions and act as the nucleation centers,[17,18] thus changing the resultant morphology of the sample. It is also worth to mention that in the case of the 3% Eu-doped $Pr(OH)_3$ sample, two types of nanorods were formed–narrow nanorods with diameters in the range 7–15 nm (similar to pure $Pr(OH)_3$) and wider nanorods, with diameters of the order of 50 nm (shown in the inset of Fig. S1(c), ESI†).

The nature of the Eu ion incorporation was further studied by Raman spectroscopy through analyzing the influence that Eu doping has on the vibrational properties of the starting material, $Pr(OH)_3$. The crystal symmetry of $Pr(OH)_3$ is hexagonal with a symmetry group $P6_3/m$, for which the group theory predicts 11 Raman active modes: $4A_g$, $2E_{1g}$ and $5E_{2g}$ modes.[19,20] In Fig. 3, the room-temperature Raman spectra of pure and Eu-doped $Pr(OH)_3$ are shown. The main Raman modes of $Pr(OH)_3$ are present in the spectra of the pure and doped samples and are positioned at the energies: 140 cm^{-1} (peak 1), 240 cm^{-1} (peak 2), 294 cm^{-1} (peak 3), 359 cm^{-1} (peak 4), and 465 cm^{-1} (peak 5). The modes positioned at 240 cm^{-1} and 294 cm^{-1} are ascribed to the E_{1g} and E_{2g} lattice vibrations of OH^- anion, whereas the E_{2g} lattice vibrational mode of heavier

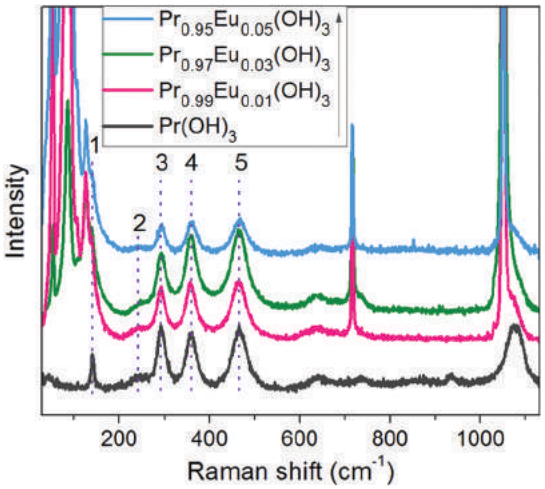

Fig. 3 Room-temperature Raman spectra of $Pr_{1-x}Eu_x(OH)_3$ nanostructures.

Pr^{3+} ions is positioned at a lower energy of 140 cm^{-1}. The vibration frequencies of the OH^- atomic group are positioned at 359 cm^{-1} and 465 cm^{-1} (E_{2g} and E_{1g} modes).[19,20] The Raman peaks 3, 4 and 5 shifted slightly to higher wavenumbers in the $Pr_{0.95}Eu_{0.05}(OH)_3$ spectrum, which can be explained by a certain degree of Eu substitutional incorporation onto the Pr sites as these peaks are positioned at higher wavenumbers in $Eu(OH)_3$ compared to $Pr(OH)_3$.[20] Several low-frequency modes at ~53 cm^{-1}, ~85 cm^{-1}, ~107 cm^{-1}, ~127 cm^{-1}, and ~137 cm^{-1} are present in the Raman spectra of the Eu-doped samples. These modes correspond to nitrates, in the form of either nitrate monohydrate layers interconnected with hydrogen bonds[21,22] or KNO_3.[23,24] Both of these compounds can be formed from the unreacted nitrate ions originating from the precursor. The sharp Raman modes positioned at 715 cm^{-1} and 1050 cm^{-1} correspond to the vibrations of NO_3^- ions.[23,24] Based on the results of Raman spectroscopy and keeping in mind the X-ray diffraction results, we can conclude that some amount of the crystalline KNO_3 phase is present in the Eu-doped $Pr(OH)_3$ samples. The XPS measurements of the $Pr_{1-x}Eu_x(OH)_3$ samples enabled the elucidation of changes in the chemical composition and electronic structures with Eu doping and determined the valence states of various species present in the pure and doped samples.

Fig. 4(a) shows the survey XPS spectra of the $Pr_{1-x}Eu_x(OH)_3$ samples, while the Pr 3d, Eu 3d, O 1s, and K 2p/C 1s XPS spectra are shown in Fig. 4(b). The Pr 3d spectra (Fig. 4(b), upper left) contain two spin–orbit doublets, labeled c/c' and b/b' with approximate energies of 929/949 eV and 933/954 eV, respectively. These doublets represent the $3d_{5/2}$ (c, b) and $3d_{3/2}$ (c', b') components of the Pr 3d spectra. An additional structure t is present in the $3d_{3/2}$ component and its presence can be explained by multiple effects. The doublets c/c' and b/b' are found both in Pr^{4+} and Pr^{3+}, so they cannot be used to distinguish between these two valence states of Pr. The small peaks observed at ~923 eV and ~943 eV are identified as X-ray satellites, originating from the non-monochromatic X-ray source. From the Eu 3d spectra (Fig. 4(b), upper right), we can observe that the

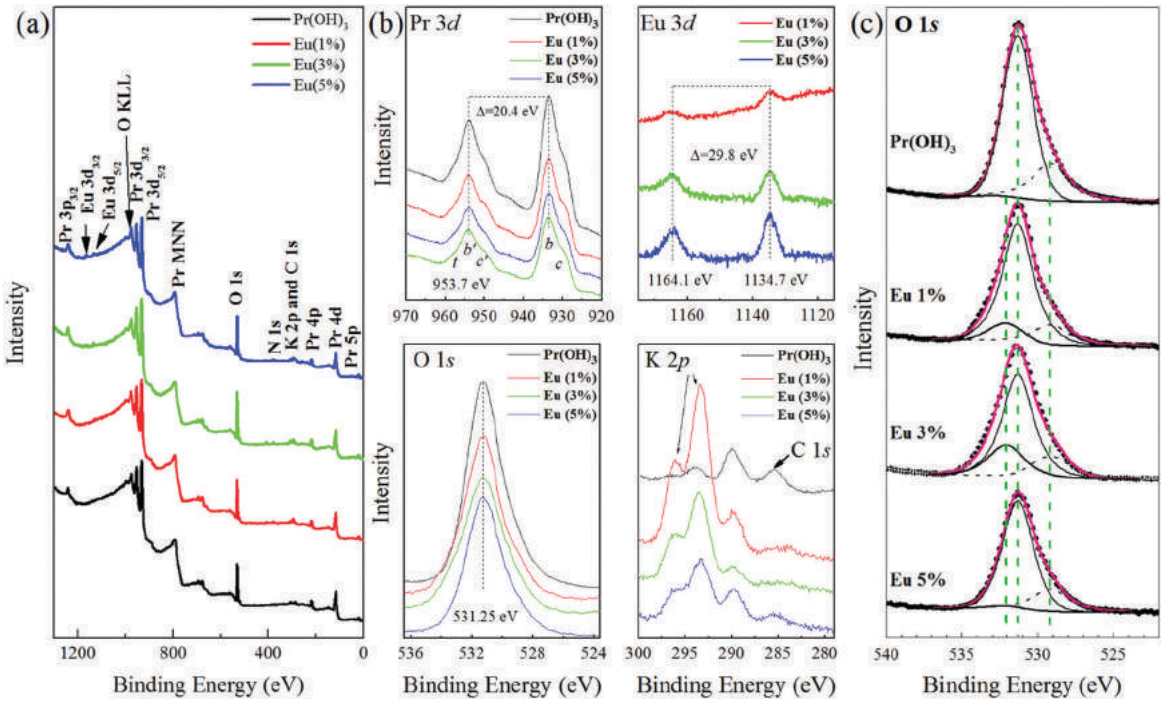

Fig. 4 XPS spectra of $Pr_{1-x}Eu_x(OH)_3$ nanostructures: (a) survey spectra, (b) high-resolution spectra of Pr 3d, Eu 3d, O 1s and K 2p/C 1s regions and (c) deconvolution of O 1s region into three peaks.

components Eu $3d_{5/2}$ and $3d_{3/2}$ are positioned at ~1134.7 eV and ~1164.1 eV, respectively. These values correspond to the Eu^{3+} valence state. When compared to the literature values for Eu_2O_3 (1133.7),[25] $Eu(OH)_3$ (1134.3)[26] and $Eu(NO_3)_3$ (1136.4),[25] it can be observed that these peaks are closest to those of $Eu(OH)_3$, which confirms the substitutional incorporation of Eu^{3+} and the absence of europium oxide/nitrate. More evidence indicating that Eu_2O_3 is not present in these samples is the fact that the strong Raman mode of Eu_2O_3 at ~330 cm^{-1} was not registered in the Raman spectra. The K 2p states are particularly prominent in the 1% and 3% Eu-doped samples (see Fig. 4(b)) and originate from the KNO_3 phase, as already observed in the XRD and Raman spectra of the doped samples. A low-intensity C 1s peak (see Fig. 4(b)) originates from the surface impurity carbons, while the N1s states are characterized by very low-intensity peaks visible in the survey XPS spectra. The O 1s peaks of $Pr_{1-x}Eu_x(OH)_3$ samples (Fig. 4(c)) are asymmetric and have been deconvoluted into three components positioned at ~529 eV, ~531 eV, and ~532 eV. The vertical dashed lines shown in Fig. 4(c) indicate the binding energy (BE) position of these three components. The latter two are generally ascribed to the lattice oxygen and adsorbed –OH groups, possibly from water,[25–27] while the peak at ~529 eV can be ascribed to the surface oxygen vacancies.[20]

The elemental composition of the investigated samples obtained by XPS measurements is represented in Table 3. The atomic concentrations, shown in Table 3, were obtained considering the sensitivity factors of PHI (Physical Electronics) and the peak features of Pr($3d_{5/2}$), O(1s) and Eu($3d_{5/2}$) (Fig. 4). It can be noticed that the relative atomic concentrations of Eu, calculated as Eu/(Eu + Pr), were higher than the nominal stoichiometric concentrations of this element. This can be a consequence of the segregation of the dopant atoms on the materials surface as already registered by XPS in other rare earth nanocomposites.[28] This finding suggests that Eu^{3+} ions are segregated at the surfaces of nanocrystals, but mostly connected to oxygen ions as deduced from the Eu 3d binding energies. From the peak area fitting data of the components that belong to lattice oxygen and oxygen vacancies, we have calculated the oxygen molar ratio, which is also summarized in Table 3. Although XPS provides the information about the surface stoichiometry, the obtained ratio is in agreement with the XRD results (see Table 1), confirming that the Eu-doped samples are more oxygen deficient.

Table 3 Elemental composition of $Pr(OH)_3$, pure and Eu-doped as determined by XPS

	Atomic concentration (%)				
Sample	Pr	O	Eu	Eu/(Eu+Pr)	Vacancy/lattice
$Pr(OH)_3$	24.501	75.499	0.000		0.16
1% Eu	21.674	77.846	0.480	2.0%	0.20
3% Eu	19.189	78.369	2.441	11.3%	0.22
5% Eu	21.213	75.030	3.757	15.0%	0.26

Infrared spectroscopy (IR) was employed to evidence the presence of the –OH groups as well as other organic and inorganic species. The IR transmission spectra of the pure and Eu-doped $Pr(OH)_3$, obtained in the range 500–4000 cm^{-1}, are shown in Fig. 5. The peak at 670 cm^{-1} represents the Pr–O–H lattice vibration.[13,20] The prominent broad peaks at 1382 cm^{-1}

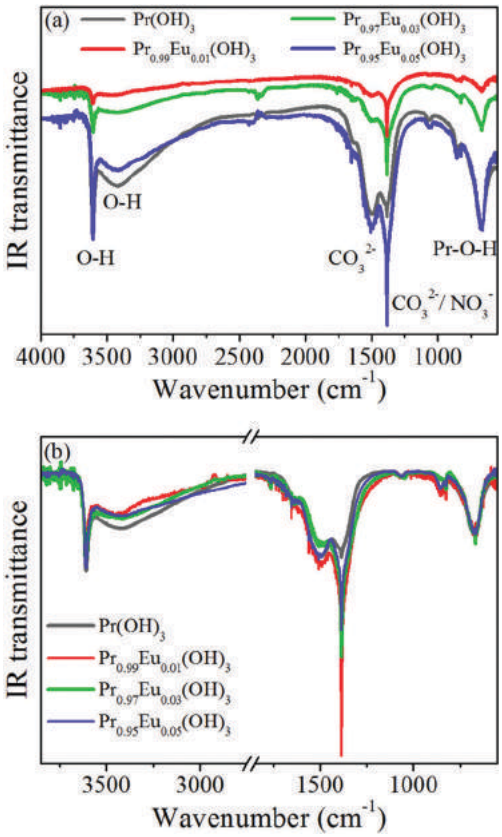

Fig. 5 (a) IR transmission spectra and (b) normalized IR spectra of pure and Eu-doped $Pr(OH)_3$ nanostructures.

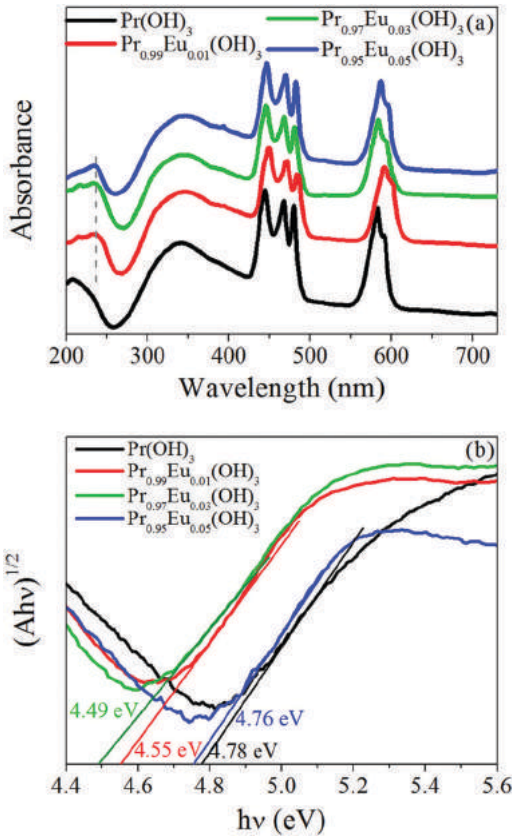

Fig. 6 (a) Absorption spectra and (b) Tauc plots of $(Ah\nu)^{1/2}$ *vs.* $(h\nu)$ for $Pr_{1-x}Eu_x(OH)_3$ nanostructures.

and 1505 cm^{-1} belong to the symmetric and asymmetric COO^- vibrations[29] due to the adsorbed carbon species. Another sharp peak at 1385 cm^{-1} with a much higher intensity in the spectra of the doped samples is observed. This sharp peak can be ascribed to the NO_3^- vibrations[30] together with the observed low-intensity peak at ~828 cm^{-1}, which also corresponds to the NO_3^- vibrations and is present only in the doped samples.[30] The intensity of this sharp peak (1385 cm^{-1}) is very high in the 1% Eu-doped sample and decreases with the increase in the dopant concentration as shown in the normalized IR spectra in Fig. 5(b) (normalized to the Pr–OH vibration peak), which is in agreement with the XPS K 2p spectra of the pure and doped samples. Another sharp peak at 3600 cm^{-1} represents the vibrations of the OH^- groups from $Pr(OH)_3$/$Eu(OH)_3$, while the broad peak at 3400 cm^{-1} corresponds to the delocalized OH^- vibrations from the adsorbed H_2O on the sample surface.[29,31]

The UV-vis absorption spectra of $Pr_{1-x}Eu_x(OH)_3$ are presented in Fig. 6(a). A strong absorption band can be observed in the region below 270 nm, corresponding to the band gap, and is shifted to a lower wavelength for the Eu-doped samples compared to that in the $Pr(OH)_3$ spectrum. Several sharper peaks at 446 nm, 462 nm, 470 nm, 583 nm and 591–597 nm represent the Pr^{3+} electronic transitions. These peaks were observed in both pure and doped samples.

There are no peaks that can be ascribed to the intraband 4f–4f Eu^{3+} electronic transitions due to the fact that the doping percentage is low. Another very broad absorption peak at ~340 nm can be ascribed to the formation of oxygen-vacancy impurity levels within the band gap. These states are already seen in the defective $La(OH)_3$ nanorods (with the absorption around 280 nm) and ascribed to the surface oxygen vacancy states formed during the synthesis process.[3]

From the absorption spectra shown in Fig. 6(a), by applying the absorption spectra fitting method for the indirect electronic transitions,[32] the band gap of these materials was estimated. Fig. 6(b) presents the Tauc plots[33] for the indirect transition of the $Pr_{1-x}Eu_x(OH)_3$ samples. It was deduced that the pure $Pr(OH)_3$ band gap of ~4.78 eV was shifted to ~4.5 eV in $Pr_{0.99}Eu_{0.01}(OH)_3$ and $Pr_{0.97}Eu_{0.03}(OH)_3$, while it increased again in $Pr_{0.95}Eu_{0.05}(OH)_3$, approaching the $Pr(OH)_3$ value. The lower gap of the 1% and 3% Eu-doped samples can be explained by the presence of a higher amount of the KNO_3 phase in these samples, which have a lower band gap[14,34] compared to that of $Pr(OH)_3$.

In order to probe the intraband defect states, the PL measurements were performed using a 340 nm excitation light with the purpose of exciting the states corresponding to the broad peak centered at 340 nm in the absorption spectra (see Fig. 6(a)). The PL spectra of $Pr_{1-x}Eu_x(OH)_3$ samples shown in Fig. S2 (ESI†) consist of an intense PL peak centered at 430 nm and several lower intensity Pr^{3+} emission peaks that are red-shifted, compared to those of their counterparts in the

absorption spectra. The characteristic Eu^{3+} peaks are not observed because of the presence of the hydroxyl groups, which act as the luminescence quenching centers and can increase the non-radiative processes.[35] The intensive blue emission peak can be attributed to the deep level oxygen vacancy defect states and originates from the recombination of an electron occupying the vacancy and the photogenerated holes.[3,36] The intensity of this peak increases in the 3% and 5% Eu-doped samples. This is in accordance with the XPS and XRD results, which showed that the oxygen deficiency increased with increased Eu content.

Although the determined band gap values of $Pr_{1-x}Eu_x(OH)_3$ nanostructures are relatively high, the sub-band gap state observed from the PL and UV-vis absorption spectra (see Fig. 6(a) and Fig. S2, ESI†) allows for these structures to be tested as the potential photocatalysts in the UV region. Therefore, the photocatalytic degradation of the RO16 dye was tested for $Pr_{1-x}Eu_x(OH)_3$ nanostructures under UV light.

The kinetics of the degradation of RO16 under UV light is shown in Fig. 7(a). It is evident that RO16 can be effectively removed by the $Pr_{1-x}Eu_x(OH)_3$ nanostructures. The pure $Pr(OH)_3$ sample showed a moderate adsorption in the dark and its photocatalytic removal efficiency was more than 90% after 180 min. A pronounced adsorption in the equilibrium period of 60 min before the exposure to UV light was seen in the 3% Eu-doped sample. On the contrary, the 1% and 5% Eu-doped samples showed no adsorption. The iso-electric point of a photocatalyst influences the adsorption process to a great extent. Therefore, the zeta potentials for pure, 1%, and 3% Eu-doped $Pr(OH)_3$ (shown in Fig. 8(b)) were measured in the pH

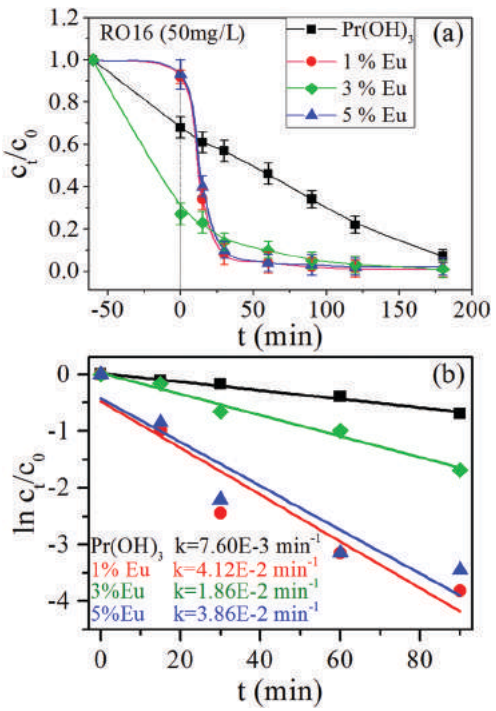

Fig. 7 (a) Degradation of RO16 dye under UV light in the presence of the pure and Eu-doped $Pr(OH)_3$ nanostructures and (b) the first-order reaction kinetics and constant k values.

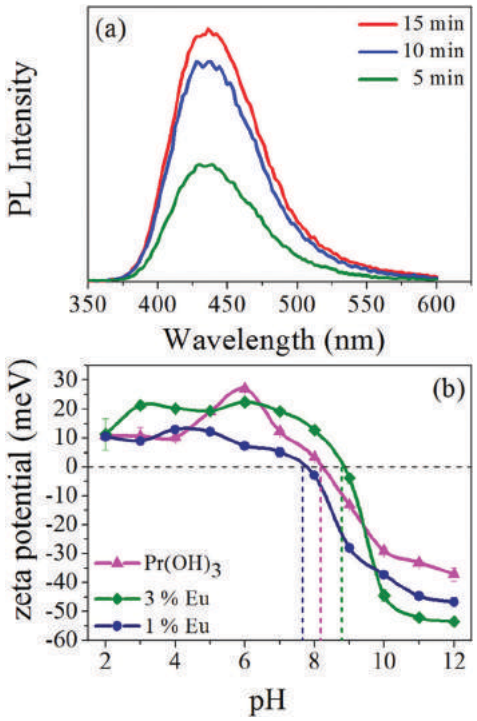

Fig. 8 (a) PL spectral changes observed during UV illumination of the $Pr_{0.95}Eu_{0.05}(OH)_3$ sample in the solution of terephthalic acid after 5, 10, and 15 min and (b) zeta potential dependence on pH value for pure, 1%, and 3% Eu-doped $Pr(OH)_3$.

range of 2.0–12.0 and their iso-electric points were 8.2, 7.6 and 8.8 respectively. At pH = 4.7, which was the natural pH value of the solution, the surface charge of the catalysts is positive in the following order: 3% Eu > $Pr(OH)_3$ > 1% Eu. As the RO16 dye molecule is negatively charged, the best adsorption is expected in the 3% Eu-doped sample due to the stronger electrostatic interaction between the adsorbent and the adsorbate. A slightly weaker adsorption is expected in $Pr(OH)_3$ and the lowest is in the 1% Eu-doped $Pr(OH)_3$ sample. This is in good agreement with the experimental results. The changes in the morphology of the 3% Eu-doped $Pr(OH)_3$ (*i.e.* the existence of two types of nanorods with diameters of the orders of magnitude ~10 nm and ~50 nm as shown in Fig. S1(c), ESI†) and the increased amount of oxygen vacancies (deduced from the Rietveld analysis) in this sample can be additional reasons for the enhanced adsorption.

The Eu-doped $Pr(OH)_3$ nanostructures exhibited a much faster removal efficiency than pure $Pr(OH)_3$ and a faster dye removal at the beginning of the reaction (Fig. 7(a)). A rapid removal of RO16 was observed in the first 30 min and after 70 min, the dye was almost completely removed. Under the similar conditions, the Eu-doped $Pr(OH)_3$ nanostructures demonstrated a much better photocatalytic activity than Degussa.[37,38] The photocatalytic degradation of RO16 followed the first-order kinetics (Fig. 7(b)), expressed by the equation $\ln(C/C_0) = kt$, where C_0 is the initial dye concentration and C is the dye concentration at time t. The first-order rate constant k values, obtained from the slope of $\ln(C/C_0)$ *vs.* t, for the $Pr_{1-x}Eu_x(OH)_3$ samples are presented in Fig. 7(b).

It can be deduced that the Eu-doped samples have significantly higher k values than that of pure $Pr(OH)_3$, confirming that these samples are better photocatalysts than the pure $Pr(OH)_3$ sample.

The XRD, XPS and UV-vis absorption spectra have revealed that the $Pr_{1-x}Eu_x(OH)_3$ samples are oxygen deficient. In addition, the XRD results have confirmed that the oxygen deficiency increases with Eu doping. The XPS measurements suggested the high segregation of Eu ions on the surface of the doped nanostructures. The presence of lattice defects such as oxygen vacancies (V_O) and Eu^{3+} ions, particularly on the surface of Eu-doped nanostructures, can influence, to a great extent, the photocatalytic activity of the $Pr_{1-x}Eu_x(OH)_3$ samples.

The photo-generated electrons or holes can be captured by V_O, which forms impurity levels inside the band gap and serves as charge carrier trap, suppressing the e–h recombination process.[39] Moreover, the vacancies facilitate the charge transfer to the adsorbed species on the catalyst surface such as O_2 or H_2O, forming reactive radicals (superoxide radical ($O_2^{\bullet -}$) or $OH^{\bullet}$), the existence of which is important for a fast and successful photocatalytic degradation of organic dyes. It is well-documented that at the surface of oxide nanostructures such as TiO_2 or CeO_2, water dissociation takes place exclusively on the oxygen vacancy defect sites, where every surface V_O enables the formation of two hydroxyl groups.[40–43] The infrared study of $Pr_{1-x}Eu_x(OH)_3$ nanostructures confirmed the presence of hydroxyl groups from water.

The formation of the $OH^{\bullet}$ radicals was tested on the surface of the $Pr_{0.95}Eu_{0.05}(OH)_3$ photocatalyst under UV irradiation and detected by the PL method. The PL spectra of the reaction solution were measured at room temperature and are presented in Fig. 8(a). Terephthalic acid reacts with the $OH^{\bullet}$ radicals producing 2-hydroxyterephthalic acid, which exhibits a PL peak at 425 nm.[44] The intensity of this peak is proportional to the amount of $OH^{\bullet}$ radicals produced in the solution.[44,45] As shown in Fig. 8(a), a substantial increase of the intensity of the 425 nm peak with prolonged illumination time indicates the increasing amount of $OH^{\bullet}$ radicals produced at the surface of the $Pr_{0.95}Eu_{0.05}(OH)_3$ sample.

The existence of the surface and subsurface vacancies also enables better adsorption of O_2, which can capture the photogenerated electrons or electrons located on V_O, producing the superoxide radical groups.[41,46] In addition, due to a high oxidative potential of the holes, they can directly attack the dye, leading to its oxidation (h^+ + dye → $dye^{\bullet +}$ → oxidation of the dye). Furthermore, the photogenerated holes can easily react with the surface-bound H_2O or hydroxyls (OH^-), forming the hydroxyl radicals ($OH^{\bullet}$). Although similar studies, to the best of our knowledge, have not been performed for the $Pr(OH)_3$ nanostructures, it is reasonable to assume that the oxygen vacancies have an important role in the photocatalytic process at the $Pr_{1-x}Eu_x(OH)_3$ surface. Furthermore, the recent papers of Dong *et al.*[3] and Wang *et al.*,[11] aimed at the investigation of the photocatalytic properties of the defective $La(OH)_3$ nanorods and $La(OH)_3$ nanorods doped with 4f elements, demonstrated the crucial role of oxygen vacancies in the photocatalytic degradation of dyes and strongly support our findings. The oxygen vacancy states in the band gap were registered by the PL and absorption measurements.

Moreover, Eu^{3+} ions are often used as the dopants that can prevent rapid recombination of the photogenerated electrons and holes because they create the surface states that present a barrier for electrons.[47] The emission from these states was not observed in the PL spectra excited with 340 nm probably due to the OH bond quenching. However, since the Eu^{3+} states were registered by XPS, they can be responsible for the enhanced photocatalytic activity of the Eu-doped nanostructures due to the abovementioned electron trapping effect.

In the recent paper of Mahlalela *et al.*, it was demonstrated that TiO_2 nanoparticles exhibited an enhanced photocatalytic activity in the presence of KNO_3. This was ascribed to the increased production of the hydroxyl radicals due to the presence of NO_3^- anions. The direct photolysis of nitrate ions (NO_3^-) during irradiation with $\lambda > 280$ nm can result in the formation of the $NO_2^{\bullet}$ and $O^{\bullet -}$ radicals. In the presence of water, the $O^{\bullet -}$ radicals can be protonated, leading to the formation of the hydroxyl radicals ($OH^{\bullet}$) and OH^- ions according to the following reaction:[48]

$$(NO_3^-) \xrightarrow{h} (NO_3^-)^* \rightarrow NO_2^{\bullet} + O^{\bullet -} + H_2O \rightarrow NO_2^{\bullet} + OH^{\bullet} + OH^- \quad (1)$$

In this way, the concentration of the $OH^{\bullet}$ radicals is increased, thus enhancing the photodegradation of the dyes. Furthermore, nitrate ions are good acceptors for the photoinduced electrons, forming the nitrogen trioxide anion radicals ($NO_3^{\bullet 2-}$). These radicals on reacting with water would form powerful nitrogen dioxide ($NO_2^{\bullet}$) anions, which are capable of oxidizing the dyes.[48]

The XPS, XRD and Raman analysis confirmed the presence of the KNO_3 phase in the Eu-doped samples. The presence of NO_3^- ions at the surface of the doped samples can additionally improve their photocatalytic properties due to the abovementioned radical formation. Considering all previously mentioned results, a mechanism of photocatalytic reactions in Eu-doped $Pr(OH)_3$ is proposed and presented in Fig. 9.

The photocatalytic stability was tested on the $Pr_{0.95}Eu_{0.05}(OH)_3$ sample. Fig. S3 (ESI†) shows the repeated photocatalytic runs under the UV light irradiation. Although there was a certain drop in the efficiency in the second run, these results indicated that the Eu-doped $Pr(OH)_3$ catalysts were stable. The drop in the efficiency after the first run is ascribed to the adsorbed dye molecules and the reduction of a number of the active sites since the catalyst is recycled by centrifugation and deionized water washing without any additional chemical treatment.

Therefore, an enhanced photocatalytic activity of the Eu-doped $Pr(OH)_3$ nanostructures can be explained by the presence of oxygen vacancies, Eu^{3+} trapping states and KNO_3-mediated hydroxyl radical production at the surface of our as-prepared samples. The synergy of these three factors resulted in the efficient separation of the photogenerated electrons and holes and their transfer to adsorbed species at the surface, thus enabling excessive formation of the reactive radicals and efficient dye degradation.

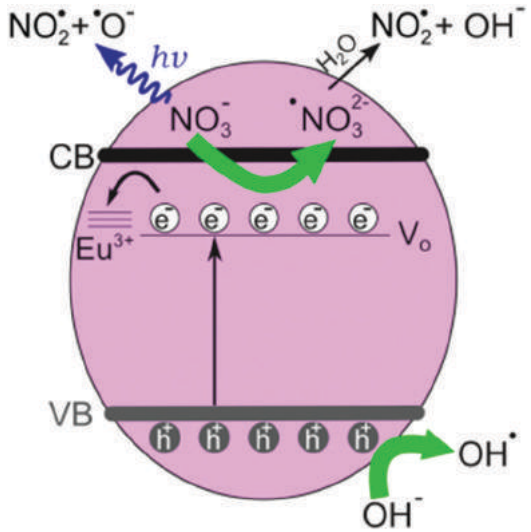

Fig. 9 Illustration of the photocatalytic mechanism of Eu-doped $Pr(OH)_3$ under the UV light irradiation.

This study provides a new insight into the role of oxygen vacancies, 4f dopants and a proper choice of alkaline metal hydroxides in promoting the photocatalytic efficiency of $Pr(OH)_3$. Our future studies would be dedicated to the investigation of the influence of other 4f dopants on the morphology, the electronic structure and the photocatalytic performances of $Pr(OH)_3$ nanostructures.

Conclusions

In summary, the defective $Pr_{1-x}Eu_x(OH)_3$ nanostructures were synthesized by a simple microwave-assisted hydrothermal method and the comprehensive characterization has been performed by XRD, XPS, ICP-OES, FE-SEM, Raman, IR and DR spectroscopy. It is observed that Eu^{3+} doping promotes the formation of oxygen vacancies and changes the morphology of $Pr(OH)_3$ nanorods. Eu^{3+} ions also have a tendency to segregate at the surface of the nanostructure. Furthermore, the presence of KNO_3 phase is registered in the doped samples. The Eu-doped nanostructures exhibit an excellent photocatalytic activity towards the photodegradation of an azo dye compared to that of pure $Pr(OH)_3$ nanorods. Oxygen vacancies, the change in the morphology and the presence of Eu^{3+} and NO_3^- ions at the $Pr(OH)_3$ surface play a significant role in improving the photocatalytic properties of the $Pr(OH)_3$ nanostructures. The enhanced photocatalytic activity of the $Pr_{1-x}Eu_x(OH)_3$ nanostructures originates from the combined effect of oxygen vacancies and Eu^{3+} ions, which act as trapping centres, subsequently enabling the facile charge transfer to the adsorbed species. In this way, a fast electron–hole recombination can be suppressed and more reactive radicals can be formed. The presence of the KNO_3 phase in the $Pr_{1-x}Eu_x(OH)_3$ samples additionally improves the photocatalytic performances of $Pr(OH)_3$ nanostructures, *i.e.*, the presence of NO_3^- ions can enhance the production of $NO_2^{\bullet}$ and $OH^{\bullet}$ radicals. Furthermore, the 3% Eu-doped sample exhibited very good adsorption properties due to a higher electrostatic attraction of anionic dye and different morphology compared to those of other samples. The possibility of tuning the ratio of photocatalytic *versus* adsorptive activity of the Eu-doped $Pr(OH)_3$ nanostructures makes them desirable for environmental applications.

Conflicts of interest

There are no conflicts of interest to declare.

Acknowledgements

This work was supported by Serbian Ministry of Education, Science and Technological Development under projects OI 171032 and III 45018. V. D. Araújo and M. I. B. Bernardi wish to thank Brazilian agencies FAPESP, FACEPE, and CNPq for the financial support. The authors wish to thank Prof. Tamara Radetic for TEM images, Dr Aleksandar Matković and MSc Marijana Milićević for SEM images and to Dr Nenad Tadić for DRS measurements.

References

1 X. Wang and Y. Li, *Chem. – Eur. J.*, 2003, **9**, 5627–5635.
2 X. Ouyang, S. Yuan, Q. Qiu, W. Zeng, G. A. Hope and H. Li, *Inorg. Chem. Commun.*, 2014, **46**, 21–23.
3 F. Dong, X. Xiao, G. Jiang, Y. Zhang, W. Cui and J. Ma, *Phys. Chem. Chem. Phys.*, 2015, **17**, 16058–16066.
4 D. Zhang, T. Yan, L. Shi, H. Li and J. F. Chiang, *J. Alloys Compd.*, 2010, **506**, 446–455.
5 S. Zhang and C. Yao, *Mater. Lett.*, 2013, **94**, 143–146.
6 X. Sun, T. Zhai, X. Lu, S. Xie, P. Zhang, C. Wang, W. Zhao, P. Liu and Y. Tong, *Mater. Res. Bull.*, 2012, **47**, 1783–1786.
7 T. Zhai, S. Xie, X. Lu, L. Xiang, M. Yu, W. Li, C. Liang, C. Mo, F. Zeng, T. Luan and Y. Tong, *Langmuir*, 2012, **28**, 11078–11085.
8 J. Tang, J. Chen, W. Huang, D. Li, Y. Zhu, Y. Tong and Y. Zhang, *Chem. Eng. J.*, 2014, **252**, 202–209.
9 A. Dodd, *J. Colloid Interface Sci.*, 2013, **392**, 137–140.
10 X. Wang and Y. Li, *Angew. Chem., Int. Ed.*, 2002, **41**, 4790–4793.
11 Y. Wang, S. Liu, Y. Cai, S. Deng, B. Han, R. Han, Q. Li and Y. Wang, *Ceram. Int.*, 2014, **40**, 5091–5095.
12 A. C. Larson and R. B. Von Dreele, *Report LAUR 86-748*, Los Alamos National Laboratory, 2004.
13 D. F. Mullica, W. O. Milligan and G. W. Beall, *J. Inorg. Nucl. Chem.*, 1979, **41**, 525–532.
14 M. Hafez, I. S. Yahia and S. Taha, *Acta Phys. Pol., A*, 2015, **127**, 734–740.
15 R. Shannon, *Acta Crystallogr., Sect. A: Found. Crystallogr.*, 1976, **32**, 751–767.
16 S. Deshpande, S. Patil, S. V. N. T. Kuchibhatla and S. Seal, *Appl. Phys. Lett.*, 2005, **87**, 133113.

17 J. D. Bryan and D. R. Gamelin, *Prog. Inorg. Chem.*, John Wiley & Sons, Inc., 2005, ch. 2, pp. 47–126, DOI: 10.1002/0471725560.
18 C. Li, H. Liu and J. Yang, *Nanoscale Res. Lett.*, 2015, **10**, 1–6.
19 K. Ahrens, H. Gerlinger, H. Lichtblau, G. Schaack, G. Abstreiter and S. Mroczkowski, *J. Phys. C: Solid State Phys.*, 1980, **13**, 4545.
20 J.-G. Kang, Y. Jung, B.-K. Min and Y. Sohn, *Appl. Surf. Sci.*, 2014, **314**, 158–165.
21 R. M. Escribano, D. Fernández-Torre, V. J. Herrero, B. Martín-Llorente, B. Maté, I. K. Ortega and H. Grothe, *Vib. Spectrosc.*, 2007, **43**, 254–259.
22 H. Grothe, C. E. Lund Myhre and C. J. Nielsen, *J. Phys. Chem. A*, 2006, **110**, 171–176.
23 M. H. Brooker, *Can. J. Chem.*, 1977, **55**, 1242–1250.
24 D. Liu, F. G. Ullman and J. R. Hardy, *Phys. Rev. B: Condens. Matter Mater. Phys.*, 1992, **45**, 2142–2147.
25 F. Mercier, C. Alliot, L. Bion, N. Thromat and P. Toulhoat, *J. Electron Spectrosc. Relat. Phenom.*, 2006, **150**, 21–26.
26 H. Wu, Y. Zhang, M. Zhou, C. Yao and X. Ge, *Cryst. Res. Technol.*, 2016, **51**, 508–512.
27 J.-C. Dupin, D. Gonbeau, P. Vinatier and A. Levasseur, *Phys. Chem. Chem. Phys.*, 2000, **2**, 1319–1324.
28 N. Paunovic, Z. Dohcevic-Mitrovic, R. Scurtu, S. Askrabic, M. Prekajski, B. Matovic and Z. V. Popovic, *Nanoscale*, 2012, **4**, 5469–5476.
29 J.-G. Kang, Y.-I. Kim, D. Won Cho and Y. Sohn, *Mater. Sci. Semicond. Process.*, 2015, **40**, 737–743.
30 J. T. Kloprogge and R. L. Frost, Infrared and Raman spectroscopic studies of layered double hydroxides (LDHs), in *Layered double hydroxides: Present and future*, ed. V. Rives, Nova Science Publishers, Inc., New York, 2001, pp. 139–192.
31 F. Cui, J. Zhang, T. Cui, S. Liang, L. Ming, Z. Gao and B. Yang, *Nanotechnology*, 2008, **19**, 065607.
32 N. Ghobadi, *Int. Nano Lett.*, 2013, **3**, 2.
33 M. Wang, P. Guo, T. Chai, Y. Xie, J. Han, M. You, Y. Wang and T. Zhu, *J. Alloys Compd.*, 2017, **691**, 8–14.
34 M. K. Aydinol, J. V. Mantese and S. P. Alpay, *J. Phys.: Condens. Matter*, 2007, **19**, 496210.
35 Z. Zuo, D. Liu, J. Liu, H. Liu, S. Qin and F. Zheng, *Mater. Chem. Phys.*, 2010, **123**, 502–506.
36 D. Liu, Y. Lv, M. Zhang, Y. Liu, Y. Zhu, R. Zong and Y. Zhu, *J. Mater. Chem. A*, 2014, **2**, 15377–15388.
37 D. Mijin, M. Radulović, D. Zlatić and P. Jovančić, *Chem. Ind. Chem. Eng. Q.*, 2007, **13**, 179–185.
38 R. C. Hsiao, L. S. Roselin, H.-L. Hsu, R. Selvin and R. S. Juang, *Int. J. Mat. Eng. Innov.*, 2011, **2**, 96–108.
39 F. Kayaci, S. Vempati, I. Donmez, N. Biyikli and T. Uyar, *Nanoscale*, 2014, **6**, 10224–10234.
40 R. Schaub, P. Thostrup, N. Lopez, E. Lægsgaard, I. Stensgaard, J. K. Nørskov and F. Besenbacher, *Phys. Rev. Lett.*, 2001, **87**, 266104.
41 X. Pan, M.-Q. Yang, X. Fu, N. Zhang and Y.-J. Xu, *Nanoscale*, 2013, **5**, 3601–3614.
42 Z. Yang, Q. Wang, S. Wei, D. Ma and Q. Sun, *J. Phys. Chem. C*, 2010, **114**, 14891–14899.
43 N. M. Tomić, Z. D. Dohčević-Mitrović, N. M. Paunović, D. Ž. Mijin, N. D. Radić, B. V. Grbić, S. M. Aškrabić, B. M. Babić and D. V. Bajuk-Bogdanović, *Langmuir*, 2014, **30**, 11582–11590.
44 K.-i. Ishibashi, A. Fujishima, T. Watanabe and K. Hashimoto, *Electrochem. Commun.*, 2000, **2**, 207–210.
45 T.-M. Su, Z.-L. Liu, Y. Liang, Z.-Z. Qin, J. Liu and Y.-Q. Huang, *Catal. Commun.*, 2012, **18**, 93–97.
46 C. L. Muhich, Y. Zhou, A. M. Holder, A. W. Weimer and C. B. Musgrave, *J. Phys. Chem. C*, 2012, **116**, 10138–10149.
47 D. Yue, D. Chen, W. Lu, M. Wang, X. Zhang, Z. Wang and G. Qian, *RSC Adv.*, 2016, **6**, 81447–81453.
48 L. C. Mahlalela and L. N. Dlamini, *Surf. Interfaces*, 2016, **1–3**, 21–28.

THE JOURNAL OF PHYSICAL CHEMISTRY C

Article

pubs.acs.org/JPCC

Realization of Enhanced Magnetoelectric Coupling and Raman Spectroscopic Signatures in 0−0 Type Hybrid Multiferroic Core−Shell Geometric Nanostructures

Ann Rose Abraham,[†] B. Raneesh,[‡] Tesfakiros Woldu,[§] Sonja Aškrabić,[∥] Saša Lazović,[∥] Zorana Dohčević-Mitrović,[∥] Oluwatobi Samuel Oluwafemi,[*,⊥,#] Sabu Thomas,[g] and Nandakumar Kalarikkal[*,†,g]

[†]School of Pure and Applied Physics, Mahatma Gandhi University, Kottayam, Kerala-686560, India

[‡]Department of Physics, Catholicate College, Pathanamthitta, Kerala-689 645, India

[§]Department of Physics, Osmania University, Hyderabad 500007, India

[∥]Institute of Physics Belgrade, University of Belgrade, Pregrevica 118, 11080, Belgrade, Serbia

[⊥]Department of Applied Chemistry, University of Johannesburg, Doornfontein Campus, P.O Box 17011, Doornfontein 2028, South Africa

[#]Centre for Nanomaterials Science Research, University of Johannesburg, Johannesburg, South Africa

[g]International & Inter University Centre for Nanoscience and Nanotechnology, Mahatma Gandhi University, Kottayam, Kerala-686 560, India

ABSTRACT: Multiferroic heterostructures' contribution to the persistent growth of ultrafast wireless communications may pave the way for future 5G technology. In line with this, we herein report the development of an engineered hybrid multiferroic core−shell nanostructure with a soft magnetic core and a ferroelectric shell. In this system, the attributes of the ferromagnetic core were modulated by a ferroelectric coating over it, in order to impart a bifunctionality to it and thus induce magnetoelectric coupling in it for multifunctional device applications. The phase, crystal structure and morphology of these composites have been investigated using X-ray diffraction (XRD), transmission electron microscopy (TEM), scanning electron microscopy (SEM), and confocal Raman spectroscopy. The origin of strain mediated magnetoelectric coupling effect at the ferromagnetic core and ferroelectric shell interface was also investigated. Raman spectroscopy is efficiently utilized to manifest the multiferroism in the core−shell samples. High resolution transmission electron microscopy images and domain structure mapping using confocal Raman microscopy along with Raman images substantiate the core−shell nature of the samples. The findings manifest how tuning of the ferromagnetic phase influences the magnetoelectric coupling at the interface and reveal novel approaches for manipulating the attributes of a ferromagnetic−ferroelectric interface for innovative device applications. The outcome of the experiments indicates an energy efficient move toward the control of the *E*-field by the magnetic field, which demonstrates an enormous prospective for novel low power electronic, magnonic, and spintronic devices.

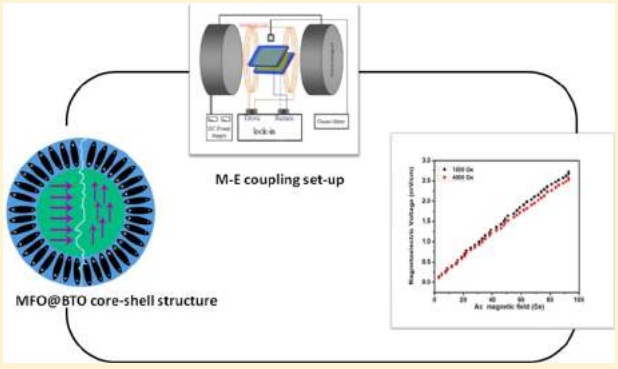

1. INTRODUCTION

The voltage control of magnetism, exhibited by multiferroics, makes them attractive and promising for multifunctional device applications.[1−3] Hence, the exploration of hybrid multiferroic materials or artificial multiferroics in which ferromagnetism and ferroelectricity coexist is highly appealing and of great technological significance.[4−6] Multiferroic materials are rare in nature[7−9] and of great demand due to their potential to conserve power and space and their amazing applications in information technology,[8] data storage,[11] magnetoelectric sensors,[11] multiple-state memories,[12,13] and emerging ultra-low-power spintronics technology.[10−13] The electromagnons[13,14] or the quantized hybrid spin−lattice excitations in multiferroics[15,16] have opened up vast doors in the emerging magnonic and spintronics technology and production of fast, reliable, and low power magnetoelectric devices.

Multiferroics are fascinating for engineering of future generation of fast and nonvolatile hybrid type memories like multiferroic or magnetoelectric memories (MERAMS) with unlimited write-erase cycles and enormous data transfer

Received: December 13, 2016
Revised: January 26, 2017
Published: January 30, 2017

DOI: 10.1021/acs.jpcc.6b12461
J. Phys. Chem. C 2017, 121, 4352−4362

rate.[17−20] They magnificently assist one to realize a highly energy efficient and switchable four-state (+P, + M), (+P, −M), (−P, + M), (−P, −M) memory. The quest for development of engineered hybrid multiferroic structures[4] for energy efficient spintronics and magnetoelectric memories[17−20] was propelled by the enhanced values of magnetoelectric coupling (ME) demonstrated by ferromagnetic−ferroelectric heterostructures[1] at room temperature, rather than that exhibited by the single phase multiferroics that exhibit multiferroicity at cryogenic temperatures.[21−26] Engineered hybrid multiferroic heterostructures[27] with large values of magnetoelectric coupling have been reported in ferromagnetic−ferroelectric composites, such as cobalt ferrite−barium titanate ceramic composites,[28] $BaTiO_3$−$MgFe_2O_4$ composites,[29] $BaTiO_3$−$MgFe_2O_4$ composite powders (synthesized by a Pechini one-pot method),[30] $(x)MgFe_2O_4$−$(1 - x)BaTiO_3$ systems composites[31] and also in hybrid multiferroic core−shell structures like Ni@$BiFeO_3$,[32] $NiFe_2O_4$@$BaTiO_3$,[33−35] $Ni_{0.5}Zn_{0.5}Fe_2O_4$@$BaTiO_3$,[36] and $CoFe_2O_4$@$BaTiO_3$.[37] However, as far as the authors know, the preparation of $MgFe_2O_4$@$BaTiO_3$ core−shell nanocomposites with varying magnetic core sizes has never been reported.

We focus on composite structures of spinel ferrite of AB_2O_4 structure[38] and perovskites of (ABO_3) structure.[39] Ferrites, the most desirable magnetic materials, have wide applications as waveguides for electromagnetic radiation and in high-density data storage, sensors, microwave devices, food pathogen detection, and nanomedicine.[40−42] Furthermore, $MgFe_2O_4$[38] is highly promising in spintronics, owing to its high curie temperature.[40] On the other hand, $BaTiO_3$ (BTO) possesses exceptional ferroelectric attributes at room temperature, in addition to the multiferroic nature at the nanoscale; hence, we found no best candidate other than $BaTiO_3$ (BTO)[43] to realize our objective of achieving ferromagnetic−ferroelectric systems with enhanced multiferroicity.

Functionality of the hybrid multiferroic nanostructures is highly dependent on the morphology of the magnetic and ferroelectric counterparts and could be extensively tailored by playing around with their geometry.[44] As far as the authors know there are no reports that explains how the magnetoelectric coupling gets tuned in a hybrid[45] core−shell multiferroic system by varying the magnetic core sizes. The existence of spin−phonon coupling[12] mediated by the lattice distortion[46] has been investigated by several researchers in multiferroics like $YMnO_3$,[47] $TbMn_2O_5$.[46]

In this work, we have focused our attention on preparing three core−shell systems in which soft magnesium ferrite core of different particle sizes were coated with $BaTiO_3$ shell to study its influence in enhancing the magnetoelectric coupling between the magnetic and ferroelectric phases. Emphasis is given to the development of core−shell multiferroic composite structures with enhanced ME coupling than the individual phases. The sketch map of a ferroelectric shell over a ferromagnetic core (FM@FE) as shown in Figure 1 is attractive because of the interfacial magnetoelectric effects, due to coupling at FE (ferroelectric)/(FM) ferromagnetic interfaces.

The Morphology of the developed core−shell samples were verified using X-ray diffraction, transmission electron microscopy, scanning electron microscopy, and Raman spectroscopy while the coupling between the ferromagnetic and ferroelectric phases was studied by a magnetoelectric coupling setup and confocal Raman spectroscopy.

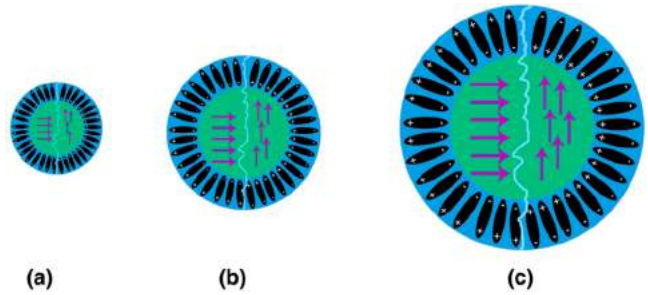

Figure 1. Sketch map of ferromagnetic@ferroelectric core−shell nanocomposites of varying cores sizes.

2. EXPERIMENTAL SECTION

2.1. Materials. Magnesium nitrate, $Mg(NO_3)_2.6H_2O$ (99% purity, Fisher Scientific Chemicals), ferric nitrate $Fe(NO_3)_3 \cdot 9H_2O$ (99.99% purity, Fisher Scientific Chemicals), poly(vinyl alcohol) (PVA) (99.99% purity, Fisher Scientific chemicals), citric acid, barium carbonate, and titanium isopropoxide (Sigma- Aldrich).

2.2. Synthesis. The $MgFe_2O_4$ @ $BaTiO_3$ (MFO@BTO) core−shell nanoparticles were synthesized by a two-step method. Nanoparticles of polycrystalline $MgFe_2O_4$ were prepared by a sol−gel method, using high purity nitrates of magnesium and iron. In a typical reaction, aqueous solution of 0.1 M magnesium nitrate and 0.2 M ferric nitrate was prepared and sonicated. PVA with a weight equal to the weight of the metal ions in the solution was added to the mixed solution. The solution was evaporated until the formation of a viscous sol and dried completely so that it can be powdered. The powder obtained was divided into three and calcined at three different high temperatures to obtain $MgFe_2O_4$ nanoparticles of different particle sizes labeled as MFO1, MFO2, and MFO3. The $MgFe_2O_4$ nanoparticles (MFO1, MFO2, and MFO3) were dispersed under vigorous stirring into the $BaTiO_3$ precursor solution containing a mixture of $BaCO_3$, citric acid, and titanium isopropoxide, probe sonicated, dried, and calcined at 800 °C to obtain $MgFe_2O_4$@$BaTiO_3$ core−shell nanoparticles (MFO@BTO1, MFO@BTO2 and MFO@BTO3).

The $MgFe_2O_4$/$BaTiO_3$ composite samples were synthesized by mixing the two phases, prepared independently, followed by annealing. $MgFe_2O_4$ nanoparticles (MFO3) prepared by sol−gel method, and $BaTiO_3$ prepared by sol−gel method, were mixed at ratio 1:1 in the presence of acetone, grinded and sintered at 800 °C for 2 h. The obtained powder was pressed into pellets at 500 MPa and sintered at 800 °C for 2 h. Silver paste was coated on the sintered pellets to get electrical contacts.

2.3. Characterization. X-ray diffraction (XRD) measurements of the core and core−shell samples were carried out by using X'PERT PRO PANalytical X-ray diffractometer with Cu Kα radiation. The scanning electron microscopy (SEM) study was carried out by an energy-filtered 200 kV JEOL 6390 scanning electron microscope. The transmission electron microscopy (TEM) images were obtained from JEOL GEM 2100 transmission electron microscope equipped with an Oxford energy transmission electron microscope for elemental analysis operated at 200 kV. Confocal Raman spectra and Raman image was acquired using WITEC alpha300 RA confocal Raman microscope with a 100×/NA= 0.9 air objective and an excitation wavelength of 532 nm (600 g/mm grating blazed at 500 nm). The ME coupling studies were performed

DOI: 10.1021/acs.jpcc.6b12461
J. Phys. Chem. C 2017, 121, 4352−4362

by using a dynamic lock-in amplifier ME coupling measurement set up. Micro-Raman spectra were acquired in the back-scattering configuration using the micro-Raman system Jobin Yvon T64000.

3. RESULTS AND DISCUSSION

X-ray diffraction (XRD) patterns of $MgFe_2O_4$ (MFO), $BaTiO_3$ (BTO), and $MgFe_2O_4$@$BaTiO_3$ (MFO@BTO) samples are shown in Figure 2. A well crystallized single phase of

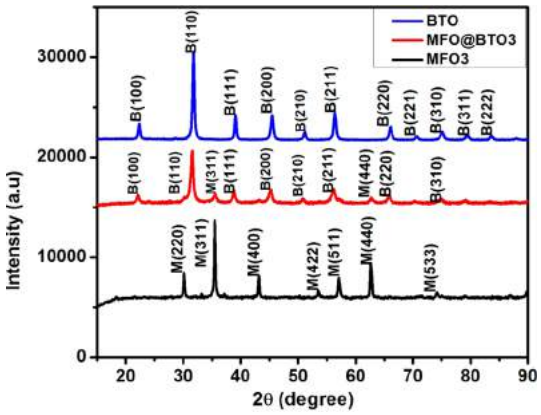

Figure 2. XRD patterns of MFO3 BTO, and MFO@BTO3.

magnesium ferrite with cubic spinel structure was detected. The fundamental peak at $2\theta = 36.45°$ with maximum intensity correspond to the (311) plane of magnesium ferrite (PDF data 71−1232). Peaks corresponding to the reflections from other planes, (220), (400), (440), and (422), are also detected but with weak intensities. The nonexistence of any additional intermediate phases indicates the high purity level of the samples. The crystalline size of the nanoparticle was calculated using the Scherrer equation. The crystalline size increased with increasing annealing temperature. The particle diameter of the core is 5, 14, and 20 nm for MFO1, MFO2, and MFO3, respectively. The formation of cubic perovskite structure of Barium titanate was confirmed from the XRD pattern (PDF 89-2475). The peaks corresponding to the magnesium ferrite with cubic spinel structure and Barium titanate with cubic perovskite structure were observed in the XRD patterns of MFO@BTO. In the XRD pattern of MFO@BTO, the fundamental reflections from the planes (311), (400), (511), and (440) characterizing the cubic spinel structures and from the planes (110), (111), and (211) characterizing the ferroelectric barium titanate were strongly observed.

The SEM images for both pure MFO powder and MFO@BTO composite powders are shown in Figure 3. The SEM images of MFO nanoparticles show that the particles are spherical in shape and are slightly agglomerated. After coating the ferrite particles with ferroelectric shell, the agglomeration decreases and spherical shape particles with uniform particle size are produced.

A typical transmission electron microscopy image of the core is shown in Figure 4. The TEM image shows that the materials are spherical in shape with uniform size distribution. The average grain size is found to be 5−6 nm which should be superparamagnetic in nature. The TEM images confirm the grain size calculations from XRD. The formation of spinel structure of Magnesium ferrite is confirmed by *d*-spacing values. The *d*-spacing of 0.284 nm corresponds to the (110) plane of BTO while the *d*-spacing of 0.295 nm corresponds to the (220) plane of MFO. This confirms the cubic spinel and the perovskite structure of the core−shell samples. (PDF No. 89-3084). The crystal planes identified from the selected area diffraction (SAED) pattern are found to be in conformity with that from XRD pattern.

The TEM images (Figure 5 and 6) confirm the formation of core−shell structure of MFO@BTO samples. The darker core and brighter shell can be clearly seen in the TEM images. Figure 5b shows the HRTEM image of the core−shell sample. The *d*-spacing of 0.284 nm corresponds to the (110) plane of BTO while the *d*-spacing of 0.295 nm corresponds to the (220) plane of MFO. This confirms the cubic spinel and the perovskite structure of the core−shell samples. The SAED patterns of core−shell samples shown in Figure 5 and Figure 6 also confirm the crystallinity of as-synthesized core−shell samples.

Chemical purity and stoichiometry of the $MgFe_2O_4$ sample was confirmed by EDX (Figure 7a) before encapsulating it in ferroelectric matrix. The EDAX spectrum shows strong peaks corresponding to magnesium, oxygen and iron. The elemental composition and atomic concentration is shown in Table. 1. EDAX spectrum of the core−shell sample (Figure 7b) was also studied to confirm the stoichiometry of the prepared sample. The spectrum reveals the presence of elements Mg, Fe, O, Ba, Ti and O in the magnesium ferrite@barium titanate core−shell sample. Their atomic concentrations are given in Table 2.

Raman spectroscopy is reported to be highly promising in studying the spin dynamics and the effect of the spin- phonon coupling in multiferroics at local scale. It has played an important role in the study of spin−phonon coupling in $BiFeO_3$,[48,49] $Ba_{1.6}Sr_{1.4}Co_2Fe_{24}O_{41}$[50] and other compounds.[51] Confocal Raman spectroscopy[52] that probes the vibrational energy levels within a molecule is employed to acquire the molecular fingerprints and high resolution Raman image of the core−shell samples. Confocal Raman image of the MFO@BTO samples shown in Figure 8a−c helps to study the structural

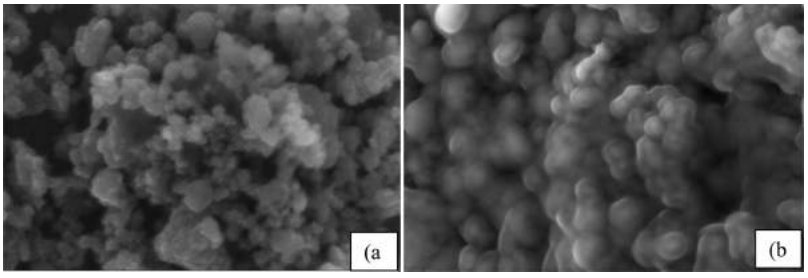

Figure 3. SEM images of (a) MFO3 at 100 nm and (b) MFO@BTO3 core−shell sample: Scale bar = 100 nm.

DOI: 10.1021/acs.jpcc.6b12461
J. Phys. Chem. C 2017, 121, 4352−4362

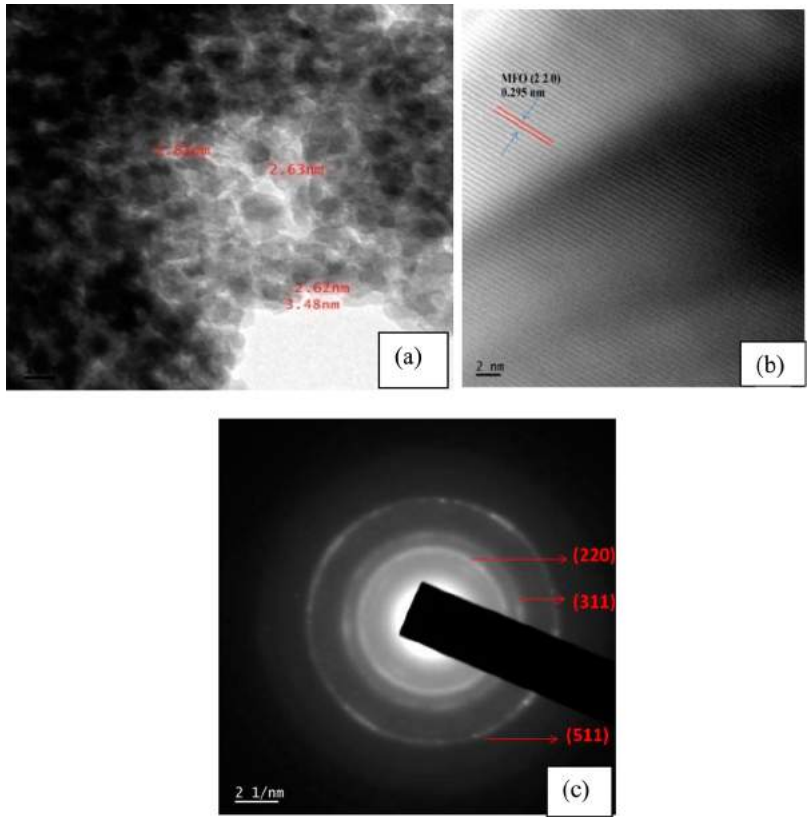

Figure 4. (a) TEM image: scale bar = 2 nm. (b) HRTEM image. (c) SAED pattern of magnesium ferrite (MFO1).

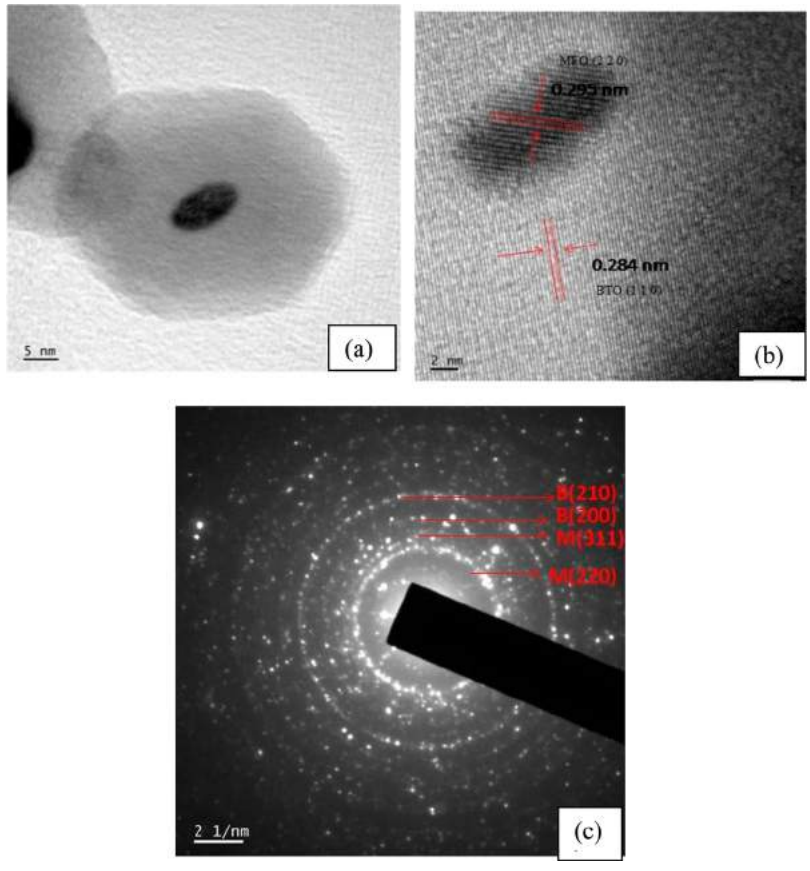

Figure 5. (a) TEM image: scale bar = 5 nm. (b) HRTEM images and (c) SAED pattern of MFO@BTO1.

DOI: 10.1021/acs.jpcc.6b12461
J. Phys. Chem. C 2017, 121, 4352−4362

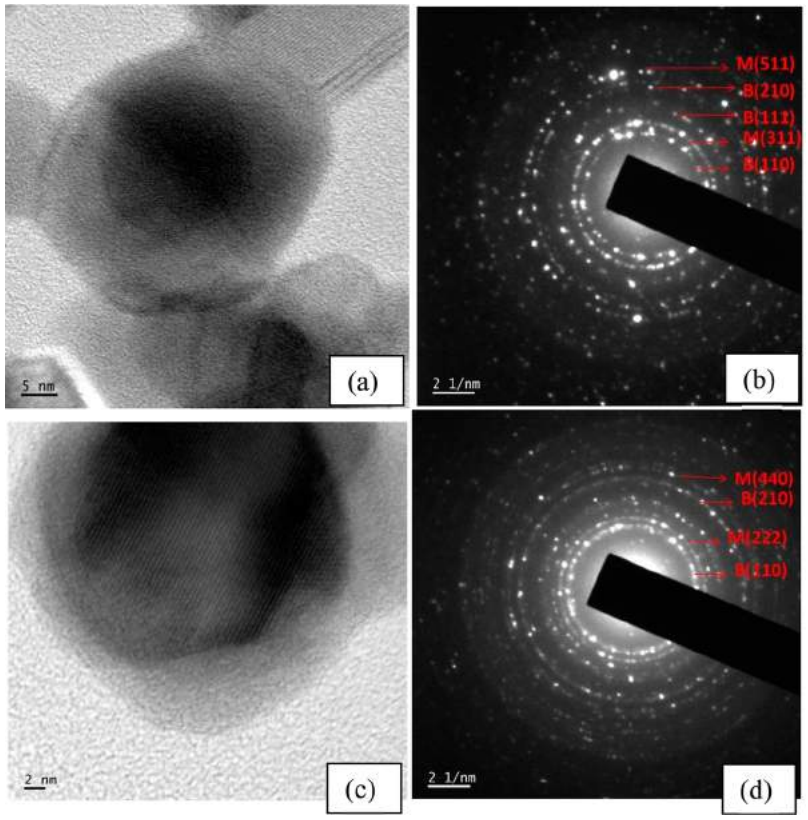

Figure 6. (a) TEM and (b) SAED pattern of MFO@BTO2 and (c) TEM and (d) SAED pattern of MFO@BTO3.

deformations of the sample. Raman image shows the ferromagnetic and ferroelectric domain allocation at the sample surface by color distribution.[53] Contrast in the Raman image confirms the multiferroic nature of the samples. The confocal Raman spectra show characteristic mode at 220 cm^{-1} attributed to the ferroelectric[54] nature of the multiferroic sample. The Raman modes between 300 to 700 cm^{-1} are the two-phonon peaks due to the Fe−O bonding[55] and are assigned to magnetic character of multiferroic MFO@BTO. The band observed at ∼1300−1500 cm^{-1} is associated with two-phonon Raman scattering,[48] and the strong band observed at 1320 cm^{-1} is the two phonon scattering band[54] observed in MFO. Thus, confocal Raman spectroscopy manifest the strong spin−phonon coupling[12] in MFO@BTO samples.

3.1. Magnetoelectric (ME) Coupling Responses. The coexistence of the ferroelectric and magnetic phases in MFO@BTO samples brings about the magnetoelectric (ME) effect, which is characterized by the magnetoelectric voltage coefficient,[53,55,56] $\alpha = dE/dH$. The investigation of the magnetoelectric (ME) coupling of the samples was performed by using a dynamic lock-in amplifier ME coupling[57−60] measurement set up to quantitatively figure out the actual magnitude of α. The details of the experimental setup are mentioned elsewhere.[59]

In multiferroic composites composed of magnetostrictive and ferroelectric phases, the magnetoelectric effect depends on the applied magnetic field. The ac magnetic field (H_{ac}) dependence of the ME voltage developed at room temperature in the BTO (Figure 9), MFO@BTO core−shell samples (Figure 10), and MFO/BTO composite sample (Figure 11) at a fixed frequency of 850 Hz with constant dc bias field of 1000 and 4000 Oe are shown below. The variation of ME voltage as a function of dc magnetic field for the MFO@ BTO core−shell samples is shown in Figure 12.

The magnetoelectric (ME) coupling responses of the BTO and $MgFe_2O_4$@$BaTiO_3$ core−shell samples were investigated. ME voltage coefficient was 5 $mVcm^{-1}Oe^{1-}$ for the synthesized nanomultiferroic $BaTiO_3$ sample (Figure 9). However, an enhanced ME voltage coefficient α_{ME} as high as 25 $mVcm^{-1}$ Oe^{-1} (MFO@BTO1) and 28 $mVcm^{-1}$ Oe^{-1} (MFO@BTO3) was obtained for the artificial multiferroic $MgFe_2O_4$@$BaTiO_3$ core−shell samples (Figure 10), higher than that reported for $MgFe_2O_4$/$BaTiO_3$ composite samples[31] (Figure 11). Thus, the results can be summarized as the magnetoelectric (ME) coupling response of the samples follows the trend $ME_{BTO} < ME_{MFO/BTO} < ME_{MFO@BTO}$.

The higher ME coefficient of the $MgFe_2O_4$@$BaTiO_3$ core−shell samples may be attributed to better coupling between the two phases at the ferromagnetic−ferroelectric interface. This can be elucidated by the proximity effects and larger interfacial area offered by the core−shell structure. The core−shell structure guarantee firm and compact coupling between ferroelectric and ferromagnetic phases to a great extent and hence, an improved magnetoelectric coupling response was achieved in ferromagnetic−ferroelectric core−shell nanoparticles as expected.[26] It can be clearly seen that the spin-dependent transport mechanism in multiferroics is highly influenced by the interface between the two phases and core−shell geometry has an appreciable role to play in significantly enhancing the magnetoelectric effect. The enhanced ME voltage coefficient displayed by the core−shell samples (Figure 10) indicate the strong spin−lattice correlations in the synthesized samples. Strain mediated elastic coupling at the core (ferromagnetic)−shell (ferroelectric) interface is attributed

DOI: 10.1021/acs.jpcc.6b12461
J. Phys. Chem. C 2017, 121, 4352−4362

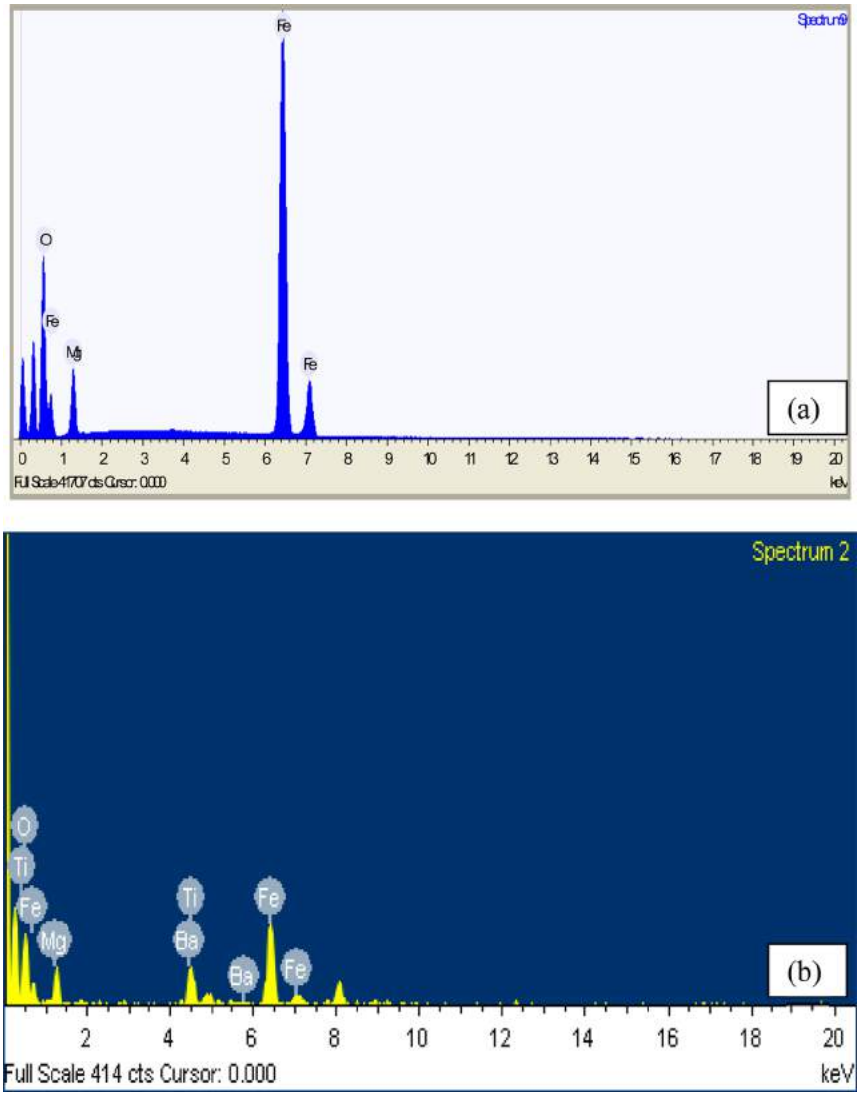

Figure 7. EDAX spectrum of (a) MFO3 and (b) MFO@BTO3.

Table 1. Elemental Composition and Atomic Concentration of MFO from EDAX Spectrum

element	weight (%)
magnesium	3.113
iron	73.719
oxygen	23.168

Table 2. Elemental Composition and Atomic Concentration of MFO@BTO from EDAX Spectrum

element	weight (%)	atomic (%)
O	24.28	50.40
Mg	10.20	13.93
Fe	39.79	23.66
Ti	12.81	8.88
Ba	12.93	3.13
totals	100	100

to account for the magnetoelectric coupling in the core−shell samples. Comparing the magnetoelectric response of the core−shell structured samples, it can be observed that, $ME_{MFO@BTO1} < ME_{MFO@BTO2} < ME_{MFO@BTO3}$. The underlying reason may be basically that, due to the smaller size of MFO grains in sample MFO@BTO1, reduced magnetic properties is expected as a result of the size effect which is influenced by the sintering temperature and consequently a weaker ME coupling. In addition, the comparatively larger size of $MgFe_2O_4$ grains in sample MFO@BTO3 yields superior magnetic properties that couple with ferroelectric properties of BTO and contribute to the large value of observed ME coupling coefficient, which indicate a strong ME coupling between the phases. Thus, the somewhat superior ME response of the MFO@BTO3 sample, compared to the MFO@BTO1 sample, may be due to the improved ferromagnetic and ferroelectric functionalities of the constituent phases that contribute to a larger piezoelectric strain at the MFO@BTO interface. The noticed variations in the magnetoelectric coefficients is indicative of the probable domain structure modification[8] that occurs in the in these hybrid systems.

These findings pave the way for experimental achievement for the development of system with strong ME coupling[59] responses, and they provide important implications for the design and performance optimization of related devices comprising of this kind of core−shell magnetoelectric[60] materials.

DOI: 10.1021/acs.jpcc.6b12461
J. Phys. Chem. C 2017, 121, 4352−4362

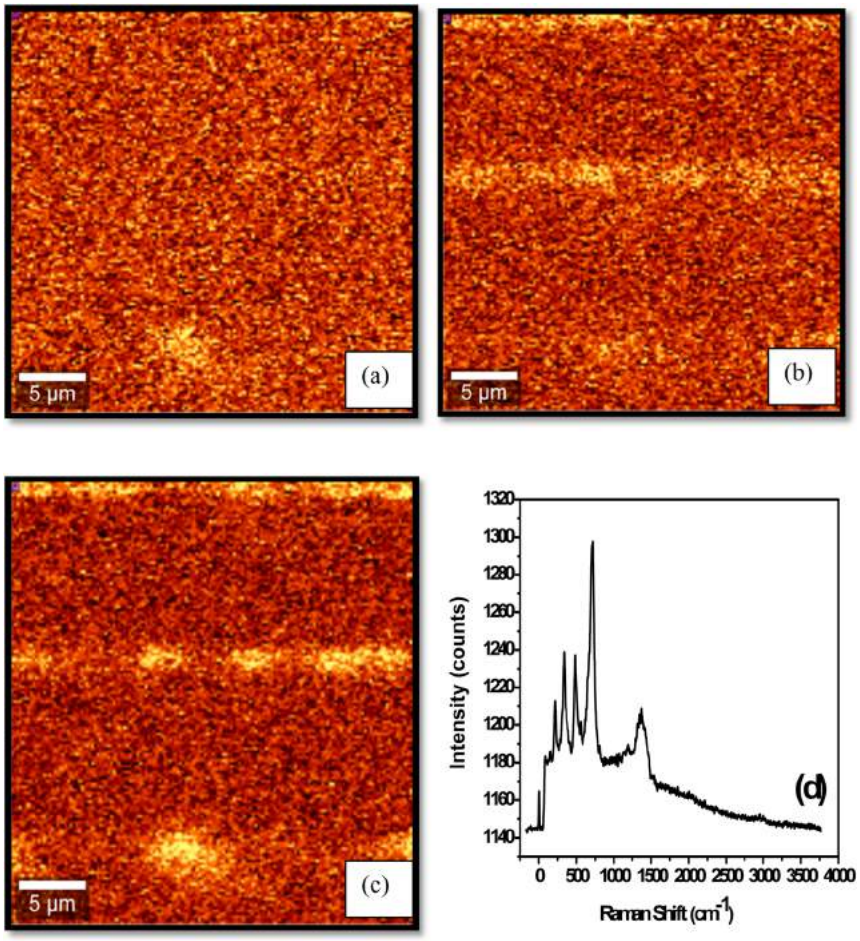

Figure 8. Domain structure mapping of (a) MFO@BTO1, (b) MFO@BTO2, and (c) MFO@BTO3 by confocal Raman spectroscopy. (d) Confocal Raman spectra of MFO@BTO3 Raman image.

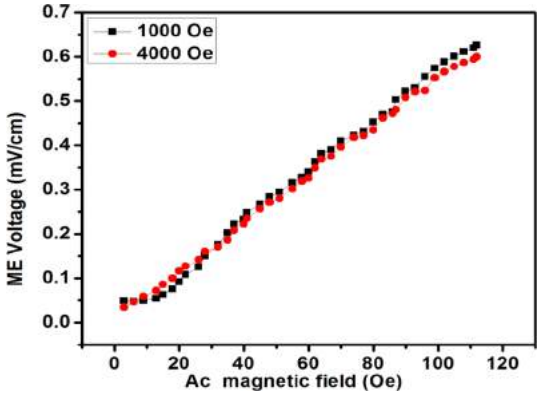

Figure 9. ME voltage vs ac magnetic field with constant dc bias magnetic field for BTO.

3.2. Raman Spectroscopic Studies. $MgFe_2O_4$ is a spinel ferrite with $Fd\bar{3}m$ crystal symmetry. It is a partially inverse spinel;[40] i.e., some of the Mg^{2+} ions are not positioned on tetrahedral sites only but also appear on the octahedral sites. The crystal symmetry $Fd\bar{3}m$ defines five Raman active modes in the center of Brillouine zone: $\Gamma = A_{1g} + E_g + 3F_{2g}$. Observed Raman spectra of $MgFe_2O_4$, $BaTiO_3$, and core−shell particles with $MgFe_2O_4$ core and $BaTiO_3$ shell (MFO@BTO3) are shown in Figure 13. The spectra of core−shell nanoparticles (Figure 13a) are almost identical to the spectrum of their core material, $MgFe_2O_4$ (Figure 13b). The assignation of the modes was performed according to the literature data for $MgFe_2O_4$ and similar spinels.[61] Three F_{2g} modes present in the pure $MgFe_2O_4$ and core−shell particles are positioned at 212, 487, and 550 cm^{-1}. The mode positioned at 329 cm^{-1} was assigned to the E_g vibration, whereas the mode positioned at ∼706 cm^{-1} with a broad shoulder at ∼654 cm^{-1} was assigned to the A_{1g} vibration. Correlation of the highest wavenumber mode, A_{1g}, with particular atomic movements is not consistent with the literature data reported so far. This mode represents symmetric breathing vibration of oxygen atoms around cation on the tetrahedaral position,[62] but the question of whether the cation positioned on the octahedral site influences the wavenumber of this mode remains opened. Hosterman[63] in his thesis compared the literature A_{1g} mode wavenumber values for a normal spinel ZnB_2O_4 (B = Cr, Fe), where trivalent B cations are positioned on octahedral sites only and concluded that the discrepancy between the wavenumber values of A_{1g} mode in $ZnCr_2O_4$ and $ZnFe_2O_4$ is too large if it is presumed that octahedral site cations do not influence A_{1g} mode.[63] Furthermore, splitting of the Raman A_{1g} mode in several inverse or partially inverse spinels was reported by Errandonea,[64] and this was explained by the fact that, both types of cations are present on the octahedral sites which results in different wavenumbers of A_{1g} vibrational modes. Such splitting was observed in $MgFe_2O_4$@ $BaTiO_3$ core−shell particles. Weak intensity modes positioned at 223, 298, and 411 cm^{-1} were also observed in the Raman

DOI: 10.1021/acs.jpcc.6b12461
J. Phys. Chem. C 2017, 121, 4352−4362

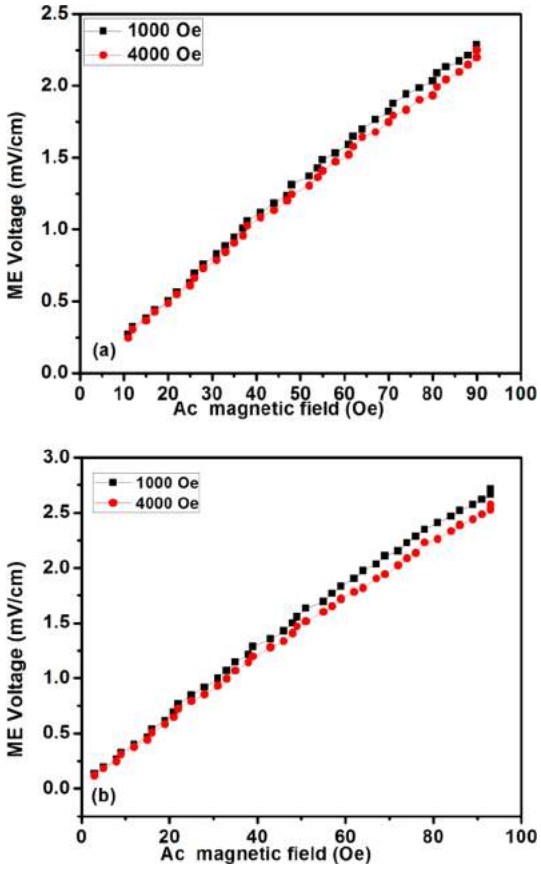

Figure 10. ME voltage vs ac magnetic field with constant dc bias magnetic field for (a) MFO@BTO1 and (b) MFO@BTO3.

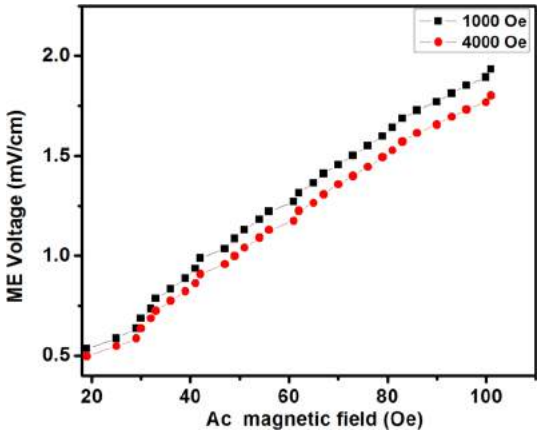

Figure 11. ME voltage vs ac magnetic field with constant dc bias magnetic field for MFO/BTO3 composite.

spectra of pure $MgFe_2O_4$ and $MgFe_2O_4$@$BaTiO_3$ core−shell particles (Figure 13a). These modes are marked with arrows in Figure 13a and represent hematite vibrations.[65] The appearance of these modes leads to the conclusion that hematite phase is present in small amounts and randomly distributed in the shell. Positions of the A_{1g} higher wavenumber mode differ slightly in the spectrum obtained from the hematite−containing surrounding (blue curve) and the hematite free surrounding (pink curve) shown in Figure 13a. This can be ascribed to the decrease in Fe^{3+} concentration in the shells due to the formation of iron oxide phase.

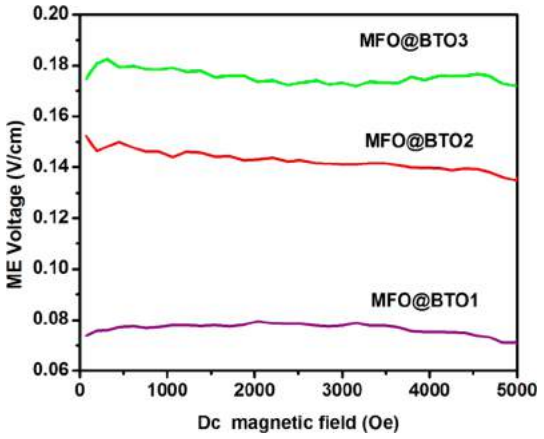

Figure 12. Variation of ME voltage as a function of dc magnetic field.

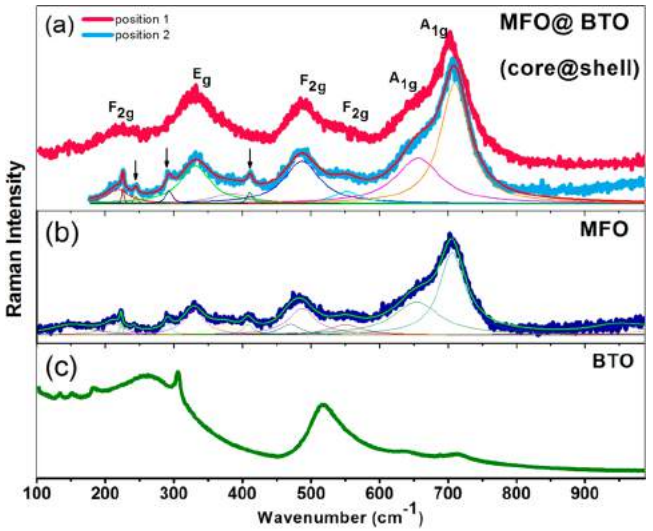

Figure 13. Raman spectra of (a) core−shell $MgFe_2O_4$@$BaTiO_3$ (MFO@BTO3) particles, (b) $MgFe_2O_4$ (MFO), and (c) $BaTiO_3$ (BTO).

Pink and blue curves from the graph (Figure 13a) represent spectra obtained from two different positions on the sample. The blue spectrum is deconvoluted with Lorentzian profile and the fit (red curve) is shown in graph a. The arrows present the modes of the hematite phase.

Raman active phonons of the $BaTiO_3$ tetragonal phase which belong to *P4 mm* crystal symmetry are $\Gamma = 3A_1+B+4E$.[66] In $BaTiO_3$ (Figure 13c), the most intense modes of tetragonal phase are positioned at 260, 305, 519, and 715 cm^{-1}. A broad peak at 264 cm^{-1} belong to the A_1 (TO) mode, whereas sharper peaks at 305, 519, and 715 cm^{-1} belong to the [B_1, E(TO + LO)], [A_1(TO), E(TO)], and [A_1(LO), E(LO)] modes.[66]

Data presented in Table 3 show that some of the vibrational modes in the spectrum of $MgFe_2O_4$,[67] positioned at 329 and 706 cm^{-1} were shifted in the spectra of core−shell particles and broadened. This is due to the influence of $BaTiO_3$ modes positioned at 260, 305, and 715 cm^{-1}. Unfortunately, the latter $BaTiO_3$ modes are broad and of low intensity which is why they could not be modeled in order to obtain meaningful results; their existence is confirmed by the broadening of $MgFe_2O_4$ modes. The narrowing of the mode at 649 cm^{-1} is probably caused by the higher crystallinity in the spots where less of

DOI: 10.1021/acs.jpcc.6b12461
J. Phys. Chem. C 2017, 121, 4352−4362

Table 3. Fit-Obtained Values of the Characteristic Peak Wavenumbers and the Widths in the Spectra of $MgFe_2O_4$ and $MgFe_2O_4/BaTiO_3$ Core−Shell Particles at Two Different Positions

$MgFe_2O_4$		$MgFe_2O_4/BaTiO_3$ position 1		$MgFe_2O_4/BaTiO_3$ position 2	
ω (cm^{-1})	fwhm (cm^{-1})	ω (cm^{-1})	fwhm (cm^{-1})	ω (cm^{-1})	fwhm (cm^{-1})
212	34	218	39	219	53
329	36	331	55	329	56
487	48	487	50	488	45
550	50	552	50	535	53
654	80	656	80	649	56
706	45	709	50	704	55

hematite is present and therefore less iron vacancies in the original lattice.

4. CONCLUSION

The 0−0 type multiferroic magnesium ferrite @ barium titanate core−shell structure, with enhanced coupling between the electric and magnetic phases was proficiently developed. The vibrational modes in the spectrum of $MgFe_2O_4$ and the shift in the spectra of core−shell particles was efficiently studied by micro Raman spectra. Raman spectroscopy indicated the encapsulation of ferrite inside the ferroelectric particles. The Raman spectrum of the core−shell particles was excitingly found to be almost identical to the spectrum of their core material, $MgFe_2O_4$. Confocal Raman mapping was used to identify the domain arrangement within the core−shell structure. Existence of strong spin−phonon coupling and mapping of ferromagnetic and ferroelectric domains within the core−shell structure was made possible through confocal Raman spectroscopy. The clear indication of strong magneto-electric coupling realized in the developed core−shell hybrid structures, which is not present in any of the parent phases (MFO or BTO) and is greater than that achieved in the multiferroic composite sample at room temperature, highlights the significance of the core−shell architecture. Remarkably, among the developed core−shell structures, enhanced coupling with a large magnetoelectric coupling coefficient value is identified in the multiferroic core−shell structure with a comparatively larger ferromagnetic core (diameter ∼20 nm) within the ferroelectric BTO shell. It is worth finding out that, the magnetoelectric coupling effects in hybrid multiferroic structures are dependent on the geometry of magnetic phase and is enhanced by enrichment of the ferromagnetic phase (increasing magnetic core sizes). The observations unearthed in this study are promising in the deeper perception of the dynamics of magnetoelectric coupling that originate between ferromagnetic and ferroelectric phases in hybrid multiferroic systems and proves helpful when employing these materials for futuristic device applications.

AUTHOR INFORMATION

Corresponding Authors

*(O.S.O.) E-mail: oluwafemi.oluwatobi@gmail.com.
*(N.K.) E-mail: nkkalarikkal@mgu.ac.in.

ORCID

Oluwatobi Samuel Oluwafemi: 0000-0001-8964-5646
Sabu Thomas: 0000-0003-4726-5746

Notes

The authors declare no competing financial interest.

ACKNOWLEDGMENTS

The authors acknowledge the DST-Sophisticated Analytical Instruments Facility (SAIF), Mahatma Gandhi University, and the financial support from the DST-Government of India for funding through Nano Mission, FIST, and PURSE programs and the UGC-Government of India through the SAP program. N.K. also acknowledges the KSCSTE-Government of Kerala for funding. B.R. acknowledges SERB- Govt. of India (ECR/2015/000536) for providing financial assistance. S.A. and Z.D.M. acknowledge the support from the project OI 171032, and S.L. from the projects OI171037 and III41011, Ministry of Education, Science and Technological Development of the Republic of Serbia.

REFERENCES

(1) Kim, T. Y.; Song, S.; Jang, H. M.; Peters, J. A.; Jeong, Y. K. Piezoelectrically Enhanced Exchange Bias in Multiferroic Hetero-structures. *J. Mater. Chem. C* **2014**, *2*, 8018−8022.
(2) Fernandes Vaz, C. A.; Staub, U. Artificial Multiferroic Heterostructures. *J. Mater. Chem. C* **2013**, *1*, 6731−6742.
(3) Jones, S. P.; Gaw, S. M.; Doig, K. I.; Prabhakaran, D.; Hétroy Wheeler, E. M.; Boothroyd, A. T.; Lloyd-Hughes, J. High-Temperature Electromagnons in the Magnetically Induced Multiferroic Cupric Oxide Driven by Intersublattice Exchange. *Nat. Commun.* **2014**, *5*, 3787.
(4) Scott, J. F. Applications of Magnetoelectrics. *J. Mater. Chem.* **2012**, *22*, 4567.
(5) Van Aken, B. B.; Rivera, J. P.; Schmid, H.; Fiebig, M. Observation of Ferrotoroidic Domains. *Nature* **2007**, *449*, 702−705.
(6) Lee, J. H.; Fang, L.; Vlahos, E.; Ke, X.; Jung, Y. W.; et al. A Strong Ferroelectric Ferromagnet Created by Means of Spin-Lattice Coupling. *Nature* **2010**, *466*, 954−958.
(7) Ramesh, R. Materials Science: Emerging Routes to Multiferroics. *Nature* **2009**, *461*, 1218−1219.
(8) Naik, V. B.; Mahendiran, R. Magnetic and Magnetoelectric Studies in Pure and Cation Doped $BiFeO_3$. *Solid State Commun.* **2009**, *149*, 754−758.
(9) Naik, V. B.; Mahendiran, R. Electrical, Magnetic, Magnetodi-electric, and Magnetoabsorption Studies in Multiferroic $GaFeO_3$. *J. Appl. Phys.* **2009**, *106* (12), 123910.
(10) Gilioli, E.; Ehm, L. High Pressure and Multiferroics Materials: A Happy Marriage. *IUCrJ* **2014**, *1*, 590−603.
(11) Trassin, M. Low Energy Consumption Spintronics Using Multiferroic Heterostructures. *J. Phys.: Condens. Matter* **2016**, *28* (3), 033001.
(12) Scott, J. F. Room-Temperature Multiferroic Magnetoelectrics. *NPG Asia Mater.* **2013**, *5*, e72.
(13) Popov, M.; Sreenivasulu, G.; Petrov, V. M.; Chavez, F. A.; Srinivasan, G. High Frequency Magneto-Dielectric Effects in Self-Assembled Ferrite-Ferroelectric Core-Shell Nanoparticles. *AIP Adv.* **2014**, *4*, 097117.
(14) Cano, A.; Kats, E. I. Electromagnon Excitations in Modulated Multiferroics. *Phys. Rev. B: Condens. Matter Mater. Phys.* **2008**, *78* (1), 012104.

DOI: 10.1021/acs.jpcc.6b12461
J. Phys. Chem. C 2017, 121, 4352−4362

(15) Morelli, A.; Johann, F.; Burns, S. R.; Douglas, A.; Gregg, J. M. Deterministic Switching in Bismuth Ferrite Nanoislands. *Nano Lett.* **2016**, *16* (8), 5228−5234.
(16) Bahoosh, S. G.; Wesselinowa, J. M.; Trimper, S. Modified Heisenberg Model for the Zig-Zag Structure in Multiferroic RMn_2O_5. *J. Appl. Phys.* **2015**, *118* (8), 084102−1.
(17) Jeong, D. S.; Thomas, R.; Katiyar, R. S.; Scott, J. F.; Kohlstedt, H.; Petraru, A.; Hwang, C. S. Emerging Memories: Resistive Switching Mechanisms and Current Status. *Rep. Prog. Phys.* **2012**, *75*, 076502.
(18) Bibes, M.; Barthélémy, A. Multiferroics: Towards a Magnetoelectric Memory. *Nat. Mater.* **2008**, *7*, 425−426.
(19) Scott, J. F. Data Storage Multiferroic memories. *Nat. Mater.* **2007**, *6*, 256.
(20) Chung, A.; Deen, J.; Lee, J. S.; Meyyappan, M. Nanoscale Memory Devices. *Nanotechnology* **2010**, *21*, 412001.
(21) Wang, J.; Fu, Z.; Liu, M.; Sun, S.; Huang, H.; Li, L.; et al. Low Magnetic Field Response Single-Phase Multiferroics under High Temperature. *Mater. Horiz.* **2015**, *2*, 232−236.
(22) Martin, L. W. Engineering Functionality in the Multiferroic $BiFeO_3$− Controlling Chemistry to Enable Advanced Applications. *Dalt. Trans.* **2010**, *39*, 10813.
(23) Rao, C. N. R.; Serrao, C. R. New Routes to Multiferroics. *J. Mater. Chem.* **2007**, *17*, 4931−4938.
(24) Wang, W.; Zhao, J.; Wang, W.; Gai, Z.; Balke, N.; Chi, M.; Lee, H. N.; Tian, W.; Zhu, L.; Cheng, X.; Keavney, D. J.; et al. Room-Temperature Multiferroic Hexagonal $LuFeO_3$ Films. *Phys. Rev. Lett.* **2013**, *110*, 237601.
(25) Chang, C. M.; Mani, B. K.; Lisenkov, S.; Ponomareva, I. Thermally Mediated Mechanism to Enhance Magnetoelectric Coupling in Multiferroics. *Phys. Rev. Lett.* **2015**, *114*, 177205.
(26) Sun, D.; Fang, M.; Xu, X.; Jiang, L.; Guo, H.; Wang, Y.; Yang, W.; Yin, L.; Snijders, P. C.; Ward, T. Z.; Gai, Z.; et al. Active Control of Magnetoresistance of Organic Spin Valves Using Ferroelectricity. *Nat. Commun.* **2014**, *5*, 1−12.
(27) Pradhan, D. K.; Puli, V. S.; Kumari, S.; Sahoo, S.; Das, P. T.; Pradhan, K.; Katiyar, R. S.; et al. Studies of Phase Transitions and Magnetoelectric Coupling in PFN-CZFO Multiferroic Composites. *J. Phys. Chem. C* **2016**, *120* (3), 1936−1944.
(28) Etier, M.; Schmitz-Antoniak, C.; Salamon, S.; Trivedi, H.; Gao, Y.; Nazrabi, A.; Landers, J.; Gautam, D.; Winterer, M.; Schmitz, D.; et al. Magnetoelectric Coupling on Multiferroic Cobalt Ferrite−Barium Titanate Ceramic Composites with Different Connectivity Schemes. *Acta Mater.* **2015**, *90*, 1−9.
(29) Tadi, R.; Kim, Y. I.; Sarkar, D.; Kim, C.; Ryu, K. S. Magnetic and Electrical Properties of Bulk $BaTiO_3$+$MgFe_2O_4$ Composite. *J. Magn. Magn. Mater.* **2011**, *323*, 564−568.
(30) Koferstein, R.; Walther, T.; Hesse, D.; Ebbinghaus, S. G. Fine-Grained $BaTiO_3$-$MgFe_2O_4$ Composites Prepared by a Pechini-Like Process. *J. Alloys Compd.* **2015**, *638*, 141−147.
(31) Tan, S. Y.; Shannigrahi, S. R.; Tan, S. H.; Tay, F. E. H. Synthesis and Characterization of Composite $MgFe_2O_4$−$BaTiO_3$ Multiferroic System. *J. Appl. Phys.* **2008**, *103*, 094105.
(32) Shi, D. W.; Javed, K.; Ali, S. S.; Chen, J. Y.; Li, P. S.; Zhao, Y. G.; Han, X. F. Exchange-Biased Hybrid Ferromagnetic−Multiferroic Core−Shell Nanostructures. *Nanoscale* **2014**, *6*, 7215.
(33) Sreenivasulu, G.; Popov, M.; Chavez, F. A.; Hamilton, S. L.; Lehto, P. R.; Srinivasan, G. Controlled Self-Assembly of Multiferroic Core-Shell Nanoparticles Exhibiting Strong Magneto-Electric Effects. *Appl. Phys. Lett.* **2014**, *104*, 052901.
(34) Srinivasan, G.; Sreenivasulu, G.; Benoit, C.; Petrov, V. M.; Chavez, F. Magnetic Field Directed Assembly of Superstructures of Ferrite-Ferroelectric Core-Shell Nanoparticles and Studies on Magneto-Electric Interactions. *J. Appl. Phys.* **2015**, *117*, 17B904.
(35) Verma, K. C.; Kotnala, R. K. Nanostructural and Lattice Contributions to Multiferroism in $NiFe_2O_4$/$BaTiO_3$. *Mater. Chem. Phys.* **2016**, *174*, 120−128.
(36) Curecheriu, L. P.; Buscaglia, M. T.; Buscaglia, V.; Mitoseriu, L.; Postolache, P.; Ianculescu, A.; Nanni, P. Functional Properties of $BaTiO_3$−$Ni_{0.5}Zn_{0.5}Fe_2O_4$ Magnetoelectric Ceramics Prepared from Powders with Core-Shell Structure. *J. Appl. Phys.* **2010**, *107*, 104106.
(37) Chaudhuri, A.; Mandal, K. Large Magnetoelectric Properties in $CoFe_2O_4$:$BaTiO_3$ Core−Shell Nanocomposites. *J. Magn. Magn. Mater.* **2015**, *377*, 441−445.
(38) Koferstein, R.; Walther, T.; Hesse, D.; Ebbinghaus, S. G. Preparation and Characterization of Nanosized Magnesium Ferrite Powders by a Starch-Gel Process and Corresponding Ceramics. *J. Mater. Sci.* **2013**, *48*, 6509−6518.
(39) Rao, C. N. R.; Sundaresan, A.; Saha, R. Multiferroic and Magnetoelectric Oxides: The Emerging Scenario. *J. Phys. Chem. Lett.* **2012**, *3*, 2237−2246.
(40) Wu, H. C.; Mauit, O.; Coileáin, C. O.; Syrlybekov, A.; et al. Magnetic and Transport Properties of Epitaxial Thin Film $MgFe_2O_4$ Grown on MgO (100) by Molecular Beam Epitaxy. *Sci. Rep.* **2014**, *4*, 7012.
(41) Frey, N. A.; Peng, S.; Cheng, K.; Sun, S. Magnetic Nanoparticles: Synthesis, Functionalization, and Applications in Bioimaging and Magnetic Energy Storage. *Chem. Soc. Rev.* **2009**, *38* (9), 2532−2542.
(42) Augustine, R.; Abraham, A. R.; Kalarikkal, N.; Thomas, S. Monitoring and Separation of Food-Borne Pathogens using Magnetic Nanoparticles. *Novel Approaches of Nanotechnology in Food* **2016**, 271−312.
(43) Smith, M. B.; Page, K.; Siegrist, T.; Redmond, P. L.; Walter, E. C.; Seshadri, R.; Brus, L. E.; Steigerwald, M. L. Crystal Structure and the Paraelectric-to-Ferroelectric Phase Transition of Nanoscale $BaTiO_3$. *J. Am. Chem. Soc.* **2008**, *130*, 6955−6963.
(44) Wang, B. Y.; Wang, H. T.; Singh, S. B.; Shao, Y. C.; Wang, Y. F.; Chuang, C. H.; Yeh, P. H.; Chiou, J. W.; Pao, C. W.; Tsai, H. M.; et al. Effect of Geometry on the Magnetic Properties of $CoFe_2O_4$−$PbTiO_3$ Multiferroic Composites. *RSC Adv.* **2013**, *3*, 7884.
(45) Stroppa, A.; Picozzi, S. Hybrid Functional Study of Proper and Improper Multiferroics. *Phys. Chem. Chem. Phys.* **2010**, *12*, 5405−16.
(46) Dela Cruz, C. R.; Yen, F.; Lorenz, B.; Park, S.; Cheong, S. W.; Gospodinov, M. M.; Ratcliff, W.; Lynn, J. W.; Chu, C. W. Evidence for Strong Spin-Lattice Coupling in Multiferroic RMn_2O_5 (R= Tb, Dy, Ho) via Thermal Expansion Anomalies. *J. Appl. Phys.* **2006**, *99*, 08R103.
(47) Gupta, M. K.; Mittal, R.; Zbiri, M.; Sharma, N.; Rols, S.; Schober, H.; Chaplot, S. L. Spin-Phonon Coupling and High-Temperature Phase Transition in Multiferroic Material $YMnO_3$. *J. Mater. Chem. C* **2015**, *3*, 11717−11728.
(48) Ramirez, M. O.; Krishnamurthi, M.; Denev, S.; Kumar, A.; Yang, S. Y.; Chu, Y. H.; Saiz, E.; Seidel, J.; Pyatakov, A. P.; Bush, A.; et al. Two-Phonon Coupling to the Antiferromagnetic Phase Transition in Multiferroic $BiFeO_3$. *Appl. Phys. Lett.* **2008**, *92*, 022511.
(49) Jaiswal, A.; Das, R.; Maity, T.; Vivekanand, K.; Adyanthaya, S.; Poddar, P. Temperature-Dependent Raman and Dielectric Spectroscopy of $BiFeO_3$ Nanoparticles: Signatures of Spin-Phonon and Magnetoelectric Coupling. *J. Phys. Chem. C* **2010**, *114*, 12432−12439.
(50) Santos, Y. P.; Andrade, B. C.; Machado, R.; Macêdo, M. A. Spin−Phonon Coupling in Multiferroic $Ba_{1.6}Sr_{1.4}Co_2$ $Fe_{24}O_{41}$. *J. Magn. Magn. Mater.* **2014**, *364*, 95−97.
(51) Sklyadneva, I. Y.; Heid, R.; Bohnen, K. P.; Echenique, P. M.; Benedek, G.; Chulkov, E. V. The Effect of Spin−Orbit Coupling on the Surface Dynamical Properties and Electron−Phonon Interaction of Tl (0001). *J. Phys. Chem. A* **2011**, *115* (25), 7352−7355.
(52) Trivedi, H.; Shvartsman, V. V.; Lupascu, D. C.; Medeiros, M. S. A.; Pullar, R. C.; Kholkin, A. L.; Shur, V. Y.; et al. Local Manifestations of a Static Magnetoelectric Effect in Nanostructured $BaTiO_3$−$BaFe_{12}$ O_9 Composite Multiferroics. *Nanoscale* **2015**, *7* (10), 4489−4496.
(53) Rubio-Marcos, F.; Del Campo, A.; Marchet, P.; Fernández, J. F. Ferroelectric Domain Wall Motion Induced by Polarized Light. *Nat. Commun.* **2015**, *6*, 6594.
(54) Ummer, R. P.; B, R.; Thevenot, C.; Rouxel, D.; Thomas, S.; Kalarikkal, N. Electric, Magnetic, Piezoelectric and Magnetoelectric Studies of Phase Pure $(BiFeO_3$−$NaNbO_3)$−(P(VDF-TrFE)) Nano-

DOI: 10.1021/acs.jpcc.6b12461
J. Phys. Chem. C 2017, 121, 4352−4362

composite Films Prepared by Spin Coating. *RSC Adv.* **2016**, *6*, 28069−28080.
(55) Muneeswaran, M.; Jegatheesan, P.; Gopiraman, M.; Kim, I. S.; Giridharan, N. V. Structural, Optical, and Multiferroic Properties of Single Phased $BiFeO_3$. *Appl. Phys. A: Mater. Sci. Process.* **2014**, *114*, 853−859.
(56) Nguyen, T. H. L.; Laffont, L.; Capsal, J. F.; Cottinet, P. J.; Lonjon, A.; Dantras, E.; Lacabanne, C. Magnetoelectric Properties of Nickel Nanowires-P(VDF−TrFE) Composites. *Mater. Chem. Phys.* **2015**, *153*, 195−201.
(57) Stephanovich, V. A.; Laguta, V. V. Transversal Spin Freezing and Re-entrant Spin Glass Phases in Chemically Disordered Fe-Containing Perovskite Multiferroics. *Phys. Chem. Chem. Phys.* **2016**, *18*, 7229−7234.
(58) Meher, K. R. S. P.; Martin, C.; Caignaert, V.; Damay, F.; Maignan, A. Multiferroics and Magnetoelectrics: A Comparison Between Some Chromites and Cobaltites. *Chem. Mater.* **2014**, *26*, 830−836.
(59) Woldu, T.; Raneesh, B.; Reddy, M. V. R.; Kalarikkal, N. Grain Size Dependent Magnetoelectric Coupling of $BaTiO_3$ Nanoparticles. *RSC Adv.* **2016**, *6*, 7886−7892.
(60) Nuraje, N.; Su, K. Perovskite Ferroelectric Nanomaterials. *Nanoscale* **2013**, *5*, 8752−80.
(61) Wang, Z.; Lazor, P.; Saxena, S. K.; O'Neill, H. St. C. High Pressure Raman Spectroscopy of Ferrite $MgFe_2O_4$. *Mater. Res. Bull.* **2002**, *37* (8), 1589−1602.
(62) Wang, Z.; Schiferl, D.; Zhao, Y.; O'Neill, H. St. C. High Pressure Raman Spectroscopy of Spinel-Type Ferrite $ZnFe_2O_4$. *J. Phys. Chem. Solids* **2003**, *64*, 2517−2523.
(63) Hosterman, B. D. *Raman Spectroscopic Study of Solid Solution Spinel Oxides*. Thesis. University of Nevada, Las Vegas: 2011.
(64) Errandonea, D.; Kumar, R. S.; Manjón, F. J.; Ursaki, V. V.; Rusu, E. V. Post-Spinel Transformations and Equation of State in $ZnGa_2O_4$: Determination at High Pressure by in situ X-ray Diffraction. *Phys. Rev. B: Condens. Matter Mater. Phys.* **2009**, *79*, 024103.
(65) De Faria, D. L. A.; Venâncio Silva, S. V.; De Oliveira, M. T. Raman Microspectroscopy of Some Iron Oxides and Oxyhydroxides. *J. Raman Spectrosc.* **1997**, *28*, 873−878.
(66) Shiratori, C.; Pithan, J.; Dornseiffer; Waser, R. Raman Scattering Studies on Nanocrystalline $BaTiO_3$ Part II—consolidated polycrystalline ceramics. *J. Raman Spectrosc.* **2007**, *38* (10), 1300−1306.
(67) Perumbilavil, S.; Sridharan, K.; Abraham, A. R.; Janardhanan, H. P.; Kalarikkal, N.; Philip, R. Nonlinear Transmittance and Optical Power Limiting in Magnesium Ferrite Nanoparticles: Effects of Laser Pulsewidth and Particle Size. *RSC Adv.* **2016**, *6*, 106754−106761.

DOI: 10.1021/acs.jpcc.6b12461
J. Phys. Chem. C 2017, 121, 4352−4362

Materials Research Bulletin 83 (2016) 217–224

Contents lists available at ScienceDirect

Materials Research Bulletin

journal homepage: www.elsevier.com/locate/matresbu

WO_3/TiO_2 composite coatings: Structural, optical and photocatalytic properties

Zorana Dohčević-Mitrović[a,*], Stevan Stojadinović[c], Luca Lozzi[d], Sonja Aškrabić[a], Milena Rosić[e], Nataša Tomić[a], Novica Paunović[a], Saša Lazović[b], Marko G. Nikolić[b], Sandro Santucci[d]

[a] Center for Solid State Physics and New Materials, Institute of Physics Belgrade, University of Belgrade, Pregrevica 118, 11080 Belgrade, Serbia
[b] Institute of Physics Belgrade, University of Belgrade, Pregrevica 118, 11080 Belgrade, Serbia
[c] Faculty of Physics, University of Belgrade, Studentski Trg 12-16, 11000 Belgrade, Serbia
[d] Department of Physical and Chemical Sciences, University of L'Aquila, Via Vetoio 67100, L'Aquila, Italy
[e] Laboratory for Material Science, Institute of Nuclear Sciences, Vinča, University of Belgrade, P.O. Box 522, 11001 Belgrade, Serbia

ARTICLE INFO

Article history:
Received 24 February 2016
Received in revised form 19 May 2016
Accepted 6 June 2016
Available online 7 June 2016

Keywords:
A. Nanostructures
A. Oxides
D. Crystal structure
B. Optical properties
D. Catalytic properties

ABSTRACT

WO_3/TiO_2 and TiO_2 coatings were prepared on titania substrates using facile and cost-effective plasma electrolytic oxidation process. The coatings were characterized by X-ray diffraction, scanning electron microscopy, Raman, UV–vis diffuse reflectance spectroscopy, and X-ray photoelectron spectroscopy. With increasing duration of PEO process, the monoclinic WO_3 phase became dominant and new monoclinic $WO_{2.96}$ phase appeared. The optical absorption edge in the WO_3/TiO_2 samples, enriched with $WO_3/WO_{2.96}$ phase, was shifted to the visible region. The photocatalytic efficiency of WO_3/TiO_2 and pure TiO_2 samples was evaluated by performing the photodegradation experiments in an aqueous solution of Rhodamine 6G and Mordant Blue 9 under the visible and UV light. The WO_3/TiO_2 catalysts are much more efficient than pure TiO_2 under visible light and slightly better under UV light. The improvement of photocatalytic activity in the visible region is attributed to better light absorption, higher adsorption affinity and increased charge separation efficiency.

1. Introduction

Among semiconductor materials, titanium dioxide (TiO_2) in anatase phase has been shown as excellent and widely used photocatalyst for the degradation of different organic contaminants, because of its physical and chemical stability, high oxidative power, high catalytic activity, long-term photostability, low cost and ease of production. Many organic compounds can be decomposed in an aqueous solution in the presence of TiO_2, illuminated by photons with energies greater than or equal to the band gap energy of titanium dioxide (3.2 eV for anatase TiO_2) [1–6]. The major drawback for TiO_2 commercial use lies in its wide band gap, and relatively high recombination rate of photoinduced electron-hole pairs. The modification of TiO_2 by doping with metals and non-metals [7–12] or by Ti^{3+} self-doping [13,14] have been extensively performed in order to improve its photocatalytic activity under the visible irradiation.

Another very promising approach is the combination of TiO_2 with metal oxides like V_2O_5, ZnS, $InVO_4$, WO_3 [15–19] or graphene [20]. Among the metal oxides, WO_3 has smaller band gap (2.8 eV) than TiO_2 and better absorbs visible light. Moreover, WO_3 has a suitable conduction band potential and acts as a trapping site for photoexcited electrons from TiO_2. The photogenerated holes from the valence band of WO_3 move towards and accumulate in the valence band of TiO_2. In such a way the efficiency of charge separation is increased, enhancing at the same time the photocatalytic acivity of TiO_2 [21]. Additionally, the formation of WO_3 monolayer on TiO_2 increases the acidity of the WO_3/TiO_2 surface enabling the adsorption of greater amount of hydroxyl groups and organic reactants on the surface [21,22]. In recent years, WO_3/TiO_2 composites were synthesized using different methods such as sol-gel, ultrasonic spray pyrolysis, ball milling, hydrothermal, sol-precipitation, and impregnation to improve photocatalytic activity of TiO_2 under the visible light [23–28]. Thin films of TiO_2/WO_3 have also been prepared by dip and spin coating [29,30] or by one-step oxidation method [31]. In most of these reports it was demonstrated that WO_3/TiO_2 composites were found to have much

* Corresponding author
E-mail address: zordoh@ipb.ac.rs (Z. Dohčević-Mitrović).

http://dx.doi.org/10.1016/j.materresbull.2016.06.011
0025-5408/

higher photocatalytic activity under the visible light than pure TiO_2 [24,26,28,31]. Therefore, the combination of these two materials can lead to increased charge carrier lifetime and improved photocatalytic activity under the visible irradiation. Among different synthesis routs, plasma electrolytic oxidation (PEO) process is very facile, cost-effective and environmentally benign process for producing of well-adhered and crystalline oxide films, but the studies on structural and photocatlytic properties of WO_3/TiO_2 films (coatings), produced by PEO process, are limited [32–34].

In this study WO_3/TiO_2 coatings were synthetized on titanium substrate by using PEO process. Structural and optical properties of the coatings were fully characterized by XRD, SEM, Raman, XPS, and diffuse reflectance spectroscopy. The aim of this work was to tailor the band gap energy of WO_3/TiO_2 coatings towards the visible spectral region, varying the time of PEO process and to explore the photocatalytic properties of the coatings. The photocatalytic efficiency of WO_3/TiO_2 coatings was tested under the visible and UV light irradiation using Rhodamine 6G and Mordant Blue 9 as model pollutants. We demonstrated that this approach provides an efficient route for the formation of cost-effective and improved visible-light-driven photocatalysts.

2. Experimental

2.1. Preparation of WO_3/TiO_2 coatings

WO_3/TiO_2 coatings were prepared on titanium substrate using plasma electrolytic oxidation (PEO) process. PEO process is an anodizing process of lightweight metals (aluminum, magnesium, zirconium, titanium, etc.) or metal alloys above the dielectric breakdown voltage, when thick, highly crystalline oxide coating with high corrosion and wear resistance, and other desirable properties are produced. During the PEO process, numerous small sized and short-lived discharges are generated continuously over the coating's surface, accompanied by gas evolution. Due to increased local temperature, plasma-chemical reactions are induced at the discharge sites modifying the structure, composition, and morphology of such oxide coatings. The oxide coatings formed by PEO process usually contain crystalline and amorphous phases with constituent species originating both from metal and electrolyte. WO_3/TiO_2 coatings were formed on the rectangular titanium samples (99.5% purity, Alfa Aesar) of dimensions 25 mm $\times$ 10 mm $\times$ 0.25 mm, which were used as working electrodes in the experiment. The working electrodes were sealed with insulation resin leaving only an area of 1.5 cm^2 as an active surface. Before starting the PEO process, titanium samples were degreased in acetone, ethanol, and distilled water, using ultrasonic cleaner and dried in a warm air stream. The anodic oxidation process was conducted in an aqueous solution of 10^{-3} M 12-tungstosilicic acid ($H_4SiW_{12}O_{40}$), at constant current density (150 mA/cm^2). During PEO process, the electrolyte circulated through the chamber–reservoir system. The temperature of the electrolyte was kept fixed at (20 $\pm$ 1) °C. Detailed description of PEO process is given in the ref. [33].

After plasma electrolytic oxidation, the samples were rinsed in distilled water to prevent additional deposition of electrolyte components during drying. The WO_3/TiO_2 samples were obtained by varying the time of PEO process from 90 s up to 300 s. The pure TiO_2 sample was obtained after 300 s of PEO process.

2.2. Characterization of WO_3/TiO_2 coatings

The crystal structure of WO_3/TiO_2 samples was analyzed by X-ray diffraction (XRD), using a Rigaku Ultima IV diffractometer in Bragg-Brentano geometry, with Ni-filtered CuKα radiation (λ = 1.54178 Å). Diffraction data were acquired over the scattering angle 2θ from 15° to 75° with a step of 0.02° and acquisition rate of 2°/min. The XRD spectra refinement was performed with the software package Powder Cell. The TCH pseudo-Voigt profile function gave the best fit to the experimental data.

Scanning electron microscope (SEM) JEOL 840A equipped with an EDS detector was used to characterize the morphology and chemical composition of formed oxide coatings.

Micro-Raman scattering measurements were performed at room temperature in a backscattering geometry, using a Jobin-Yvon T64000 triple spectrometer system and Nd:YAG laser line of 532 nm as an excitation source. The incident laser power was kept less than 10 mW in order to prevent the heating effects.

UV-vis diffuse reflectance spectra were acquired using the Specord M40 Carl Zeiss spectrometer.

X-ray photoelectron spectroscopy (XPS) was used for the surface composition analysis of WO_3/TiO_2 coatings. XPS was carried out on a VG ESCALAB II electron spectrometer with a base pressure in the analysis chamber of 10^{-8} Pa. The X-ray source was monochromatized AlKα radiation (1486.6 eV) and the instrumental resolution was 1 eV. The spectra were calibrated using the C 1 s line (284.8 eV) of the adventitious carbon and corrected by subtracting a Shirley-type background.

2.3. Photocatalytic experiments

The photocatalytic activity of WO_3/TiO_2 samples was evaluated by monitoring the decomposition of Rhodamine 6G (R6G) and Mordant Blue 9 (MB9) under the irradiation of two different light sources: fluorescent and UV lamps. The photocatalytic measurements on R6G solution (initial concentration in water: 10 mg/L) have been performed using a 36 W visible fluorescent lamp (Hyundai eagle), whose emission spectrum, compared to sunlight spectrum, is given in Ref. [9]. The cuvette (3 mL) was placed at about 5 cm from the lamp. The evolution of the rhodamine concentration was followed by measuring the variation of the intensity of main absorption peak at ~525 nm. UV–vis absorption measurements as a function of the light exposure time were performed by using USB2000 spectrometer by Ocean Optics. The solution was placed in the dark for 60 min to reach the adsorption/desorption equilibrium before visible light exposure.

The photocatalytic activity of WO_3/TiO_2 samples under UV light irradiation was evaluated using aqueous solution of MB9 as a model pollutant. Batch type experiments were performed in an open thermostated cell (at 25 °C). The cell was equipped with a water circulating jacket to maintain the solution at room temperature. A mercury lamp (125 W) was used as a light source and was placed 13 cm above the surface of the dye solution. The initial concentration of MB9 in an aqueous suspension was 50 mg/L and the working volume was 25 mL. Before the lamp was switched on, the cell was kept in dark for 60 min in order to achieve the adsorption-desorption equilibrium. At regular time intervals the aliquots were taken and the concentration of the dye was determined by UV–vis spectrophotometer (Super Scan) at λ_{max} = 516 nm. The photocatalytic experiments were conducted at the natural pH of the dyes (pH = 7 in a case of R6 G solution and at pH = 6 in a case of MB9 solution). All photocatalytic measurements were repeated at least twice to check their reproducibility.

In order to detect the formation of free hydroxyl radicals ($OH^•$) on the UV illuminated WO_3/TiO_2 surface, photoluminescence (PL) measurements were performed using terephthalic acid, which is known to react with $OH^•$ radicals and produces highly fluorescent 2-hydroxyterephthalic acid. The experiment was conducted at ambient temperature. The WO_3/TiO_2 photocatalyst (TW300) was placed in open termostated cell filled with 20 mL of the 5×10^{-4} mol L^{-1} terephthalic acid in a diluted NaOH aqueous solution with

a concentration of 2×10^{-3} mol L^{-1}. UV lamp (125 W) was used as a light source. Sampling was performed after 15, 30, 60 and 90 min. PL spectra of reaction solution, using excitation wavelength of 315 nm, were measured on a Spex Fluorolog spectrofluorometer system at wavelength of 425 nm for which the 2-hydroxytereph-thalic acid exhibits intense PL peak.

3. Results and discussion

3.1. Crystal structure and morphology

XRD patterns of the WO_3/TiO_2 samples obtained for 90 (TW90), 120 (TW120), and 300 s (TW300) of PEO process are presented in Fig. 1. The diffraction peaks which appear in TW90 sample at $2\theta = 23.3°$, 33.4°, 54.2° belong to (002), (022) and (042) planes of monoclinic WO_3 phase, which crystallizes in $P2_1/c$ (No. 14) space group. Besides these XRD peaks, the XRD pattern also shows peak at 25.3° which belongs to TiO_2 anatase crystal phase (space group $I4_1/amd$ (No. 141)) and intense peaks of elemental Ti (space group $P6_3/mmc$ (No. 194)). This indicates that Ti substrate is not completely oxidized to form TiO_2 during the PEO process. With increasing duration of PEO process, for the TW120 and TW300 samples, the XRD peaks of WO_3 phase became more intense. The spectra refinement, using Powder Cell program, showed that besides WO_3 phase a monoclinic $WO_{2.96}$ phase appeared (space group $P2/c$ (No. 13)). Furthermore, the intensities of XRD peaks which belong to TiO_2 phase and elemental Ti decreased implying that the WO_3/TiO_2 coatings were enriched with $WO_3/WO_{2.96}$ phase. According to the JCPDS database for WO_3, $WO_{2.96}$, TiO_2, and elemental Ti (JCPDS: 43-1035 (WO_3), 30-1387 ($WO_{2.96}$), 16-0934 (TiO_2) and 44-1294 (elemental Ti)) very good agreement is obtained between experimental and calculated diffraction patterns of the WO_3/TiO_2 samples. In Fig. 1 are marked main XRD peaks of WO_3 and $WO_{2.96}$ phases for clarity. The lattice parameters and the estimated volume fractions (%) of different phases for the WO_3/TiO_2 samples are given in Table 1.

In Fig. 2 are presented SEM images of WO_3/TiO_2 samples. In the TW90 sample produced with shorter PEO time, certain number of microdischarge channels together with molten regions was present because of the rapid cooling of the electrolyte. With increasing time of PEO process, when the thickness of the oxide coating was increased, the number of microdischarge channels and micropores decreased followed by increased roughness of the coating's surface.

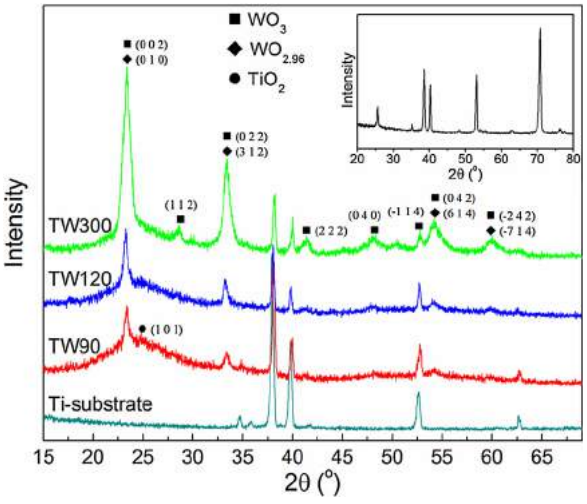

Fig. 1. XRD patterns of TW90, TW120 and TW300 samples formed in various stages of PEO process, together with the XRD spectrum of Ti-substrate. In the inset is given XRD spectrum of anatase TiO_2 obtained on Ti-substrate after 300 s of PEO process.

Table 1
Phase fraction (vol%) and cell parameters (Å) of WO_3/TiO_2 samples.

Phase	TW90	TW120	TW300
WO_3	$a = 7.4060$ $b = 7.6400$ $c = 7.6455$ 29.6%	$a = 7.3026$ $b = 7.5398$ $c = 7.6933$ 29.1%	$a = 7.4060$ $b = 7.5177$ $c = 7.5920$ 54.5%
$WO_{2.96}$	/	$a = 11.9006$ $b = 3.8258$ $c = 59.6312$ 36.70%	$a = 11.8000$ $b = 3.8098$ $c = 59.7400$ 20.90%
TiO_2	$a = 3.7778$, $c = 9.4440$, 66.0%	$a = 3.7841$, $c = 9.5105$, 32.2%	$a = 3.7790$ $c = 9.4124$ 23.8%
Ti	$a = 2.9481$ $c = 4.7325$ 4.3%	$a = 2.9594$ $c = 4.7254$ 2.0%	$a = 3.0510$ $c = 4.7820$ 0.9%

The quantitative elemental analysis confirmed the presence of Ti, O and W and the elemental composition of the samples is shown in Table 2. EDS analysis confirmed the increasing trend of W content with increasing of PEO time.

3.2. Raman and diffuse reflectance spectra

The Raman spectra of WO_3/TiO_2 samples produced for different duration of PEO process are shown in Fig. 3a. Several modes originating from two crystalline oxide phases can be identified (marked on Fig. 3a as T and W).

The Raman modes positions were determined using Lorentzian fit procedure and the deconvoluted spectra of TW90, TW120 and TW300 samples are presented in Fig. 3b. Besides the modes at about 144 cm^{-1} ($E_{g(1)}$), 197 cm^{-1} ($E_{g(2)}$), 393 cm^{-1} ($B_{1g(1)}$), 516 cm^{-1} (A_{1g}, $B_{1g(2)}$) and 638 cm^{-1} ($E_{g(3)}$) which belong to anatase phase of TiO_2 [35], several modes characteristic for monoclinic WO_3 phase are present [22,36,37]. The broad band at ~703 cm^{-1} and strong band at ~793 cm^{-1} are assigned to the stretching (O–W–O) modes of the bridging oxygen of the WO_6 octahedra. The bands observed at ~272 cm^{-1} and at ~316 cm^{-1} are assigned to the bending (O—W—O) vibrations of bridging oxygen in monoclinic m-WO_3 [22,37]. The band positioned at ~989 cm^{-1} is assigned to the dioxo $(W=O)_2$ symmetric vibration of the isolated surface WO_4 structure, whereas its weak shoulder at ~942 cm^{-1} represents asymmetric vibration of the same atomic group [22,37]. The low frequency mode at 58 cm^{-1} belongs to the to lattice modes of monoclinic WO_3 phase [38].

Further, from the Lorentzian fit procedure it was obtained that the ratio between the intensity of the peak positioned at 639 cm^{-1} and the sum of the intensities of the 703 cm^{-1} and 793 cm^{-1} peaks decreased with the increase of PEO time. This fact supports the XRD results that WO_3 content increases with prolonged duration of PEO process.

In Fig. 4 are presented the Raman spectra of TW90, TW120 and TW300 samples in the C—H and O—H region. The Raman band at around 2885 cm^{-1} originates from the overlapped CH_3 and CH_2 stretching vibrations [39]. Broad Raman peak in the 3000–3600 cm^{-1} frequency range can be assigned to the O—H stretching vibration of water molecules adsorbed on the surface of the WO_3/TiO_2 coatings [3,5].

The absorption spectra of TW90, TW120 and TW300 samples are given in Fig. 5a. With increasing content of WO_3 phase the absorption edge shifts to higher wavelengths. In the spectra of TW120 a structure around 380–400 nm can be observed, which is

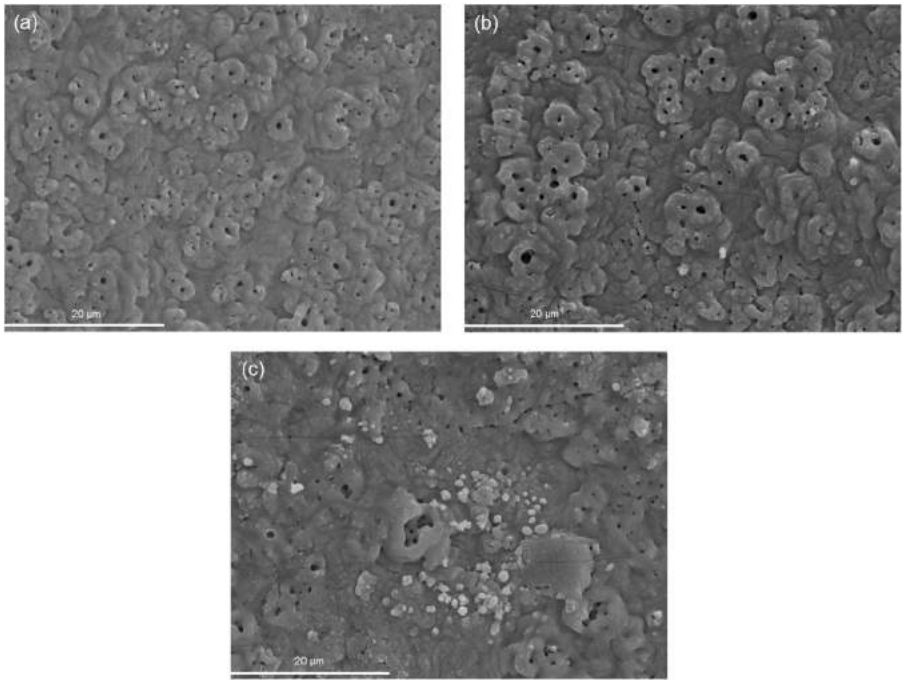

Fig. 2. SEM micrographs of WO_3/TiO_2 samples formed in various stages of PEO process: (a) TW90, (b) TW120 and (c) TW300 sample.

very pronounced in the TW300 sample. The appearance of this absorption structure can be attributed to the electronic population of WO_3 conduction band [40]. From the absorption spectra from Fig. 4a, applying the same procedure as Ghobadi in his work [41], the band gap energies for pure TiO_2 and WO_3/TiO_2 samples were estimated. In Fig. 5b are presented the Tauc plots for indirect transition, as TiO_2 and WO_3 are indirect band gap semiconductors [26]. The band gap (E_g) energies are 3.19 eV for pure TiO_2, and 2.84, 2.77 and 2.6 eV for TW90, TW120 and TW300 samples, respectively. It is obvious that with increasing WO_3 content the band gap decreases compared to pure TiO_2 and shifts to the visible spectral range. Patrocinio et al. [40] have shown that in TiO_2/WO_3 films, the WO_3 conduction band introduces new low lying electronic levels with respect to the conduction band of TiO_2, causing the lowering of the band gap energy of composite samples compared to pure TiO_2. This finding is in accordance with the band gap behavior of our WO_3/TiO_2 samples from Fig. 5b.

3.3. XPS analysis

The XPS study was further used to confirm the chemical binding states of W 4f. The W 4f XPS spectra of the TW90 and TW300 samples and the results of their decomposition into peaks are shown in Fig. 6. The W 4f spectrum of TW90 sample (Fig. 6a) can be deconvoluted into one doublet with binding energies of 35.8 (W $4f_{7/2}$) and 38.1 eV (W $4f_{5/2}$), respectively. The energy position of this doublet corresponds to the W^{6+} oxidation state [42].

In the TW300 sample (Fig. 6c) the contribution of W^{5+} states from nonstoichiometric oxide phase can be seen. The W 4f spectrum can be deconvoluted with two doublets. The first two characteristic peaks at 36 (W $4f_{7/2}$) and 38.3 eV (W $4f_{5/2}$) correspond to W^{6+} state as in the case of TW90. The binding energies of these peaks are somewhat higher than that for TW90 sample. The up-shift in binding energy can be ascribed to the presence of defects and OH-groups on the surface [43], existence of

Table 2
EDS analysis of the WO_3/TiO_2 composites.

Sample	EDS data			
	Ti (at%)	W (at%)	O (at%)	W/Ti
TW90	6.98	14.17	78.85	2.03
TW120	6.22	16.12	77.66	2.59
TW300	4.09	17.16	78.75	4.1

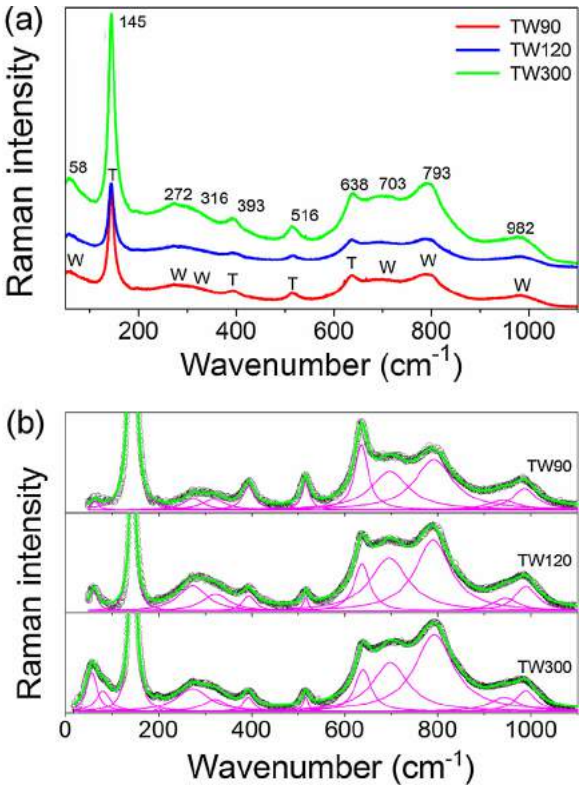

Fig. 3. Room-temperature Raman spectra of WO_3/TiO_2 samples (a). The TiO_2 and WO_3 Raman modes are marked as T and W. Deconvoluted Raman spectra of TW90, TW120 and TW300 samples (b).

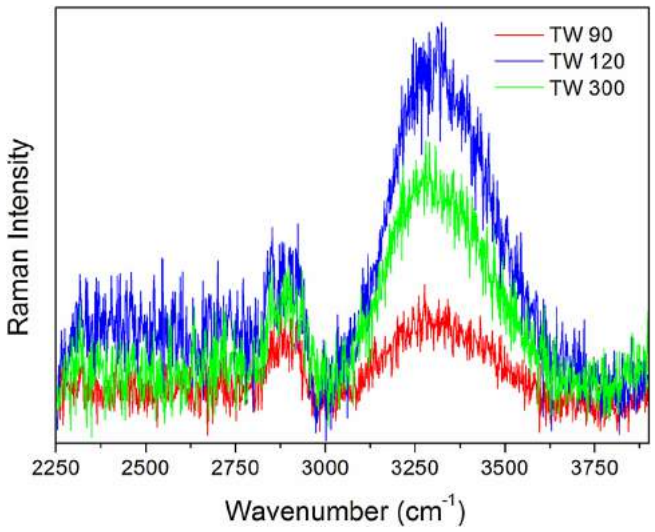

Fig. 4. Raman spectra of WO_3/TiO_2 samples in the C–H and O–H spectral region.

which is confirmed by Raman analysis (Fig. 4). The binding energies of the second doublet at 34.5 (W $4f_{7/2}$) and 36.5 eV (W $4f_{5/2}$) correspond to W^{5+} state [42]. These results are in accordance with XRD analysis.

The O 1s spectra of TW90 and TW300 samples (Fig. 6b, d) are decomposed into three peaks. The major peak at binding energy of 531.2 eV can be assigned to the oxygen atoms in WO_3 and to the OH-groups present on the surface [32,44]. The second peak observed at 530.6 eV has been attributed to oxygen bound to Ti [26], whereas the binding energy of the third peak at 533.1 eV corresponds to the oxygen in water molecules bound in the coating's structure or adsorbed on its surface [45]. The relative intensity of the XPS peaks at 531.2 eV and 533.1 eV was increased in the TW300 sample. The intensity increase of these peaks can be related to the presence of sub-stoichiometric WO_{3-x} phase ($WO_{2.96}$). Similar behavior was reported in the paper of Shpak et al. [44] in which these peaks were more intense in WO_{3-x} oxides than in stoichiometric WO_3. This finding is also supported by the Raman spectrum of TW300 sample (Fig. 4), for which the intensity of the Raman mode, corresponding to the water molecules adsorbed on the surface, is higher than in TW90 sample.

3.4. Photocatalytic performances of WO_3/TiO_2 coatings

Fig. 7a shows the kinetics of degradation of R6G for pure TiO_2 and WO_3/TiO_2 samples under the visible light. No detectable degradation of R6G was registered without the presence of WO_3/TiO_2 samples (black circles on Fig. 7a). As can be seen from Fig. 7a, both TiO_2 and WO_3/TiO_2 coatings adsorbed the dye in the equilibrium period of 60 min before the exposure to visible light. It is known from the literature that the zero point charge (pH_{zpc}) of TiO_2 lies between 6 and 6.8 [46–48], whereas the isoelectric point of WO_3 is even lower and lies in the range 1.5–2.5 [49]. At higher pH values than these WO_3 and TiO_2 surfaces should be negatively charged. Therefore, the adsorption of the R6G as cationic dye at pH = 7, points out that the surfaces of WO_3/TiO_2 and TiO_2 coatings are negative and attract the positively charged R6G. The dye adsorption ability can be crucial for the high catalytic activity of the catalyst, because it can enhance the electron/hole transfer efficiency and contact with photogenerated active species.

When TiO_2 and WO_3/TiO_2 samples were subjected to visible radiation, composite coatings have shown much better photo-efficiency and demonstrated to be far superior than pure TiO_2. The highest activity was observed for the TW90 and TW120 samples for which the photodegradation of R6G reached almost 80% after 60 min. With further increase of WO_3 content, the photocatalytic efficiency slightly decreased, but is still much higher than for pure TiO_2.

Further, the photocatalytic activity of WO_3/TiO_2 coatings for degradation of MB9 was tested under the UV light. In Fig. 7b is presented the photodegradation of MB9 in the presence of WO_3/TiO_2 samples. In the dark, WO_3/TiO_2 coatings showed no adsorption of MB9. The absence of adsorption can be explained by highly anionic character of MB9 and electrostatic repulsion between the dye and negatively charged surface of WO_3/TiO_2 coatings.

The photocatalytic activity of WO_3/TiO_2 samples was improved with increased content of WO_3 phase, and the TW300 sample exhibited better activity than pure TiO_2. As can be seen from Fig. 7b, after 240 min more than 80% of dye was degraded in the presence of WO_3/TiO_2 coatings.

Photocatalytic degradation of both dyes can be well described by first-order kinetic equation, $ln(C/C_o) = kt$, where C_o is the initial dye concentration and C is the dye concentration at time t. The first order kinetic constant k is obtained from the slope of the $ln(C/C_o)$ versus t for both dyes. In Table 3 are given the first order rate constants for R6G and MB9 (k_{R6G}, k_{MB9}), together with the corresponding linear correlation coefficient (R^2). In a case of R6 G degradation under the visible light, the highest k value (k_{R6G}) was obtained for the TW90 sample. In a case of MB9 degradation under UV light, value of k_{MB9} increased with increasing amount of WO_3.

The degradation rate constant k of WO_3/TiO_2 coatings under visible light is almost five times higher than that of TiO_2, whereas its value under UV light are comparable with TiO_2, suggesting that

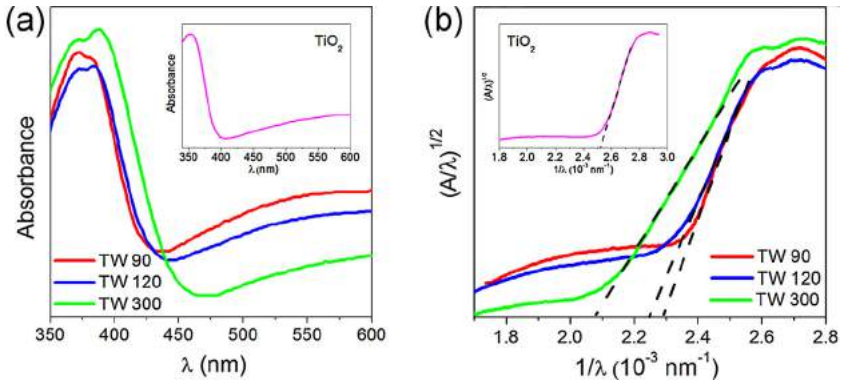

Fig. 5. Absorbance spectra (a) and Tauc plots for indirect band gap for WO_3/TiO_2 samples (b). In the inset is given Tauc plot for indirect band gap for pure TiO_2.

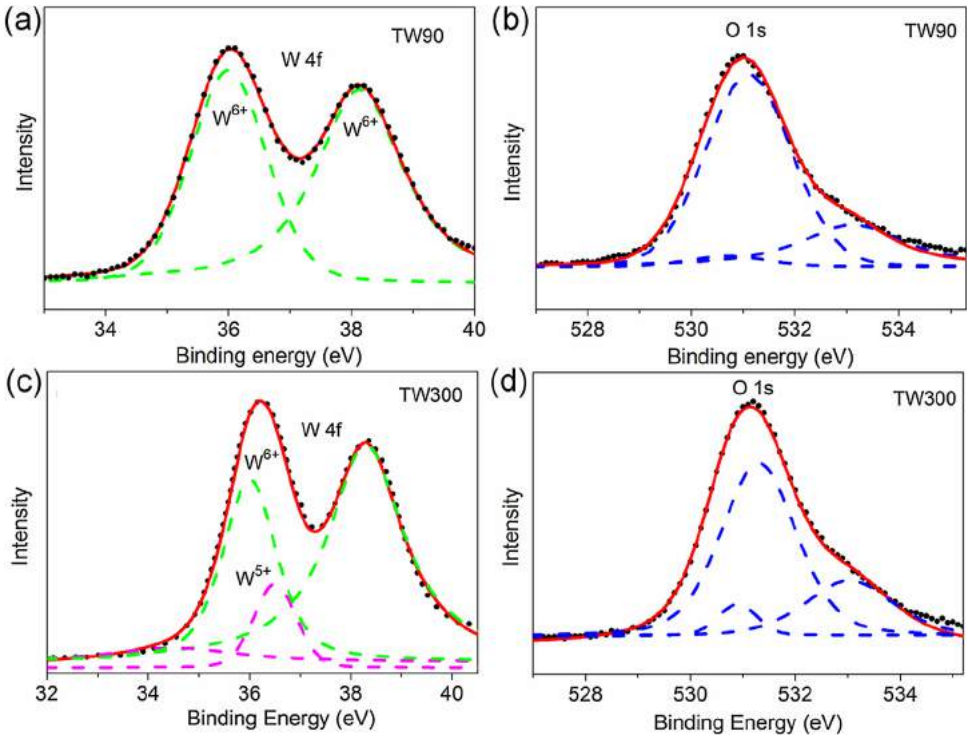

Fig. 6. XPS spectra of W 4f and O 1s regions for TW90 and TW300 samples.

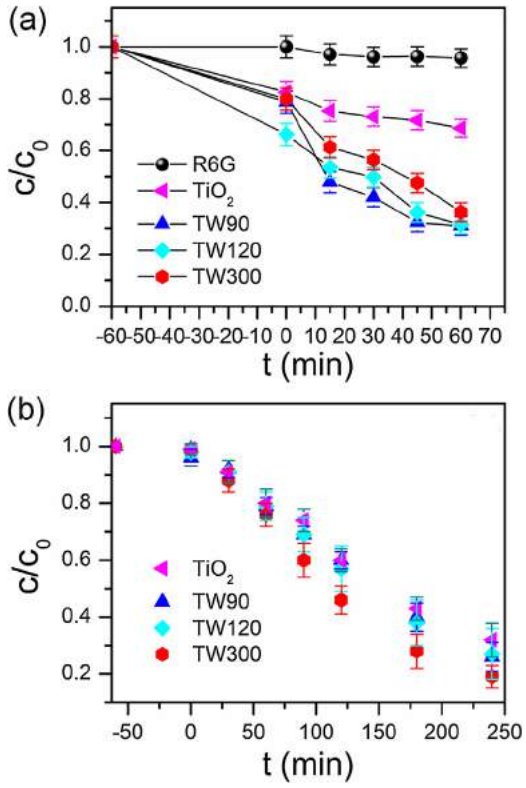

Fig. 7. Photocatalytic degradation of R6G under visible light (a) and MB9 under UV light (b) in the presence of WO_3/TiO_2 and TiO_2 coatings.

composite coatings are very efficient photocatalysts under visible light.

3.5. Hydroxyl radical analysis

The formation of free hydroxyl radicals ($OH^•$) was tested on the surface of TW300 photocatalyst under UV irradiation and detected by PL method. Applying similar procedure as described in the paper of Su et al. [50], TW300 sample was placed in terephthalic acid solution and illuminated by UV light. PL spectra of the reaction solution were measured at room temperature after 15, 30, 60 and 90 min, and these spectra are presented in Fig. 8. The terephthalic acid reacts with $OH^•$ producing 2-hydroxyterephthalic acid, which exhibits PL peak at 425 nm [51]. The intensity of this peak is proportional to the amount of $OH^•$ produced in water [50,51]. As can be seen from Fig. 8, gradual increase of PL intensity at 425 nm with prolonged illumination time points at increasing amount of $OH^•$ radicals produced at the surface of TW300 sample.

3.6. Mechanism of the reaction

The photocatalytic degradation of R6G or MB9 is initiated by the photoexcitation of the WO_3/TiO_2 coatings when the electron-hole pairs are formed on the catalyst's surface. According to the

Table 3
The pseudo-first rate constants for R6G and MB9 together with R^2.

Sample	$k_{R6G} \times 10^{-2}$ (min^{-1})	R^2	$k_{MB9} \times 10^{-2}$ (min^{-1})	R^2
TW90	1.52	0.975	0.44	0.990
TW120	1.24	0.957	0.47	0.982
TW300	1.20	0.963	0.65	0.966
TiO_2	0.28	0.888	0.41	0.963

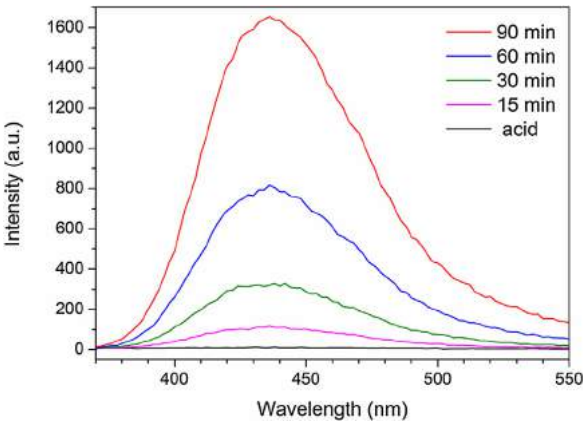

Fig. 8. PL spectral changes observed during UV illumination of TW300 sample in the solution of terephthalic acid after 15, 30, 60 and 90 min. The PL spectra of pure terephthalic acid is also presented.

generally accepted photoexcitation mechanism, electrons from the conduction band of TiO_2 can easily diffuse into the conduction band of WO_3 [40,52]. Since W(VI) can be easily reduced to W(V), WO_3 acts as an acceptor of conduction band electrons from TiO_2, whereas the photogenerated holes migrate in the opposite direction, i.e. from the lower-lying valence WO_3 band to the valence band of TiO_2. In such a way the charge separation efficiency can be increased.

In Fig. 9 is given an illustration of photo-induced electron-hole separation and reacting radicals formation. The presence of holes in the dye solution permits a direct oxidation of the dye, due to high oxidative potential of the holes (h^+):

$$h^+ + \text{dye} \rightarrow \text{dye}^{\bullet+} \rightarrow \text{oxidation of the dye} \quad (1)$$

Further, hydroxyl radicals ($OH^\bullet$) are usually formed by the reaction between the holes and OH^- or water molecules present on the surface of the catalyst. The $OH^\bullet$ radicals attack the dye in aqueous solution leading to its degradation:

$$OH^\bullet + \text{dye} \rightarrow \text{photodegradation of the dye} \quad (2)$$

The photo-induced electrons can also react with dissolved oxygen to form superoxide ions ($O_2^{-\bullet}$) which in contact with H_2O molecules form OH^- ions and finally $OH^\bullet$ radicals.

It is known from the literature that WO_3 is almost 15 times more acidic than TiO_2 [21,22,31], so it is expected that the surface of PEO produced WO_3/TiO_2 coatings is more acidic than that of TiO_2, and has a higher affinity for chemical species having unpaired electrons. Because of higher acidity, the surface of WO_3/TiO_2 coatings can absorb more H_2O and OH^- generating more $OH^\bullet$ radicals. The XPS and Raman spectra of WO_3/TiO_2 composite coatings gave an evidence that adsorbed H_2O and hydroxyls are present on the surface of WO_3/TiO_2 coatings, existence of which is important for the formation of $OH^\bullet$ radicals. PL measurements, performed on TW300 sample, (Fig. 8) clearly demonstrated that with increasing illumination time the increasing amount of $OH^\bullet$ radicals is formed on the surface of photocatalysts, which manifests through higher photocatalytic activity of TW300 sample.

The absorption measurements have shown that the band gap energy of TiO_2 is higher than that of WO_3/TiO_2 coatings. Namely, with prolonged time of PEO process, the WO_3 content increases followed by an appearance of $WO_{2.96}$ phase. As the conduction band of nonstoichiometric WO_{3-x} oxides is lower with respect to WO_3 and TiO_2 (Fig. 9) [53], the presence of $WO_{2.96}$ phase will further reduce the band gap of WO_3/TiO_2 samples towards the visible spectral range, as already noticed from the Tauc plots from Fig. 5. As a result, the electron-hole recombination will be more difficult and more reactive radicals can be produced at the WO_3/TiO_2 surface. Therefore, WO_3/TiO_2 coatings should be more efficient as catalysts under the visible light. The photocatalytic degradation of R6G and kinetics of the reaction confirmed that WO_3/TiO_2 coatings are efficient photocatalysts in the visible region. Slight decrease of photocatalytic activity of TW300 sample in a case of R6G photodegaradation (Fig. 7a) can be explained by the occurrence of photochromism [27,40]. Namely, the electron accumulation at the WO_3 conduction band can be more pronounced with increased WO_3 content. The accumulated electrons can react with $OH^\bullet$ radicals forming OH^- ions or can reduce the number of superoxide radicals [27,40] degrading at some extent the photocatalytic activity of WO_3/TiO_2 coatings. The presence of pronounced absorption feature around 380–400 nm in the absorbance spectrum of TW300 sample confirms this assumption. Another reason can be found in the formation of small polarons, appearance of which is characteristic for WO_3 and WO_{3-x} phases. The photoexcited electron-hole pairs can be rapidly quenched by recombination of photoexcited holes with electrons from localized polaron states, whereas photoexcited electrons

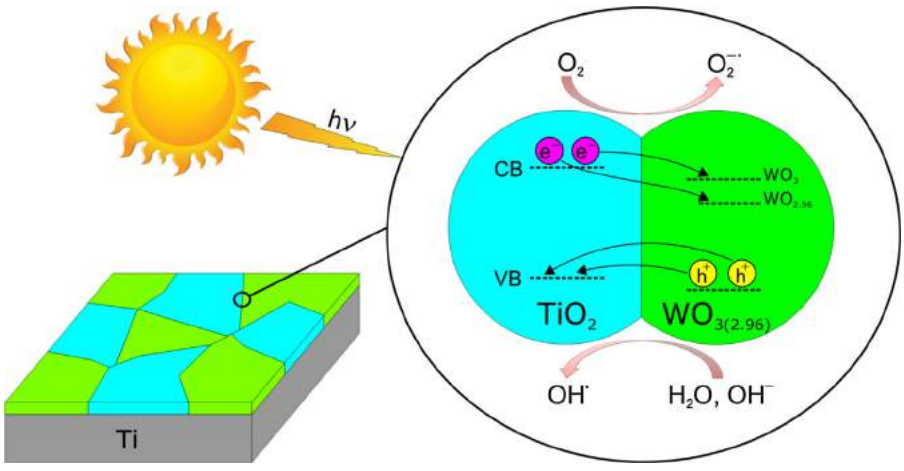

Fig. 9. Schematic diagram of electron-hole pairs separation and proposed mechanism of photodegradation over WO_3/TiO_2 photocatalysts.

populate polaron states [54], reducing on the other side the photocatalytic efficiency of the catalyst.

4. Conclusion

WO_3/TiO_2 composite and pure TiO_2 coatings have been prepared on titania substrates using facile and cost-effective PEO process. The structural, morphological, optical properties and chemical composition of these samples were investigated by different methods such as XRD, SEM, Raman, UV–vis diffuse reflectance spectroscopy and XPS. XRD and Raman analysis revealed that the coatings are mainly composed of monoclinic WO_3 and anatase TiO_2. With increasing duration of PEO process the crystallinity of the samples was improved, the WO_3 phase become dominant and a certain amount of monoclinic $WO_{2.96}$ phase appeared. XPS analysis confirmed the XRD results and revealed the presence of OH-groups and adsorbed H_2O on the surface of WO_3/TiO_2 coatings. The increasing amount of $WO_3/WO_{2.96}$ phase caused a decrease of optical band gap, i.e. shift from near UV to visible spectral region. The photocatalytic activity of WO_3/TiO_2 samples has been measured by monitoring photodecolouration of two model pollutants in aqueous solution, R6G under visible and MB9 under UV light irradiation. The WO_3/TiO_2 samples have shown enhanced photocatalytic activity compared to pure TiO_2 under the visible light irradiation. Slight decrease of photocatalytic activity under the visible light in the sample enriched with $WO_3/WO_{2.9}$ phase can be ascribed to the occurrence of photochromism and/or small polaron formation. Under the UV light, the WO_3/TiO_2 photocatalysts have shown slightly better photocatalytic activity than pure TiO_2. PL mesurements demonstrated the correlation between photoactivity and the formation rate of $OH^{\bullet}$ radicals under UV light irradiation, i.e. higher amount of $OH^{\bullet}$ radicals formed, the better photoactivity of WO_3/TiO_2 photocatalysts was achieved. The kinetics of the reaction in the case of both azo dyes followed the pseudo-first order. The degradation rate constant k of WO_3/TiO_2 coatings under the visible light is almost five times higher than that of TiO_2. Much better photocatalytic activity of the WO_3/TiO_2 samples compared to pure TiO_2 in the visible range can be attributed to better light absorption, higher adsorption affinity and increased charge separation efficiency with increasing content of $WO_3/WO_{2.96}$ phase.

Acknowledgements

This work was financially supported by the Ministry of Education, Science and Technological Development of the Republic of Serbia under the projects OI171032, III45018 and bilateral project Serbia-Italy No. RS13MO11.

References

[1] L. Ren, Y. Li, J. Hou, X. Zhao, C. Pan, ACS Appl. Mater. Interfaces 6 (2014) 1608–1615.
[2] F. Ruggieri, A.A. D'Archivio, M. Fanellia, S. Santucci, RSC Adv. 1 (2011) 611–618.
[3] M. Šćepanović, B. Abramović, A. Golubović, S. Kler, M. Grujić-Brojčin, Z. Dohčević-Mitrović, B. Babić, B. Matović, Z.V. Popović, J. Sol-Gel Sci. Technol. 61 (2012) 390–402.
[4] A. Golubović, B. Abramović, M. Šćepanović, M. Grujić-Brojčin, S. Armaković, I. Veljković, B. Babić, Z. Dohčević-Mitrović, Z.V. Popović, Mater. Res. Bull. 48 (2013) 1363–1371.
[5] S. Watson, D. Beydoun, J. Scott, R. Amal, J. Nanoparticle Res. 6 (2004) 193–207.
[6] A.N. Banerjee, Nanotechnol. Sci. Appl. 4 (2011) 35–65.
[7] M. Xing, D. Qi, J. Zhang, F. Chen, Chem. Eur. J. 17 (2011) 11432–11436.
[8] Y. Niu, M. Xing, J. Zhang, B. Tian, Catal. Today 201 (2013) 159–166.
[9] F. Ruggieri, D. Di Camillo, L. Maccarone, S. Santucci, L. Lozzi, J. Nanopart. Res. 15 (2013) 1–11.
[10] W. M. Xing, Y. Li, J. Wu, X. Gong Zhang, J. Phys. Chem. C 115 (2011) 7858–7865.
[11] M. Janus, B. Tryba, E. Kusiak, T. Tsumura, M. Toyoda, M. Inagaki, A.W. Morawski, Catal. Lett. 128 (2009) 36–39.
[12] M. Takeuchi, M. Matsuoka, M. Anpo, Res. Chem. Intermed. 38 (2012) 1261–1277.
[13] X. Chen, L. Liu, P.Y. Yu, S.S. Mao, Science 331 (2011) 746–750.
[14] W. Fang, M. Xing, J. Zhang, Appl. Catal. B: Environ. 160–161 (2014) 240–246.
[15] Y. Wang, J. Zhang, L. Liu, C. Zhu, X. Liu, Q. Su, Mater. Lett. 75 (2012) 95–98.
[16] Y. Xiaodan, W. Qingyin, J. Shicheng, G. Yihang, Mater. Charact. 57 (2006) 333–341.
[17] J. Rashid, M.A. Barakat, S.L. Pettit, J.N. Kuhn, Environ. Technol. 35 (2014) 2153–2159.
[18] B. Gao, Y. Ma, Y. Cao, W. Yang, J. Yao, J. Phys. Chem. B 110 (2006) 14391–14397.
[19] X. Luo, F. Liu, X. Li, H. Gao, G. Liu, Mat. Sci. Semicon. Proc. 16 (2013) 1613–1618.
[20] N.R. Khalid, E. Ahmed, Z. Hong, M. Ahmad, Y. Zhang, S. Khalid, Ceram. Int. 39 (2013) 7107–7113.
[21] Y. Li, P.C. Hsu, S.M. Chen, Sensor. Actuat. B-Chem. 174 (2012) 427–435.
[22] K.K. Akurati, A. Vital, J.P. Dellemann, K. Michalowa, T. Graule, D. Ferri, A. Baiker, Appl. Catal. B: Environ. 79 (2008) 53–62.
[23] D. Ke, H. Liu, T. Peng, X. Liu, K. Dai, Mater. Lett. 62 (2008) 447–450.
[24] H. Song, H. Jiang, X. Liu, G. Meng, J. Photoch. Photobio. A 181 (2006) 421–428.
[25] C. Shifu, C. Lei, G. Shen, C. Gengyu, Powder Technol. 160 (2005) 198–202.
[26] F. Riboni, L.G. Bettini, D.W. Bahnemann, E. Selli, Catal. Today 209 (2013) 28–34.
[27] J. Yang, X. Zhang, H. Liu, C. Wang, S. Liu, P. Sun, L. Wang, Y. Liu Catal, Today 201 (2013) 195–202.
[28] S. Bai, H. Liu, J. Sun, Y. Tian, S. Chen, J. Song, R. Luo, D. Li, A. Chen, C.-C. Liu, Appl. Surf. Sci. 338 (2015) 61–68.
[29] A. Rampaul, I.P. Parkin, S.A. O'Neill, J. DeSouza, A. Mills, N. Elliott, Polyhedron 22 (2003) 35–44.
[30] J.H. Pan, W. In Lee, Chem. Mater. 18 (2006) 847–853.
[31] M. Long, B. Tan, P. Hu, B. Zhou, Y. Zhou, J. Mater. Chem. A 3 (2015) 10195–10198.
[32] J. He, Q. Luo, Q.Z. Cai, X.W. Li, D.Q. Zhang, Mater. Chem. Phys. 129 (2011) 242–248.
[33] S. Stojadinović, N. Radić, R. Vasilić, M. Petković, P. Stefanov, Lj. Zeković, B. Grbić, Appl. Catal. B: Environ. 126 (2012) 334–341.
[34] S. Petrović, S. Stojadinović, Lj. Rožić, N. Radić, B. Grbić, R. Vasilić, Surf. Coat. Technol. 269 (2015) 250–257.
[35] T. Ohsaka, F. Izumi, Y. Fujiki, J. Raman Spectrosc. 7 (1978) 321–324.
[36] Y. Djaoued, S. Balaji, N. Beaudoin, J. Sol-Gel Sci. Technol. 65 (2013) 374–383.
[37] C. Santato, M. Odziemkowski, M. Ulmann, Jan Augustynski, J. Am. Chem. Soc. 123 (2001) 10639–10649.
[38] E. Cazzanelli, C. Vinegoni, G. Mariotto, A.J. Purans, Solid State Ionics 123 (1999) 67–74.
[39] Y. Yu, K. Lin, X. Zhou, H. Wang, S. Liu, X. Ma, J. Phys. Chem. C 111 (2007) 8971–8978.
[40] A.O.T. Patrocinio, L.F. Paula, R.M. Paniago, J. Freitag, D.W. Bahnemann, ACS Appl. Mater. Interfaces 6 (2014) 16859–16866.
[41] N. Ghobadi, Int. Nano Let. 3 (2013) 1–4.
[42] K. Senthil, K. Yong, Nanotechnology 18 (2007) 395604 (1–7).
[43] H. Ling, J. Lu, S. Phua, H. Liu, L. Liu, Y. Huang, D. Mandler, P.S. Lee, X. Lu, J. Mater. Chem. A 2 (2014) 2708–2717.
[44] A.P. Shpak, A.M. Korduban, V.O. Medvedskij, J. Electron. Spectrosc. Relat. Phenom. 156–158 (2007) 172–175.
[45] H.Y. Wong, C.W. Ong, R.W.M. Kwok, K.W. Wong, S.P. Wong, W.Y. Cheung, Thin Solid Films 376 (2000) 131–139.
[46] A.A. Khodja, A. Boulkamh, C. Richard, Appl. Catal. B: Environ. 59 (2005) 147–154.
[47] C.C. Wang, J.Y. Ying, Chem. Mater. 11 (1999) 3113–3120.
[48] M.D. Hernández-Alonso, F. Fresno, S. Suarez, J.M. Coronado, Energy Environ. Sci. 2 (2009) 1231–1257.
[49] M. Anik, T. Cansizoglu, J. Appl. Electrochem. 36 (2006) 603–608.
[50] T.M. Su, Z.L. Liu, Y. Liang, Z.Z. Qin, J. Liu, Y.Q. Huang, Catal. Comm. 18 (2012) 93–97.
[51] K. Ishibashi, A. Fujishima, T. Watanabe, K. Hashimoto, Electrochem. Commun. 2 (2000) 207–210.
[52] H. Park, A. Bak, T.H. Jeon, S. Kim, W. Choi, Appl. Catal. B: Environ. 115–116 (2012) 74–80.
[53] A.K.L. Sajjad, S. Shamaila, B. Tian, F. Chen, J. Zhang, Appl. Catal. B: Environ. 91 (2009) 397–405.
[54] M.B. Johansson, G.A. Niklasson, L. Österlund, J. Mater. Res. 27 (2012) 3130–3140.

Available online at www.sciencedirect.com

ScienceDirect

Ceramics International 41 (2015) 6970–6977

CERAMICS INTERNATIONAL

www.elsevier.com/locate/ceramint

Structural dependent room-temperature ferromagnetism in yttrium doped HfO_2 nanoparticles

Z. D. Dohčević-Mitrović[a,*], N. Paunović[a], B. Matović[b], P. Osiceanu[c], R. Scurtu[c,d], S. Aškrabić[a], M. Radović[a]

[a]Institute of Physics, University of Belgrade, Pregrevica 118, 11080 Belgrade, Serbia
[b]Institute of Nuclear Sciences 'Vinča', University of Belgrade, 11000, Serbia
[c]Institute of physical chemistry, Romanian academy, Bucharest 060021, Romania
[d]National Institute for Research and Development in Microtechnologies, Bucharest 060021, Romania

Received 18 September 2014; received in revised form 30 January 2015; accepted 2 February 2015
Available online 7 February 2015

Abstract

Y-doped HfO_2 nanopowders, produced by metathesis synthesis, exhibit ferromagnetism at room temperature. The X-ray diffraction and Raman measurements have shown that HfO_2 nanopowders undergo phase transformation from monoclinic to tetragonal and cubic phase with increasing of Y content. The X-ray photoelectron spectroscopy and Raman analysis gave evidence that Y-doped HfO_2 nanopowders are oxygen deficient. The ferromagnetic properties of Y-doped HfO_2 nanocrystals are dependent on crystal structure changes. The structural transformation from monoclinic to tetragonal phase with Y doping is followed by increased ferromagnetic ordering because of the increased concentration of oxygen vacancies (V_O) in different charge states. Higher Y content favors the formation of cubic phase and the ferromagnetism significantly weakens. In cubic hafnia phase, yttrium can form (V_O–Y_{Hf}) defect complexes in different charge states. The appearance of these complexes can be responsible for the degradation of ferromagnetic ordering.

Keywords: A. Powders: chemical preparation; X-ray method and spectroscopy; Optical and magnetic properties; HfO_2

1. Introduction

Hafnia (HfO_2) is very promising and technologically important material because of potential applications in spintronic devices, high-temperature fuel cells and has attracted much attention as high-*k* dielectric gate material to replace the SiO_2 in metal-oxide-semiconductor devices. HfO_2 has three polymorphs, i.e. monoclinic (M), tetragonal (T) and cubic (C) phase. Under ambient conditions the monoclinic phase of hafnia is stable phase and undergoes transition to tetragonal or cubic phase at high temperature [1]. These last two phases are far more important in technological applications than the low-temperature monoclinic phase. Stabilization of the tetragonal and cubic hafnia phases at room temperature can be achieved by doping with divalent or trivalent cation dopants such as Mg^{2+} or Y^{3+} which brings additional oxygen vacancies in the lattice and stabilize one of two high-temperature phases of hafnia [2,3].

HfO_2 is an insulating oxide and is expected to be nonmagnetic because Hf^{4+} and O^{2-} are not magnetic ions with full or empty f and d shells of Hf^{4+} ion. The discovery of unexpected room-temperature ferromagnetism (RTFM) in undoped monoclinic HfO_2 thin films [4] has opened a path to a new class of ferromagnetic materials which can play important role in new generation of spintronic devices. The magnetic ordering was up to now presumably investigated in monoclinic hafnia thin films and possible mechanism for the observed magnetism is still controversial. Different types of defects like oxygen (V_O) or hafnia vacancies (V_{Hf}) were claimed responsible for the FM in hafnia. The FM ordering in M-phase of HfO_2, proposed by Coey and coworkers [5], can arise from unpaired electrons in bonding molecular orbitals formed by hybridization of hafnium orbitals

*Corresponding author. Tel.: +381 11 3713024; fax: +381 11 3162190.
E-mail address: zordoh@ipb.ac.rs (Z.D. Dohčević-Mitrović).

http://dx.doi.org/10.1016/j.ceramint.2015.02.002
0272-8842/

surrounding a neutral three-coordinated oxygen vacancy. Direct exchange between defect-related molecular orbitals will be ferromagnetic and may be strong if defects are situated in the interface layer [5]. Recent calculations of Glinchuk et al. [6], based on the direct variational method, showed that neutral oxygen vacancies in the vicinity of the film–substrate interface can become magnetic and mediate long range FM order in HfO_2 thin films. Furthermore, theoretical calculations of Muñoz Ramo et al. [7], based on DFT periodic and embedded cluster methods, showed that in monoclinic HfO_2 four-coordinated oxygen vacancies can exist in five different charge states (V^{2+}, V^{+}, V^{0}, V^{-}, and V^{2-}). These defects form localized levels in the hafnia band gap. Some of these states have different electron occupancies and bear different magnetic moments [7]. Contrary to these findings, the first principle calculations [8,9] showed that hafnium vacancies, as cation vacancies, can be responsible for the ferromagnetism in monoclinic HfO_2. The removal of neutral Hf atoms introduces holes in the valence band formed of oxygen 2p levels. This leads to the splitting of the valence band and formation of high-spin defect states, causing the FM order for short V_{Hf}–V_{Hf} distances. On the other hand, the first-principles calculations of Zheng at al. [10], performed on undoped monoclinic HfO_2, showed that there are no stable defects that can carry a magnetic moment and confirmed that it is unlikely that hafnia vacancies are formed since their formation energy is high. From the above cited reports, it can be summarized that the appearance of ferromagnetism in hafnium oxide and its origin, still remains a matter of debate and deserves further investigation.

In the present work, we report room temperature ferromagnetism in Y-doped HfO_2 nanopowders. The ferromagnetic ordering is dependent on the crystal structure changes induced by Y. To the best of our knowledge, magnetic properties of hafnia nanopowders doped with yttrium have not been studied yet. HfO_2-based oxides, as high-*k* metal-oxide dielectrics, are already under consideration to replace silicon dioxide as gate dielectric for next generation of complementary metal-oxide semiconductors. The combination of ferromagnetic response at room temperature and above with dielectric properties of HfO_2-based oxides should enable the integration of metal-oxide semiconductors with spintronics technology. Therefore, Y-doped HfO_2 can be a promising candidate for the applications in spintronics.

2. Experiment

A highly pure, nanosized yttrium doped HfO_2 powders ($Hf_{1-x}Y_xO_{2-\delta}$, $0.05 \le x \le 0.2$) are obtained by metathesis synthesis described in detail elsewhere [11]. Starting chemicals were hafnium chloride ($HfCl_4$), yttrium nitrate hexahydrate ($Y(NO_3)_3 \cdot 6H_2O$) and sodium hydroxide (NaOH) from Alfa Aesar GmbH, Germany. The purity of starting chemicals was 99.9% without any magnetic ion impurity presence (such as Fe, Co etc.). The samples were always handled with Teflon tweezers to avoid any metal contamination. The compositions of the starting reacting mixtures were calculated according to the nominal composition of the final reaction product. Yttrium doped hafnia solid solutions were prepared varying weight fraction of yttrium (Y) in the range 5–20 mol%. All samples were annealed at 600 °C for 5 min in order to obtain better crystallinity. The obtained $Hf_{1-x}Y_xO_{2-\delta}$ nanopowders were characterized using different methods.

The X-ray diffraction (XRD) spectra of the samples have been measured on a Simens X-ray Diffractometer (Kristaloflex 500) with Ni filtered CuKα radiation. The room temperature measurements were performed in the 2θ range from 20° to 80° in a continuous scan mode with a step width of 0.02° and at a 2θ scanning rate of 1°/min.

Non-contact atomic force microscopy (NC-AFM) measurements were carried out using Omicron B002645 SPM probe VT AFM 25. NC-AFM images were obtained in the constant frequency shift mode (−20 Hz) and with constant vibrating amplitude (0.2 V).

Micro-Raman scattering measurements were performed at room temperature using a Jobin-Yvon T64000 triple spectrometer system and Ar^+/Kr^+ mixed laser line of 488 nm as an excitation source. The incident laser power was kept low (less than 10 mW) in order to prevent heating effects.

X-ray photoelectron spectroscopy (XPS) was used for the oxidation state and atomic ratio analysis. XPS was carried out on a PHI Quantera equipment with a base pressure in the analysis chamber of 10^{-9} Torr. The X-ray source was monochromatized AlKα radiation (1486.6 eV). The spectra were calibrated using the C 1s line (284.8 eV) of the adsorbed hydrocarbon on the sample surface.

The magnetic properties of the $Hf_{1-x}Y_xO_{2-\delta}$ samples were performed on a vibrating sample magnetometer in a high field measuring system (HFMS, Cryogenic Ltd).

3. Results and discussion

X-ray diffraction spectra of pure and Y-doped HfO_2 samples are presented in Fig. 1a. The XRD spectra of pure HfO_2 and $Hf_{1-x}Y_xO_{2-\delta}$ samples up to 10% of Y, show the monoclinic and tetragonal phase coexistence. With further increasing Y content, in 15% and 20% Y-doped samples the cubic phase appears. The main reflections of the monoclinic, tetragonal and cubic phases are marked with M, T and C in Fig. 1a. All diffraction peaks for the M, T and C phases in pure and Y-doped HfO_2 samples are indexed with the $P2_1/c$, $P4_2/nmc$ and Fm3m space group, respectively. The lattice parameters of the monoclinic, tetragonal and cubic phases are given in Table 1.

The volume fractions of different hafnia polymorphs in undoped and Y-doped HfO_2 samples were estimated from the integrated intensities of the M (−111), M (111) and T (111) diffraction peaks following the procedure proposed by Toraya et al. [12]. The estimated volume fractions for HfO_2 and Y-doped samples (given in %) are presented in Table 1.

As can be seen from Fig. 1a and Table 1, the monoclinic phase prevails over the tetragonal phase in pure HfO_2 sample. The XRD peaks are broadened which is characteristic of small (about 5 nm), oxygen deficient nanocrystals [11]. The XRD patterns of the Y-doped HfO_2 samples (labeled as HfY5-HfY20 according to the mol% of yttrium in doped samples) indicate the formation of solid solutions in the entire dopant compositional range without a presence of yttrium oxide or hydroxide phases. The yttrium substitution of Hf (Y_{Hf}) introduces oxygen vacancies in hafnia lattice and induces crystal structure changes of the HfO_2 nanopowders. The

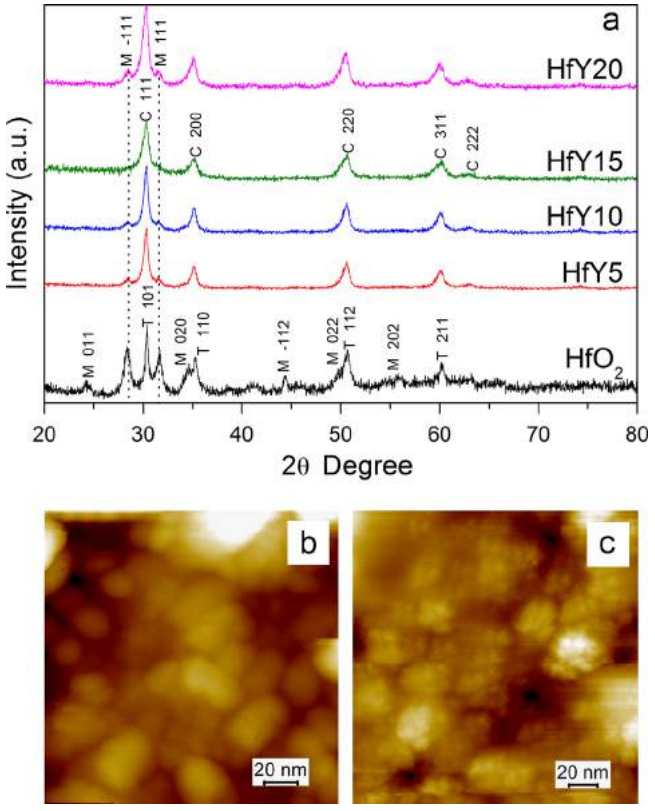

Fig. 1. (a) XRD patterns of Y-doped HfO_2 nanopowders at room temperature. The pure HfO_2 sample is given as a reference. The symbols stand for: M-monoclinic, T-tetragonal and C-cubic phase. The corresponding AFM images of (b) HfY10 and (c) HfY15 samples are presented.

Table 1
Composition and cell parameters of HfY samples obtained from XRD measurements.

Sample	Monoclinic $P2_1/c$				Tetragonal $P4_2/nmc$			Cubic $Fm3m$	
	(%)	a	b	c	(%)	a	c	(%)	a
HfY0	58	5.1453	5.1788	5.2919	42	3.5994	5.1191	–	–
HfY5	21	5.1418	5.1613	5.2928	79	3.6103	5.0980	–	–
HfY10	14	5.1265	5.1416	5.2830	86	3.6009	5.1835	–	–
HfY15	3	5.1169	5.1686	5.2967	46	3.6086	5.1800	51	5.1003
HfY20	16	5.1250	5.1797	5.2945	58	3.5737	5.1462	26	5.1166

structural transformation from monoclinic to tetragonal and cubic phase is a consequence of combined effect of doping with a lower valence state dopant and oxygen deficiency [2,3,11]. In the HfY5 sample the intensity of monoclinic reflections decreases implying that the content of monoclinic phase decreases on account of the tetragonal phase. This trend is even more pronounced for the HfY10 sample. In a case of the HfY15 sample, the XRD peaks which belong to M-phase are not visible anymore. The position of main diffraction peaks at 30.35°, 35.20°, 50.63° and 60.17° indicate that the cubic phase is formed [13] as dominant phase in this sample (see Table 1).

The tetragonal-cubic phase transformation is difficult to follow by an XRD method because of very low sensitivity of this method to the structural changes induced by oxygen displacement and nonstoichiometry. However, disappearance of M-phase, position of diffraction peaks and their significant broadening in a case of the HfY15 sample indicate the tetragonal-cubic phase transformation, as suggested by Fujimori and coauthors [14]. For the HfY20 sample, the content of T and M phases increases on the account of the cubic phase. This fact was somehow surprising because the cubic phase in HfO_2 is stabilized around 18 mol% of yttrium [15] or even less [16].

The morphology of the Y-doped nanopowders was analyzed by an AFM method. The AFM images of HfY10 and HfY15 samples, given in Fig. 1b and c, showed that the $Hf_{1-x}Y_xO_{2-\delta}$ nanopowders are composed of very small and agglomerated particles.

Raman scattering is much more sensitive method than the XRD to the structural changes induced by oxygen displacement and is powerful tool to investigate the tetragonal-cubic phase transformation in Y-doped HfO_2. The Raman spectra of $Hf_{1-x}Y_xO_{2-\delta}$ samples are shown in Fig. 2.

All Raman modes in HfY5 sample can be assigned to the monoclinic phase [17] except the mode at 500 cm^{-1} (marked as M/T1 in Fig. 2), which is also characteristic for the tetragonal phase [14]. The Raman modes are broadened because of the increased oxygen vacancy concentration when hafnia is doped with trivalent ions like Y [15]. With further increase of the Y content in the HfY10 sample, the Raman modes become broader implying that oxygen vacancy concentration further increases. New modes (marked as T2 and T3 in Fig. 2) appear and can be ascribed to the tetragonal phase [18]. The Raman mode denoted with asterisk (*) at ~190 cm^{-1} can originate from a small amount of γ-phase of HfO_2. The γ-phase can be identified only by Raman scattering [15]. In the HfY15 sample, the intensity of the Raman peaks which belong to the monoclinic and tetragonal phase decreases and the Raman modes became smeared out. Intensity drop of the mode at ~500 cm^{-1} reflects the tetragonal-cubic phase transition [14]. The F_{2g} mode of C-phase is not seen, because it is usually of very low intensity [17]. In the Raman spectrum of the HfY20 sample, the modes of T-phase became

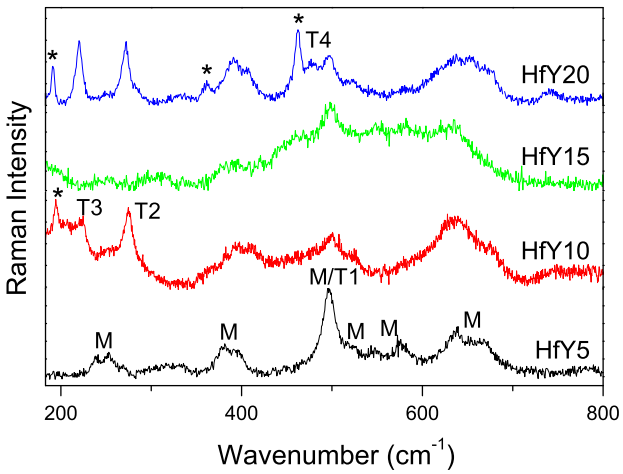

Fig. 2. Raman spectra of $Hf_{1-x}Y_xO_{2-\delta}$ ($0.05 \le x \le 0.2$) samples. The bands of monoclinic and tetragonal phases are designated by M, T1, T2, T3 and T4. Additional modes which can originate from γ-HfO_2 and cubic Y_2O_3 phases are denoted by asterisk (*).

more intensive than the modes of M-phase implying that the T-phase is dominant phase in this sample. This is in accordance with the XRD results. Additional modes at 360 cm^{-1} and 460 cm^{-1} can be ascribed to the cubic-Y_2O_3 phase probably formed at the nanoparticle surface [19].

The chemical state and composition of the $Hf_{1-x}Y_xO_{2-\delta}$ nanopowders were studied by XPS analyses. The XPS spectra of Hf 4f, O 1s and Y 3d region for Y-doped samples are given in Fig. 3a–c.

The deconvolution of the Hf 4f, O 1s and Y 3d spectra is performed for Y-doped samples using mixed Gaussian and Lorentzian functions. In Fig. 4a–c are presented deconvoluted XPS spectra of Hf 4f, Y 3d and O 1s region in a case of HfY5 sample for brevity.

The same procedure is applied for the rest of the samples and the binding energies (BE) of the most prominent XPS transitions

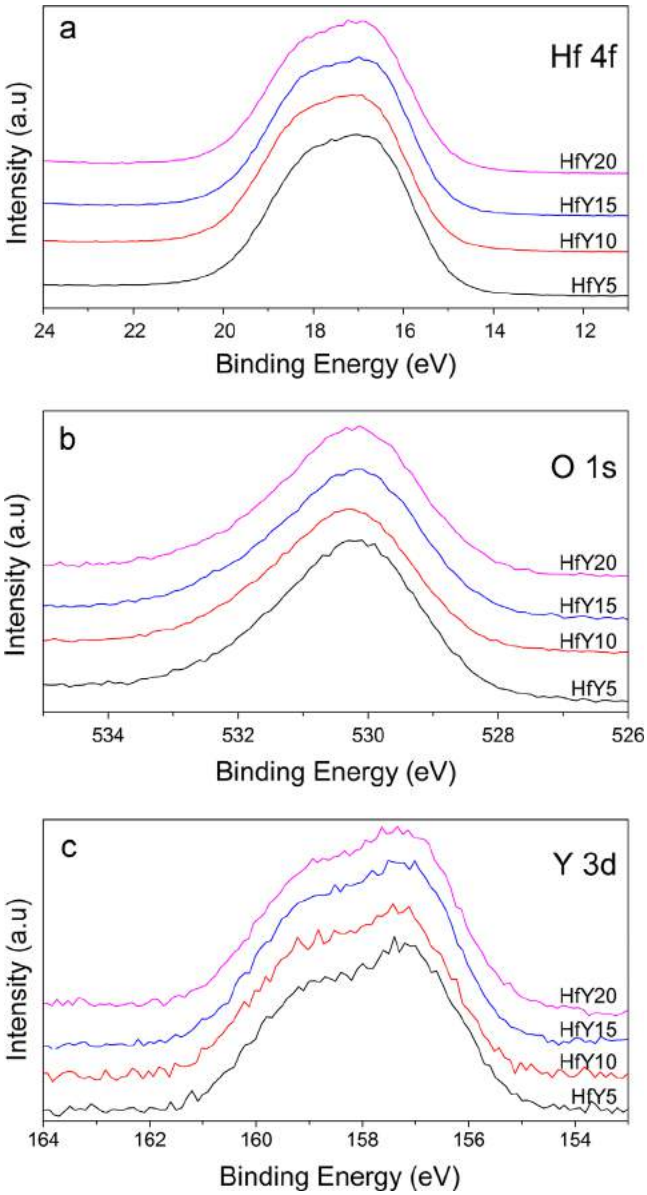

Fig. 3. The XPS spectra of (a) Hf 4f, (b) O 1s and (c) Y 3d region for Y-doped HfO_2 nanopowders.

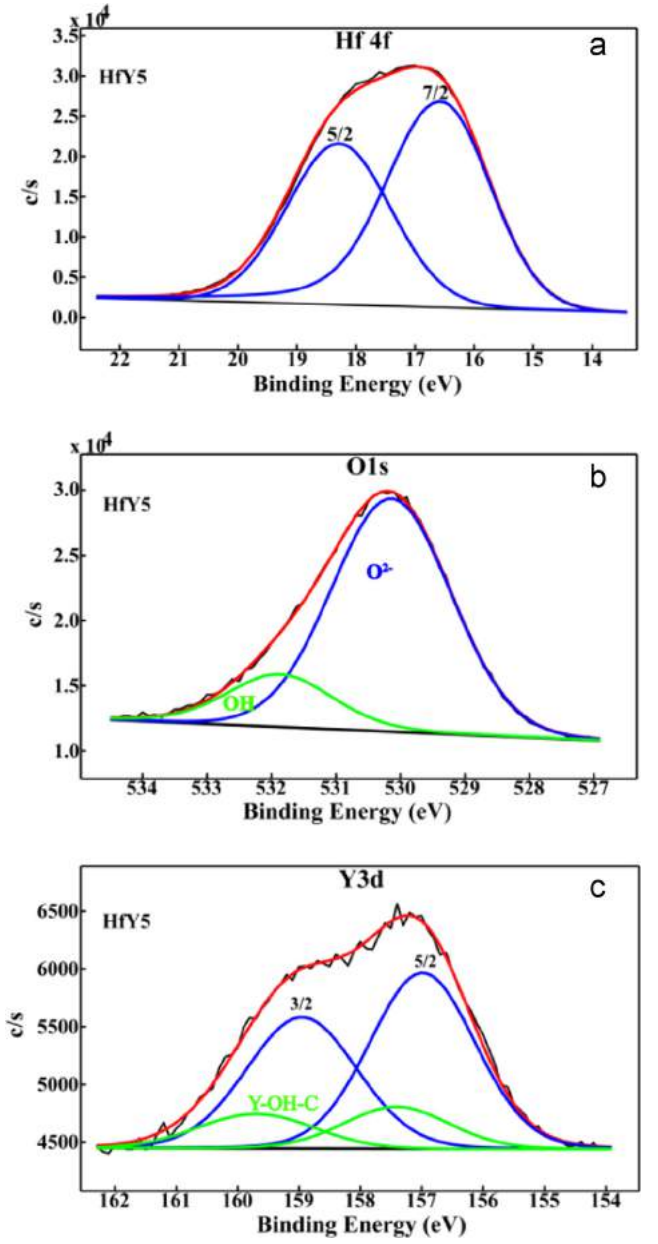

Fig. 4. Deconvoluted XPS spectra of (a) Hf 4f, (b) O 1s and (c) Y 3d region for HfY5 sample.

(Hf 4f, Y 3d, O 1s and C 1s) for $Hf_{1-x}Y_xO_{2-\delta}$ nanopowders are summarized in Table 2. No other contamination except carbon was detected in all investigated samples. XPS analysis of H 4f and O 1s gave evidence that the $Hf_{1-x}Y_xO_{2-\delta}$ samples are nonstoichiometric. From the O/Hf ratio, given in Table 2, it can be seen that the oxygen-deficiency increases with increasing Y content, with the exception of the HfY20 sample. This fact can be explained by the formation of the cubic-Y_2O_3 phase, already seen in the Raman spectrum of this sample.

The cations relative concentration for $Hf_{1-x}Y_xO_{2-\delta}$ samples, presented in Table 3, confirmed very good agreement between the surface and the nominal (bulk) stoichiometry. The errors regarding the quantitative data are found in the range of $\pm 10\%$, whereas the accuracy for BEs assignments is ± 0.2 eV.

Table 2
XPS binding energies (eV) of the individual peaks and composition of the HfY samples.

Sample	C 1s	O 1s		Hf 4f		Y 3d		Y–OH–C		Stoichiometry
		O^{2-}	OH	7/2	5/2	5/2	3/2			O/Hf
HfY5	284.8	530.1	531.8	16.6	18.3	156.9	159.0	157.4	159.6	1.9
HfY10	284.8	530.2	531.9	16.7	18.4	157.0	159.1	157.5	159.8	1.8
HfY15	284.8	530.1	531.9	16.6	18.3	157.0	158.9	157.5	159.8	1.83
HfY20	284.8	530.1	531.8	16.7	18.4	157.0	159.1	157.4	159.7	1.95

Table 3
Composition of HfY samples.

Sample	Y3d at%	Hf4f at%
HfY5	4.9	95.1
HfY10	9.3	90.7
HfY15	14.6	85.4
HfY20	19.1	80.9

The Hf 4f spectrum from Fig. 4a is composed of two spin-orbit doublet peaks (Hf $4f_{5/2}$ and Hf $4f_{7/2}$) which originate from the Hf bound to the oxygen. The Hf $4f_{7/2}$ peak is situated at 16.6 eV with a difference of 1.7 eV in binding energy between doublets. This peak is shifted to higher binding energies compared to the HfO_2 standard powdered sample (16.2 eV) [20] in all Y-doped samples (see Table 2). The higher binding energies of Hf $4f_{7/2}$ peak in Y-doped samples suggest that these nanopowders are deficient in oxygen and are non-stoichiometric [21,22]. The primary peak at 530.1 eV in the O 1s spectrum of Y-doped samples (see Fig. 4b and Table 2) is also shifted towards higher BE. This peak is ascribed to the oxygen bonded into the lattice and exhibits the shift probably because of the oxygen deficiency in the samples. Another subpeak in the O 1s spectrum at 531.8 eV (see Table 2) is assigned to adsorbed OH groups in the outermost surface layer [23,24]. The deconvoluted XPS spectrum of the Y 3d doublet ($3d_{5/2}$ and $3d_{3/2}$) is presented in Fig. 4c for the HfY5 sample. The average positions of the Y $3d_{5/2}$ peaks in $Hf_{1-x}Y_xO_{2-\delta}$ samples are given in Table 2 and are located around 157 eV. These peaks are slightly shifted to higher energy compared to the position of $3d_{5/2}$ peak in Y_2O_3 standard sample (156.5 eV) [20]. The shift to higher BE is expected if we have the formation of the Hf–Y–O bonds [16]. The fitting of the Y 3d spectra of doped samples requires additional doublet (binding energies are given in Table 2). The second doublet can be attributed to Y–OH–C bonds confined to the surface as a result of the OH and hydrocarbon adsorption from the atmosphere.

In summary, XPS and Raman analysis of the $Hf_{1-x}Y_xO_{2-\delta}$ samples confirmed that yttrium doping increases the concentration of oxygen vacancies, whereas XRD and Raman results showed that the incorporation of yttrium induces structural phase transformation. These findings are in agreement with Manory et al. [13] who reported that tetragonal and cubic phase of HfO_2 are stable at room temperature in nonstoichiometric HfO_2. In Fig. 5 we gave an illustration of the phase transformation in HfO_2 with Y doping. In Fig. 5a is presented the monoclinic phase of nonstoichiometric undoped HfO_2 with three- and four-coordinated oxygen vacancies. Yttrium as a dopant ion in 3^+ valence state brings additional vacancies in the hafnia lattice in order to keep the charge neutrality (Fig. 5b). With further addition of Y, the concentration of the oxygen vacancies should be increased and the monoclinic phase of HfO_2 transforms first into the tetragonal and then into the cubic phase as presented in Fig. 5c and d.

The room temperature magnetization versus magnetic field (M–H) data for pure HfO_2 and Y-doped samples is shown in Fig. 6a. It can be seen that all samples show a ferromagnetic signal at room temperature superimposed onto a diamagnetic background. The observed ferromagnetism is characteristic for the nanostructured nature of the investigated samples [25] and is intrinsic as there are no magnetic impurities present in the samples (see experimental part). The susceptibility of the diamagnetic component, i.e. the slope of the high-field parts of the curve, remains constant with yttrium doping because of the closed Y^{3+} shells. After subtracting the diamagnetic component, the corrected magnetization curves are shown in Fig. 6b. The magnetization curves are almost anhysteretic, as it is often the case for ferromagnetic oxides [26]. The saturation magnetization value (M_S) for the undoped sample is about 2.2×10^{-3} emu g^{-1}. The obtained value is comparable with the other reports on ferromagnetism in undoped oxide nanocrystals [25–29], but higher than the reported value on HfO_2 powders [5]. The value of M_S increases for the HfY5 sample and reaches its maximum of 2.9×10^{-3} emu g^{-1} for the HfY10 sample. The saturation magnetization significantly drops off in the HfY15 and HfY20 samples to the values of 1.2×10^{-3} emu g^{-1} and 0.7×10^{-3} emu g^{-1} respectively. The change of the M_S for pure HfO_2 and $Hf_{1-x}Y_xO_{2-\delta}$ samples is presented in Fig. 6c.

The experimental reports [30–33] confirmed the existence of RTFM in pure and doped hafnia films and clearly proved that the RTFM originates from the presence of oxygen vacancies. The lack of oxygen vacancies or filling up vacancies can degrade or even completely destroy the FM ordering. Scarce literature data concerning the appearance of the FM in other hafnia nanostructures like nanopowders or nanorods [33–35] have also pointed out that the oxygen vacancies play a major role in the magnetic exchange mechanism. The appearance of RTFM in pure HfO_2 can be interpreted in the framework of the impurity band exchange model proposed by Venkatesan et al. [4]. According to this model, the intrinsic oxygen vacancies act as a donor of electrons, leading to the n-type doping of the hafnia. The electrons trapped in oxygen vacancies in HfO_2 form extended hydrogen-like orbitals because of the relatively high dielectric constant of hafnia. When the defect

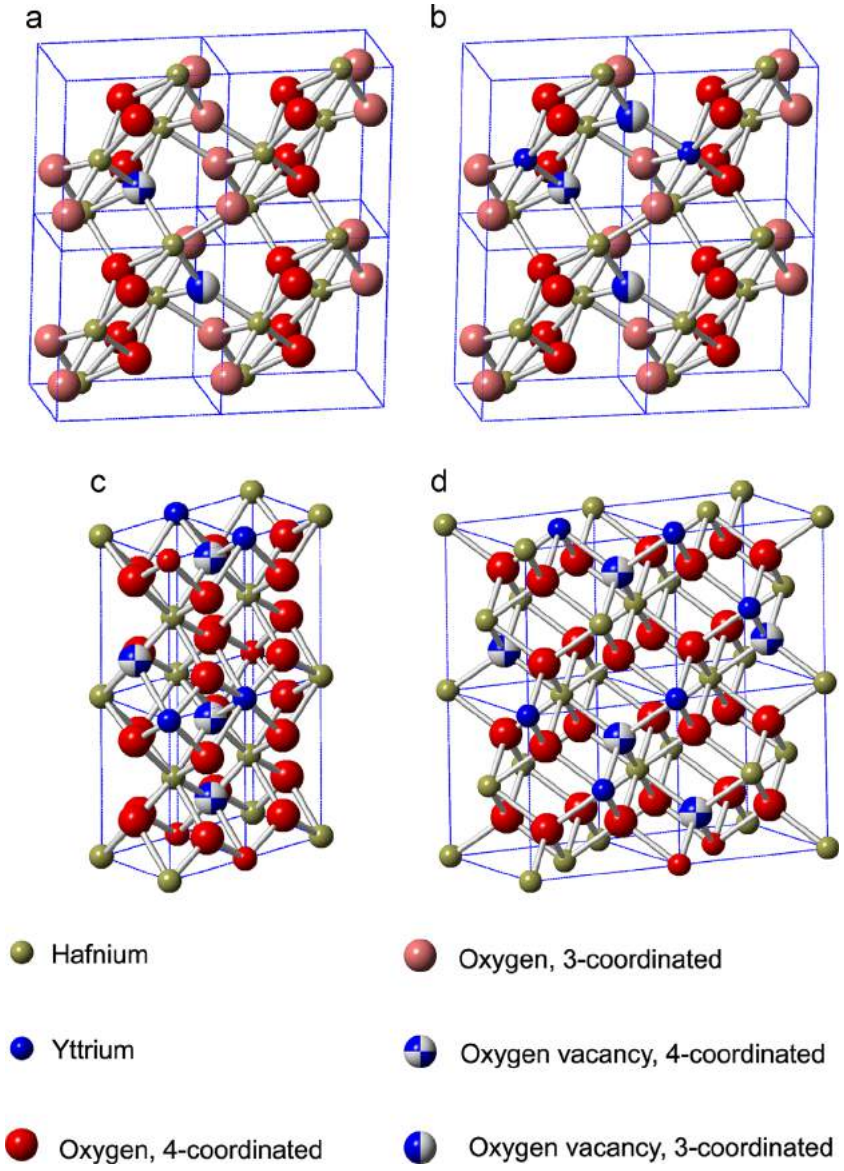

Fig. 5. Structural phase transformation with Y doping (a) pure HfO_2 monoclinic phase, (b) monoclinic phase of HfO_2 doped with Y, (c) tetragonal phase and (d) cubic phase of HfO_2 with increased Y content.

concentration increases, the overlapping of the defect-related orbitals can form an impurity (defect) band. The mixing of the defect band with empty 5d states of hafnia enables the transfer of some of the electrons to the 5d band. The 5d electrons will in turn polarize the defect band establishing the ferromagnetic coupling [4]. The oxygen vacancies in monoclinic hafnia can be in different charge states having different number of trapped electrons and bearing different magnetic moment [7,36]. Some of these defects like negatively (V_O^-) or positively (V_O^+) charged vacancies form levels near the conduction band, as shown in the paper of Xiong et al. [36]. They calculated the energy levels of the oxygen vacancy defects in different charge states for HfO_2 and showed that the energy levels of the V_O^- and V_O^+ defects lie very near to the conduction band (approximately at 0.8 and 1.1 eV below the conduction band edge). Consequently, it is reasonable to assume that the defect band, formed from V_O^- and V_O^+ states, will lie near the conduction band. The fraction of the electrons from defect band can be transferred to the 5d states causing the spin splitting of the defect band. The formation of the spin-split defect band provides necessary condition for the appearance of ferromagnetism [4]. In Fig. 7a is given the schematic representation of the defect levels induced by oxygen vacancies in different charge states according to the calculations performed in Ref. [34]. The mixing of the defect band with the 5d states of hafnia and its spin-splitting is presented in Fig. 7b.

Having in mind theoretical calculations [7,36] and experimental observations [30–33] and knowing from the Raman and XPS results that $Hf_{1-x}Y_xO_{2-\delta}$ nanopowders are oxygen deficient, we concluded that the oxygen vacancies can be attributed to be the main source of ferromagnetism in undoped and Y-doped HfO_2 nanopowders. In the HfY5 sample, with Y doping the concentration of oxygen vacancies should increase (see Fig. 5b) in order to

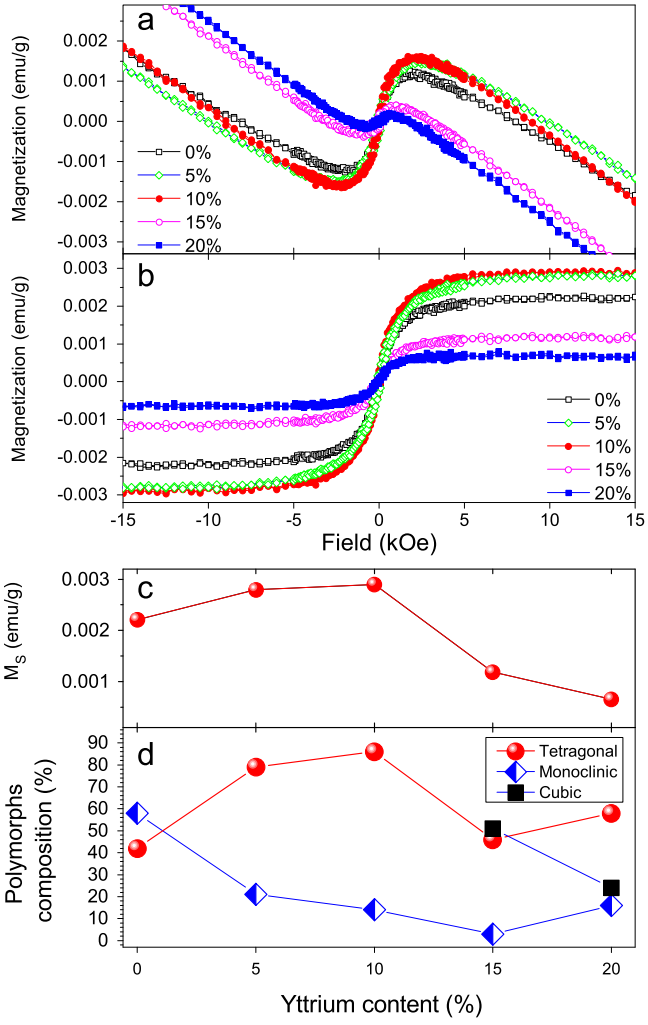

Fig. 6. Magnetic properties of $Hf_{1-x}Y_xO_{2-\delta}$ samples. (a) Raw magnetization curves versus magnetic field, $M(H)$, (b) $M(H)$ after subtraction of the linear diamagnetic component, (c) Saturation magnetization (M_S) change and (d) relative polymorph composition change with yttrium content.

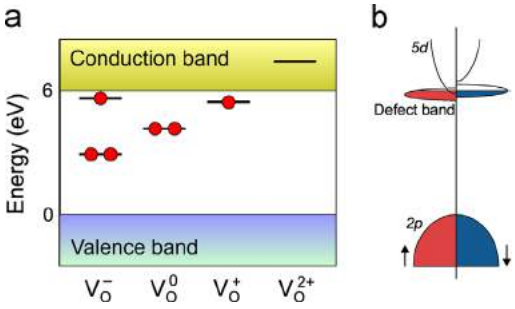

Fig. 7. Schematic representation of the (a) defect levels which originate from point defects and (b) a spin-split defect band.

keep electroneutrality. At the same time the content of tetragonal phase begins to prevail over the monoclinic one. The FM signal is stronger than that in undoped HfO_2. With increasing Y content up to 10%, the saturation magnetization and the strength of FM ordering further increase, when the content of the tetragonal phase in HfY10 sample becomes dominant (Fig. 5c). In the HfY15 sample the cubic phase appears and the strength of FM interaction weakens, reaching the lowest value of M_S (0.7×10^{-3} emu g^{-1}) for HfY20. This value of M_S is almost three times lower than for HfY10 sample. From the change of the polymorphs composition with increasing Y content presented in Fig. 6d, it can be seen that the change of M_S and T-phase content have similar trend. In a case of HfY20 sample, M_S continues to decrease despite the fact that the amount of T-phase is slightly increased.

The theoretical calculations performed by Chen et al. [37] can offer the explanation for the degradation of FM ordering in HfY15 and HfY20 samples. Namely, Chen et al. [37] calculated the formation energies of the oxygen vacancies in different charge states for Y-doped cubic HfO_2. It is found that with higher Y content, oxygen vacancies form complex defects with yttrium (V_O–Y_{Hf}) in different charge states ((V_O–$Y_{Hf})^+$, (V_O–$Y_{Hf})^{++}$ and (V_O–$Y_{Hf})^0$ complexes). Among these complexes, the single positively charged complexes (V_O–$Y_{Hf})^+$ are the most stable ones. Y as dopant changes the charge state of oxygen vacancies and lowers the highest occupied levels induced by V_O^+ and V_O^{++} vacancies into the valence band. Therefore, the highest occupied levels of (V_O–$Y_{Hf})^+$ and (V_O–$Y_{Hf})^{++}$ complex defects will lie in the vicinity of the valence band. With further increasing of Y content the highest occupied levels of (V_O–$Y_{Hf})^0$ complexes would also fall into the valence band [37]. Considering the results from Ref. [37], it is reasonable to assume that in HfY15 and HfY20 samples, because of the increased Y content and the presence of cubic phase, certain number of (V_O–Y_{Hf}) defect complexes can be formed. The appearance of (V_O–Y_{Hf}) defect complexes will degrade the ferromagnetic interaction because the defect band formed from (V_O–Y_{Hf}) complex defects states will lie near to the valence band. The mechanism of electron transfer from defect band to 5d empty states which leads to its polarization and establishing of ferromagnetic interaction is not applicable anymore. The formation of cubic-Y_2O_3 phase at nanoparticle surface, seen in the Raman spectrum of HfY20 sample can explain further degradation of ferromagnetism in this sample.

4. Conclusions

In summary, nonstoichiometric $Hf_{1-x}Y_xO_{2-\delta}$ nanosized powders ($0 \le x \le 0.2$) are obtained by metathesis synthesis. The transformation of crystal structure from monoclinic to tetragonal and cubic phase (M→T→C) with increased Y doping was confirmed by XRD and Raman measurements. The XPS and Raman studies testified that the $Hf_{1-x}Y_xO_{2-\delta}$ nanopowders are nonstoichiometric. All samples exhibit room temperature ferromagnetism which increases with increased tetragonal phase content and degrades with the appearance of cubic phase. The FM ordering in $Hf_{1-x}Y_xO_{2-\delta}$ samples can be explained in the framework of impurity band exchange model where oxygen vacancies in different charge state, as n-type dopants, play major role in establishing ferromagnetism. Further increasing of Y content stabilizes the cubic phase in 15% and 20% Y doped samples and the ferromagnetic interaction weakens. In a cubic phase certain number of oxygen vacancy-yttrium complexes (V_O–Y_{Hf}) can be formed. Those complexes form defect states inside the

bandgap of hafnia. The highest occupied defect states will lie in the vicinity of the valence band. The electron transfer from deep lying defect states to the 5d empty states of hafnia, which enables the establishing of ferromagnetic interaction is not realistic anymore. The presence of cubic-Y_2O_3 phase additionally degrades ferromagnetic ordering in the 20% Y doped sample.

Acknowledgments

This work was financially supported by the Ministry of Education, Science and Technological Development of the Republic of Serbia under the projects ON171032 and III45018. Dr Rareş Scurtu acknowledges the support of the Sectorial Operational Programme Human Resource Development (SOPHRD) under the contract number POSDRU/89/1.5/S/63700.

References

[1] R. Ruh, V.A. Patel, Proposed phase relations in the HfO_2-rich portion of the system Hf-HfO_2, J. Am. Ceram. Soc. 56 (1973) 606–607.
[2] E. Rauwel, C. Dubourdieu, B. Hollander, N. Rochat, F. Ducroquet, M.D. Rossell, G. Van Tendeloo, B. Pelissier, Stabilization of the cubic phase of HfO_2 by Y addition in films grown by metal organic chemical vapor deposition, Appl. Phys. Lett. 89 (2006) 012902.
[3] L. Gao, L. Zhou, J. Feng, L. Bai, C. Li, Z. Liu, J.-L. Soubeyroux, Y. Lu, Stabilization of cubic structure in Mn-doped hafnia, Ceram. Int. 38 (2012) 2305–2311.
[4] M. Venkatesan, C.B. Fitzgerald, J.M.D. Coey, Thin films: unexpected magnetism in a dielectric oxide, Nature 430 (2004) 630.
[5] J.M.D. Coey, M. Venkatesan, P. Stamenov, C.B. Fitzgerald, L.S. Dorneles, Magnetism in hafnium dioxide, Phys. Rev. B 72 (2005) 024450.
[6] M.D. Glinchuk, E.A. Eliseev, V.V. Khist, A.N. Morozovska, Ferromagnetism induced by magnetic vacancies as a size effect in thin films of nonmagnetic oxides, Thin Solid Films 534 (2013) 685–692.
[7] D. Muñoz Ramo, J.L. Gavartin, A.L. Shluger, G. Bersuker, Spectroscopic properties of oxygen vacancies in monoclinic HfO_2 calculated with periodic and embedded cluster density functional theory, Phys. Rev. B 75 (2007) 205336.
[8] C. Das Pemmaraju, S. Sanvito, Ferromagnetism driven by intrinsic point defects in HfO_2, Phys. Rev. Lett. 94 (2005) 217205.
[9] J.I. Beltrán, M.C. Muñoz, J. Hafner, Structural, electronic and magnetic properties of the surfaces of tetragonal and cubic HfO_2, New J. Phys. 10 (2008) 063031.
[10] J.X. Zheng, G. Ceder, T. Maxisch, W.K. Chim, W.K. Choi, First-principles study of native point defects in hafnia and zirconia, Phys. Rev. B 75 (2007) 104112.
[11] B. Matović, D. Bučevac, M. Prekajski, V. Maksimović, D. Gautam, K. Yoshida, T. Yano, Synthesis and characterization of nanometric yttrium-doped hafnia solid solutions, J. Eur. Ceram. Soc. 32 (2012) 1971–1976.
[12] H. Toraya, M. Yoshimura, S. Somiya, Calibration curve for quantitative analysis of the monoclinic-tetragonal ZrO_2 system by X-ray diffraction, J. Am. Ceram. Soc. 67 (1984) C-119–C-121.
[13] R.R. Manory, T. Mori, I. Shimizu, S. Miyake, G. Kimmel, Growth and structure control of HfO_{2-x} films with cubic and tetragonal structures obtained by ion beam assisted deposition, J. Vac. Sci. Technol. A 20 (2002) 549–554.
[14] H. Fujimori, M. Yashima, S. Sasaki, M. Kakihana, T. Mori, M. Tanaka, M. Yoshimura, Cubic–tetragonal phase change of yttria-doped hafnia solid solution: high-resolution X-ray diffraction and Raman scattering, Chem. Phys. Lett. 346 (2001) 217–223.
[15] M. Yashima, H. Takahashi, K. Ohtake, T. Hirose, M. Kakihana, H. Arashi, Y. Ikuma, Y. Suzuki, M. Yoshimura, Formation of metastable forms by quenching of the HfO_2–$RO_{1.5}$ melts (R=Gd, Y and Yb), J. Phys. Chem. Solids 57 (1996) 289–295.
[16] C. Dubourdieu, E. Rauwel, H. Roussel, F. Ducroquet, B. Hollander, M. Rossell, G. Van Tendeloo, S. Lhostis, S. Rushworth, Addition of yttrium into HfO_2 films: microstructure and electrical properties, J. Vac. Sci. Technol. A 27 (2009) 503–514.
[17] X. Zhao, D. Vanderbilt, First-principles study of structural, vibrational, and lattice dielectric properties of hafnium oxide, Phys. Rev. B 65 (2002) 233106.
[18] G.M. Rignanese, X. Gonze, G. Jun, K. Cho, A. Pasquarello, First-principles investigation of high-κ dielectrics: comparison between the silicates and oxides of hafnium and zirconium, Phys. Rev. B 69 (2004) 184301.
[19] A. Ubaldini, M.M. Carnasciali, Raman characterisation of powder of cubic RE_2O_3 (RE=Nd, Gd, Dy, Tm, and Lu), Sc_2O_3 and Y_2O_3, J. Alloy. Compd. 454 (2008) 374–378.
[20] J.F. Moulder, W.F. Stickle, P.E. Sobol, K.D. Bomben, Handbook of X-ray Photoelectron Spectroscopy, Perkin-Elmer Corp, Minnesota, 1992.
[21] N. Selvakumar, H.C. Barshilia, K.S. Rajam, A. Biswas, Structure, optical properties and thermal stability of pulsed sputter deposited high temperature HfO_x/Mo/HfO_2 solar selective absorbers, Sol. Energy Mater. Sol. Cells 94 (2010) 1412–1420.
[22] G. He, M. Liu, L.Q. Zhu, M. Chang, Q. Fang, L.D. Zhang, Effect of postdeposition annealing on the thermal stability and structural characteristics of sputtered HfO_2 films on Si(1 0 0), Surf. Sci. 576 (2005) 67–75.
[23] X. Qiu, J.Y. Howe, H.M. Meyer Iii, E. Tuncer, M.P. Paranthaman, Thermal stability of HfO_2 nanotube arrays, Appl. Surf. Sci. 257 (2011) 4075–4081.
[24] J.C. Hackley, T. Gougousi, Properties of atomic layer deposited HfO_2 thin films, Thin Solid Films 517 (2009) 6576–6583.
[25] A. Sundaresan, C.N.R. Rao, Ferromagnetism as a universal feature of inorganic nanoparticles, Nano Today 4 (2009) 96–106.
[26] J.M.D. Coey, Dilute magnetic oxides, Curr. Opin. Solid State. Mater. Sci. 10 (2006) 83–92.
[27] M.Y. Ge, H. Wang, E.Z. Liu, J.F. Liu, J.Z. Jiang, Y.K. Li, Z.A. Xu, H.Y. Li, On the origin of ferromagnetism in CeO_2 nanocubes, Appl. Phys. Lett. 93 (2008) 062505.
[28] Z.D. Dohčević-Mitrović, N. Paunović, M. Radović, Z.V. Popović, B. Matović, B. Cekić, V. Ivanovski, Valence state dependent room-temperature ferromagnetism in Fe-doped ceria nanocrystals, Appl. Phys. Lett. 96 (2010) 203104.
[29] N. Paunović, Z. Dohčević-Mitrović, R. Scurtu, S. Aškrabić, M. Prekajski, B. Matović, Z.V. Popović, Suppression of inherent ferromagnetism in Pr-doped CeO_2 nanocrystals, Nanoscale 4 (2012) 5469–5476.
[30] Y.H. Chang, Y.L. Soo, W.C. Lee, M.L. Huang, Y.J. Lee, S.C. Weng, W.H. Sun, M. Hong, J. Kwo, S.F. Lee, J.M. Ablett, C.C. Kao, Observation of room temperature ferromagnetic behavior in cluster-free, Co doped HfO_2 films, Appl. Phys. Lett. 91 (2007) 082504.
[31] K.K. Bharathi, S. Venkatesh, G. Prathiba, N.H. Kumar, C.V. Ramana, Room temperature ferromagnetism in HfO_2 films, J. Appl. Phys. 109 (2011) 07C318.
[32] N.H. Hong, J. Sakai, N. Poirot, V. Brizé, Room-temperature ferromagnetism observed in undoped semiconducting and insulating oxide thin films, Phys. Rev. B 73 (2006) 132404.
[33] X. Liu, Y. Chen, L. Wang, D.-L. Peng, Transition from paramagnetism to ferromagnetism in HfO_2 nanorods, J. Appl. Phys. 113 (2013) 076102.
[34] M.K. Sharma, D.K. Mishra, S. Ghosh, D. Kanjilal, P. Srivastava, R. Chatterjee, Oxygen vacancy mediated large magnetization in chemically synthesized Ni-doped HfO_2 nanoparticle powder samples, J. Appl. Phys. 110 (2011) 063902.
[35] E. Tirosh, G. Markovich, Control of defects and magnetic properties in colloidal HfO_2 nanorods, Adv. Mater. 19 (2007) 2608–2612.
[36] K. Xiong, J. Robertson, M.C. Gibson, S.J. Clark, Defect energy levels in HfO_2 high-dielectric-constant gate oxide, Appl. Phys. Lett. 87 (2005) 183505.
[37] G.H. Chen, Z.F. Hou, X.G. Gong, Q. Li, Effects of Y doping on the structural stability and defect properties of cubic HfO_2, J. Appl. Phys. 104 (2008) 074101.

Langmuir

Article

pubs.acs.org/Langmuir

Nanocrystalline $CeO_{2-\delta}$ as Effective Adsorbent of Azo Dyes

Nataša M. Tomić,[†] Zorana D. Dohčević-Mitrović,*[,†] Novica M. Paunović,[†] Dušan Ž. Mijin,[‡] Nenad D. Radić,[§] Boško V. Grbić,[§] Sonja M. Aškrabić,[†] Biljana M. Babić,[∥] and Danica V. Bajuk-Bogdanović[⊥]

[†]Institute of Physics, University of Belgrade, Pregrevica 118, 11080 Belgrade, Serbia

[‡]Faculty of Technology and Metallurgy, University of Belgrade, Karnegijeva 4, 11000 Belgrade, Serbia

[§]IChTM, Department of Catalysis and Chemical Engineering, University of Belgrade, Njegoševa 12, 11000 Belgrade, Serbia

[∥]Institute of Nuclear Sciences "Vinča", University of Belgrade, 11001 Belgrade, Serbia

[⊥]Faculty of Physical Chemistry, University of Belgrade, Studentski Trg 12-16, 11000 Belgrade, Serbia

Supporting Information

ABSTRACT: Ultrafine $CeO_{2-\delta}$ nanopowder, prepared by a simple and cost-effective self-propagating room temperature synthesis method (SPRT), showed high adsorption capability for removal of different azo dyes. Batch type of adsorption experiments with fixed initial pH value were conducted for the removal of Reactive Orange 16 (RO16), Methyl Orange (MO), and Mordant Blue 9 (MB9). The equilibrium adsorption data were evaluated using Freundlich and Langmuir isotherm models. The Langmuir model slightly better describes isotherm data for RO16 and MO, whereas the Freundlich model was found to best fit the isotherm data for MB9 over the whole concentration range. The maximum adsorption capacities, determined from isotherm data for MO, MB9, and RO16 were 113, 101, and 91 mg g^{-1} respectively. The adsorption process follows the pseudo-second-order kinetic model indicating the coexistence of chemisorption and physisorption. The mechanism of azo dye adsorption is also discussed.

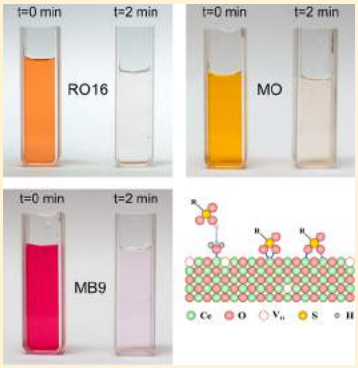

INTRODUCTION

Synthetic dyes are widely used in a number of industries such as textile and leather industries, paper printing, cosmetics, and pharmaceuticals. It is estimated to be more than 10 000 commercially available dyes with over 7×10^5 tons of dyestuff produced annually.[1,2] Azo dyes represent about 60−70% of the dyes used in the textile industry. Some of them show aquatic toxicity or allergenic effects, and under reductive conditions they produce aromatic amines that are carcinogenic.[2,3] Azo dyes represent a class of synthetic, colored, organic compounds, which are characterized by the presence of one or more azo bonds. These dyes belong to the most toxic ones compared to other forms of dyes.[1] Large quantities of these dyes (10−15% of the total world production) are released into the wastewater (typical concentration 10−200 mg L^{-1}), the presence of which poses a major threat to the aquatic organisms as well as animals and humans because of their nonbiodegradability, toxicity, and potential carcinogenic nature.[4−6]

Dye removal from textile effluents is a major environmental problem because of the difficulty to treat such streams by conventional physicochemical and biological treatment methods. The methods such as filtration, coagulation, flocculation, ion exchange, and photocatalytic degradation are unsatisfactory for wastewater treatment because they are expensive and may produce more toxic byproducts. Among the various available water treatment techniques, adsorption is the most reliable and efficient technique for dye removal, despite the fact that usually the adsorbent needs to be regenerated, which increases the cost of the process and can be a time-consuming procedure. The liquid phase adsorption has been shown to be an efficient way for removing the suspended solids, organic matter, and oil from aqueous solutions. Adsorption appears to offer the best perspective over all the other treatments because it can handle fairly large flow rates, producing a high quality effluent and does not result in the formation of harmful substances, such as ozone and free radicals which are present during the photodegradation process using UV.

Activated carbon is the most widely used adsorbent for this purpose, because it has a high surface area and high capacity for adsorption of organic matter, but its use is limited because of its high production cost and significant problems with the regeneration of the spent activated carbon.[7,8] A great variety of low-cost biomass materials[9−13] have been used to produce activated carbon for the treatment of wastewaters. In recent years, low cost agricultural wastes have been investigated as potential biosorbents,[14] but most of these cheap substitutes have to be subjected to the process of carbonization which increases process costs. Therefore, there is still a high demand for cheaper adsorbent materials with high adsorption capacity.

Received: March 6, 2014
Revised: September 8, 2014
Published: September 14, 2014

Nowadays, nanoscience and nanotechnology play important role in environmental protection. There is a strong need to develop simple and economical methods for producing nanomaterials with higher adsorption rates which can efficiently remove various contaminants. Nanomaterials with high surface area are the most promising candidates as adsorbents in organic dye removal.[5,15−19]

Among various metal oxide semiconductors, CeO_2 is widely used in many application areas such as catalysis, fuel cells, sensors, and UV shielding, owing to its outstanding physical and chemical properties. The application of ceria as effective sorbent is not so often studied. There are few reports in which it is demonstrated that ceria is effective sorbent for the removal of high toxic pollutants such as[17] As(V) and Cr(VI) and azo dyes such as Congo Red[18] or Acid Orange[4] from water. The adsorption experiments, performed to remove Reactive Orange 16 and Methyl Orange from wastewaters, mainly used as adsorbent waste biomass,[20] various types of sludge, and biosorbents.[1,13,14,20−26] Although most of these sorbents were relatively cheap and effective in dye removal, they showed modest and rarely high sorption capacities. On the other side, to the best of our knowledge there is almost no study which concerns the adsorption of Mordant Blue 9.

Herein we present the adsorption capability of ceria nanoparticles for removal of different azo dyes such as Reactive Orange 16, Methyl Orange, and Mordant Blue 9. Ceria nanopowder, obtained by a simple and cost-effective method, has shown very high efficiency toward azo dye removal and has been proven to be a promising alternative for wastewater treatment.

EXPERIMENTAL SECTION

1. Materials Preparation. The ultrafine $CeO_{2-\delta}$ nanopowder was fabricated via a simple and economical self-propagating room temperature synthesis method (SPRT).[27,28] Starting reactants were cerium nitrate hexahydrate ($Ce(NO_3)_3{\cdot}6H_2O$) (Acros Organics 99.5%) and sodium hydroxide (Carlo Erba). Hand-mixing of nitrate with NaOH was performed in alumina mortar for ∼10 min until the mixture turned light brown. After being exposed to air for 4 h, the mixture was suspended in water. Rinsing of $NaNO_3$ was performed in a centrifuge at 3500 rpm for 10 min. This procedure was performed four times with distilled water and twice with ethanol. The precipitate was dried at 60 °C overnight. The reaction based on the self-propagating room temperature method can be written as follows:

$$2[(Ce(NO_3)_3{\cdot}6H_2O] + 6NaOH + (1/2 - \delta)O_2 \rightarrow 2CeO_{2-\delta} + 6NaNO_3 + 15H_2O \quad (1)$$

2. Characterization Methods. X-ray powder diffraction (XRD) data of the sample were collected on a Siemens D-5000 diffractometer with Cu Kα radiation over the 2θ range from 20° to 80°. Atomic force microscope (AFM) images were taken using the Omicron B002645 SPM PROBE VT AFM 25 instrument in noncontact mode at room temperature. The powder specific surface area of the sample was calculated following the multipoint BET procedure on the Quantachrome ChemBet-3000 setup. The pore size distribution was derived from nitrogen adsorption-desorption isotherm obtained at 77 K. The infrared (IR) transmission spectra of $CeO_{2-\delta}$ pellets before and after dye adsorption were measured on a Thermo Nicolet 6700 Fourier transform infrared spectrophotometer at room temperature. Micro-Raman spectra were collected in the backscattering configuration using the TriVista 557 Raman system. The 488 nm line of an Ar^+/Kr^+ mixed gas laser was used as an excitation source. In order to avoid sample heating, the incident laser power on the samples was kept below 20 mW. Surface charge (zeta potential) of ceria nanoparticles at different pH was measured using Zetasizer Nano ZS90 (Malvern Instruments) apparatus. Suspensions were prepared using deionized water as dispersing medium and were ultrasonicated for 15 min prior to the measurements using an ultrasonic bath. The pH values of suspensions were adjusted by adding HCl and NaOH solutions to the starting suspension of $CeO_{2-\delta}$ nanopowder.

3. Adsorption Experiments. The adsorption experiments were carried out as batch tests in a magnetically stirred thermostated glass vessel with three different concentrations (50, 100, and 200 mg L^{-1}) of Reactive Orange 16 (RO16), Methyl Orange (MO), and Mordant Blue 9 (MB9). All measurements were performed at initial pH values of 6.2, 6, and 4.6 for MO, MB9, and RO16 dye solutions, respectively. The suspensions were stirred for 2 min at room temperature in the dark. The adsorption capacity (for the 200 mg L^{-1} concentration of dyes) of coconut-based powdered activated carbon (PAC), of large specific surface area (1200 m^2/g), was determined for comparison. The working volume (25 mL) and the quantity of ceria nanopowders and PAC (50 mg) were kept fixed in all adsorption experiments. At fixed contact time, the samples were taken, centrifuged, and analyzed on a Shimadzu 1700 UV-vis spectrophotometer within the spectral range where maximum absorption for each dye occurs. In Table S1 (see the Supporting Information) are given the chemical structure and the wavelength of maximal absorption (λ_{max}) for each dye.

RESULTS AND DISCUSSION

The powder XRD pattern of $CeO_{2-\delta}$ nanopowder is presented in Figure 1a. Diffraction peaks corresponding to cubic fluorite structure are clearly observed. All XRD peaks are broadened, indicating that the crystallite size is within the nanometer range. The average size of $CeO_{2-\delta}$ nanocrystals, estimated by the Wiliamson-Hall method,[29] is about 6 nm. The noncontact AFM image of $CeO_{2-\delta}$ sample (Inset of Figure 1b) shows small and agglomerated nonporous $CeO_{2-\delta}$ particles. The pores between agglomerated $CeO_{2-\delta}$ nanoparticles are also visible on the AFM image. Particle size distribution obtained from the AFM image of $CeO_{2-\delta}$ sample is presented in Figure 1b, and it was modeled by asymmetric double sigmoidal function. The average particle size is 11.4 nm.

To determine the surface area and pore size distribution, nitrogen adsorption−desorption isotherms at 77 K were recorded, and these are given in the inset of Figure 1c. According to the IUPAC classification,[30] the nitrogen adsorption−desorption isotherm is attributed to the Langmuir IV type. The pore size distribution was determined from the desorption branch of the isotherms using the BJH (Barrett−Joyner−Halenda) method and is shown in Figure 1c. It can be observed that the sample has bimodal pore size distribution in the mesoporous area with the first mode peak around 2 nm and the second one in the range 3−4 nm. The value of the BET specific surface area (S_{BET}) is 74 m^2 g^{-1}.

Further, we examined the performances of $CeO_{2-\delta}$ nanopowder as a potential adsorbent for removal of RO16, MO, and MB9. The adsorption measurements were carried out with three different concentrations of the dye solutions (50, 100, and 200 mg L^{-1}), and absorption spectra of the dye solutions were collected after certain time intervals. The UV−vis spectrum of RO16 is given in Figure 2a (blue line) for the concentration of 50 mg L^{-1}. The absorption spectrum of RO16 in the presence of $CeO_{2-\delta}$ nanoparticles after 2 min is also presented in Figure 2a (red line). As can be seen, the RO16 characteristic bands decreased promptly, indicating that RO16 was removed from the solution. The corresponding photo image (right panel of Figure 2a) shows that the solution is almost colorless. The absorption spectra of the MO and MB9 before (blue line) and after 2 min (red line) in the presence of $CeO_{2-\delta}$ nanoparticles are given in Figure 2b,c. Absorption spectra of these two dye

dx.doi.org/10.1021/la502969w | Langmuir 2014, 30, 11582−11590

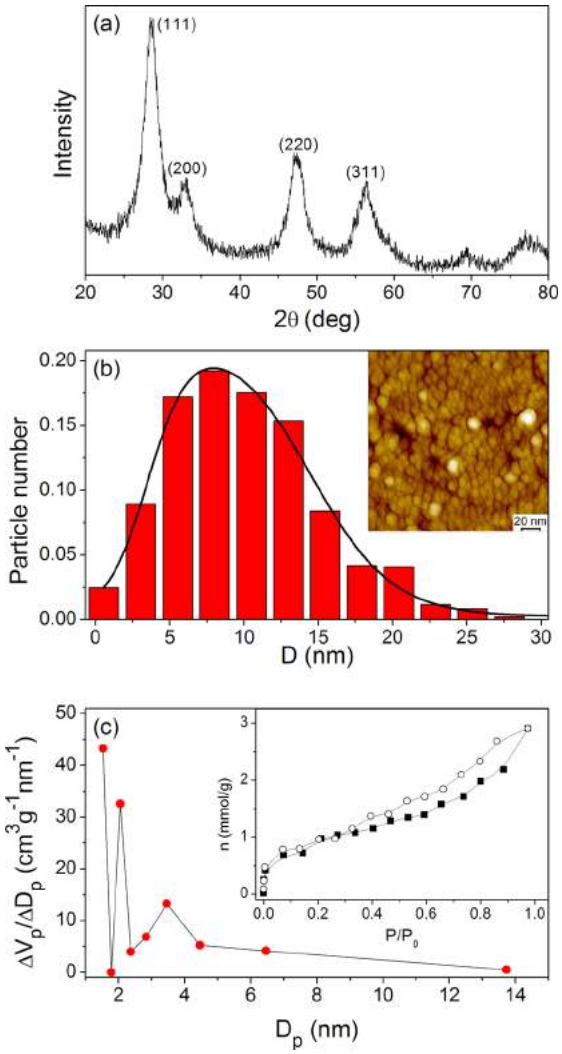

Figure 1. XRD spectrum (a), particle size distribution obtained from AFM (b), and pore size distribution curve obtained from the desorption branch of the isotherm (c) for $CeO_{2-\delta}$ nanopowder. Insets present the AFM image and the nitrogen adsorption−desorption isotherm of $CeO_{2-\delta}$ nanopowder.

solutions after 2 min showed that the dyes were present in a very low concentration. From the photo images (right panel of Figure 2b,c), it can be noticed that the solutions were almost colorless after 2 min. The experiment was repeated with an increased concentration for all three dyes (100 mg L^{-1}), and the obtained results were similar.

The concentration of RO16 in the solution was further increased to 200 mg L^{-1}. The absorption spectra of RO16 dye solution in the presence of $CeO_{2-\delta}$ nanoparticles, presented in Figure S1a (Supporting Information), demonstrate that $CeO_{2-\delta}$ quickly removes the RO16 from the solution. After 40 min, the equilibrium state was reached. The adsorption measurements were also performed on the solutions of MO and MB9 (200 mg L^{-1}) in the presence of $CeO_{2-\delta}$ nanopowder, in order to compare the efficiency of adsorption process onto ceria nanopowder for all three dyes. The adsorption capacity of $CeO_{2-\delta}$ nanopowder was determined from the mass balance relationship:[1,13,15,22]

$$q_e = \frac{(C_0 - C_e)V}{m} \quad (2)$$

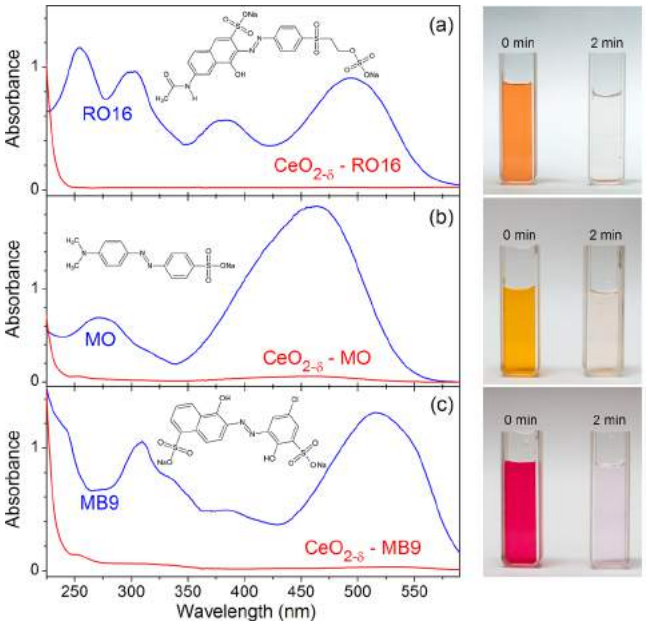

Figure 2. Absorption spectra with corresponding photo images of (a) RO16, (b) MO, and (c) MB9 dye solutions (50 mg L^{-1}) before and 2 min after introducing $CeO_{2-\delta}$ nanoparticles (2 g L^{-1}). Mass of adsorbent = 50 mg; solution volume = 25 mL.

where q_e represents the amount of dye adsorbed per unit mass of adsorbent (mg g^{-1}), C_0 and C_e are the initial and equilibrium liquid phase concentrations (mg L^{-1}), respectively, V is the volume of the solution (L), and m is the mass (g) of $CeO_{2-\delta}$ used.

The adsorption rate and the amount of adsorbed dye with contact time for the solutions of RO16, MO, and MB9 (200 mg L^{-1}) are illustrated in Figure 3a,b. As can be noticed from Figure 3, for all three curves, it is characteristic that the adsorption process is rapid in the initial stage, whereas in the later stage it becomes much slower. The adsorption rate for RO16 was higher at the beginning, but after 60 min much better elimination of MO from the solution was observed, whereas the adsorption rate of MB9 was still lower. The equilibrium was achieved after 40 (60) min for RO16 (MO), whereas for MB9 it was achieved after 180 min. The adsorption capacities of $CeO_{2-\delta}$ nanopowder in the case of MO, MB9, and RO16 were 100, 94, and 91 mg g^{-1}, respectively.

Further, the adsorption capacities of $CeO_{2-\delta}$ nanopowder and activated carbon were compared. The adsorption capacity of commercial activated carbon (50 mg) is presented in Figure 4 for MO (a) , RO16 (b), and MB9 (c) solutions (200 mg L^{-1}). In the case of MO dye solution, it can be noticed that at the beginning of the adsorption process the activated carbon was slightly faster than $CeO_{2-\delta}$ nanopowder and reached the equilibrium state after 20 min. After 60 min, both curves overlapped. In the case of RO16 dye solution, activated carbon was much slower compared to $CeO_{2-\delta}$. After 40 min, $CeO_{2-\delta}$ nanopowder reached equilibrium and eliminated almost 90% of RO16 from the solution, whereas activated carbon needed 2 h to reach the final adsorption capacity of 85 mg g^{-1} which was still lower than that of ceria nanopowder (91 mg g^{-1}). The adsorption capability of $CeO_{2-\delta}$ for MB9 is lower than that for activated carbon, although after 2 h the final adsorption capacities were comparable.

dx.doi.org/10.1021/la502969w | Langmuir 2014, 30, 11582−11590

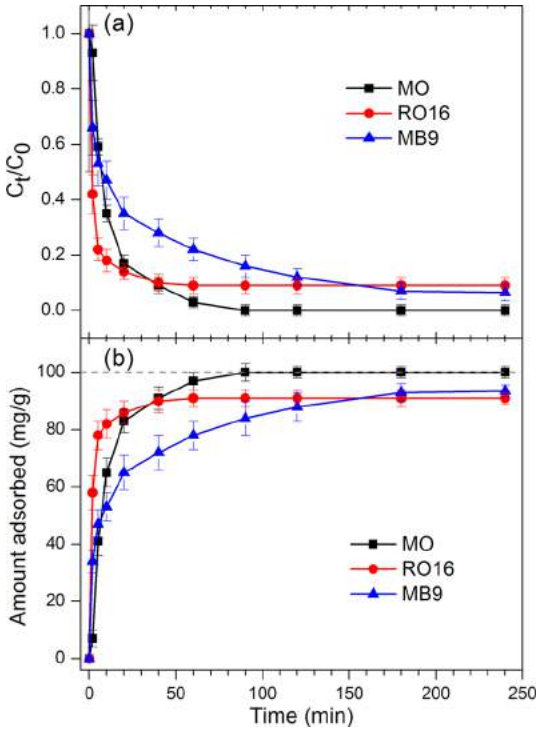

Figure 3. Adsorption rate (a) and amount of adsorbed dyes (b) for the solutions of MO, RO16, and MB9 (200 mg L^{-1}) in the presence of $CeO_{2-\delta}$ nanopowder. Mass of adsorbent = 50 mg; solution volume = 25 mL.

In Figure 5a–c are shown the IR transmission spectra of pure dyes and $CeO_{2-\delta}$ nanopowders after dye adsorption. For comparison, the IR spectrum of pure $CeO_{2-\delta}$ nanopowder is also given in Figure 5a–c.

The IR spectra of pure dyes have some common characteristic bands.[4,6,31−36] The bands at 1040/1120 cm^{-1} in MO, 1054/1139 cm^{-1} in RO16, and 1044/1136 cm^{-1} in MB9 originate from the symmetric stretching vibrations of the SO_3^- group ($\nu_s(SO_3^-)$). The band at 1204 cm^{-1} in MO, 1236 cm^{-1} in RO16, and 1190 cm^{-1} in MB9 represents the asymmetric stretching vibrations of the SO_3^- group ($\nu_{as}(SO_3^-)$). The band at 1368 cm^{-1} in MO and 1372 cm^{-1} in RO16 belongs to the C−N stretching vibrations. The bands at 1422, 1410, and 1409 cm^{-1} in MO, RO16, and MB9, respectively, are assigned to the N═N stretching vibrations. The bands at 1520/1608 cm^{-1} in MO and 1586 cm^{-1} in RO16 are from the aromatic ring stretching vibrations. The band at 1672 cm^{-1} in the spectra of RO16 originates from the stretching vibrations of the carbonyl C═O group.

In the IR spectrum of MO dye adsorbed on $CeO_{2-\delta}$ (shown in Figure 5a), the IR bands of the MO dye are of much lower intensity. The pronounced changes of the IR bands characteristic for sulfonate stretching vibration mode are observed. The $\nu_{as}(SO_3^-)$ band at 1204 cm^{-1} is much weaker after MO adsorption on $CeO_{2-\delta}$ and shifted to ∼1193 cm^{-1} (marked with arrow in Figure 5a). The $\nu_s(SO_3^-)$ band at 1040 cm^{-1} in MO is slightly shifted to 1034 cm^{-1} (marked with arrow in Figure 5a) in the CeO_2−MO spectrum, the intensity of which is much lower after adsorption. All these changes can indicate that the sulfonate group is strongly involved in the adsorption of MO onto $CeO_{2-\delta}$.[34] In the IR spectrum of RO16 adsorbed onto $CeO_{2-\delta}$ (Figure 5b), a significant intensity decrease of the IR bands at 1054/1139 and 1500 cm^{-1}, characteristic for SO_3^-

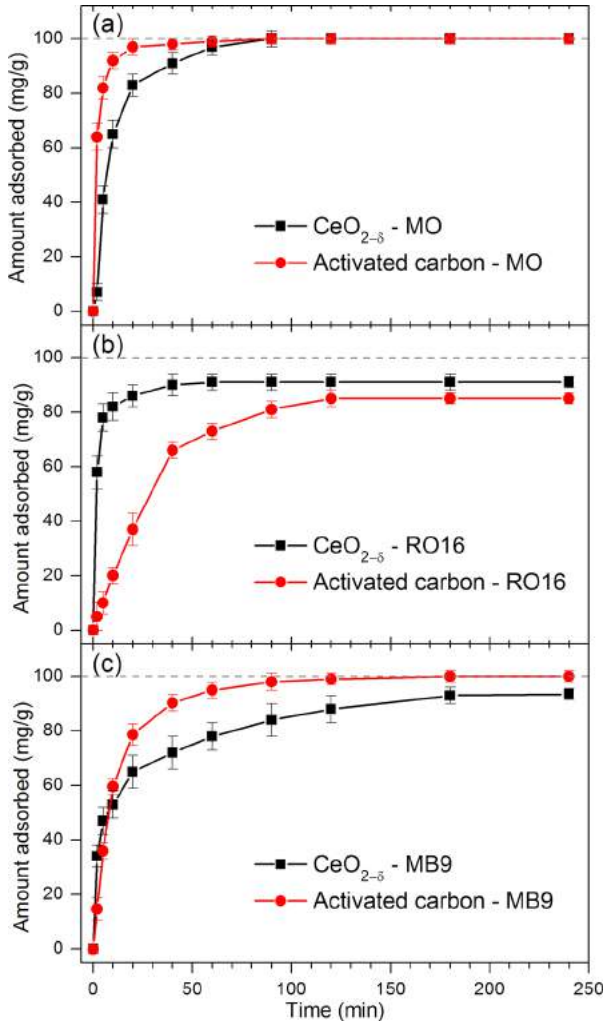

Figure 4. Comparison of adsorption capacities between $CeO_{2-\delta}$ nanopowder and activated carbon in the case of (a) MO, (b) RO16, and (c) MB9 dye solutions (200 mg L^{-1}). Mass of adsorbent = 50 mg; solution volume = 25 mL.

group and N−H bending vibrations,[4,6] is observed too. Many other bands which belong to pure RO16 dye are much weaker or barely visible in the $CeO_{2-\delta}$−RO16 spectrum, as for instance the band at 1410 cm^{-1} for N═N stretching vibrations. The carbonyl C═O peak at 1672 cm^{-1} in the IR spectrum of RO16, is almost absent from the $CeO_{2-\delta}$−RO16 spectrum. The $\nu_s(SO_3^-)$ band is shifted from 1139 to 1136 cm^{-1} in the $CeO_{2-\delta}$−RO16 spectrum. In the IR spectrum of $CeO_{2-\delta}$−MB9 (Figure 5c), a major decrease of the MB9 band intensity is observed and the slight shift of the asymmetric $\nu_s(SO_3^-)$ band is barely visible (marked with arrow in Figure 5c). All this indicates that RO16 and MB9 are also strongly adsorbed onto the $CeO_{2-\delta}$ surface. In Figure 5d is presented the IR transmission spectrum of pure $CeO_{2-\delta}$ in the extended spectral range. As can be seen, strong bands near 3400 and 1620 cm^{-1} are attributed to the adsorbed H_2O and hydroxyls.[37,38] The absorption band at 1384 cm^{-1} originates from CO_2 molecule vibrations.

Raman spectra, obtained on $CeO_{2-\delta}$ nanopowder before and after dye adsorption, are presented in Figure 6 and are consistent with the IR measurements. In the Raman spectra of nanocrystalline $CeO_{2-\delta}$ treated with dyes, besides the F_{2g} mode of pure $CeO_{2-\delta}$ positioned at ∼456.5 cm^{-1} and the mode at

dx.doi.org/10.1021/la502969w | Langmuir 2014, 30, 11582−11590

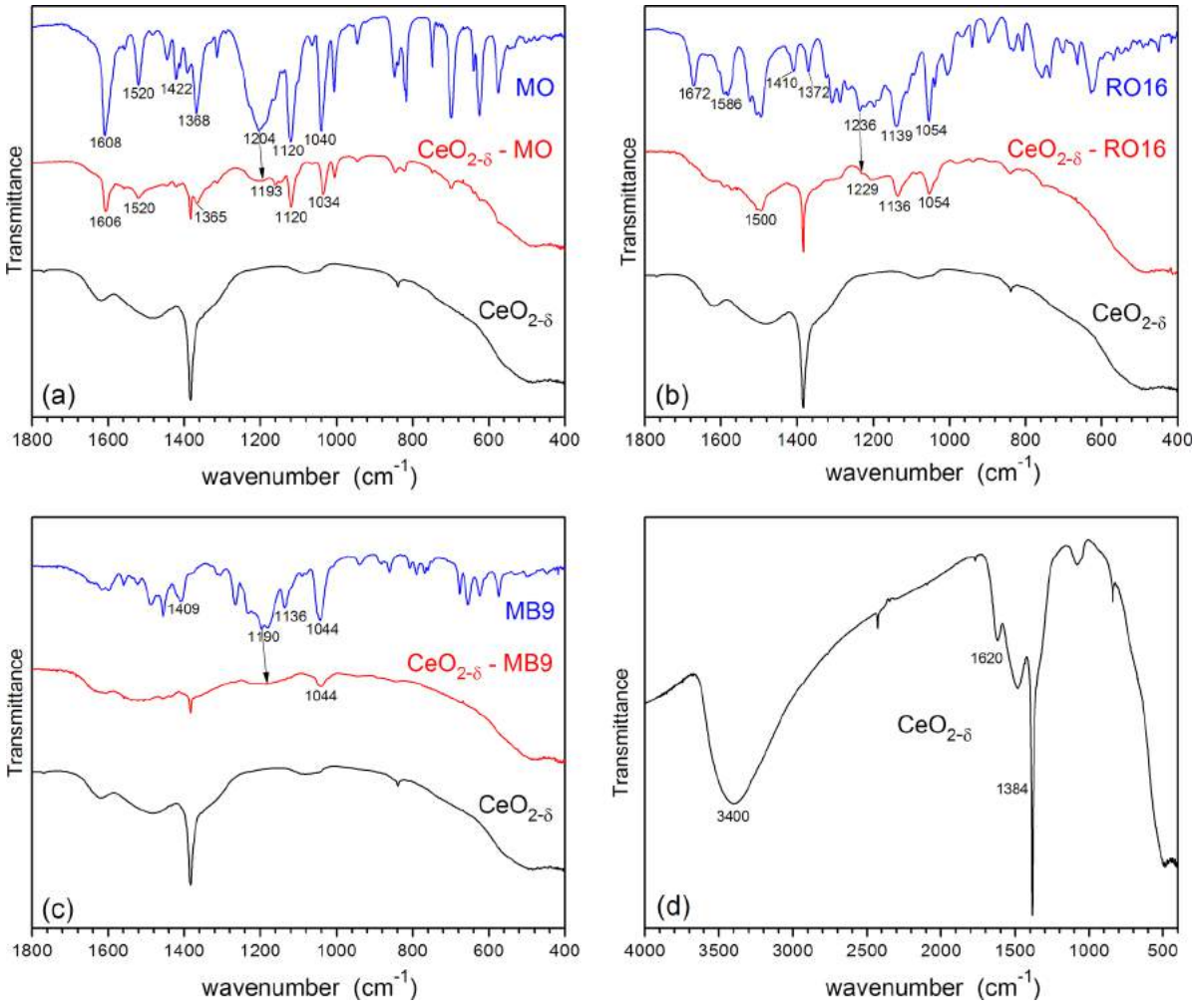

Figure 5. IR transmission spectra of (a) MO, (b) RO16, and (c) MB9 adsorbed on $CeO_{2-\delta}$ together with the transmission spectra of pure dyes and $CeO_{2-\delta}$ nanopowder. (d) IR transmission spectrum of $CeO_{2-\delta}$ nanopowder in the extended range.

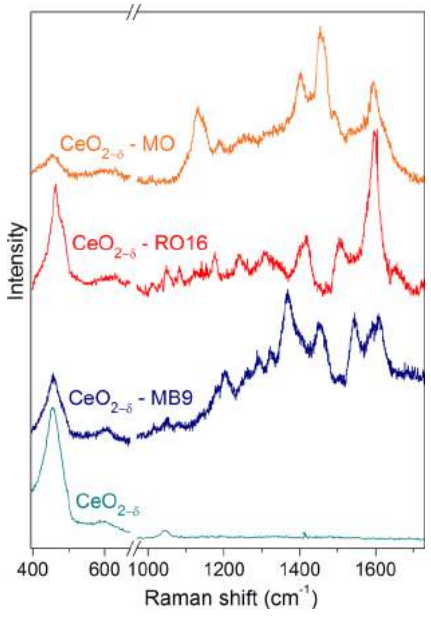

Figure 6. Room temperature Raman spectra of $CeO_{2-\delta}$ nanopowder before and after adsorption of MO, RO16, and MB9 dyes.

~600 cm^{-1} which belongs to intrinsic oxygen vacancies,[39] additional modes are observed. These new modes correspond to the vibrations of different atomic groups of dye molecules, such as −N═N−, −C═O, −S═O, −O−H, and aromatic ring vibrations. The most prominent mode frequencies deduced from the spectra of ceria treated with MO, RO16, and MB9 are summarized in the Table S2 (see the Supporting Information). As the majority of the atomic group vibrations characteristic for the dye molecules in question are observed in the Raman spectra of dyed ceria nanopowder, it can be concluded that in all three cases the adsorption of dye molecules took place.

The IR and Raman spectra unambiguously showed that MO, RO16, and MB9 are adsorbed on $CeO_{2-\delta}$ surface. In addition, from the IR spectra of three azo dyes adsorbed on $CeO_{2-\delta}$ nanopowders, we concluded that ν_{as} and ν_s bands of sulfonate groups are affected considerably. The intensity ratio of these bands ($\nu_{as}(SO_3^-)/\nu_s(SO_3^-)$ = 0.4) for adsorbed MO onto ceria is different from the same ratio in the spectrum of isolated MO ($\nu_{as}(SO_3^-)/\nu_s(SO_3^-)$ = 0.9). The changes of the ν_{as} and ν_s band intensities of sulfonate groups are also registered in the IR spectra of adsorbed RO16 and MB9 onto ceria. It is further worth mentioning that the frequency difference $\Delta\nu_{as\text{-}s}$ ($\nu_{as}(SO_3^-) - \nu_s(SO_3^-)$) in the MO, RO16, and MB9 spectra is higher than that in the corresponding spectra of adsorbed dyes on ceria (see Figure 5). This is characteristic of the

dx.doi.org/10.1021/la502969w | Langmuir 2014, 30, 11582−11590

bidentate type coordination according to the Deacon and Phillips[40] empirical rule and the work of Bauer et al.,[41] formed when OH groups situated on the surface metal cations are substituted with oxygen atoms from azo dyes. Ji et al.[4] noticed similar changes to ours in the IR spectra of acid orange adsorbed onto CeO_2 surface and proposed that a bidentate type bridge is formed between sulfonate group and Ce^{4+} cations. According to the observed changes in the IR spectra of MO, RO16, and MB9 adsorbed on $CeO_{2-\delta}$ nanopowder, it is reasonable to assume that all three dyes form a bidentate type bridge on the ceria surface, where two oxygen atoms of the SO_3^- group are bound to one or two Ce^{4+} cations in a process that involves the substitution of surface coordinated OH groups on Ce^{4+} cations with oxygen atoms from azo dyes.

Another very important factor for dye removal concerns the capability of $CeO_{2-\delta}$ nanopowders to easily form oxygen vacancies on the surface which accompany functional groups. The surface functional groups can interact with dye molecules via hydrogen bonds and/or electrostatic forces promoting the adsorption of dye molecules. The first principle density functional theory calculations performed by Yang et al.[42] have shown that, in oxygen deficient ceria, the adsorbed water molecules prefer to decompose near the oxygen vacancy site, forming surface hydroxyls, where H atoms are bonded with surface oxygen atoms. Therefore, they concluded that in reduced ceria both adsorbed H_2O and surface hydroxyls coexist. Their calculations are in good agreement with experimental work of Kundakovic et al.[43] performed on oxidized and reduced CeO_2 thin films, who detected surface hydroxyls only in reduced ceria films.

Having in mind that our ceria is oxygen deficient, it is reasonable to assume that hydroxyl groups, already observed in the IR spectra, are present on the surface of $CeO_{2-\delta}$ nanopowder. The experimental determination of the pH value at zero point charge (pH_{ZPC}) revealed that $CeO_{2-\delta}$ has pH_{ZPC} = 6.3 (Figure S2 in the Supporting Information). As pH values of the dye solutions are lower than pH_{ZPC} of $CeO_{2-\delta}$ (see section 3 in Experimental Section), $CeO_{2-\delta}$ as adsorbent acts as a positive surface. The electrostatic attraction between ceria nanoparticles and negatively charged dye ions is an operable mechanism. In that case, the ceria surface hydroxyls are protonated:

$$Ce{-}OH + H^+ \rightarrow Ce{-}OH_2^+ \quad (3)$$

In aqueous solution, the sulfonate groups ($R{-}SO_3Na$) dissociate and are converted to anionic dye ions. The adsorption process further proceeds due to the electrostatic attraction between these two oppositely charged ions:

$$Ce{-}OH_2^+ + R{-}SO_3^- \rightleftarrows Ce{-}OH_2^+ \cdots {}^-O_3S{-}R \quad (4)$$

Illustration of the adsorption mechanisms between dye molecules and $CeO_{2-\delta}$ adsorbent is shown in Figure 7.

As we stated earlier, the adsorption rate at the beginning of the process (presented in Figure 3a) is higher for RO16 than for MO and MB9. The difference in removal efficiency between three dyes can be explained by the fact that the pH value of the RO16 solution is close to the pH value where ceria net positive charge surface has maximum, whereas the pH values of MO and MB9 dye solutions are close to the pH_{ZPC} value of $CeO_{2-\delta}$. Therefore, the electrostatic interaction between RO16 dye molecules and $CeO_{2-\delta}$ at the beginning will be stronger than that for MB9 and MO. It is important to emphasize that

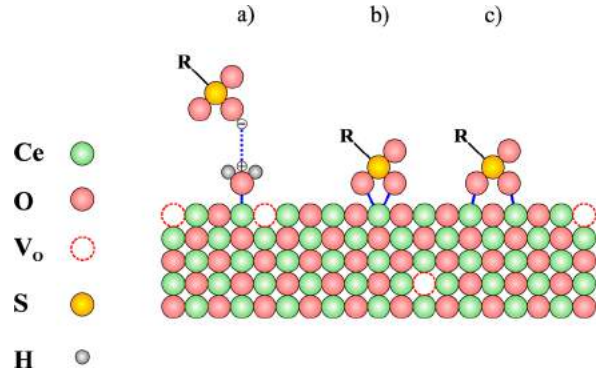

Figure 7. Schematic representation of RO16, MO, and MB9 adsorption on $CeO_{2-\delta}$ surface. (a) Electrostatic interaction between protonated ceria surface and sulfonate group in the dye molecule; (b, c) bidentate type structures between sulfonate group and Ce^{4+} cations.

sulfonic groups, which dissociate in aqueous solution and convert to $R{-}SO_3^-$ anions, are negatively charged even at higher acidic solutions, because their pK_a values are lower than zero.[44] Finally, the interaction between OH groups on the surface of $CeO_{2-\delta}$ and NH groups of the RO16 is also a possible mechanism for RO16 dye adsorption[19] and can explain the higher adsorption rate in the case of RO16 at the beginning of the process.

The study of the adsorption equilibrium isotherm is helpful in determining the maximum adsorption capacity of adsorbent for given adsorbate. These isotherms relate the dye uptake per unit mass of adsorbent, q_e, to the equilibrium liquid phase concentration C_e. In Figure 8 are presented the adsorption isotherms for RO16 (a), MO (b), and MB9 (c) dye solutions, measured at room temperature. Adsorption isotherms were analyzed according to Langmuir and Freundlich models in order to determine the best-fit model. Langmuir's model predicts the monolayer coverage of the adsorbate, assuming that all adsorption sites are identical and energetically equivalent, whereas the Freundlich's model assumes the adsorption on heterogeneous surface composed of nonidentical adsorption sites with different energy of adsorption. The isotherm equations and isotherm parameters for both models are listed in Supporting Information Table S3.

The adsorption isotherms of RO16 and MO from Figure 8a,b can be fitted by both the Langmuir and Freundlich equations. Both models give reasonable good fit in the case of MO and RO16, although the values of correlation coefficients (Supporting Information Table S3) are slightly higher for the Langmuir isotherm. The sorption data of MB9 are much better represented by the Freundlich model (Figure 8c and Supporting Information Table S3) which expresses adsorption in a multilayer manner on an energetically heterogeneous surface.

The parameter $1/n$ from the Freundlich equation characterizes the heterogeneity of the site energies and the adsorption intensity, that is, the degree of nonlinearity of adsorption isotherm. In their work, Tseng and Wu[45] have defined a favorable level for the adsorption isotherm curves and gave a classification for the values of parameter $1/n$. Despite the fact that the Langmuir model seems more suitable to describe the sorption of MO and RO16 onto ceria, according to Tseng's classification, the parameter $1/n$ (listed in Supporting Information Table S3) lies in the range of strongly favorable (for RO16 and MO) and favorable (for MB9) adsorption.

dx.doi.org/10.1021/la502969w | Langmuir 2014, 30, 11582−11590

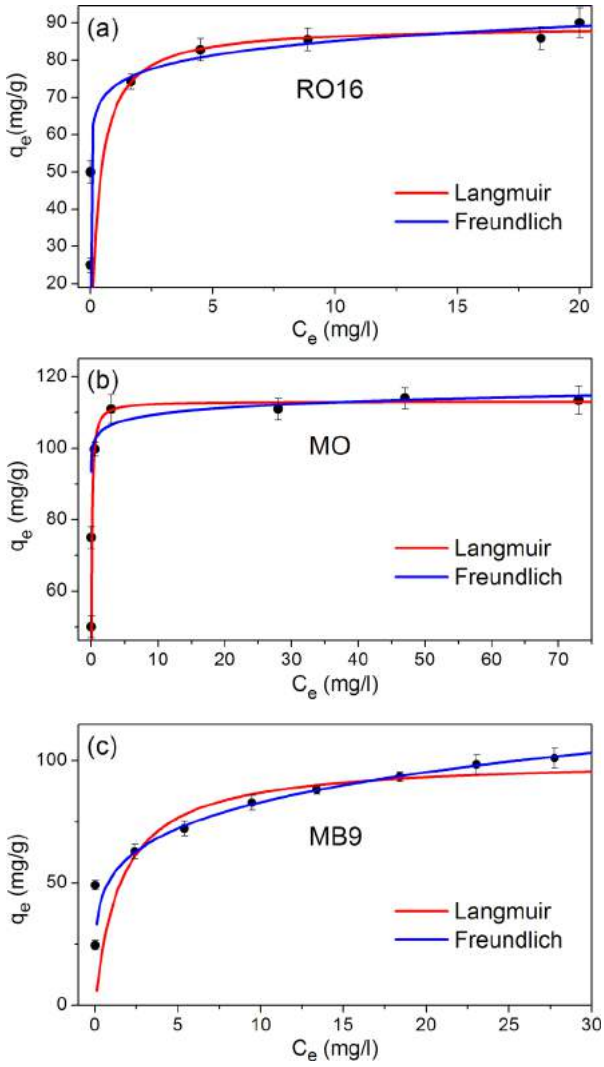

Figure 8. Adsorption isotherms of (a) RO16, (b) MO, and (c) MB9 dye solutions on $CeO_{2-\delta}$ at room temperature. Initial dye concentration = 50–230 mg L^{-1}; mass of adsorbent = 50 mg; solution volume = 25 mL.

Therefore, keeping in mind that oxygen-deficient surface of nanosized ceria is more heterogeneous than homogeneous, it is reasonable to conclude that adsorption of MB9, MO, and RO16 on $CeO_{2-\delta}$ nanopowders reflects the presence of more than one kind of adsorbent–adsorbate surface interaction. The maximal adsorption capacity values of $CeO_{2-\delta}$ nanopowder from isotherm data were found to be 113, 101, and 91 mg g^{-1} in the case of MO, MB9, and RO16 respectively.

To get further insight into the mechanism of adsorption, pseudo-first- and pseudo-second-order models were used to simulate the adsorption data for various contact times from Figure 3b. The pseudo-first-order model didn't give a good fit of the experimental data and will be omitted in further discussion. Kinetic data were further analyzed with the pseudo-second-order kinetic model shown in Figure 9. The linear form of the pseudo-second-order model is expressed as follows:

$$\frac{t}{q_t} = \frac{1}{k_2 q_e^{\,2}} + \frac{t}{q_e} \tag{4}$$

where q_e and q_t refer to the amount of adsorbed dye at equilibrium and at time t, respectively, and k_2 is the equilibrium

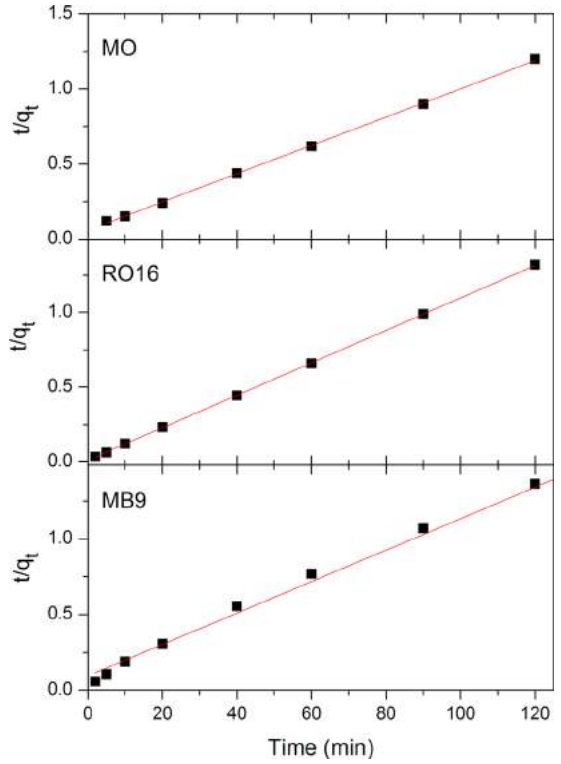

Figure 9. Pseudo-second-order kinetics of MO, RO16, and MB9 onto $CeO_{2-\delta}$ nanopowder. Initial dye concentration = 200 mg L^{-1}; mass of adsorbent = 50 mg; solution volume = 25 mL.

rate constant of the pseudo-second-order kinetic model. The linear plots of t/q_t vs t (Figure 9) show that the experimental data agree well with the pseudo-second-order kinetic model for all three dyes. The values of q_e and k_2 were calculated from the slope and intercept of eq 4, and their values are given in Table 1, together with experimental q_e values and correlation

Table 1. Pseudo-Second-Order Kinetic Model Parameters Together with Experimental q_e Values for Adsorption of Each Dye

	$q_{e,cal}$ (mg g^{-1})	$q_{e,exp}$ (mg g^{-1})	k_2 (g mg^{-1} min^{-1})	R^2
MO	106.3	100	1.44×10^{-3}	0.9994
RO16	100	91	9.09×10^{-3}	0.9999
MB9	96.3	93.6	1.13×10^{-3}	0.9977

coefficients. Calculated q_e values, tabulated in Table 1, are in quite good agreement with experimental ones and the correlation coefficients have large values ($R^2 > 0.99$). It can be concluded that the adsorption of MO, RO16, and MB9 on $CeO_{2-\delta}$ nanopowder follows the pseudo-second-order kinetic model which relies on the assumption that chemisorption and effective electrostatic interactions play a major role in the adsorption process.[46,47] Comparing the adsorption capacities of $CeO_{2-\delta}$ nanopowder with other adsorbents mentioned in the Introduction, we can conclude that $CeO_{2-\delta}$ nanopowder, produced by cost-effective SPRT method, shows efficient adsorption properties and is a promising candidate for environmentally friendly adsorbents in water treatment.

CONCLUSIONS

The $CeO_{2-\delta}$ nanopowder, synthesized by a facile and cost-effective SPRT method, appeared to be a very effective sorbent

dx.doi.org/10.1021/la502969w | *Langmuir* 2014, 30, 11582–11590

for the MO, RO16, and MB9 azo dyes. The adsorption process was monitored at fixed initial pH value and varying dye concentration and contact time. Infrared and Raman spectroscopy measurements confirmed that the adsorption of azo dyes on the $CeO_{2-\delta}$ surface took place. The experimental adsorption data for the MO and RO16 were slightly better fitted with the Langmuir isotherm, whereas the Freundlich isotherm was a better fit for MB9 over the whole concentration range. According to the values of the Freundlich constant ($1/n$), the adsorption of MB9, MO, and RO16 lies in a favorable and strongly favorable zone. The highest adsorption capacity of $CeO_{2-\delta}$ was obtained for MO (113 mg g^{-1}) and then for MB9 (101 mg g^{-1}) and RO16 (91 mg g^{-1}). The formation of a bidentate type bridge between sulfonate group and Ce^{4+} cations and the protonation of ceria surface hydroxyls can be responsible for effective adsorption process. Adsorption of MO, RO16, and MB9 dyes follows the pseudo-second-order equation with good correlation. These results imply that, besides strong electrostatic sorption, chemisorption mechanism may play an important role for the dye adsorption. Based on our results, ceria nanopowder prepared by the SPRT method represents an effective dye adsorbent and can be a promising substitute in wastewater treatment.

■ ASSOCIATED CONTENT

Supporting Information

Figures showing absorption spectra of RO16 (200 mg L^{-1}) and photo image of RO16 solutions in the presence of $CeO_{2-\delta}$ nanopowders, and zeta potential of $CeO_{2-\delta}$ nanoparticles. Tables showing dye structures and their wavelengths of maximal absorption, values of the Raman shifts extracted from the experimental Raman spectra of $CeO_{2-\delta}$ nanopowder after adsorption of MO, RO16, and MB9, and isotherm equations and parameters for azo dyes at room temperature. This material is available free of charge via the Internet at http://pubs.acs.org.

■ AUTHOR INFORMATION

Corresponding Author

*E-mail: zordoh@ipb.ac.rs.

Notes

The authors declare no competing financial interest.

■ ACKNOWLEDGMENTS

We thank Bojan R. Stojadinović for the AFM image and Bojan Čalija for the zeta potential measurements. This work was financially supported by the Serbian Ministry of Education, Science and Technological Development under Projects ON171032 and III45018 and bilateral Project Serbia-Italy No. RS13MO11.

■ REFERENCES

(1) Lee, J. W.; Choi, S. P.; Thiruvenkatachari, R.; Shim, W. G.; Moon, H. Evaluation of the performance of adsorption and coagulation processes for the maximum removal of reactive dyes. *Dyes Pigm.* **2006**, *69*, 196−203.

(2) Gomez, V.; Larrechi, M. S.; Callao, M. P. Kinetic and adsorption study of acid dye removal using activated carbon. *Chemosphere* **2007**, *69*, 1151−1158.

(3) Silva, J. P.; Sousa, S.; Rodrigues, J.; Antunes, H.; Porter, J. J.; Goncalves, I.; Ferreira-Dias, S. Adsorption of acid orange 7 dye in aqueous solutions by spent brewery grains. *Sep. Purif. Technol.* **2004**, *40*, 309−315.

(4) Ji, P. F.; Zhang, J. L.; Chen, F.; Anpo, M. Study of adsorption and degradation of acid orange 7 on the surface of CeO_2 under visible light irradiation. *Appl. Catal., B* **2009**, *85*, 148−154.

(5) Venkatesha, T. G.; Viswanatha, R.; Nayaka, Y. A.; Chethana, B. K. Kinetics and thermodynamics of reactive and vat dyes adsorption on MgO nanoparticles. *Chem. Eng. J.* **2012**, *198*, 1−10.

(6) Sahasrabudhe, M.; Pathade, G. Biodegradation of azo dye C.I. Reactive Orange 16 by an actinobacterium Georgenia sp. CC-NMPT-T3. *Int. J. Adv. Res.* **2013**, *1*, 91−99.

(7) Mohan, D.; Pittman, C. U., Jr Activated carbons and low cost adsorbents for remediation of tri- and hexavalent chromium from water. *J. Hazard. Mater.* **2006**, *137*, 762−811.

(8) Pollard, S. J. T.; Fowler, G. D.; Sollars, C. J.; Perry, R. Low-cost adsorbents for waste and wastewater treatment: a review. *Sci. Total Environ.* **1992**, *116*, 31−52.

(9) Amin, N. K. Removal of direct blue-106 dye from aqueous solution using new activated carbons developed from pomegranate peel: Adsorption equilibrium and kinetics. *J. Hazard. Mater.* **2009**, *165*, 52−62.

(10) Sharma, Y. C.; Uma; Upadhyay, S. N. Removal of a cationic dye from wastewaters by adsorption on activated carbon developed from coconut coir. *Energy Fuels* **2009**, *23*, 2983−2988.

(11) Aygün, A.; Yenisoy-Karakaş, S.; Duman, I. Production of granular activated carbon from fruit stones and nutshells and evaluation of their physical, chemical and adsorption properties. *Microporous Mesoporous Mater.* **2003**, *66*, 189−195.

(12) Kannan, N.; Sundaram, M. M. Kinetics and mechanism of removal of methylene blue by adsorption on various carbons—a comparative study. *Dyes Pigm.* **2001**, *51*, 25−40.

(13) Annadurai, G.; Juang, R. S.; Lee, D. J. Use of cellulose-based wastes for adsorption of dyes from aqueous solutions. *J. Hazard. Mater.* **2002**, *92*, 263−274.

(14) Haddadian, Z.; Shavandi, M. A.; Abidin, Z. Z.; Fakhru'l-Razi, A.; Ismail, M. H. S. Removal methyl orange from aqueous solutions using dragon fruit (Hylocereusundatus) foliage. *Chem. Sci. Trans.* **2013**, *2*, 900−910.

(15) Cheung, W. H.; Szeto, Y. S.; Mckay, G. Enhancing the adsorption capacities of acid dyes by chitosan nano particles. *Bioresour. Technol.* **2009**, *100*, 1143−1148.

(16) Wu, C. H. Adsorption of reactive dye onto carbon nanotubes: Equilibrium, kinetics and thermodynamics. *J. Hazard. Mater.* **2007**, *144*, 93−100.

(17) Zhong, L. S.; Hu, J. S.; Cao, A. M.; Liu, Q.; Song, W. G.; Wan, L. J. 3D flowerlike ceria micro/nanocomposite structure and its application for water treatment and CO removal. *Chem. Mater.* **2007**, *19*, 1648−1655.

(18) Ouyang, X. W.; Li, W.; Xie, S. L.; Zhai, T.; Yu, M. H.; Gan, J. Y.; Lu, X. H. Hierarchical CeO_2 nanospheres as highly-efficient adsorbents for dye removal. *New J. Chem.* **2013**, *37*, 585−588.

(19) Zhai, T.; Xie, S. L.; Lu, X. H.; Xiang, L.; Yu, M. H.; Li, W.; Liang, C. L.; Mo, C. H.; Zeng, F.; Luan, T. G.; Tong, Y. X. Porous $Pr(OH)_3$ nanostructures as high-efficiency adsorbents for dye removal. *Langmuir* **2012**, *28*, 11078−11085.

(20) Won, S. W.; Yun, H. J.; Yun, Y.-S. Effect of pH on the binding mechanisms in biosorption of Reactive Orange 16 by Corynebacterium glutamicum. *J. Colloid Interface Sci.* **2009**, *331*, 83−89.

(21) Won, S. W.; Choi, S. B.; Yun, Y.-S. Performance and mechanism in binding of Reactive Orange 16 to various types of sludge. *Biochem. Eng. J.* **2006**, *28*, 208−214.

(22) Janaki, V.; Vijayaraghavan, K.; Ramasamy, A. K.; Lee, K. J.; Oh, B. T.; Kamala-Kannan, S. Competitive adsorption of Reactive Orange 16 and Reactive Brilliant Blue R on polyaniline/bacterial extracellular polysaccharides composite-A novel eco-friendly polymer. *J. Hazard. Mater.* **2012**, *241*, 110−117.

(23) Suteu, D.; Zaharia, C.; Malutan, T. Removal of orange 16 reactive dye from aqueous solutions by waste sunflower seed shells. *J. Serb. Chem. Soc.* **2011**, *76*, 17.

(24) Zhao, D.; Zhang, W.; Chen, C.; Wang, X. Adsorption of Methyl Orange dye onto multiwalled carbon nanotubes. *Procedia Environ. Sci.* **2013**, *18*, 890−895.
(25) Saha, T. K.; Bhoumik, N. C.; Karmaker, S.; Ahmed, M. G.; Ichikawa, H.; Fukumori, Y. Adsorption of Methyl Orange onto Chitosan from Aqueous Solution. *J. Water Resour. Prot.* **2010**, *2*, 8.
(26) Ai, L.; Zhang, C.; Meng, L. Adsorption of Methyl Orange from Aqueous Solution on Hydrothermal Synthesized Mg−Al Layered Double Hydroxide. *J. Chem. Eng. Data* **2011**, *56*, 4217−4225.
(27) Yu, X.; Li, F.; Ye, X.; Xin, X.; Xue, Z. Synthesis of cerium(IV) oxide ultrafine particles by solid-state reactions. *J. Am. Ceram. Soc.* **2000**, *83*, 964−966.
(28) Boskovic, S.; Djurovic, D.; Dohcevic-Mitrovic, Z.; Popovic, Z.; Zinkevich, M.; Aldinger, F. Self-propagating room temperature synthesis of nanopowders for solid oxide fuel cells (SOFC). *J. Power Sources* **2005**, *145*, 237−242.
(29) Zhou, X.-D.; Huebner, W. Size-induced lattice relaxation in CeO_2 nanoparticles. *Appl. Phys. Lett.* **2001**, *79*, 3512−3514.
(30) Lowell, S. *Characterization of Porous Solids and Powders: Surface Area, Pore Size and Density*; Kluwer Academic Publishers: Dordrecht, The Netherlands, 2004.
(31) Jia, T.-J.; Song, G.; Li, P.-W.; He, T.-C.; Mo, Y.-J.; Cui, Y.-T. Vibrational modes study of methyl orange using SERS-measurement and the DFT method. *Mod. Phys. Lett. B* **2008**, *22*, 2869−2879.
(32) Sathiyabama, J.; Rajendran, S.; Selvi, J. A.; Amalraj, A. J. Methyl orange as corrosion inhibitor for carbon steel in well water. *Indian J. Chem. Technol.* **2008**, *15*, 462−466.
(33) Liu, Y.; Sun, D. Z. Development of Fe_2O_3-CeO_2-TiO_2/gamma-Al_2O_3 as catalyst for catalytic wet air oxidation of methyl orange azo dye under room condition. *Appl. Catal., B* **2007**, *72*, 205−211.
(34) Hua, Q.; Shi, F. C.; Chen, K.; Chang, S. J.; Ma, Y. S.; Jiang, Z. Q.; Pan, G. Q.; Huang, W. X. Cu_2O-Au nanocomposites with novel structures and remarkable chemisorption capacity and photocatalytic activity. *Nano Res.* **2011**, *4*, 948−962.
(35) Telke, A. A.; Kalyani, D. C.; Dawkar, V. V.; Govindwar, S. P. Influence of organic and inorganic compounds on oxidoreductive decolorization of sulfonated azo dye CI Reactive Orange 16. *J. Hazard. Mater.* **2009**, *172*, 298−309.
(36) Galindo, C.; Jacques, P.; Kalt, A. Photodegradation of the aminoazobenzene acid orange 52 by three advanced oxidation processes: UV/H_2O_2 UV/TiO_2 and VIS/TiO_2 - Comparative mechanistic and kinetic investigations. *J. Photochem. Photobiol., A* **2000**, *130*, 35−47.
(37) Yue, L.; Zhang, X.-M. Structural characterization and photo-catalytic behaviors of doped CeO2 nanoparticles. *J. Alloys Compd.* **2009**, *475*, 702−705.
(38) Danish, M.; Hashim, R.; Ibrahim, M. N. M.; Sulaiman, O. Characterization of physically activated acacia mangium wood-based carbon for the removal of methyl orange dye. *BioResources* **2013**, *8*, 16.
(39) Dohčević-Mitrović, Z. D.; Šćepanović, M. J.; Grujić-Brojčin, M. U.; Popović, Z. V.; Bošković, S. B.; Matović, B. M.; Zinkevich, M. V.; Aldinger, F. The size and strain effects on the Raman spectra of $Ce_{1-x}Nd_xO_{2-d}$ ($0 \leq x \leq 0.25$) nanopowders. *Solid State Commun.* **2006**, *137*, 387−390.
(40) Deacon, G. B.; Phillips, R. J. Relationships between the carbon-oxygen stretching frequencies of carboxylato complexes and the type of carboxylate coordination. *Coord. Chem. Rev.* **1980**, *33*, 227−250.
(41) Bauer, C.; Jacques, P.; Kalt, A. Investigation of the interaction between a sulfonated azo dye (AO7) and a TiO_2 surface. *Chem. Phys. Lett.* **1999**, *307*, 397−406.
(42) Yang, Z.; Wang, Q.; Wei, S.; Ma, D.; Sun, Q. The effect of environment on the reaction of water on the ceria(111) surface: A DFT+U study. *J. Phys. Chem. C* **2010**, *114*, 14891−14899.
(43) Kundakovic, L.; Mullins, D. R.; Overbury, S. H. Adsorption and reaction of H_2O and CO on oxidized and reduced Rh/CeO_x(111) surfaces. *Surf. Sci.* **2000**, *457*, 51−62.
(44) Lima, E. C.; Royer, B.; Vaghetti, J. C. P.; Simon, N. M.; da Cunha, B. M.; Pavan, F. A.; Benvenutti, E. V.; Cataluña-Veses, R.; Airoldi, C. Application of Brazilian pine-fruit shell as a biosorbent to removal of reactive red 194 textile dye from aqueous solution: Kinetics and equilibrium study. *J. Hazard. Mater.* **2008**, *155*, 536−550.
(45) Tseng, R.-L.; Wu, F.-C. Inferring the favorable adsorption level and the concurrent multi-stage process with the Freundlich constant. *J. Hazard. Mater.* **2008**, *155*, 277−287.
(46) Zhu, Y.-P.; Liu, Y.-L.; Ren, T.-Z.; Yuan, Z.-Y. Hollow manganese phosphonate microspheres with hierarchical porosity for efficient adsorption and separation. *Nanoscale* **2014**, *6*, 6627−6636.
(47) Yeddou-Mezenner, N. Kinetics and mechanism of dye biosorption onto an untreated antibiotic waste. *Desalination* **2010**, *262*, 251−259.

DENTAL MATERIALS 30 (2014) 476–486

Available online at www.sciencedirect.com

ScienceDirect

journal homepage: www.intl.elsevierhealth.com/journals/dema

Nano-structural and compositional basis of devitalized tooth fragility

Ksenija Zelic[a], *Petar Milovanovic*[a], *Zlatko Rakocevic*[b], *Sonja Askrabic*[c], *Jelena Potocnik*[b], *Miroslav Popovic*[d], *Marija Djuric*[a,*]

[a] *University of Belgrade, School of Medicine, Institute of Anatomy, Laboratory for Anthropology, 4/2 Dr. Subotica, 11000 Belgrade, Serbia*

[b] *University of Belgrade, INS Vinca, Laboratory of Atomic Physics, 12-14 Mike Alasa, 11001 Belgrade, Serbia*

[c] *University of Belgrade, Institute of Physics, Center for Solid State Physics and New Materials, 118 Pregrevica, 11000 Belgrade, Serbia*

[d] *University of Belgrade, Faculty of Physics, 12-16 Studentski trg, 11000 Belgrade, Serbia*

ARTICLE INFO

Article history:
Received 17 December 2012
Received in revised form
28 July 2013
Accepted 22 January 2014

Keywords:
Endodontics
Dentin
Atomic force microscopy
Micro-Raman spectroscopy
Energy dispersive X-ray analysis

ABSTRACT

Objective. Increased tooth fragility after devitalization is commonly observed but there is no definite mechanistic explanation for such phenomenon. Therefore, it is important to analyze more profoundly structural and compositional properties of this altered form of dentin. The present study investigates the differences between normal and devitalized dentin using advanced techniques.

Methods. Atomic force microscopic imaging (AFM), energy dispersive X-ray analysis (EDX) and micro-Raman spectroscopy were performed on 16 dentin specimens, eight vital and eight that underwent root-canal treatment at least two years before extraction and had no infection in root canals before or after devitalization.

Results. The mean size of mineral crystals showed by AFM was larger in devitalized than in healthy dentin in the same age category. AFM phase shifts in devitalized cases revealed altered mechanical characteristics and suggested differences in composition of material between devitalized teeth and healthy controls. No significant difference in Ca/P ratio between vital and devitalized teeth was found using EDX. However, micro-Raman analyses showed that in devitalized teeth, apart from hydroxyapatite, dentin contained significant amounts of apatite phases with lower calcium content: octacalcium phosphate, dicalcium phosphate dihydrate and tricalcium phosphate.

Significance. Differences between vital and devitalized dentin bring new insights into the basis of devitalized tooth fragility. Larger mineral crystals could account for decreased mechanical strength in devitalized teeth. Moreover, calcium–phosphate phases with lower Ca content have lower material strength, and the presence of these phases in devitalized teeth may explain their increased fragility.

* *Corresponding author at*: Laboratory for Anthropology, Institute of Anatomy, School of Medicine, University of Belgrade, 4/2 Dr. Subotica, 11000 Belgrade, Serbia. Tel.: +381 11 2686 172; fax: +381 11 2686 172.
E-mail address: marijadjuric5@gmail.com (M. Djuric).

0109-5641/$ – see front matter © 2014 Academy of Dental Materials. Published by Elsevier Ltd. All rights reserved.
http://dx.doi.org/10.1016/j.dental.2014.01.014

1. Introduction

Tooth fracture remains one of the major problems in dentistry. As it is commonly observed in dental practice, one of the main factors leading to increased tooth fragility is its devitalization [1–3]. However, hitherto there have been no definite mechanistic explanations for devitalized teeth fragility.

Many factors contributing to weakening of devitalized teeth have been proposed [4]. First of all, a large amount of tooth tissue that has to be removed during endodontic procedure impairs tooth geometry which may reduce its fracture resistance [5,6]. Use of irrigants and medications, during root canal treatment, could demineralize the dentin around the pulp cavity [7,8]. Bacterial collagenolytic activity with subsequent deterioration of dentin structure [9] could also contribute to tooth weakening. Additional hypothesis that has been a subject of several studies proposed that the moisture content of dentin changes after devitalization [4,10–12], consequently changing dentin mechanical properties. However, these factors cannot fully explain why endodontically treated teeth are more susceptible to fracture [4].

Since dentin is the most abundant tissue in human tooth, it is expected that alterations in its structure can lead to increased fragility of the tooth [1,3]. Dentin is a biological composite of mineral phase (hydroxyapatite – approximately 50% by volume), organic phase (type I collagen fibrils, approximately 30% by volume), and fluid [13]. In recent years, novel techniques have been extensively used to study the morphology of dentin as well as other calcified tissues [14–16]. Using various advanced characterization methods (X-ray diffraction, small angle X-ray scattering, atomic force microscopy, transmission electron microscopy) the size and shape of mineral crystals, their orientation, molecular/chemical composition and mechanical properties of dentin were closely studied [1,3,17–21].

Micro- and nano-structural alterations due to caries, sclerosis and aging, as well as the effects of the dental procedures can have significant impact on tooth strength. Recently, novel techniques have been used to analyze some altered forms of dentin with the aim to predict the influence of the microstructural alteration on tooth strength [3].

However, up to now, there have been no attempts to analyze the possible changes in the shape, size and composition of the nanocrystalline apatite mineral of the devitalized dentin.

Therefore, in this study we have performed combined atomic force microscopy, scanning electron microscopy/energy dispersive X-ray analysis and micro-Raman spectroscopy characterization of the intertubular dentin material in vital and devitalized teeth, with the aim to examine the nano-structural and compositional basis for observed mechanical deterioration of devitalized teeth. We hypothesized that losing blood supply and subsequent elimination of the dentin fluid in devitalized teeth could leave traces on the nano-structure and material composition of the dentin, resulting in its altered mechanical characteristics.

2. Materials and methods

2.1. Specimen selection and preparation

The experimental group consisted of eight specimens of freshly extracted human premolars with root canal treatment performed at least two years before extraction. The exclusion criteria associated with root canal infection were: history of a previous root canal infection, current radiological signs of acute or chronic periapical infection and macroscopically visible deterioration of periapical tooth cement and dental socket which were examined after extraction. All teeth were filled with gutta-percha. The control group consisted of eight specimens of intact (vital) teeth. The specimens of both vital and devitalized groups were divided according to the age of individuals at the moment of extraction into two categories: young (18–22 years of age) and old (55–60 years of age). All teeth were extracted for orthodontic or periodontal reasons at Department of Oral Surgery, School of Dentistry, University of Belgrade according to the protocol approved by The Ethical Committee of The School of Dentistry, University of Belgrade and for every tooth the Patient's Informed Consent was obtained. The teeth were cleaned, stored frozen and analyzed shortly after the extraction. Each specimen was taken from different tooth.

The whole teeth were mounted in epoxy resins (Mecaprex KM-U, Grenoble, France) and were cut longitudinally (parallel with the tooth canal) to provide 1 mm thick sections using a diamond-saw microtome (Leica SP1600, Nussloch (Germany) under constant water irrigation (Fig. 1A). A low-speed diamond wheel saw 650 with water soluble coolant (South Bay Technology Inc., San Clemente, CA, USA) was used to obtain dentin specimens (Fig. 1B). To avoid influence of endodontic irrigants on dentin the specimens were cut at least 2 mm away from the root wall (Fig. 1B). At this point influence of endodontic irrigants cannot be expected [22]. The specimens were approximately 3 mm × 3 mm × 1 mm in size.

2.2. Atomic force microscopy (AFM) imaging

Each dentin specimen was ultrasonicated for 5 min to remove any possible debris and organic dirt as previously suggested [23–25] and then placed horizontally onto the sample disk, and imaged by Multimode quadrex Scanning Probe Microscopy (SPM) with NanoscopeIIIe controller (Veeco Instruments Inc., New York, NY, USA) under ambient conditions. Height and phase images were simultaneously acquired under standard AFM tapping mode using a commercial SNC (solid nitride cone) AFM probe (NanoScience Instruments, Inc. Phoenix, Arizona, USA). As specified by the manufacturer, the cantilever was 125 μm in length, with force constant 40 N/m, the tip radius less than 10 nm and resonant frequency of 275 kHz. At least 10 images were taken per specimen to account for possible spatial variability. Images of various sizes were made: 3 μm × 3 μm, 2 μm × 2 μm, 1 μm × 1 μm, 500 nm × 500 nm and 300 nm × 300 nm. The scans were taken with 256 lines per scan (256 × 256 pixels). The images were acquired from various locations of intertubular dentin to assure representativeness of the observed properties. Particular care was taken to

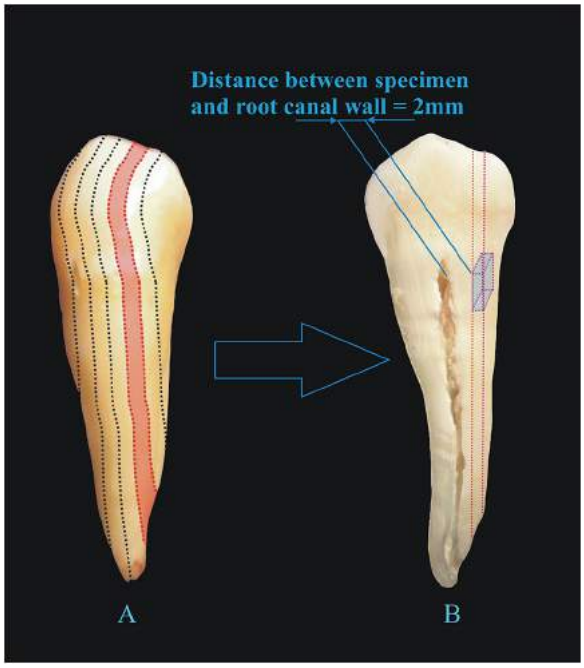

Fig. 1 – Schematic sequence illustrating the procedure of obtainment of the specimen. Each tooth was cut longitudinally (parallel with the tooth canal) to provide 1 mm thick sections (A). Red area on picture A refers the longitudinal section from which the specimen was obtained. Blue section on picture B shows the exact specimen location. (For interpretation of the references to color in this legend, the reader is referred to the web version of the article.)

prepare and analyze all specimens in the same manner to assure validity of inter-specimen comparisons. Hydroxyapatite crystal size was determined by measuring maximum dimension of each crystal using Veeco Nanoscope III software (version 5.31r1) like in previous studies [26,27]. Following estimation of sample size using MedCALC software ver. 9.1.0.1, about 100 crystals per study group were considered for the quantitative analysis. Statistical analysis was performed using analysis of variance in SPSS ver.15 and the values $p < 0.05$ were considered statistically significant. Tapping mode AFM is able to map simultaneously the topography of the specimen (height image) and the compositional variations (phase image) of the specimen's surface [28]. Variations in material properties lead to a phase lag of the cantilever oscillation. This phase lag is simultaneously monitored by the AFM control electronics and transformed into phase image. Specifically, the relationship of phase-shifts and energy dissipation enables linking experimental data to materials properties such as stiffness, viscoelasticity, etc. Therefore, phase image gives non-quantitative information about specimen material properties [28].

The measuring conditions for all images and all the specimens were constant to allow comparison of the results obtained during AFM characterization. Drive frequency of 87.68 kHz was maintained constant during the imaging, while the drive amplitude was 851 mV. Origin Lab 8.0 program was used for curve fitting and determination of peak positions and areas under the curve.

2.2.1. *AFM imaging: power spectral density and fractal dimension*

Power spectral density (PSD) analysis was performed on AFM topography images using the software WSxM (WSxM v5.0, developed by Horcas et al. [29]). Power spectral density is an advanced approach for roughness analysis that arises from Fourier decomposition of an image into the waves of particular wavelengths [30–33]. PSD analysis reveals characteristics of the surface structure [31–33] and describes the contribution of various morphological elements to the surface roughness [30,33]. The power spectral density data were extracted from the images of various sizes and the data points collected from all images belonging to one specimen were then represented on a single graph showing log PSD vs. log spatial frequency of the specimen. The data points were fitted linearly as previously suggested [30,33,34], obtaining the slope of the trendline in each specimen ($p < 0.05$). In addition, fractal dimension (FD) – a descriptor of the complexity of object's structure [35] corresponding to visual perception of roughness [36] – was calculated from log PSD vs. log spatial frequency graphs according to the following equation: $FD = 0.5*(7 - \beta)$ (β = absolute value of the slope of PSD trendline) [30,37,38].

2.3. *Scanning electron microscopy (SEM) and energy dispersive X-ray analysis (EDX)*

To provide adequately flat surface for microanalyses, the dentin specimens were polished using carbide papers of increasing smoothness (from 600 up to 4000 grit) under constant water irrigation on semiautomatic Unipol 810 polishing machine (MTI Corporation, Richmond, CA, USA). The specimens were ultrasonicated to remove any polishing-related debris and were left to dry naturally at room temperature.

Following sputter coating with gold (Au) in Ion Sputter Coater (Bal-Tec SCD 005, Leica Microsystems, Nussloch, Germany; WD 50 mm, 30 mA, 90 s), the specimens were mounted on a scanning electron microscope (SEM, JEOL JSM 6460 LV, Peabody, MA, USA) equipped with electron dispersive X-ray spectroscopy (EDX, OXFORD-Inca X sight). For EDX analysis, the system was operated at 20 kV, with constant working distance in line with previous studies [39]. Spectra of atomic composition of the specimens' surface were obtained by spot EDX analysis in five spots located in intertubular dentin in each specimen, under visual control of SEM. The EDX software automatically evaluates relative contribution of each of the detected elements within the region of interest to a total of 100%.

2.4. *Micro-Raman spectroscopy*

Micro-Raman spectroscopy measurements were performed using DXR Raman Microscope (Thermo Scientific, Waltham, MA, USA). Nd:YAG doubled frequency line of 532 nm was used as an excitation source, whereas the applied power was 10 mW. Objective with 10× magnification was used with the resulting average spot diameter of 2.1 μm on the specimen. All the spectra were collected at room temperature in high

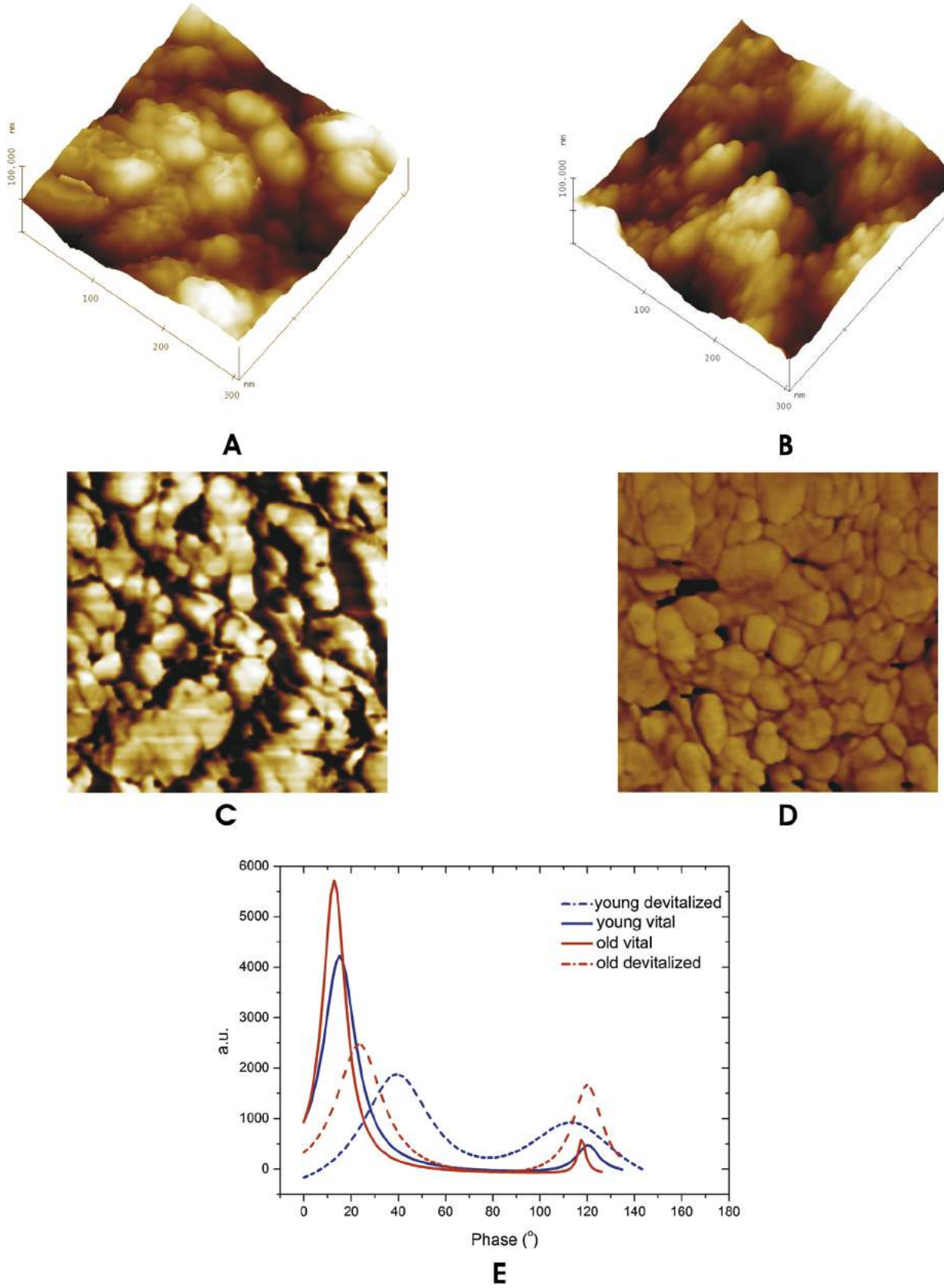

Fig. 2 – Atomic force microscopic characterization of dentin in vital and devitalized teeth. AFM 3D topographic images (305 nm × 305 nm) of devitalized (A) and vital dentin (B); corresponding AFM phase images of devitalized (C) and vital dentin (D); differences in surface phase composition of dentin in devitalized and vital teeth (E). For all phase images z-range is 100°.

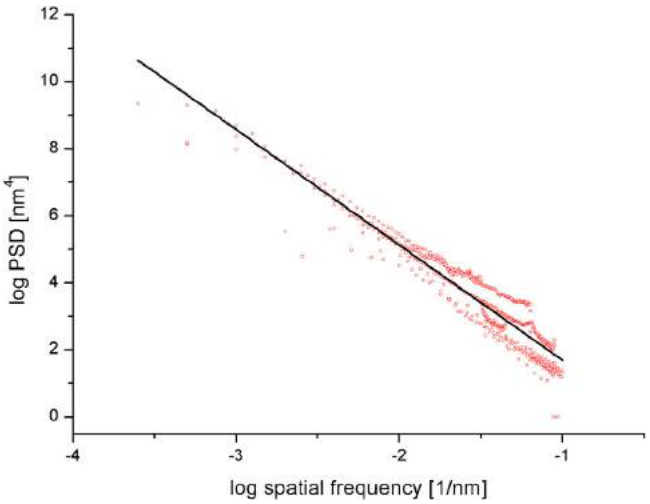

Fig. 3 – An illustrative power spectral density graph showing contribution (power) of surface morphological features of various sizes (spatial frequencies) to overall surface roughness. Linear fitting of the PSD data allowed calculation of the PSD slope which is considered as a true material characteristic.

resolution mode, in the range (300–1800) cm^{-1}, from the dentin tooth area of the teeth specimens (Fig. 1). Spectra acquisition and background fluorescence correction were performed in software package OMNIC (Thermo Scientific, Waltham, MA, USA). Raman spectra were analyzed using OriginPro 8 Software. Multiple-point baseline correction and smoothing were performed as previously suggested [21]. Raman band positions were compared with those of dentin and apatite known from the literature [40–51]. A selected subregion of each spectrum was fitted with Lorentzian profile [52].

3. Results

3.1. AFM

3.1.1. AFM topography and crystal size analysis

AFM topography images revealed granular organization of dentin apatite structure (Fig. 2A and B). Quantitative analysis of the observed surfaces demonstrated that the mean size of mineral crystals was larger in devitalized when compared with healthy teeth (young: 51.4 ± 19.5 nm vs. 36.2 ± 14.4 nm, old: 35.2 ± 14.5 nm vs. 32.6 ± 13.7 nm; $p < 0.001$).

3.1.2. Power spectral density and fractal analyses

Power spectral density analysis was obtained based on AFM topography images, providing quantitative characterization of the surface structure (Fig. 3). Linear fitting of PSD data ($p < 0.05$) revealed differences in the pattern of surface roughness between vital and devitalized teeth, where the PSD slopes showed a trend to steeper values in the vital teeth (young: $PSD_{slope} = -3.985$, old: $PSD_{slope} = -3.885$) when compared to devitalized cases (young: $PSD_{slope} = -3.646$, old: $PSD_{slope} = -3.719$).

In both young and old cases, the fractal dimension was calculated from the PSD data showing higher values in devitalized specimens when compared to vital specimens (young: 1.677 vs. 1.508; old: 1.640 vs. 1.558), indicating their higher degree of structural complexity and surface roughness. This is in line with larger mineral crystals observed in devitalized dentin. The differences in surface morphology were more pronounced between devitalized and vital teeth in young cases than in the elderly, where healthy elderly teeth already presented a changed surface complexity in comparison with the young.

3.1.3. AFM phase analysis

AFM phase imaging of dentin surfaces mapped spatial distribution of material properties as reflected in different phase shifts of the cantilever during the tip-sample interaction across the specimens' surface (Fig. 2C and D). Further evaluation of the phase images revealed that dentin surfaces reflected two distinct phase peaks on histograms derived from the AFM phase images: the peak corresponding to a lower phase shift (left peak), and the peak corresponding to a higher phase shift during the tip-specimen interaction (right peak) (Fig. 2E). Since all the specimens were imaged under the same scanning conditions, it was possible to compare the peak positions between the specimens. The AFM phase images and related histograms showed notable differences in material properties between different groups of specimens (Fig. 2C–E). Fig. 2E shows that the exact position of the peaks, as well as their area under the curve, differed among the groups. In particular, not only that the histograms of phase images of the devitalized dentin showed a slight shift of the left peak to the right when compared to vital dentin, but also the relative area under the right peak increased remarkably in devitalized specimens (in old: 28% vs. 2.5%; in young: 32% vs. 5.3%), revealing that a higher proportion of the devitalized dentin surface was composed of a material producing a higher phase shift during the tip-specimen interaction.

3.2. EDX analysis

EDX analysis showed similar Ca/P ratio between vital and devitalized specimens. The averaged weight Ca/P ratios were: 1.87 ± 0.01 in young vital dentin, 1.85 ± 0.08 in young devitalized dentin, 1.91 ± 0.02 in old vital dentin and 1.90 ± 0.10 in old devitalized dentin ($p > 0.05$). However, the average content of calcium was slightly lower in devitalized teeth (32.45 ± 0.03 wt% – young vital dentin, 29.17 ± 0.50 wt% – young devitalized dentin, 30.9 ± 0.30 wt% – old vital dentin and 28.17 ± 0.90 wt% – old devitalized dentin).

3.3. Micro-Raman spectroscopy

In Table 1 Raman shifts observed in Raman spectra are presented (see Fig. 4A), together with the reference data. Regions of the spectra, characterized by the appearance of the vibrational modes of hydroxyapatite (HAP), other calcium orthophosphates (octacalcium phosphate – OCP, dicalciumphosphatedihydrate – DCPD and tricalcium phosphate – TCP) and collagen, were analyzed.

Table 1 – Raman modes positions and assignments observed in the evaluated dentin specimens.

Raman shifts	Assignment	Relevant calcium phosphate phases/protein structure	Reference	Experimental positions of Raman modes found in the samples			
				Young devitalized dentin	Young vital dentin	Old vital dentin	Old devitalized dentin
413	$\nu_2HPO_4^{2-}$	OCP	[40]	411			413
424	$\nu_2PO_4^{3-}$	OCP	[40]	422	426w		422
432m	$\nu_2PO_4^{3-}$	HAP	[41]	432	430	430	432
439	$\nu_2PO_4^{3-}$	TCP	[42]	439			
857	C—C	Proline, collagen	[43]	857m	857w	857m	857m
871–891	872-$\nu_2CO_3^{2-}$	B-type	[44]	879w			
					879w	878w	
	878-$\nu_1PO_4^{3-}$	DCPD	[42]	885m			881
	878-$\nu_2CO_3^{2-}$	A-type	[44]				883w
							886m
	883-$\nu_1HPO_4^{2-}$	OCP	[42]				
938	$\nu_1PO_4^{3-}$	PO_4^{3-} in aqueous medium	[45]	933	933	938	933
958vs	$\nu_1PO_4^{3-}$	HAP	[41]	958	958	958	958
985	$\nu_1PO_4^{3-}$	DCPD	[42]	984		980vw	980
			[46]				
1046m	$\nu_3PO_4^{3-}$	HAP	[41]	1044s	1044m	1044m	1044vs
		B-type					
1060–1090	1070-$\nu_1CO_3^{2-}$	B-type	[41]				
	1074-$\nu_3PO_4^{3-}$	TCP	[42]	1076m	1078m	1078m	1078w
	1076-$\nu_3PO_4^{3-}$	HAP	[41]				
	1080-$\nu_3PO_4^{3-}$	OCP	[42]	1082m			
	1081-$\nu_3PO_4^{3-}$	DCPD	[42]				
1105–1112	$\nu_3HPO_4^{2-}$	OCP	[40]				1106
1107	$\nu_1CO_3^{2-}$	A-type	[41]		1107w	1107w	1107m
1245		Amid III	[41]	1244	1242	1246	1260
1345	(O═C)—C^{α}—H	α-Helix, secondary structure of protein	[47]	1346m	1346w	1346m	1346s
				1384m	1384vw	1384	1384m
1415	$\nu_3CO_3^{2-}$	Free ions	[48]	1407w	1407vw	1407w	1407w
1510–1550		Amide II	[49]	1523	1523vw	1521w	1521
				1546m	1546vw	1546w	1546w
1590–1720		Amide I	[50,49]	1570–1720bb	1570–1720bb	1570–1720bb	1570–1720bb
1670		Amide I	[41]	1678	1676	1676	1672
1630	H_2O bending	Crystalline hydrates, OCP, DCPD	[51,40]	1631w			1631w
1645				1645m			1645m

HAP, hydroxyapatite; OCP, octacalcium phosphate; TCP, tricalcium phosphate; DCPD, dicalcium phosphate dehydrate; A-type, A type carbonate apatite; B-type, B type carbonate apatite; vw, very weak; w, weak; m, medium; s, strong; vs, very strong Raman mode, bb, broad band.

Most prominent feature in the spectra of all the specimens is a mode positioned at ~958 cm^{-1} (Fig. 4B), representing the vibration of PO_4^{3-} group, referred to as ν_1 in the literature [41,53]. Shift of this mode to lower frequency compared to the standard HAP frequency (962 cm^{-1}) and the mode asymmetry toward lower frequencies reflect the presence of A-type carbonated HAP [29] where CO_3^{2-} group substitutes OH^- group of HAP. Other HAP PO_4^{3-} vibrational modes observed in the spectra were: ~432 cm^{-1}(ν_2), ~1043 cm^{-1} (ν_3), ~1076 cm^{-1} (ν_3).

Carbonate modes characteristic for both A-type and B-type HAP [41] were observed at positions ~870–880 cm^{-1}, ~1078 cm^{-1} and ~1107 cm^{-1} suggesting the presence of both carbonated HAP types.

Vibrational modes of HPO_4^{2-}, characteristic for OCP appeared in the spectra obtained from both young and old devitalized teeth with approximate positions: ~413 cm^{-1}, ~1106 cm^{-1} [40].

A mode positioned at ~980 cm^{-1} was observed in the spectra of devitalized teeth and old vital tooth, being the most intensive and broadest in young devitalized and remarkably weak in old vital dentin. This mode was assigned to ν_1 PO_4^{3-} in DCPD [30,34]. $\nu_3PO_4^{3-}$ mode of DCPD and OCP can also be a part of the broad band (1060–1090) cm^{-1} since it is expected to appear at ~1080 cm^{-1} [42].

Amide bands, each consisting of several modes, were registered in the regions 1230–1310 cm^{-1} (amide III),

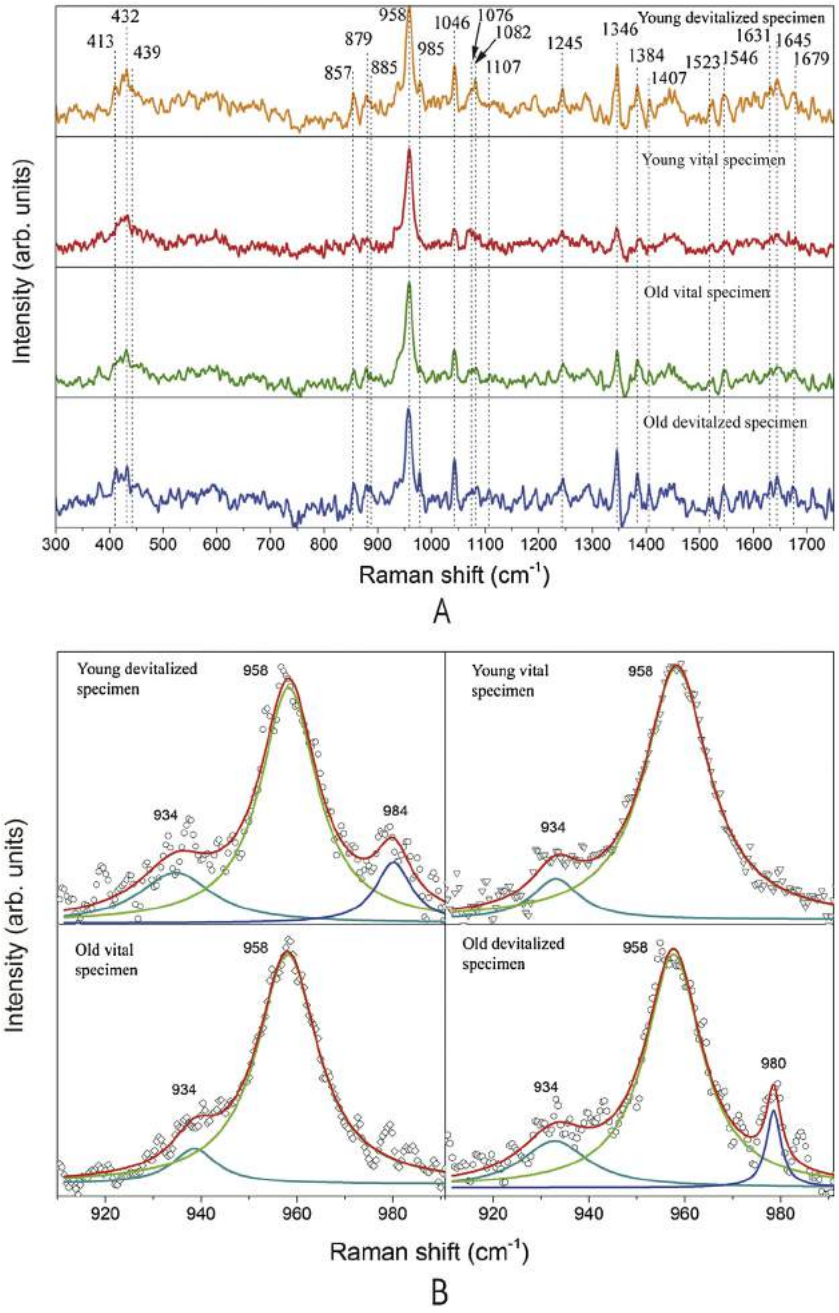

Fig. 4 – Raman micro-spectroscopy of the dentin in devitalized and vital teeth: Raman spectra of four dentin specimens (A); the most prominent Raman modes of the evaluated specimens (B).

1550–1590 cm^{-1} (amide II) and 1590–1720 cm^{-1} (amide III) [41,49,50], originating from collagen amino acids' functional groups. However, relative intensities of these bands varied throughout different specimens. Due to the large bandwidths it was difficult to resolve individual modes and use them in order to obtain mineral/matrix ratio.

Pronounced intensities of 1630 cm^{-1} and 1645 cm^{-1} H_2O bending modes [40] superposed on the broad band assigned to amide I vibrations in the spectra of devitalized teeth can be taken as a confirmation of the presence of non-HAP orthophosphates containing water molecules in these specimens, such as OCP and DCPD.

4. Discussion

Altered forms of dentin such as transparent [1,3,23] or sclerotic dentin [54] have been studied recently. However, structural and compositional alterations of endodontically treated dentin remain unclear. In this study, combined AFM, SEM/EDX and micro-Raman analyses were used to verify the

occurrence of nano-structural and compositional changes which would explain the increased fragility of devitalized teeth. First of all, larger mineral crystals that were observed in AFM images of devitalized teeth could account for their decreased mechanical strength, according to previous observations in other mineralized tissues [26,27] and mechanical behavior of various large-grained ceramics [55,56]. Namely, in large-grained structures an increased flaw size and fewer grain boundaries facilitate crack propagation, therefore decreasing overall strength of the material [56–58].

In contrast to the bone matrix of aged trabecular bone where the enlarged mineral crystals were flattened leading to a decreased roughness [27,30], higher fractal dimension observed in devitalized teeth indicates that the large crystals in these teeth are associated with increased surface roughness. Moreover, different slopes of PSD trendline in vital vs. devitalized teeth might suggest different types and characteristics of processes that participated in building the surfaces, as it was suggested in various synthetic materials [33] as well as in other biological materials [30].

Apart from crystal growth during formation when continuous deposition of mineral around nucleation sites increases their size, crystals can become bigger as a consequence of aggregation (coalescence) process of pre-formed crystals [27,59,60]. During the coalescence process the existing mineral is reorganized to larger crystals, as a result of the surface tendency to achieve thermodynamically more favorable state. Materials science suggests that this process depends on the spatial density of crystal clusters and becomes dominant with increasing the fraction of the surface occupied by the crystals [59]. This mechanism has been particularly discussed for cases without further deposition of the components [59]. In that context, it is likely that continuous flow of dentin fluid through the tubules in vital teeth is essential for exchange (dissolving and reprecipitation) of the mineral in a dynamic equilibrium; in contrast, it can be speculated that the lack of continuous mineral exchange, owing to the absence of fluid in devitalized teeth, might favor the conditions for physical processes of coalescence leading to larger crystals and increased fractal dimension, as observed in this study.

Apart from differential nano-morphological properties, material properties differed between the devitalized and vital dentin, which was evident in the AFM-based phase analysis. Namely, AFM phase imaging records the phase shift of the cantilever oscillation relative to the signal sent to piezo driving the cantilever during the tip-specimen interaction [27,33,61,62]. The phase shift is related to the amount of energy dissipated during tip-sample interaction [62] and AFM phase mode gives non-quantitative information on composition of the surface and certain mechanical properties, such as stiffness, viscoelasticity, etc. [28,62,63]. In this context, the observed phase shifts in devitalized cases revealed altered mechanical characteristics and suggested difference in the composition of the material. However, AFM does not provide precise chemical characterization of the specimens, and therefore additional spectroscopic techniques were needed to analyze the chemical basis of changed material properties observed with AFM phase imaging. As energy dispersive X-ray spectroscopy showed that the overall Ca/P ratios were not notably different between the specimens, the differences in phase composition were further examined by micro-Raman spectroscopy. Notably, Raman microanalyses clearly showed significant presence of calcium phosphate phases other than pure hydroxyapatite (HAP) in devitalized teeth. Hence, whereas in devitalized dentin (both young and old) vibrational modes assigned to octacalcium phosphate (OCP), dicalcium phosphate dihydrate (DCPD) and tricalcium phosphate (TCP) were quite prominent, these calcium phosphate phases were less intensive in an old healthy tooth and almost undetectable in a young healthy tooth.

Some recent studies [64,65] suggested that dentin nanocrystals are covered with a dynamic hydrated layer, which has a composition close to the one of DCPD [66] and demonstrates similarities with the Fourier transform infrared spectroscopy (FTIR) spectrum of OCP [67]. It was reported [64,65] that this fine substructure would be irreversibly altered after drying. Drying would likely increase crystallinity of this layer, resulting in a more detectable crystalline DCPD or OCP, which could be confirmed by a greater prominence and decreased width of the corresponding Raman vibrational modes. Therefore, significant presence of partly crystallized DCPD and OCP in devitalized teeth might suggest the following sequence: after devitalisation the teeth lose blood supply and occlusion of dentin tubules advances, which leads to progressive drying of dentin, where crystallization of water from the superficial hydrated layer of the mineral crystals would favor development of clear DCPD or OCP phases. Comparing Raman spectra of young and old healthy teeth, our data suggest that similar process, albeit slower, occurs with aging as the pulp shrinks and dentin tubules become occluded.

Raman modes, characteristic for the pure hydroxyapatite, remained unchanged in both vital and devitalized teeth. In contrast, as mentioned above, the amount of other, less ordered calcium phosphate phases (OCP, DCPD, TCP) increased probably as the hydrated layer become relatively crystalline in devitalized teeth. Those apatitic phases become incorporated on the surfaces of the crystals; however, the process of crystals aggregation would lead to presence of these phases even in the interior of the crystals, altering mechanical characteristics of dentin. Namely, previous material studies suggested that apatitic phases with lower calcium content had lower material strength [68]. Since TCP, OCP and DCPD have lower calcium content than the pure hydroxyapatite [57], their increased proportion in dentin mineralized matrix of devitalized cases (also visible in decreased calcium content in EDX analysis) might explain decreased strength of such teeth. Moreover, experimental studies confirmed that the presence of DCPD phase was associated with a decreased compressive strength [69], while similar results were found for increased content of beta TCP [56].

In addition, as properties of dental materials used in restorative dentistry should correspond to the properties of dental tissues, the assumed changes in dentin hardness and its fracture resistance should also be considered in manufacturing new materials designed for devitalized teeth.

The study limitation is relatively small number of specimens. However, our sample size is in agreement with other studies performing similar advanced examination techniques on teeth [1,3,23,70,71]. Furthermore, relatively small number of specimens allowed larger number of experimental

techniques to be performed on each, thus providing more comprehensive insight into the nano-structural basis of devitalized teeth fragility.

5. Conclusion

Our complex analysis revealed that process of tooth devitalisation does lead to alterations in dentin nano-structure which could be the basis of increased fragility of devitalized teeth.

Specifically, finding of larger mineral crystals on AFM images comparing to healthy teeth suggests that the elimination of dentin fluid disrupts the mineral dynamic equilibrium and leads to increasing in crystal size. In large-grained structures crack propagation is facilitated and therefore the overall strength of the material is decreased.

Influence of devitalization on dentin composition has been registered by AFM phase images and further confirmed and closely studied on micro-Raman spectroscopy. As dentin is the major structural component of the tooth, presence of weaker apatite phases in devitalized dentin certainly influence the whole tooth strength.

Since our study is of cross-sectional design, further experimental studies will be beneficial to clarify the exact mechanisms of morphological and chemical transformations in devitalized teeth and their influence on mechanical properties.

Acknowledgement

This study was supported by the Ministry of Education and Science of the Republic of Serbia, grant number: 45005.

The authors express gratitude to Milos Mojovic, assistant professor on the Faculty of Physical Chemistry, University of Belgrade, for technical assistance in micro-Raman analyses.

A part of this study was awarded with The Anniversary Travel Grant at the 50th Congress of Calcified Tissues Society, 2013.

REFERENCES

[1] Kinney JH, Nalla RK, Pople JA, Breunig TM, Ritchie RO. Age-related transparent root dentin: mineral concentration, crystallite size, and mechanical properties. Biomaterials 2005;26:3363–76.
[2] Gher MJ, Dunlap R, Anderson M, Kuhl L. Clinical survey of fractured teeth. Journal of American Dental Association 1987;114:174–7.
[3] Porter AE, Nalla RK, Minor A, Jinschek JR, Kisielowski C, Radmilovic V, et al. A transmission electron microscopy study of mineralization in age-induced transparent dentin. Biomaterials 2005;26:7650–60.
[4] Kishen A. Mechanisms and risk factors for fracture predilection in endodontically treated teeth. Endodontic Topics 2006;13:57–83.
[5] Sathorn C, Palamara J, Palamara D, Messer H. Effect of root canal size and external root surface morphology on fracture susceptibility and pattern: a finite element analysis. Journal of Endodontics 2005;31:288–92.
[6] Tang W, Wu Y, Smales R. Identifying and reducing risks for potential fractures in endodontically treated teeth. Journal of Endodontics 2010;36:609–17.
[7] Marshall GJ, Balooch M, Kinney J, Marshall S. Atomic force microscopy of conditioning agents on dentin. Journal of Biomedical Materials Research 1995;29:1381–7.
[8] Doyon GE, Dumsha T, von Fraunhofer JA. Fracture resistance of human root dentin exposed to intracanal calcium hydroxide. Journal od Endodontics 2005;31:895–7.
[9] Mayrand D, Grenier D. Detection of collagenase activity in oral bacteria. Canadian Journal of Microbiology 1985;31:134–8.
[10] Sedgley C, Messer H. Are endodontically treated teeth more brittle? Journal of Endodontics 1992;18:332–5.
[11] Papa J, Cain C, Messer H. Moisture content of vital vs endodontically treated teeth. Endodontics and Dental Traumatology 1994;10:91–3.
[12] Kishen A, Vedantam S. Hydromechanics in dentin: role of dentinal tubules and hydrostatic pressure on mechanical stress–strain distribution. Dental Materials 2007;23:1296–306.
[13] Mjor IA, Fejerskov O. Histology of the human tooth. 2nd ed. Copenhagen: Munksgaard; 1979.
[14] Jones FH. Teeth and bones: applications of surface science to dental materials and related biomaterials. Surface Science Reports 2001;42:75–205.
[15] Nalla RK, Porter AE, Daraio C, Minor AM, Radmilovic V, Stach EA, et al. Ultrastructural examination of dentin using focused ion-beam cross-sectioning and transmission electron microscopy. Micron 2005;36:672–80.
[16] Marshall SJ, Balooch M, Habelitz S, Balooch G, Gallagher R, Marshall GW. The dentin–enamel junction – a natural, multilevel interface. Journal of the European Ceramic Society 2003;23:2897–904.
[17] Kinney JH, Pople JA, Marshall GW, Marshall SJ. Collagen orientation and crystallite size in human dentin: a small angle X-ray scattering study. Calcified Tissue International 2001;69:31–7.
[18] Gawda H, Sekowski L, Treracz H. In vitro examination of human teeth using ultrasound and X-ray diffraction. Acta of Bioengineering and Biomechanics 2004;6:41–9.
[19] Kinney JH, Marshall SJ, Marshall GW. The mechanical properties of human dentin: a critical review and re-evaluation of the dental literature. Critical Review of Oral Biology and Medicine 2003;14:13–29.
[20] Marshall GW. Dentin: microstructure and characterization. Quintessence International 1993;24:606–17.
[21] Xu C, Yao X, Walker MP, Wang Y. Chemical/molecular structure of the dentin–enamel junction is dependent on the intratooth location. Calcified Tissue International 2009;84:221–8.
[22] Zou L, Shen Y, Li W, Haapasalo M. Penetration of sodium hypochlorite into dentin. Journal of Endodontics 2010;36:793–6.
[23] Balooch M, Demos SG, Kinney JH, Marshall GW, Balooch G, Marshall SJ. Local mechanical and optical properties of normal and transparent root dentin. Journal of Material Science: Materials in Medicine 2001;12:507–14.
[24] Habelitz S, Marshall SJ, Marshall GWJ, Balooch M. The functional width of the dentino–enamel junction determined by AFM-based nanoscratching. Journal of Structural Biology 2001;135:294–301.
[25] Balooch G, Marshall GW, Marshall SJ, Warren OL, Asif SAS, Balooch M. Evaluation of a new modulus mapping technique to investigate microstructural features of human teeth. Journal of Biomechanics 2004;37:1223–32.
[26] Milovanovic P, Potocnik J, Djonic D, Nikolic S, Zivkovic V, Djuric M, et al. Age-related deterioration in trabecular bone mechanical properties at material level: nanoindentation study of the femoral neck in women by using AFM. Experimental Gerontology 2012;47:154–9.

[27] Milovanovic P, Potocnik J, Stoiljkovic M, Djonic D, Nikolic S, Neskovic O, et al. Nanostructure and mineral composition of trabecular bone in the lateral femoral neck: implications for bone fragility in elderly women. Acta Biomaterialia 2011;7:3446–51.
[28] Jandt KD. Atomic force microscopy of biomaterials surfaces and interfaces. Surface Science 2001;491: 303–32.
[29] Horcas I, Fernandez R, Gomez-Rodriguez JM, Colchero J, Gomez-Herrero J, Baro AM. WSXM: a software for scanning probe microscopy and a tool for nanotechnology. Review of Scientific Instruments 2007;78:013705–13708.
[30] Milovanovic P, Djuric M, Rakocevic Z. Age-dependence of power spectral density and fractal dimension of bone mineralized matrix in AFM topography images: potential correlates of bone tissue age and bone fragility in female femoral neck trabeculae. Journal of Anatomy 2012;221:427–33.
[31] Lita AE, Sanchez Jr JE. Effects of grain growth on dynamic surface scaling during the deposition of Al polycrystalline thin films. Physical Review B 2000;61:7692–9.
[32] Mitchell MW, Bonnell DA. Quantitative topographic analysis of fractal surfaces by scanning tunneling microscopy. Journal of Materials Research 1990;5:2244–54.
[33] Nenadović M, Potočnik J, Ristić M, Štrbac S, Rakočević Z. Surface modification of polyethylene by Ag+ and Au+ ion implantation observed by phase imaging atomic force microscopy. Surface and Coatings Technology 2012;206:4242–8.
[34] Ulmeanu M, Serghei A, Mihailescu IN, Budau P, Enachescu M. C—Ni amorphous multilayers studied by atomic force microscopy. Applied Surface Scence 2000;165:109–15.
[35] Dougherty G, Henebry GM. Fractal signature and lacunarity in the measurement of the texture of trabecular bone in clinical CT images. Medical Engineering & Physics 2001;23:369–80.
[36] Zawada DG, Brock JC. A multiscale analysis of coral reef topographic complexity using lidar-derived bathymetry. Journal of Coastal Research 2009;53:6–15 [Special issue].
[37] Silk T, Hong Q, Tamm J, Compton RG. AFM studies of polypyrrole film surface morphology II. Roughness characterization by the fractal dimension analysis. Synthetic Metals 1998;93:65–71.
[38] Pfeifer P. Fractal dimension as working tool for surface-roughness problems. Applied Surface Science 1984;18:146–64.
[39] Busse B, Djonic D, Milovanovic P, Hahn M, Püschel K, Ritchie RO, et al. Decrease in the osteocyte lacunar density accompanied by hypermineralized lacunar occlusion reveals failure and delay of remodeling in aged human bone. Aging Cell 2010;9:1065–75.
[40] Fowler B, Markovic M, Brown W. Octacalcium phosphate 3. Infrared and raman vibrational spectra. Chemistry of Materials 1993;5:1417–23.
[41] Penel G, Leroy G, Rey C, Bres E. MicroRaman spectral study of the PO_4 and CO_3 vibrational modes in synthetic and biological apatites. Calcified Tissue International 1998;63:475–81.
[42] Koutsopoulos S. Synthesis and characterization of hydroxyapatite crystals: a review study on the analytical methods. Journal of Biomedical Materials Research 2002;62:600–12.
[43] Chalas R, Nowak J, Kuczumow A. Raman studies on amino acids profiles at the dentin–enamel-junction in human and ancient/recent animal teeth. Bulletin of the International Association for Paleodontology 2011;5:4–14.
[44] Bazin D, Chappard C, Combes C, Carpentier X, Rouzière S, André G, et al. Diffraction techniques and vibrational spectroscopy opportunities to characterise bones. Osteoporosis International 2009;20:1065–75.
[45] Frost R, Xi Y. Molecular structure of the phosphate mineral brazilianite $NaAl_3(PO_4)_2(OH)_4$: a semi precious jewel. Journal of Molecular Structure 2012;1010:179–83.
[46] Aminzadeh A. Infra-red and Raman spectroscopic studies of infected and affected dentine. Iranian Journal of Chemistry and Chemical Engineering 2002;21:87–90.
[47] Tsuboi M, Suzuki M, Overman A, Thomas GJ. Intensity of the polarized Raman band at 1340–1345 cm^{-1} as an indicator of protein R-helix orientation: application to Pf1 filamentous virus. Biochemistry 2000;39:2677–84.
[48] Wehrmeister U, Jacob DE, Soldati AL, Loges N, Hager T, Hofmeister W. Amorphous, nanocrystalline and crystalline calcium carbonates in biological materials. Journal of Raman Spectroscopy 2011;42:926–35.
[49] Desamero R, Cheng H, Cahill S, Girvin M, Deng H, Callender R, et al. Interactions of amidated acids with heparin. Biopolymers 2002;67:41–8.
[50] Maiti N, Apetri M, Zagorski M, Carey P, Anderson V. Raman spectroscopic characterization of secondary structure in natively unfolded proteins: alpha-synuclein. Journal of the American Chemical Society 2004;126:2399–408.
[51] Falk M. The frequency of the H—O—H bending fundamental in solids and liquids. Spectrochimica Acta 1984;4OA:43–8.
[52] Tsuda H, Arends J. Detection and quantification of calcium fluoride using micro Raman spectroscopy. Caries Research 1993;27:249–57.
[53] Markovic M, Fowler BO, Tung MS. Preparation and comprehensive characterization of a calcium hydroxyapatite reference material. Journal of Research of the National Institute of Standards and Technology 2004;109:553–68.
[54] Marshall GWJ, Chang YJ, Saeki K, Gansky SA, Marshall SJ. Citric acid etching of cervical sclerotic dentin lesions: an AFM study. Journal of Biomedical Materials Research – Part A 2000;49:338–44.
[55] Bose S, Dasgupta S, Tarafder S, Bandyopadhyay A. Microwave-processed nanocrystalline hydroxyapatite: simultaneous enhancement of mechanical and biological properties. Acta Biomaterialia 2010;6:3782–90.
[56] Wagoner Johnson AJ, Herschler BA. A review of the mechanical behavior of CaP and CaP/polymer composites for applications in bone replacement and repair. Acta Biomaterialia 2011;7:16–30.
[57] Dorozhkin SV. Amorphous calcium (ortho)phosphates. Acta Biomaterialia 2010;6:4457–75.
[58] Wang J, Shaw LL. Nanocrystalline hydroxyapatite with simultaneous enhancement in hardness and toughness. Biomaterials 2009;30:6565–72.
[59] Zinke-Allmang M. Clustering on surfaces. Surface Science Reports 1992;16:377–463.
[60] Boskey HL. Mineralization of bones and teeth. Elements 2007;3:387–93.
[61] Bar G, Delineau L, Brandsch R, Bruch M, Whangbo MH. Importance of the indentation depth in tapping-mode atomic force microscopy study of compliant materials. Applied Physics Letters 1999;75:4198–200.
[62] García R, Magerle R, Perez R. Nanoscale compositional mapping with gentle forces. Nature Materials 2007;6:405–11.
[63] Ahn HS, Chizhik SA, Dubravin AM, Kazachenko VP, Popov VV. Application of phase contrast imaging atomic force microscopy to tribofilms on DLC coatings. Wear 2001;249:617–25.
[64] Dorozhkin SV. Nanodimensional and nanocrystalline calcium orthophosphates. American Journal of Biomedical Engineering 2012;2:48–97.
[65] Rey C, Combes C, Drouet C, Sfihi H, Barroug A. Physico-chemical properties of nanocrystalline apatites:

implications for biominerals and biomaterials. Materials Science and Engineering C 2007;27:198–205.
[66] Jäger C, Welzel T, Meyer-Zaika W, Epple M. A solid-state NMR investigation of the structure of nanocrystalline hydroxyapatite. Magnetic Resonance in Chemistry 2006;44:573–80.
[67] Eichert D, Drouet C, Sfihi H, Rey C, Combes C. Nanocrystalline apatite-based biomaterials: synthesis, processing and characterization. In: Kendall J, editor. Biomaterials research advances. USA: Nova Science Publishers Inc.; 2007. p. 93–143.
[68] Suchanek W, Yoshimura M. Processing and properties of hydroxyapatite-based biomaterials for use as hard tissue replacement implants. Journal of Materials Research 1998;13:94–117.
[69] Charriere E, Terrazzoni S, Pittet C, Mordasini P, Dutoit M, Lematre J, et al. Mechanical characterization of brushite and hydroxyapatite cements. Biomaterials 2001;22: 2937–45.
[70] Kinney JH, Balooch M, Marshall SJ, Marshall GWJ, Weihs TP. Hardness and Young's modulus of human peritubular and intertubular dentin. Archives of Oral Biology 1996;41(1):9–13.
[71] Cuy JL, Manna AB, Livi KJ, Teaford MF, Weihs TP. Nanoindentation mapping of the mechanical properties of human molar tooth enamel. Archives of Oral Biology 2002;47:281–91.

Processing and Application of Ceramics 11 [4] (2017) 304–310
https://doi.org/10.2298/PAC1704304M

Influence of Mg doping on structural, optical and photocatalytic performances of ceria nanopowders

Branko Matović[1,*], Jelena Luković[1], Bojan Stojadinović[2], Sonja Aškrabić[2], Aleksandra Zarubica[3], Biljana Babić[1], Zorana Dohčević-Mitrović[2]

[1]*Institute for Nuclear Sciences, Centre of Excellence-CextremeLab Vinca, University of Belgrade, Belgrade, Serbia*
[2]*Institute of Physics Belgrade, Pregrevica 118, University of Belgrade, Belgrade, Serbia*
[3]*Faculty of Sciences and Mathematics, Department of Chemistry, University of Nis, Nis, Serbia*

Received 21 July 2017; Received in revised form 14 November 2017; Accepted 6 December 2017

Abstract

Nanosized Mg-doped ceria powders were obtained by self-propagating room temperature reaction without using surfactants or templates. X-ray diffraction analysis and field emission scanning microscopy results showed that the doped samples are solid solutions with fluorite-type structure and spherical morphology. Raman spectra revealed an increase in the amount of oxygen vacancies with the increase of Mg concentration. This increasing results in a narrowing of the bandgap of CeO_2. The photocatalytic performances of the Mg-doped ceria solid solutions were evaluated by decomposing an organic dye, crystal violet under UV irradiation. The Mg-doped ceria solid solutions exhibit significantly better photocatalytic activity than the pure CeO_2 and commercial TiO_2. The higher first rate constant of the Mg-doped samples demonstrated that they are much more efficient than TiO_2 and CeO_2 under UV light. Mg^{2+} dopant ions and oxygen vacancies play a significant role in the enhancement of photocatalytic performances of the Mg-doped ceria.

Keywords: *ceria, solid solution, oxygen vacancies, UV light illumination, nanocatalysis*

I. Introduction

Nano ceria (CeO_2) has been extensively studied as an active or supporting catalytic material due to its superior oxygen storage-and-release properties [1]. Since ceria is a good electron acceptor, it can provide lattice oxygen in chemical reactions because of lower formation energy for oxygen vacancy [2–4]. Also, CeO_2 promotes the chemical activity of the material by facilitating electron transfer from suitable adspecies into an oxide surface [5,6]. A higher catalytic activity is related to the type, size, and distribution of oxygen vacancies. It is demonstrated that surface defects were more readily formed in CeO_2 nanostructures with special morphology, such as cubes, nanobelts, nanowires and nanotubes. Therefore, for the design of ceria based materials with high oxygen storage and transport capacity, it is important to know how to increase the number of structural defects (oxygen vacancies) and to maintain at the same time a fluorite-type crystal structure. This can be done either by the promotion of Ce^{4+} reduction into Ce^{3+} or by doping with transition or rare-earth elements [7]. CeO_2 is not generally considered as a photocatalytic material due to its wide band gap and specific 4f electron configuration. Despite the fact that little work was carried out in the field of photocatalytic applications of CeO_2 [8–10] recent studies demonstrated that improvement of ceria photocatalytic properties can be done by proper choice of dopant elements and their incorporated amounts [11] or by creating surface defects as the most reacting sites which can enhance the visible light activity of nanostructured ceria [12]. In addition, the preparation methods have also a significant influence on the ceria structure (homogeneity, morphology, grain size, crystal defects etc.) and its optical and photocatalytic properties. Therefore, tuning the band gap energy and tailoring the reactivity of ceria-based catalysts is still a challenging task.

* Corresponding authors: tel/fax: +381 11 3408 224
e-mail: *mato@vinca.rs*

In this work the Mg-doped ceria nonpowdered solid solutions ($Ce_{1-x}Mg_xO_{2-\delta}$, $0 \le x \le 0.4$) were prepared by facile and cost-effective self-propagating room temperature reaction (SPRT). The influence of Mg content on structural, optical and photocatalytic properties was examined. The evaluation of photocatalytic activity of synthesized catalysts has been carried out by degradation of crystal violet as a model pollutant. The mechanism for the band gap narrowing of Mg-doped ceria and the enhancement of the photocatalytic performances are also proposed.

II. Materials and methods

The solid solutions of magnesium-doped samples were prepared by a SPRT method using metal nitrates and sodium hydroxide as the starting materials. This technique gives the possibility of producing very fine powders with very precise stoichiometry in accordance with the tailored compositions [13–16]. Preparation of $Ce_{1-x}Mg_xO_{2-\delta}$ powders was performed by hand mixing chemicals according to:

$$2\,[(1-x)Ce(NO_3)_3 \cdot 6\,H_2O + xMg(NO_3)_2 \cdot 6\,H_2O] + 6\,NaOH + \\ + (\tfrac{1}{2}-\delta)O_2 \longrightarrow 2\,Ce_{1-x}Mg_xO_{2-\delta} + 6\,NaNO_3 + 15\,H_2O \quad (1)$$

The compositions of the reacting mixtures were calculated according to the nominal composition of the final reaction product. Compositions of $Ce_{1-x}Mg_xO_{2-\delta}$ were synthesized with x ranging from 0.0 to 0.4. The described reaction belongs to a group of double exchange reactions and develops spontaneously after being initiated, terminating extremely rapidly. After the mixture of reactants ($Ce(NO_3)_3 \cdot 6\,H_2O$, Aldrich, $Mg(NO_3)_2 \cdot 6\,H_2O$, Aldrich) was mechanically activated (by hand mixing instead by heating) the reaction took place at room temperature and terminated very quickly. The obtained mixtures of reaction products according to Eq. (1) were subjected to a centrifuge treatment to eliminate $NaNO_3$ and drying at 80 °C.

After drying, the composition of the solid solutions was identified by means of powder XRD on a Rigaku IV, XRD diffractometer with CuKα radiation at room temperature. The average crystallite size was measured from the 111 XRD peak using the Scherrer formula. The values of the unit cell parameters of all the analysed powders are calculated on the basis of the equation:

$$\frac{4\sin^2\theta}{\lambda^2} = \frac{1}{d_{hkl}^2} = \frac{h^2+k^2+l^2}{a^2} \quad (2)$$

where θ is the Bragov angle, hkl are Miller indices, λ is the wavelength (1.54184 Å), and a is parameter of the unit cell of the crystal [17].

SEM analysis using Zeiss DSM 982 Gemini scanning electron microscope proved that the obtained powders were in the nanometric size range. The room-temperature Raman spectra were obtained using a U-1000 (Jobin-Ivon) double monochromator in back scattering geometry. The Raman spectra were excited by the 514 nm line of an Ar^+/Kr^+ ion laser operating at low incident power (~20 mW) in order to avoid sample heating. The measurements of UV-Vis absorption spectra of the samples were carried out on a Specord M40 Carl Zeiss spectrophotometer in a spectral range 200–600 nm, at room temperature.

The specific surface area and the pore size distribution (PSD) of the doped CeO_2 samples were analysed using the Surfer (Thermo Fisher Scientific, USA). PSD was estimated by applying BJH method [18] to the desorption branch of isotherms and mesopore surface and micropore volume were estimated using the t-plot method [19].

Photocatalytic activity of the synthesized Mg-doped samples was evaluated by the degradation of crystal violet (CV) under UV light irradiation. The photochemical reactor consisted of UV lamp (Roth Co., 16 W, 2.5 mW/cm^2, λ_{max} = 366 nm) positioned annularly to the 50 ml quartz flask. The acidity of solutions was not additionally adjusted and pH values were in the range from 6.7 to 7.0. The rates of photocatalytic degradations of CV were followed at initial concentration of 0.01 mmol/dm^3. The amount of used catalyst was 30 ± 2 mg. CV photolysis test was performed prior to photocatalytic measurements and no significant dye degradation was observed. The prepared $Ce_{1-x}Mg_xO_{2-\delta}$ samples were immersed into CV solution and the solution was continuously stirred and kept in the dark for 1 h to establish adsorption-desorption equilibrium before being irradiated. Photocatalytic activity of the $Ce_{1-x}Mg_xO_{2-\delta}$ solid solutions were compared to commercial standard TiO_2 sample - Degussa P25 (having specific surface area, S_{BET}, of 56 m^2/g, pore volume of 0.25 cm^3/g, average pore size of 17.5 nm, crystallite size of 21 nm and the following phase composition: anatase, 81 vol.% and rutile, 19 vol.%) and the undoped CeO_2 sample.

The reaction rate constant (k) was determined assuming quasi first order kinetics using the following equation:

$$\ln\frac{C_0}{C_t} = k \cdot t \quad (3)$$

where C_0 is the initial dye concentration, C_t is the concentration at time t. The slope of the $\ln(C_0/C_t)$ versus time plot gives the value for the rate constant k.

III. Results

3.1. Characterization of Mg-doped ceria

XRD spectra of the $Ce_{1-x}Mg_xO_{2-\delta}$ samples, presented in Fig. 1, revealed that the obtained powders are a single phase with the fluorite crystal structure. Main diffraction peaks in each sample were significantly broadened indicating small crystallite size and/or strain. New peak is observed for the sample doped with 40 at.% of Mg, indicating that the limit of Mg solubility in ceria crystal lattice is in the range from 30 to 40 at.%. This high sol-

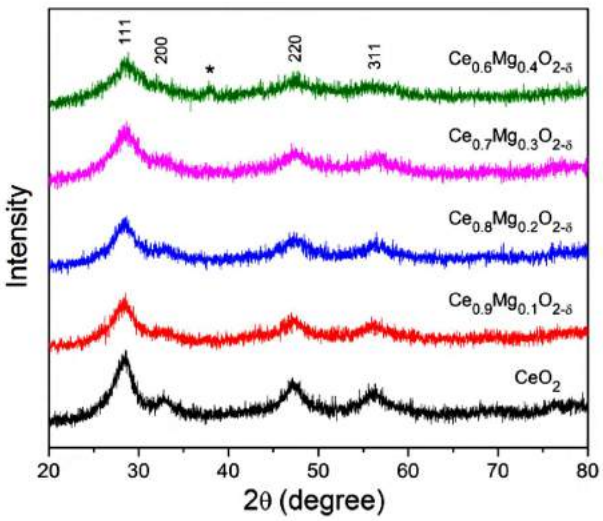

Figure 1. X-ray diffraction patterns of synthesized of $Ce_{1-x}Mg_xO_{2-\delta}$ nanopowders (* - brucite phase)

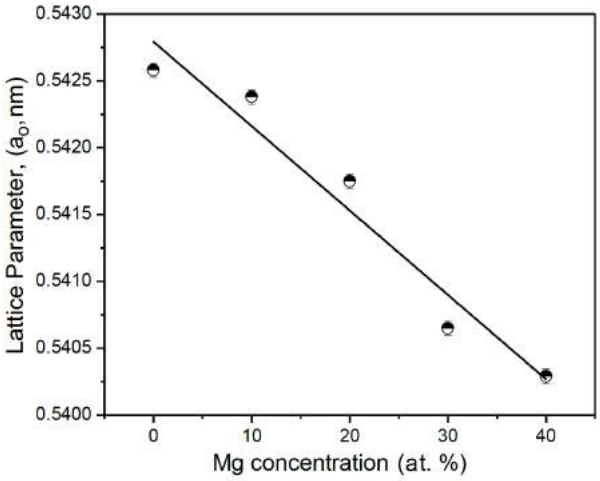

Figure 2. Lattice parameter (a_0) $Ce_{1-x}Mg_xO_{2-\delta}$ samples as a function of Mg content

ubility may be attributed to the nanometric nature of the obtained powders. Excess of Mg is very reactive and in contact with moisture make a brucite phase $Mg(OH)_2$, marked with asterisks in Fig. 1. XRD spectra exhibit very diffuse diffraction lines with increasing Mg content, which makes difficult to indicate precisely some atomic planes (*hkl*: 200, 220, 311, 420).

Calculation of cell parameters (Fig. 2) based on X-ray results, shows the linear dependence of unit cell parameter versus concentration of Mg^{2+} ions. With increasing of Mg^{2+} ion concentration the cubic ceria lattice shrinks. According to Shannon's compilation [19], the ionic radii of Ce^{4+} and Mg^{2+} for coordination number (CN) 8, are 0.97 and 0.89 Å, respectively. Thus, doping with a smaller sized Mg^{2+} ion and increasing of dopant concentration, will lead to the contraction of the ceria lattice. Also, lattice parameter (a_0) of doped ceria versus Mg^{2+} content, obeys Vegard's law, implying that Mg^{2+} substitutionally entered into ceria lattice. The crystallite size, calculated on the basis of XRD data, for all powders is less than 5 nm.

Room-temperature Raman spectra of the Mg-doped ceria are presented in Fig. 3, whereas in the inset is given the Raman spectrum of the undoped CeO_2. Room-temperature Raman spectrum of the undoped CeO_2 sample shows the strong peak at ~455 cm^{-1} corresponding to the triply degenerate F_{2g} mode characteristic for the fluorite cubic CeO_2 structure. The red shift of this mode compared to its bulk counterpart (464 cm^{-1}) and pronounced asymmetry on the low-energy side originates from the phonon confinement, strain and the presence of defects [20,21]. In the sample doped with 10 at.% of Mg, F_{2g} mode is shifted to ~457 cm^{-1}, due to the substitutional incorporation of Mg, as ion of smaller ionic radius, into ceria lattice. With further increasing of Mg content, F_{2g} mode shifts to higher energies and in the 40 at.% Mg doped sample, this mode is positioned at ~460 cm^{-1}.

Another mode of lower intensity, positioned at ~600 cm^{-1}, is characteristic for nanometric ceria and is attributed to the presence of intrinsic oxygen vacancies [20,22], due to the partial reduction of Ce^{4+} to Ce^{3+}. This mode is also presented in the Mg-doped samples. From the Lorentzian fit procedure (insets in Fig. 3), it

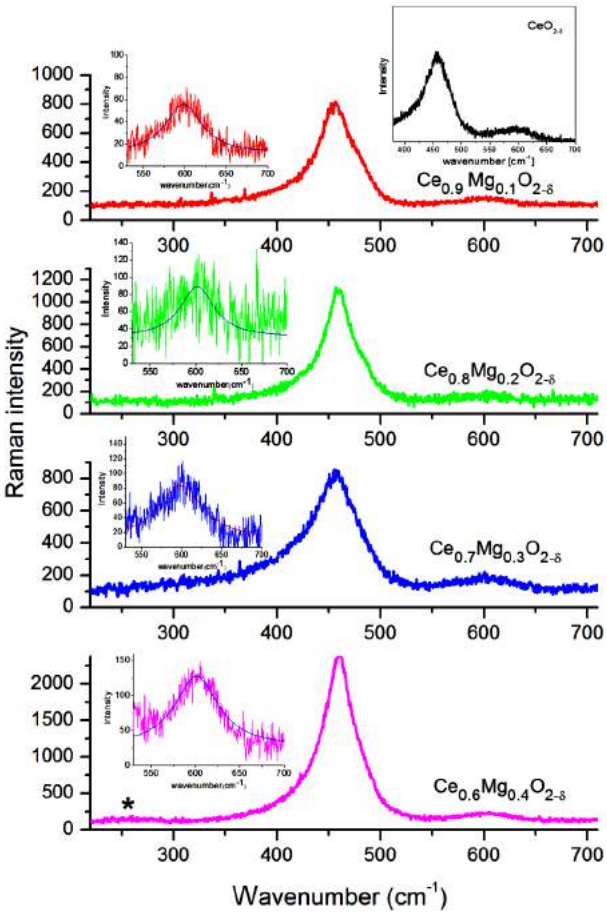

Figure 3. Room temperature Raman spectra of Mg-doped samples (insets present Raman spectrum of undoped CeO_2 and Lorentzian fits of intrinsic vacancy mode)

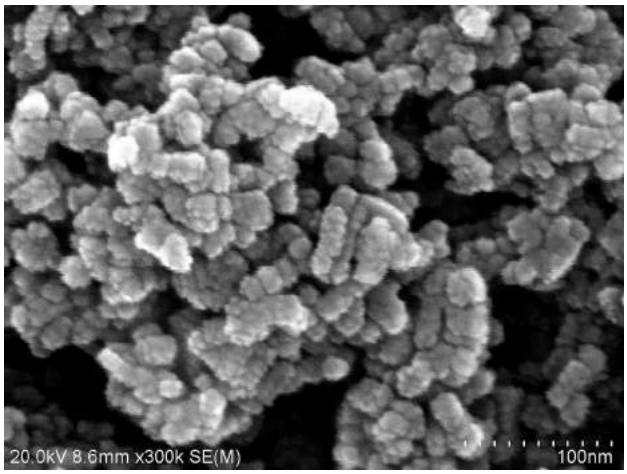

Figure 4. Typical FESEM images of 20 at.% Mg-doped ceria sample

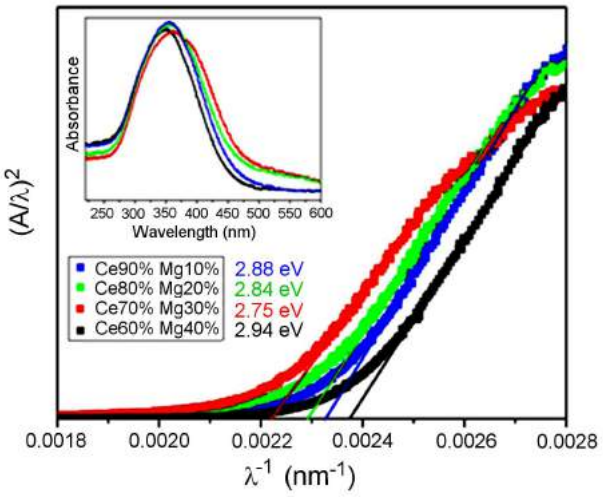

Figure 5. $(A/\lambda)^2$ plots for Mg-doped samples (inset presents absorption spectra of doped samples)

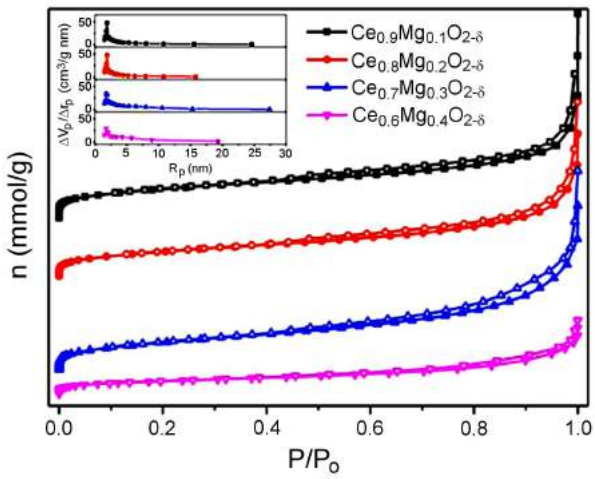

Figure 6. N_2 adsorption (solid symbols)/desorption (open symbols) isotherms and the pore size distribution (inset) of Mg-doped samples

was obtained that intensity of this mode increases with an increase of Mg content, pointing at increased intrinsic oxygen vacancy concentration [22]. In the spectra of the sample with 40 at.% Mg, new broad, low intensity mode around 270 cm^{-1} is observed. This mode (marked with asterisks in Fig. 3) can be ascribed to the E_g mode of $Mg(OH)_2$ (brucite) phase, which is in good agreement with XRD measurement [23]. It is evident from the Raman spectra of the sample with 40 at.% Mg that limits of Mg solubility in ceria crystal lattice is less than 40 at.%.

The as-prepared ceria powders consist of rounded particles with size less than 10 nm, roughly estimated (Fig. 4). The particles are linked in the form of blackberry, which together form cauliflower morphology. There is no difference of morphology and particle size between the Mg-doped ceria samples. It seems that various doping concentration has no influence on the microstructure of the powders.

The optical band gap of the undoped CeO_2, which corresponds to the O 2p ⟶ Ce $4f^0$ transition, was previously determined to be around 3.6 eV [24]. From the absorption spectra of the solid solutions $Ce_{1-x}Mg_xO_{2-\delta}$ (x = 0.1, 0.2, 0.3 and 0.4), presented in the inset of Fig. 5, the band gap energies of the Mg-doped samples were obtained using Tauc law for direct transition and applying absorption spectrum fitting method [25]. The plots of $(A/\lambda)^2$ vs. $1/\lambda$ are presented in Fig. 5, where A is the absorbance and λ is the wavelength. The linear extrapolation of $(A/\lambda)^2$ to zero gives a wavelength λ_g which corresponds to the optical band gap. The band gap values can be obtained using well known relation $E_g = 1240/\lambda_g$. The estimated direct band gap values (E_g) for $Ce_{1-x}Mg_xO_{2-\delta}$ samples are given in Fig. 5. It can be seen that with Mg doping up to 30 at.% band gap values decreased from 2.88 to 2.75 eV due to the formation of defect (localized) levels inside the gap with Mg doping [26]. In the sample with 40 at.% of Mg dopant the E_g is slightly increased to 2.94 eV. Such an increase can be a consequence of the presence of $Mg(OH)_2$ phase which has higher band gap value than CeO_2 [27] or to the Burstein-Moss effect caused by increased electron concentration and lifting of the Fermi-level because of increased Mg content and oxygen vacancies concentration [28].

Nitrogen adsorption/desorption isotherms for the Mg-doped samples, are shown in Fig. 6. According to the IUPAC classification [29] isotherms of samples are of type IV and with a hysteresis loop which is associated with mesoporous materials. In all samples, the shape of hysteresis loop is of type H3. Isotherms revealing type H3 hysteresis do not exhibit any limiting adsorption at high P/P_0, which is observed with non-rigid aggregates of plate-like particles giving rise to slit-shaped pores [30]. Specific surface areas calculated by BET equation, S_{BET}, are listed in Table 1. S_{BET} values for all Mg-doped samples are comparable (between 110–120 m^2/g), i.e. the amount of dopant does not have

Table 1. Porous properties of $Ce_{1-x}Mg_xO_{2-\delta}$ nanopowders

Sample	S_{BET} [m^2/g]	S_{meso} [m^2/g]	S_{mic} [m^2/g]	V_{mic} [cm^3/g]	r_m [nm]
CeO_2	70	45	25	0.013	-
$Ce_{0.9}Mg_{0.1}O_2$	114	104	10	0.003	3.7
$Ce_{0.8}Mg_{0.2}O_2$	110	110	0	0	4.3
$Ce_{0.7}Mg_{0.3}O_2$	120	120	0	0	5.2
$Ce_{0.6}Mg_{0.4}O_2$	113	113	0	0	4.4

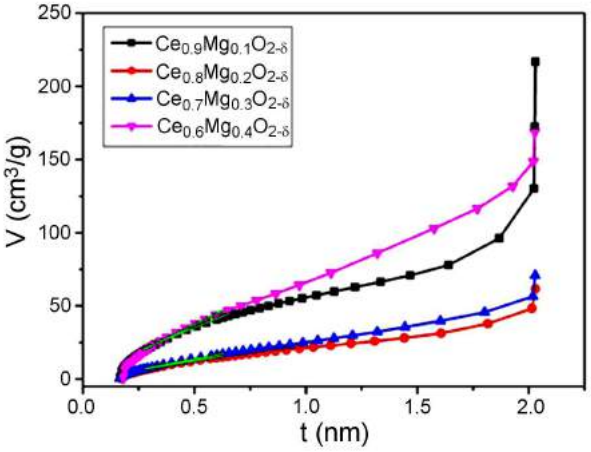

Figure 7. *t*-plots of Mg-doped samples

an essential influence on the overall specific surface area of the doped nanopowders. On the contrary, the undoped ceria sample has significantly smaller specific surface area than the doped ones. Therefore, the Mg doping increases the porosity of ceria. Pore size distribution (PSD) of samples possesses sharp PSD peak with most of the pore radius between 2–20 nm (inset of Fig. 6) implying that the samples are mesoporous. Values of mean pore radius, for all samples, are presented in Table 1.

The *t*-plot, obtained on the basis of the standard nitrogen adsorption isotherm, is shown in Fig. 7. The straight line in the medium *t*-plot region gives a mesoporous surface area including the contribution of the external surface, S_{meso}, determined by its slope, and the micropore volume, V_{mic}, which is given by the intercept. The calculated porosity parameters (S_{meso}, S_{mic}, V_{mic}) are given in Table 1. *t*-plot analysis confirmed that all samples are mesoporous, although a small amount of micropores (pore radius below 2 nm) was detected in the sample with 10 at.% of Mg and undoped ceria.

3.2. Photocatalytic performance of Mg-doped ceria

The influence of the dopant concentration on the photocatalytic activity of the Mg-doped ceria nanopowders has been studied through the photocatalytic removal of organic dye crystal violet (CV) under UV light irradiation. The kinetics of degradation of CV is represented in Fig. 8. As can be seen from Fig. 8, the pure ceria has shown modest photocatalytic activity. With increasing Mg content, the degradation of CV became significant. The samples with higher Mg content (>10 at.% Mg) have shown even better photocatalytic activity than

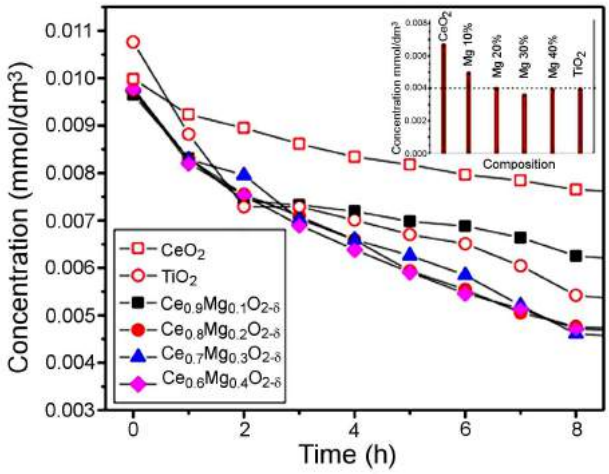

Figure 8. Photocatalytic degradation of CV in the presence of $Ce_{1-x}Mg_xO_{2-\delta}$ nanopowders and TiO_2 (insert represents photocatalytic efficiency after 24 h)

the commercial TiO_2 Degussa P25, which is known as one of the most efficient photocatalysts for dye degradation.

The reaction kinetics from Fig. 8, follows the first order and the degradation rate constants for 30 and 40 at.% Mg-doped samples, together with TiO_2 and CeO_2 as reference samples, are summarized in Table 2. It can be seen that the degradation rate constant for the $Ce_{0.7}Mg_{0.3}O_{2-\delta}$ and $Ce_{0.6}Mg_{0.4}O_{2-\delta}$ samples are higher than reference samples, implying that higher concentration of Mg in CeO_2 lattice improves the photocatalytic efficiency of ceria.

Table 2. The pseudo-first rate constants for CV after exposition time of 8 h

Sample	k [h^{-1}]	R^2
$Ce_{0.7}Mg_{0.3}O_{2-\delta}$	0.081	0.980
$Ce_{0.6}Mg_{0.4}O_{2-\delta}$	0.078	0.998
CeO_2	0.026	0.982
TiO_2	0.056	0.910

After 24 h the photocatalytic activity of the solid solutions with concentrations of 20 and 40 at.% of Mg respectively, are the same as a TiO_2 standard, whereas the $Ce_{0.7}Mg_{0.3}O_{2-\delta}$ sample exhibited higher activity (inset of Fig. 8). Such high photocatalytic activity of the $Ce_{0.7}Mg_{0.3}O_{2-\delta}$ sample can be attributed to its large specific surface area, the largest one among all the studied nanopowders, regular mesoporosity and favourable average pore size. A slightly lower photocatalytic activity of the ceria sample with 40 at.% Mg can be explained by the appearance of secondary brucite phase.

In Fig. 9 an illustration of the proposed mechanism of photocatalytic reactions is given. Upon UV light illumination photogenerated electrons and holes can be trapped by dopant ions, i.e. Mg^{2+} ions can be electron acceptors and/or hole donors. Reduction of the band gap of the Mg-doped samples implies that Mg^{2+} ions introduce states into the band gap of CeO_2. In such a

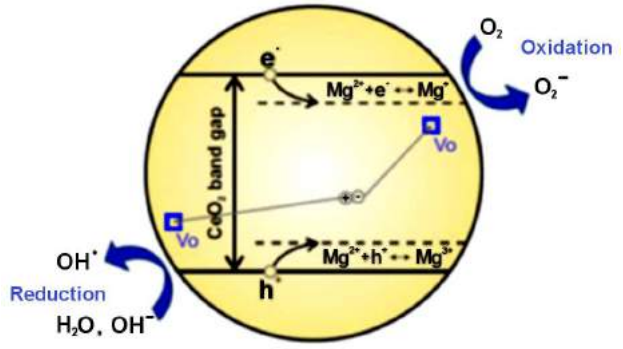

Figure 9. Illustration of the photocatalytic mechanism at Mg-doped CeO_2 interface under the UV light irradiation

way, Mg doping could be effective in delay of electron-hole recombination process, increasing the lifetime of the charge separation. The trapped electrons can be subsequently scavenged by molecular oxygen, which is adsorbed on the CeO_2 surface, to generate the superoxide radical ($O_2^{-\bullet}$). Superoxide radicals in contact with H_2O molecules form OH^- ions and finally $OH^\bullet$ radicals, which attack the dye in aqueous solution leading to its degradation. Due to high oxidative potential, the positive holes act as good oxidizing agents for dye degradation. The trapped holes can directly attack the dye or can interact with OH^- or water molecules present on the surface of the catalyst forming hydroxyl radicals ($OH^\bullet$).

Ceria nanoparticles are prone to the formation of oxygen vacancies (VO) which promote the formation of Ce^{3+} ions in the grain boundary region [30]. In order to attain charge neutrality with Mg doping, oxygen vacancies will be created in the ceria lattice. This fact is confirmed from Raman measurements. V_O as defects can also introduce localized state below the conduction band of CeO_2 [24] reducing the band gap. Furthermore, a high concentration of surface donor defects (V_O and Ce^{3+}) can serve as charge carrier traps and adsorption sites which transfer charge to adsorbed species like O_2 or H_2O on ceria surface. In such a way, oxygen vacancies can delay the electron-hole recombination process and support the charge carrier transfer to the ceria surface, improving the photocatalytic efficiency of ceria. Theoretical and experimental results on TiO_2 and ZnO have shown that excess electrons localized on the oxygen vacancy states affect surface adsorption and increase photocatalytic activity of TiO_2 and ZnO [31,32]. Therefore, it is reasonable to assume that besides Mg^{2+} ions as trapping centres, oxygen vacancies have a strong impact on the increased photocatalytic activity of Mg-doped ceria.

IV. Conclusions

Mg-doped ceria nanopowders ($Ce_{1-x}Mg_xO_{2-\delta}$, $0 \leq x \leq 0.4$) have been successfully fabricated via self-propagating room temperature reaction without any surfactant or template. The obtained samples are of fluorite cubic structure, composed of rounded particles with size less than 10 nm with the higher specific surface area than the pure CeO_2. Substitutional doping with lower valence Mg^{2+} ions promotes the formation of oxygen vacancies in ceria lattice, the amount of which increases with an increase of dopant concentration. The increased dopant concentration results in an effective red shift of the band gap value of the $Ce_{1-x}Mg_xO_{2-\delta}$ samples due to the formation of localized states inside the ceria gap. Only the sample with 40 at.% of Mg exhibited slight blueshift of the band gap due to the appearance of brucite phase. The photocatalytic activity of the Mg-doped CeO_2 for degradation of azodye crystal violet was examined under UV light irradiation. It was found that the samples with Mg content higher than 10 at.% have much better photocatalytic performances than the undoped CeO_2 and commercial Degussa P25. Localized electronic states of Mg^{2+} ions and oxygen vacancies can capture photogenerated charge carriers delaying recombination process, but can also serve as active sites on ceria surface to transfer charge to adsorbed species like O_2 or H_2O forming reactive radicals.

Acknowledgement: This work was financially supported by the Ministry of Education, Science and Technological Development of the Republic of Serbia under the projects III 45012 and ON171032. The authors would like to thank Nenad Tadić, Faculty of Physics, University of Belgrade for the UV-Vis measurements.

References

1. G.A. Deluga, J.R. Salge, L.D. Schmidt, X.E. Verykios, "Renewable hydrogen from ethanol by autothermal reforming", *Science*, **303** (2004) 993–997.
2. M.V. Ganduglia-Pirovano, J.L.F.D. Silva, J. Sauer, "Density-functional calculations of the structure of near-surface oxygen vacancies and electron localization on CeO_2 (111)", *Phys. Rev. Lett.*, **102** (2009) 026101.
3. A. Migani, G.N. Vayssilov, S.T. Bromley, F. Illas, K.M. Neyman, "Greatly facilitated oxygen vacancy formation in ceria nanocrystallites", *Chem. Commun.*, **46** (2010) 5936–5938.
4. M. Nolan, S.C. Parker, G.W. Watson, "The electronic structure of oxygen vacancy defects at the low index surfaces of ceria", *Surface Sci.*, **595** (2005) 223–232.
5. G.N. Vayssilov, Y. Lykhach, A. Migani, T. Staudt, G.P. Petrova, N. Tsud, T. Skala, A. Bruix, F. Illas, K.C. Prince, V. Matolin, K.M. Neyman, J. Libuda, "Support nanostructure boosts oxygen transfer to catalytically active platinum nanoparticles", *Nature Mater.*, **10** (2011) 310–315.
6. M. Baron, H. Abbott, O. Bondarchuk, D. Stacchiola, A. Uhl, S. Shaikhutdinov, H.J. Freund, C. Popa, M.V.G. Pirovano, A.J. Sauer, "Resolving the atomic structure of vanadia monolayer catalysts: Monomers, trimers, and oligomers on ceria", *Angewandte Chemie Int. Edition*, **48** (2009) 8006–8009.
7. M. Mogenson, N.M. Sammes, G.A. Tompsett, "Physical, chemical and electrochemical properties of pure and doped ceria ", *Solid State Ionics*, **129** (2000) 63–94.
8. J.M. Coronado, A.J. Maira, A. Martínez-Arias, J.C. Conesa, J. Soria, "EPR study of the radicals formed upon

UV irradiation of ceria-based photocatalysts", *J. Photochem. Photobio. A: Chem.*, **150** (2002) 213–221.
9. G.R. Bamwenda, T. Uesigi, Y. Abe, K. Sayama, H. Arakawa, "The photocatalytic oxidation of water to O^{-2} over pure CeO_2, WO_3, and TiO_2 using Fe^{3+} and Ce^{4+} as electron acceptors", *Appl. Catal. A: Gen.*, **205** (2001) 117–128.
10. M.D. Hernández-Alonso, A.B. Hungría, A. Martínez-Arias, M. Fernández-García, J.M. Coronado, J.C. Conesa, J. Soria, "EPR study of the photoassisted formation of radicals on CeO_2 nanoparticles employed for toluene photooxidation", *Appl. Catal. B: Environ.*, **50** (2004) 167–175.
11. L. Yue, X.-M. Zhang, "Structural characterization and photocatalytic behaviors of doped CeO_2 nanoparticles", *J. Alloys Compd.*, **475** (2009) 702–705.
12. M.M. Khan, S.A. Ansari, D. Pradhan, D.H. Han, J. Lee, M.H. Cho, "Defect-induced band gap narrowed CeO_2 nanostructures for visible light activities", *Ind. Eng. Chem. Res.*, **53** (2014) 9754–9763.
13. B. Matovic, Z. Dohcevic-Mitrovic, M. Radovic, Z. Brankovic, G. Brankovic, S. Boskovic, Z.V. Popovic, "Synthesis and characterization of ceria based nanometric powders", *J. Power Sources*, **193** (2009) 146–149.
14. B. Matovic, J. Pantic, J. Lukovic, S. Ilic, N. Stankovic, M. Kokunesovski, M. Miljevic, "Synthesis and characterization of (Ba,Yb) doped ceria nanopowders", *Process. Appl. Ceram.*, **5** (2011) 69–72.
15. M. Prekajski, Z. Dohčević-Mitrović, M. Radović, B. Babić, J. Pantić, A. Kremenović, B. Matović, "Nanocrystaline solid solution CeO_2-Bi_2O_3", *J. Eur. Ceram. Soc.*, **32** (2012) 1983–1987.
16. M. Stojmenović, S. Bošković, S. Zec, B. Babić, B. Matović, D. Bučevac, Z. Dohčević-Mitrović, F. Aldinger, "Characterization of nanometric multidoped ceria powders", *J. Alloys Compd.*, **507** (2010) 279–285.
17. Lj. Karanović, D. Poleti, *X-ray Structural Analysis*, Institute for Textbooks and Teaching Resources, Belgrade, 2003.
18. E.P. Barret, L.G. Joyner, P.P. Halenda, "The determination of pore volume and area distributions in porous substances. I. Computations from nitrogen isotherms", *J. Am. Chem. Soc.*, **73** (1951) 373–380.
19. B.C. Lippens, B.G. Linsen, J.H. d. Boer, "Studies on pore systems in catalysts I. The adsorption of nitrogen; apparatus and calculation", *J. Catal.*, **3** (1964) 32–37.
20. R.D. Shannon, "Revised effective ionic radii and systematic studies of interatomie distances in halides and chaleogenides", *Acta Crystallogra. Section A*, **32** [5] (1976) 751–767.
21. Z.D. Dohčević-Mitrović, M.J. Šćepanović, M.U. Grujić-Brojčin, Z.V. Popović, S.B. Bošković, B.M. Matović, M.V. Zinkevich, F. .Aldinger, "The size and strain effects on the Raman spectra of $Ce_{1-x}Nd_xO_{2-\delta}$ ($0 \le x \le 0.25$) nanopowders", *Solid State Commun.*, **137** (2006) 387–390.
22. P.J. Colomban, G. Gouadec, "Raman spectroscopy of nanostructures and nanosized materials", *J. Raman Spectrosc.*, **38** (2007) 598–603.
23. Z.D. Dohčević-Mitrović, M.U. Grujić-Brojčin, M.J. Šćepanović, Z.V. Popović, S.B. Bošković, B.M. Matović, M.V. Zinkevich, F. Aldinger, "$Ce_{1-x}Y(Nd)_xO_{2-\delta}$ nanopowders: potential materials for intermediate temperature SOFCs", *J. Phys.: Condens. Mat.*, **18** (2006) S2061–S2068.
24. P. Dawson, C.D. Hatfield, G.R. Wilkinson, "The polarized infra-red and Raman spectra of $Mg(OH)_2$ and $Ca(OH)_2$", *J. Phys. Chem. Solids*, **34** (1973) 1217–1225.
25. M. Radović, B. Stojadinović, N. Tomić, A. Golubović, B. Matović, I. Veljković, Z. Dohčević-Mitrović, "Investigation of surface defect states in CeO_{2-y} nanocrystals by Scanning - tunneling microscopy /spectroscopy and ellipsometry", *J. Appl. Phys.*, **116** (2014) 234305.
26. N. Ghobadi, "Band gap determination using absorption spectrum fitting procedure", *Int. Nano Lett.*, **3** (2013) 1–4.
27. M. Radović, Z. Dohčević-Mitrović, A. Golubović, V. Fruth, S. Preda, M. Šćepanović, Z.V. Popović, "Influence of Fe^{3+}-doping on optical properties of CeO_{2-y} nanopowders", *Ceram. Int.*, **39** (2013) 4929–4936.
28. K. Mageshwari, R. Sathyamoorthy, "Studies on photocatalytic performance of MgO nanoparticles prepared by wet chemical method", *Trans. Indian Instit. Metals*, **65** (2012) 49–55.
29. V. Etacheri, R. Roshan, V. Kumar, "Mg-doped ZnO nanoparticles for efficient sunlight-driven photocatalysis", *ACS Appl. Mater. Inter.*, **4** (2012) 2717–2725.
30. B. Choudhury, A. Choudhury, "Ce^{3+} and oxygen vacancy mediated tuning of structural and optical properties of CeO_2 nanoparticles", *Mater. Chem. Phys.*, **131** (2012) 666–671.
31. F. Kayaci, S. Vempati, I. Donmez, N. Biyikliab, T. Uyar, "Role of zinc interstitials and oxygen vacancies of ZnO in photocatalysis: a bottom-up approach to control defect density", *Nanoscale*, **6** (2014) 10224–10234.
32. X. Pan, M.Q. Yang, X. Fu, N. Zhang, Y.J. Xu, "Defective TiO_2 with oxygen vacancies: synthesis, properties and photocatalytic applications", *Nanoscale*, **5** (2013) 3601–3614.

Biomedical Spectroscopy and Imaging 5 (2016) 115–127
DOI 10.3233/BSI-160141
IOS Press

Design and first applications of a flexible Raman micro-spectroscopic system for biological imaging

Roman Kiselev [a], Iwan W. Schie [a], Sonja Aškrabić [b], Christoph Krafft [a,*] and Jürgen Popp [a,c]
[a] *Leibniz Institute of Photonic Technology, Albert-Einstein-Str. 9, 07745 Jena, Germany*
[b] *Institute of Physics, University of Belgrade, Pregrevica 118, 11080 Belgrade, Serbia*
[c] *Institute of Physical Chemistry and Abbe Center of Photonics, University Jena, Helmholtzweg 4, 07743 Jena, Germany*

Abstract. Typical commercial Raman micro-spectroscopic systems do not offer much flexibility to the end user, thus limiting potential research applications. We present a design of a simple, highly flexible and portable confocal Raman microscope with a detailed list of parts. The system can perform spectral acquisition in different modes: single-point spectroscopy, hyperspectral point mapping or hyperspectral line mapping. Moreover, the microscope can be easily converted between inverted and upright configurations, which can be beneficial for specific situations. Fiber coupling enables to connect various lasers for excitation and spectrometer/CCD combinations for signal detection. The performance of the instrument is demonstrated via Raman spectroscopy at 785 nm excitation wavelength, single point mapping of pancreatic cancer cells placed onto a quartz substrate and line mapping of polystyrene beads.

Keywords: Raman, spectroscopy, microscopy, instrumentation, optical design, cell analysis, confocal microscopy, prototypes

1. Introduction

Raman spectroscopy, a popular subtype of vibrational spectroscopy, evolved in last decades into a powerful technique for analysis and chemical characterization of specimens. A Raman spectrum results from inelastic light scattering on vibrating molecular bonds (see basic theory in Section 2), therefore the spectrum is specific for each particular substance and contains information about molecular composition of the specimen.

Ability to combine non-destructive chemical characterization with diffraction-limited lateral resolution makes Raman micro-spectroscopy a versatile research tool [45,50]. It is particularly well suited for biological research, because it allows to detect variations in the biomolecular composition and correlate them with the corresponding biological changes due to metabolism or pathology. Absence of lengthy sample preparation, such as staining or labeling, makes Raman spectroscopy a promising tool for rapid clinical diagnosis [7,23,26,29,44,52]. Not only biological tissues [27] and body fluids [18] can be examined by Raman spectroscopy, but even individual living cells [17,32,42]. This is a large research field with a host of promising applications, such as observation of cell metabolism, growth and aging, study of drug resistance or drug uptake [35], chemical mapping of cells [22,36], identification of cell in a mixed

*Corresponding author. E-mail: christoph.krafft@leibniz-ipht.de.

population, and many others. This could guide us to the understanding of changes within an individual cell that could lead to a disease development, because many diseases begin at the cellular level.

A range of commercial Raman microscopic systems exists. Usually, these are robust systems with built-in calibration routines and user-friendly software. However, they are often dedicated for a specific purpose and therefore have limited potential for modifications. Nonetheless, it is possible to assemble a confocal Raman microscope from off-the-shelf components. It can be further extended with special Raman detection schemes (e.g. line scanning-mode [21], modulation of the excitation wavelength [15], or dual-polarization [11]) and supplemented with additional detection techniques like fluorescence [25, 31], phase contrast [25], dark-field [31] microscopy, and others [53]. Moreover, custom systems can be combined with advanced sample handling techniques, like microfluidics [2,3,14] or optical tweezers [1,24,25,57].

This contribution presents a detailed design of a Raman microscope including a scheme of optical layout and a list of components. We discuss important parameters of excitation laser, camera and spectrometer, as well as implementation of the Raman imaging. Mechanical stability and flexibility of the system, as well as spatial resolution of the microscope are considered as well. A set of hyperspectral confocal Raman images of two cancer cell lines has been acquired to show the performance of the instrument. Finally, we demonstrate fast Raman mapping of polystyrene beads in a line-scanning imaging mode.

2. Basic theory

Raman effect is the inelastic scattering of photons on vibrational modes of molecular bonds [33,48]. An incident photon with energy $E_0 = h\tilde{\nu}c_0$, where h is the Plank's constant, c_0 is the speed of light in vacuum, and $\tilde{\nu}$ is the wavenumber (spatial frequency of the electromagnetic wave, typically expressed in cm^{-1}), excites a molecule from an initial vibrational mode with energy E_i to a virtual state. The molecule spontaneously relaxes to another vibrational mode with energy E_f, emitting a new photon (red-shifted in case of Stokes scattering) in an arbitrary direction.

The difference in energy between incoming and scattered photons $E_0 - E_s$ is equal to the energy of transition between two vibrational modes $E_f - E_i$. Thus, the Raman spectrum contains information about molecular structure and chemical composition of the specimen.

There are multiple variations of Raman effect, such as resonance Raman scattering, stimulated Raman scattering or coherent anti-Stokes Raman scattering [33,46], but this contribution deals only with spontaneous Stokes scattering.

3. Design of the Raman micro-spectroscopic system

A Raman detection system is supposed to collect Stokes-shifted scattered photons and guide them to the entrance slit of a spectrometer. As the inelastically scattered photons are emitted isotropically from the sample, an optical system is required that would collect them and refocus on the spectrometer input slit. An infinity-corrected microscope objective lens with high numerical aperture is particularly suitable for this purpose for several reasons. First, it provides high energy density for excitation in the focal spot, as well as gives a possibility to selectively probe small spots of a heterogeneous sample located at different positions. Second, it collects a large portion of the inelastically scattered photons emitted from

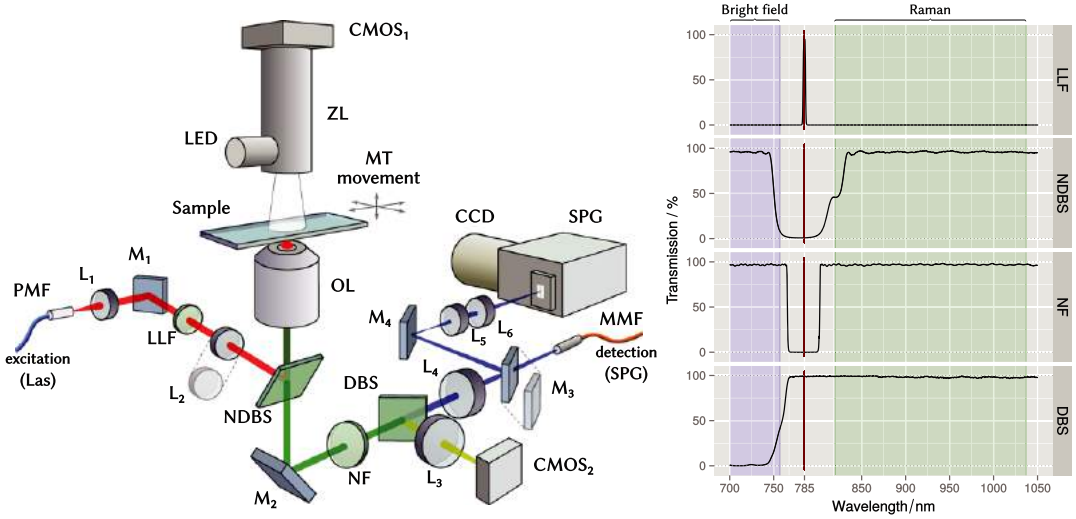

Fig. 1. *Left* – optical layout of the experimental setup. Two Raman detection paths are shown: free-space line-scanning via optical elements L4-6 and M3,4, as well as confocal detection via lens L4 and optical fiber MMF. See Table 1 for specifications of parts and abbreviations used throughout. *Right* – transmission spectra of optical filters. Spectral data provided by *Semrock Inc.*

the observation point due to its high acceptance angle. Finally, collected light leaves the objective lens as a collimated beam that can be easily focused on the spectrometer entrance slit with a tube lens.

In last decades the industry of optical filters underwent major leap forward, which revolutionized the way Raman systems are built and drastically improved their performance. Compact narrow-band optical filters superseded bulky monochromators used in past systems; dichroic filters, which offer higher transmission, replaced beam splitters/combiners. A notch dichroic beam splitter (*NDBS*) is a perfect option to couple the excitation laser beam into the optical microscope (see Fig. 1). Placed between the tube and objective lenses, it reflects the excitation light and directs it towards the objective lens. Additionally, it transmits the inelastically scattered light towards the spectrometer while suppressing the Rayleigh-scattered light.

Many optical microscopes can be upgraded to Raman microscopes by adding several additional components [10]. It is important to note that it is preferable to use an infinity-corrected optical system that features a parallel optical path between the objective lens and the tube lens. All additional components, such as filters, polarizers, prisms, etc., can be placed into this parallel path without introducing additional spherical aberrations [30]. Modern research-grade biomedical and industrial microscopes typically fall into the category of infinity-corrected optical systems.

3.1. Spatial resolution

The spatial resolution of a microscope is determined primarily by the objective lens that focuses light into a diffraction-limited spot. The spatial resolution, especially along the optical axis, can be further enhanced by using a confocal detection approach, i.e. the collected light is focused and transmitted through a pinhole located in front of the detector. The pinhole is optically conjugated with the interrogation volume, from which the Raman spectrum is acquired, such as it accepts only the light originating from the location of the laser spot and rejects the rest [49,55]. It is convenient to guide the signal to the spectrom-

Table 1
Abbreviations of the equipment depicted in Fig. 1

Abbr.	Description
CCD	Peltier-cooled back-illuminated deep depletion CCD camera *PIXIS-400BR-eXcelon*, 1340 × 400 pixels, 20 µm pixel size, quantum efficiency up to 95% at 850 nm, 3 e^- RMS read-out noise | Princeton Instruments, USA
$CMOS_{1,2}$	Color CMOS camera *DCC1645C*, 1280 × 1024 pixels, 3.6 µm pixel size | Thorlabs Inc.
DBS	Dichroic long-pass beam splitter *FF757-Di01-25x36*, 757 nm edge wavelength | Semrock Inc, USA
$L_{1,3-6}$	Plano-convex lenses with anti-reflection coating | Thorlabs Inc.
L_2	Non-axisymmetrical optical element, e.g. cylindrical lens or Powell lens
Las	Single mode laser *XTRA*, 785 nm wavelength, 450 mW optical power, line width below 10 MHz, | TOPTICA Photonics AG, Germany
LED	Cold white LED *MCWHL5*, 1000 mA current, 800 mW optical power | Thorlabs Inc.
LLF	Laser line filter, *LL01-785* | Semrock Inc, USA
$M_{1,2,4}$	Silver-coated mirrors in tilt mounts
M_3	Removable silver-coated mirror in a tilt magnetic mount
MMF	Multimode optical fiber, 105 µm core diameter
MT	Motorized table, three motorized translation stages with 25 mm travel range. Lateral axes: two *CONEX-MFACC* | Newport Corp. Vertical axis: *MTS25-Z8* | Thorlabs Inc.
NDBS	Notch dichroic beam splitter, *NFD01-785* | Semrock Inc, USA
NF	Notch filter *LC-785NF-25*, 39 nm bandwidth | Laser Components GmbH, Germany
OL	Microscope objective lenses: Nikon 60× NA 1.0 water-immersion or Nikon 100× NA 1.4 oil-immersion, in the revolver objective turret (*OT1* | Thorlabs Inc.)
PMF	Polarization-maintaining optical fiber with FC/APC ferrules | Thorlabs Inc.
SPG	Compact imaging spectrograph *IsoPlane 160*, $f = 203$ mm $f/3.88$ with 400 grooves/mm diffraction grating blazed at 850 nm | Princeton Instruments, USA
ZL	High magnification 12× zoom lens | Navitar Inc., USA

eter using a multimode optical fiber. As the fiber core acts the same way as a pinhole placed in the back focal plane of the microscope, a smaller fiber diameter improves the confocality.

Confocal Raman system allows to "look inside" a semi-transparent sample and probe its chemical composition at a particular depth. The biggest advantage of the confocal detection scheme is the suppression of the unwanted signal originating from the background (i.e. specimen locations adjacent to the interrogation volume). However, since the pinhole rejects the out-of-plane light, less signal is collected by the detector. Therefore, it is necessary to find a reasonable trade-off between the resolution and the sensitivity of the instrument. The confocality of the system is a function of several factors, such as objective lens, tube lens, and the diameter of the detection fiber core. A rigorous assessment of the confocal Raman microscopy can be found elsewhere [19,30,49].

3.2. Implementation of hyperspectral imaging

An important design question is the implementation of scanning, which is required for acquisition of hyperspectral Raman images. One of the options considered by us was laser scanning (*LS*), i.e. steering of the laser beam by a pair of mirror galvanometers [20,34].

Albeit LS system features fast operation, and successful implementations of Raman LS microscope have been reported [47,54], such a system has several inherent drawbacks. The key problem is vignetting, i.e. the deterioration of the Raman collection efficiency when the excitation spot goes off-axis. Other issues are limited field of view, as well as reduced light transmission and complicated alignment due to a high number of optical components.

Other option, which is free from the aforementioned issues, is the movement of the specimen across the fixed laser focus. In our system we use three programmable motorized linear stages, attached orthogonally to each other (see Table 1 for details). They feature 25 mm travel range with resolution down to 100 nm, thus enabling precise and reproducible sample positioning under the microscope objective.

3.3. Considerations for the excitation laser

The excitation laser is an essential component of any Raman spectroscopy system. The main relevant laser parameters are power, wavelength, line width and stability.

The Raman spectrum represents the energy difference between excitation photons and modes of molecular vibrations, as such any uncertainty or deviation of the laser wavelength directly affects the wavenumber position and, consequently, the spectral resolution. Therefore, it is important to ensure that the laser has a narrow emission line, and its wavelength is well-defined. Otherwise, the wavelength uncertainty would lead to an additional broadening of the detected spectrum.

Another important factor is the wavelength stability over time. Jumping laser wavelength would render the wavenumber calibration of an instrument invalid and make evaluation of the spectral data cumbersome.

Typically a so-called single frequency laser is used as an excitation source, which has a single longitudinal mode and thus features a very small line width, low phase noise and low intensity variations. Such lasers are very sensitive to optical feedback, so they should be carefully protected from any back-reflections, using for example a Faraday optical isolator and fiber optic connectors with pre-angled ferrules (FC/APC type).

The choice of laser power and wavelength, however, is not straightforward and is dictated by several factors [48]. The intensity of the Raman scattering is linearly proportional to the laser power, but it depends on the fourth power of the excitation light frequency, hence shorter wavelength provides higher Raman signal. However, with a short excitation wavelength a lot of undesired effects can occur. Photons of ultraviolet and visible light are capable of causing electronic excitation within molecules, which may lead to changes in chemical bonds, and consequently, to photo-degradation of a biological specimen. For example, even 5 mW power of green 514 nm laser beam suffice to cause a noticeable damage to a lymphocyte cell within several minutes; the process is accompanied by change of the Raman spectrum [40]. In contrast, it has been shown that bacterial cells can survive a prolonged exposure to 100 mW NIR excitation (790–1064 nm), which is long enough for the acquisition of a Raman spectrum [39]. An additional issue associated with the excitation laser emitting in the visible range is the autofluorescence of most biological samples. It is typically excited by wavelengths below 520 nm, and the emitted light has wavelength in the 450–600 nm range [4].

Too long excitation wavelength would be problematic as well. In addition to the decrease of scattering intensity with the forth power of the excitation frequency according to the Rayleigh law, one has to consider a rapid drop in the quantum efficiency of typical CCD detectors at wavelengths above 900–1000 nm. The sensor should have enough sensitivity to detect Stokes photons corresponding to the spectral features of interest. Since we are dealing with biological materials that typically exhibit complex

spectral features used for identification in the so-called "fingerprint region" (approx. 700–1650 cm^{-1}), it is important to ensure high detector sensitivity in the corresponding spectral range. With 785 nm excitation used in our case, the fingerprint region stretches up to 900 nm.

Another common region of interest is 2800–3000 cm^{-1}. Energies of vibrational modes of $C-H_x$ molecular bonds are located in this spectral region, which corresponds to 1006–1027 nm with 785 nm excitation. Typical CCD cameras have insufficient sensitivity above 1000 nm, so a special NIR-coated CCD sensor with enhanced quantum efficiency and suppressed etaloning is necessary.

Taking all aforementioned factors into account, we can conclude that the optimal excitation wavelength for Raman spectroscopy of biological materials would typically lie in red or NIR region.

3.4. Optical layout

The detailed optical layout of the Raman system is shown in Fig. 1 (see Table 1 for specifications of parts and abbreviations used throughout). The single mode excitation laser Las (Xtra, Toptica, Germany) provides up to 450 mW of optical power at wavelength of 785 nm with line width below 10 MHz. The laser is coupled to the microscopy setup via a polarization-maintaining fiber PMF. The PMF ensures that the polarization of the laser beam cannot fluctuate during the experiment. The laser beam is collimated using a lens L_1 ($f = 40$ mm) in a lateral translational mount and an axially-movable fiber holder. These two elements, and an additional tiltable mirror M_1, allow full control of the angle, the lateral position and the divergence of the excitation beam. The focal length of lens L_1 determines the beam diameter. The laser beam has to slightly overfill the back aperture of the objective lens OL in order to get a diffraction-limited focal spot.

The laser line filter LLF, also called a plasma filter or laser clean-up filter, is used to remove any background and emission lines other than the main exciting line of the laser. It is important to note, that the Raman effect also happens inside of the PMF that delivers excitation light to the microscope, because the high-intensity laser light scatters on the vibrational modes of the quartz (the material of the fiber core). In this case the LLF filter becomes absolutely necessary.

The notch dichroic beam splitter NDBS couples the laser beam into the optical microscope and directs it toward the objective lens OL, which focuses the beam on the sample. The sample sits on a three-axes motorized table MT.

3.4.1. Detection of the Stokes signal

The scattered light, as well as the white illumination from a LED source, are collected by the same objective lens OL and sent through three optical filters: NDBS, NF, and DBS (see Fig. 1). The notch filter NF rejects the remaining Rayleigh-scattered laser light, while the dichroic beam splitter DBS separates the visible light, which is used for bright field imaging, from the Raman signal, which lies in the near-infrared range. The tube lens L_4 focuses the parallel beam of Raman signal. Depending on the mode of operation, the Raman signal is delivered to the SPG either via MMF (confocal Raman) or free-space via mirrors $M_{3,4}$ and lenses $L_{5,6}$.

For confocal Raman micro-spectroscopy, the MMF is used to couple signal to the spectrometer. The fiber ferrule is placed into the image plane of the microscope – this way the fiber core acts as a pinhole, and the sample is scanned point-by-point to acquire a hyperspectral Raman image.

In an alternative configuration, the Raman signal is coupled to the spectrograph via free-space optical elements. In this case the signal collection is not confocal, so more light is collected, which enables faster spectrum acquisition at cost of decreased spatial resolution. The free-space coupling configuration allows to acquire Raman spectrum by fast laser line scanning. To do this, a non-axisymmetrical optical

element L_2 is introduced into the laser beam path to create a line-shaped focus. This focus is optically conjugated with the spectrometer slit, so that each line of the CCD camera sensor acquires an independent spectrum from an individual sample spot. In this way fast hyperspectral Raman imaging is performed by scanning the sample in one lateral direction only [43]. With the CCD camera used in our system it is possible to record up to 400 spectra simultaneously. The demonstration of Raman imaging with a laser line is given in Section 5. Lenses L_5, L_6 can be placed before the spectrometer to additionally magnify the image on the CCD sensor.

Hyperspectral laser-line imaging makes high demands on the imaging capabilities of the spectrograph (SPG). We used Princeton Instruments *IsoPlane 160*, which features aspherical optics that greatly reduces astigmatism and coma aberrations at all wavelengths across the entire focal plane. This makes the spectrograph particularly suitable for multichannel spectroscopy, in our case the Raman line-imaging, due to the reduced cross-talk. Additionally, sharp focusing yields higher signal-to-noise ratios for single spectral features.

The CCD camera installed in the system features low noise level and high quantum efficiency exceeding 90% across the 785–900 nm range, which is beneficial for fast data acquisition. Another important feature is the reduced etaloning (fringing), which enhances quality of the spectra acquired in the NIR region.

3.5. How to design the mechanical part

We used a computer-aided design (*CAD*) software (Autodesk Inventor) to create a computer model of the Raman system. We chose this approach for a number of reasons:

(1) Many suppliers of optomechanical components provide three-dimensional computer models of their products in the *STEP* format. These models can be downloaded and virtually assembled in the CAD software.
(2) The generated model clearly shows how the end system should look like. It is also possible to check position of every optical element and to measure any distance between arbitrary elements.
(3) Fast generation of documentation, including drawings, illustrations and bill of materials.

We used the so-called *cage system* to mount optical components, and we consider it to be the optimal choice for this task. Optical elements are firmly attached to aluminum plates that are connected together by rigid steel rods, which define a common optical axis, thus simplifying the alignment. The cage system enables modular design of the laboratory setup: different modules (e.g. detection module, laser coupling module, etc.) can be assembled and aligned independently of each other, and afterwards combined together. This also allows to quickly change the functionality of the instrument. Since the modules are small, rigid and stable, the setup can be flipped over in order to switch between upright and inverted configurations.

Usually upright and inverted microscopes are dedicated for different purposes and applications. Upright microscope, where the objective lens is located above the specimen, is well-suited for Raman spectroscopy of detached cells. The cells sink down to the substrate surface (e.g. CaF_2 or quartz), then it is possible to locate and observe them with a physiological water immersion objective lens.

Inverted microscope configuration allows to examine live specimens in a deep covered container, such as a flask [9]. It is also advantageous for micro-manipulation applications, such as Raman-based flow cytometry [13,14,16,37], because it provides a lot of space to install additional tools. In our case, it enables good direction of the tubings towards a microfluidic chip, thus preventing sedimentation of

the cells on tube walls. Additionally, we installed a 12× zoom lens ZL with CMOS_1 camera above the specimen. The lens features large adjustable field of view and thus simplifies the navigation.

The mechanical stability is a particularly important parameter of any microscopy system. Since the excitation laser focus and the pinhole in front of the detector are conjugate points, even a small mechanical movement of the optical elements in the laser beam path can lead to the significant deterioration of the Raman system performance. An additional issue is the vibrational resistance: already a minor shock to the motorized table can lead to an unpredictable movement of the specimen under the objective. For this reason, the microscope modules, which are already built using the rigid case system, are attached to a 40 mm thick steel optical breadboard. The breadboard itself is suspended on top of four cushioning isolators filled with compressed air. The air pressure in the isolators is monitored and controlled by an active self-leveling electronics (*PWA090*, Thorlabs). This configuration mechanically decouples the measurement system from the environment and effectively cushions any external impacts.

4. Application to the study of cancer cells

We demonstrated performance of the custom-built Raman system by collecting Raman maps of individual fixed cells of two different cell lines: *MIA PaCa-2*, pancreatic cancer, and *Jurkat*, T lymphocytes. In total we acquired Raman maps of 10 individual cells of each cell line; each Raman map has size of 20×20 points, with the step size of 1 μm.

The cells were placed onto a 170 μm-thick quartz cover slip, and Raman signal has been collected in the inverted configuration. We used the 100× NA 1.4 oil-immersion objective lens both for Raman excitation and for Raman signal collection in 180° back reflection geometry. All scans were carried out with 100 mW power of the excitation laser (measured in the sample plane), exposure time of 1.0 second, $f = 100$ mm tube lens, and collecting multimode optical fiber with 105 μm core diameter.

In total, 8000 Raman spectra have been collected in two batches. The spectra underwent preprocessing, which is a crucial step prior the data interpretation [8]. We used `hyperSpec` [6] package for programming language `R` [41] to perform all data manipulations, including preprocessing, analysis and visualization.

First of all, we calibrated the wavenumber axis in each of the batches using the standard calibration routine [51]. A spectrum of a Ne–Ar gas discharge lamp has been acquired, and observed peaks (about 45) have been mapped onto the atomic emission lines of Ne and Ar, provided by NIST [28]. The relationship between the CCD pixel number n and light wavelength $\lambda(n)$ has been modeled using a 3rd degree polynomial. At the next step, we collected and analyzed a Raman spectrum of polystyrene, one of standard substances for calibration of Raman spectrometers. The measured polystyrene spectrum has been matched to the reference one, which allowed us to find the laser wavelength λ_0. Then, the wavenumber axis has been calculated as $\Delta\nu(n, \lambda_0) = \frac{1}{\lambda_0} - \frac{1}{\lambda(n)}$.

In order to reduce the fixed-pattern noise and to remove the constant ADC offset, we subtracted a dark frame from each spectrum. The dark frame has been collected by reading out the CCD camera while the shutter was closed. At the next step cosmic spikes have been detected and removed. After that, data from both batches have been down-sampled using LOESS local non-parametric regression onto a common wavenumber axis that has 240 points (initially 1340) and ranges from 550–3100 cm^{-1} . As a side effect, this lead to about two-fold increase in the signal-to-noise ratio, as well as a considerable reduction of the data size.

Each individual Raman map has been separated into cell and background regions using k-means clustering. An average spectrum of the background cluster has been calculated and subtracted from the

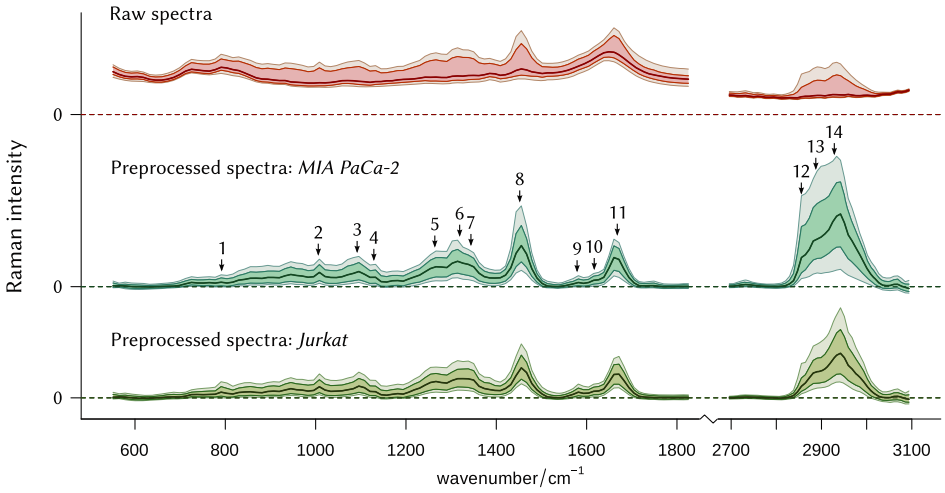

Fig. 2. Statistical overview of the collected spectral data. Lines represent, from bottom to top, the 5th, 16th, 50th (median), 84th, and 95th percentiles of the spectral intensity, respectively. The original raw dataset (8000 spectra, top) underwent smoothing interpolation, background removal, baseline subtraction and correction for the instrument response function. Then it was split into two subsets, containing spectra of *MIA PaCa-2* and *Jurkat* cell lines, respectively. Numbers **1–14**, described in Table 2, show commonly used bands for the assessment of biochemical composition. **Note on scales:** (1) Upper plot has a different scale. (2) The height of the peak located at 2700–3100 cm^{-1} in the preprocessed spectral data is reduced four times for the sake of visibility.

Raman map. The remainder baseline has been estimated as a convex hull of the bent spectrum. Finally, all spectra have been intensity-corrected using a standardized incandescent lamp as a reference light source with known emission spectrum.

After the preprocessing, only the cell signatures, random noise and some tiny baseline fluctuations were left in the cell cluster. Figure 2 compares raw dataset with the preprocessed one.

The *N-FINDR* algorithm [56] has been applied to the whole preprocessed dataset to extract three end-members, or the most different spectra. One of them is the blank background spectrum collected from points around the cell. Two other components, shown in Fig. 3(A), resemble spectra of lipid and DNA/protein mixture, respectively. We calculated concentration maps of these end-members for both cell lines (see Fig. 3(B)).

Results clearly show, that a typical *MIA PaCa-2* cell contains more lipids compared to a typical *Jurkat* cell. The concentration of proteins differs as well. Obtained data can be used for purposes of cell identification [7,38] or planning of further biospectroscopic experiments [5].

5. Demonstration of line scanning

The performance of the Raman system in the hyperspectral laser line imaging mode has been tested on 5 μm polystyrene beads located on a CaF_2 slide (see Fig. 4).

We placed a cylindrical lens L_2 (see Fig. 1) into the laser beam to perform a one-dimensional beam shaping, i.e. to create an anamorphic beam that has different divergences in two mutually orthogonal planes. The beam diameter has been matched with the entrance aperture of the 60× NA 1.0 microscope objective lens OL, producing a thin linear-shaped focus with a diffraction-limited thickness of about 0.4 μm. The intensity profile of the line was close to Gaussian with 21 μm full width at half-maximum (Fig. 4B).

Table 2
Raman bands used for assignment of biological substances [12,38]

#	Wavenumber/cm^{-1}	Description*
1	785–788	na: C, T, U, –PO_2^-– sym bk
2	1004	p: Phe
3	1090	na: –PO_2^-– bk, p: C–N str bk
4	1127	p: C–N str, lip: C–C str,
5	1262	na: G, p: amide III
6	1319	na: G, p: CH def, lip: CH_2, CH_3 twist
7	1341	na: A, G, p: CH def,
8	1451	p, lip: –CH_2– def
9	1585	na: A, G
10	1619	p: Tyr, Trp
11	1662	na: T, p: amide I β-sheet, lip: fatty acids
12	2855	p, lip: –CH_2– sym str
13	2889	p, lip: Fermi res. overtone of #8
14	2930	p, lip: –CH_2– asym str

*Abbreviations: str: stretching; def: deformation vibration; sym: symmetric; asym: asymmetric; bk: backbone chain; na: nucleic acid; U, C, T, A, G: ring breathing modes of the DNA/RNA bases; p: protein; Tyr: tyrosine; Trp: tryptophan; Phe: phenylalanine; lip: lipid.

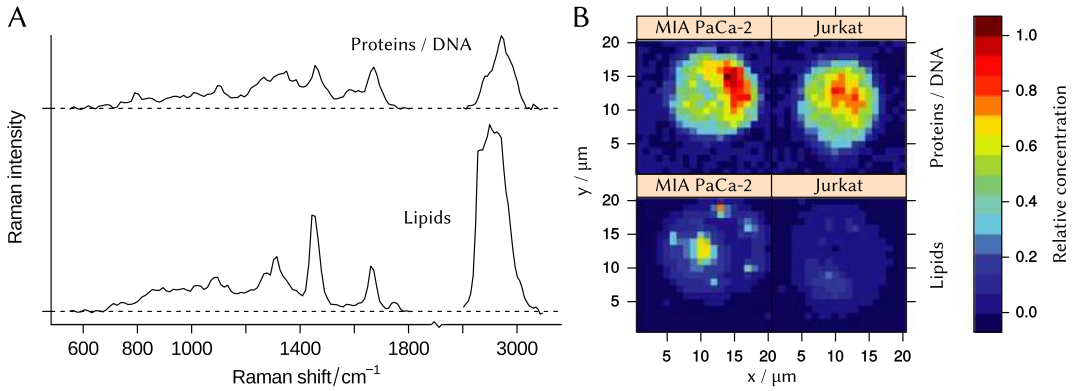

Fig. 3. (A) – N-FINDR end-members that represent spectra of lipid and protein/DNA mixture. (B) – concentration maps of the end-members in cells of *Jurkat* and *MIA PaCa-2* cell lines.

Raman signal has been collected from the area illuminated by the line-shaped focused beam in such a way, that each point along the linear focus corresponded to a specific location on the entrance slit of the spectrograph SPG. The line-shaped focus has been scanned across the sample in a single lateral direction in 1 µm steps. After each exposure of 0.5 seconds the CCD sensor has been read out, and the frame has been saved, followed by a movement to the next position on the specimen.

Use of the 60× objective lens with an $f = 100$ mm tube lens yields 30× magnification, so that each 5 µm polystyrene bead was re-imaged onto 8 lines of the CCD detector (pixel size is 20 µm), as shown in Fig. 4.

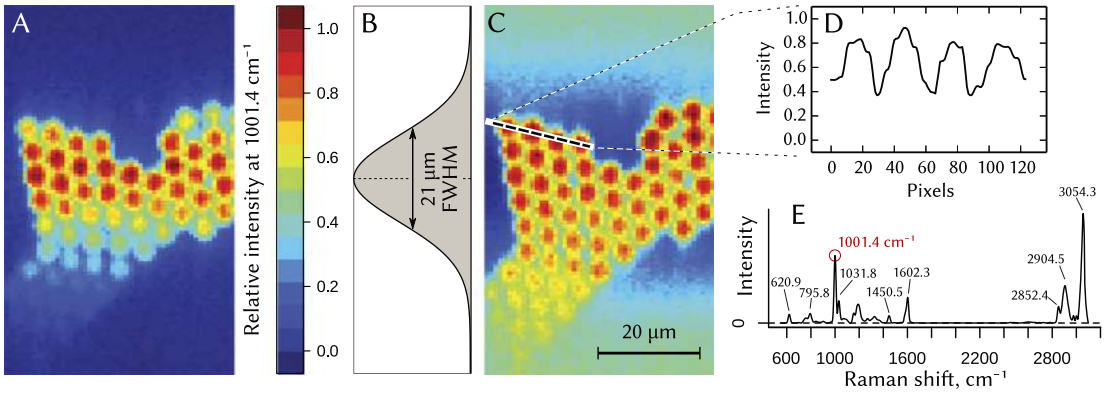

Fig. 4. Hyperspectral Raman imaging of polystyrene beads with 5 µm diameter obtained in the line-scanning mode. False-color maps (A) and (C) show relative amplitude of the 1001.4 cm^{-1} peak in the Raman spectrum of the polystyrene (plot (E)). Raw data from CCD (image (A)) underwent intensity normalization (image (C)) using Gaussian intensity profile of the illumination spot (plot (B)) as a normalization factor. (D) – intensity profile along the dashed line in the normalized image (C).

6. Conclusion

We demonstrated the construction of a very flexible Raman micro-spectroscopic system for specific needs, in our case for the Raman-assisted cell identification. The described system features several acquisition modalities, in particular bright-field imaging, acquisition of Raman spectra from a single point, Raman mapping and hyperspectral line imaging.

Since the major part of the system consists of separate general purpose optomechanical components, it can be rebuilt, modified or extended. For example, a combination with fluorescence imaging requires an additional light source, a set of optical filters and a suitable camera for detection. Moreover, the whole microscopy attachment can be flipped, so one can switch between upright and inverted configurations.

We demonstrated the performance of the instrument by acquisition of hyperspectral Raman images in two different modes: point-by-point mapping and laser line scanning.

Acknowledgements

This work was supported by the EU within the FP7 collaborative project *CanDo* (610472), as well as by the Federal Ministry of Education and Research (BMBF) within the project *RamanCTC* (13N12685). Sonja Aškrabić was supported by a short time scientific mission within the COST action *Raman4clinics* (BM1401).

References

[1] K. Ajito, C. Han and K. Torimitsu, Detection of glutamate in optically trapped single nerve terminals by Raman spectroscopy, *Analytical Chemistry* **76**(9) (2004), 2506–2510.

[2] P.C. Ashok, G.P. Singh, H.A. Rendall, T.F. Krauss and K. Dholakia, Waveguide confined Raman spectroscopy for microfluidic interrogation, *Lab. on a Chip* **11**(7) (2011), 1262.

[3] P.C. Ashok, G.P. Singh, K.M. Tan and K. Dholakia, Fiber probe based microfluidic Raman spectroscopy, *Opt. Express* **18**(8) (2010), 7642–7649.

[4] J.E. Aubin, Autofluorescence of viable cultured mammalian cells, *Journal of Histochemistry & Cytochemistry* **27**(1) (1979), 36–43.

[5] C. Beleites, U. Neugebauer, T. Bocklitz, C. Krafft and J. Popp, Sample size planning for classification models, *Anal. Chim. Acta* **760** (2013), 25–33.
[6] C. Beleites and V. Sergo, `hyperSpec`: A package to handle hyperspectral data sets in R, available at: http://hyperspec.r-forge.r-project.org [January 13 2016], 2015.
[7] N. Bergner, T. Bocklitz, B.F.M. Romeike, R. Reichart, R. Kalff, C. Krafft and J. Popp, Identification of primary tumors of brain metastases by Raman imaging and support vector machines, in: *Chemom. Intell. Lab. Syst.*, 2012.
[8] T. Bocklitz, A. Walter, K. Hartmann, P. Rösch and J. Popp, How to pre-process Raman spectra for reliable and stable models?, *Anal. Chim. Acta* **704**(1,2) (2011), 47–56.
[9] A.B. Zoladek, R.K. Johal, S. Garcia-Nieto, F. Pascut, K.M. Shakesheff, A.M. Ghaemmaghami and I. Notingher, Label-free molecular imaging of immunological synapses between dendritic and T cells by Raman micro-spectroscopy, *The Analyst* **135**(12) (2010), 3205.
[10] P.J. Caspers, G.W. Lucassen and G.J. Puppels, Combined in vivo confocal Raman spectroscopy and confocal microscopy of human skin, *Biophysical Journal* **85**(1) (2003), 572–580.
[11] L. Chiu, A.F. Palonpon, N.I. Smith, S. Kawata, M. Sodeoka and K. Fujita, Dual-polarization Raman spectral imaging to extract overlapping molecular fingerprints of living cells, *Journal of Biophotonics* **8**(7) (2015), 546–554.
[12] J. De Gelder, K. De Gussem, P. Vandenabeele and L. Moens, Reference database of Raman spectra of biological molecules, *J. Raman Spectrosc.* **38**(9) (2007), 1133–1147.
[13] S. Dochow, M. Becker, R. Spittel, C. Beleites, S. Stanca, I. Latka, K. Schuster, J. Kobelke, S. Unger, T. Henkel, G. Mayer, J. Albert, M. Rothhardt, C. Krafft and J. Popp, Raman-on-chip device and detection fibres with fibre Bragg grating for analysis of solutions and particles, *Lab. on a Chip* **13**(6) (2013), 1109.
[14] S. Dochow, C. Beleites, T. Henkel, G. Mayer, J. Albert, J. Clement, C. Krafft and J. Popp, Quartz microfluidic chip for tumour cell identification by Raman spectroscopy in combination with optical traps, *Analytical and Bioanalytical Chemistry* **405**(8) (2013), 2743–2746.
[15] S. Dochow, N. Bergner, C. Krafft, J. Clement, M. Mazilu, B.B. Praveen, P.C. Ashok, R. Marchington, K. Dholakia and J. Popp, Classification of Raman spectra of single cells with autofluorescence suppression by wavelength modulated excitation, *Analytical Methods* **5**(18) (2013), 4608.
[16] S. Dochow, C. Krafft, U. Neugebauer, T. Bocklitz, T. Henkel, G. Mayer, J. Albert and J. Popp, Tumour cell identification by means of Raman spectroscopy in combination with optical traps and microfluidic environments, *Lab. on a Chip* **11**(8) (2011), 1484.
[17] K. Eberhardt, C. Stiebing, C. Matthäus, M. Schmitt and J. Popp, Advantages and limitations of Raman spectroscopy for molecular diagnostics: An update, *Expert Review of Molecular Diagnostics* **15**(6) (2015), 773–787.
[18] A.M.K. Enejder, T.G. Scecina, J. Oh, M. Hunter, W. Shih, S. Sasic, G.L. Horowitz and M.S. Feld, Raman spectroscopy for noninvasive glucose measurements, *J. Biomed. Opt.* **10**(3) (2005), 031114-1–031114-9.
[19] N.J. Everall, Modeling and measuring the effect of refraction on the depth resolution of confocal Raman microscopy, *Appl. Spectrosc.* **54**(6) (2000), 773–782.
[20] E. Fällman and O. Axner, Design for fully steerable dual-trap optical tweezers, *Applied Optics* **36**(10) (1997), 2107–2113.
[21] L. Gao and R.T. Smith, Optical hyperspectral imaging in microscopy and spectroscopy – a review of data acquisition, *Journal of Biophotonics* **8**(6) (2015), 441–456.
[22] M. Hedegaard, C. Matthäus, S. Hassing, C. Krafft, M. Diem and J. Popp, Spectral unmixing and clustering algorithms for assessment of single cells by Raman microscopic imaging, *Theoretical Chemistry Accounts* **130**(4–6) (2011), 1249–1260.
[23] Z. Huang, G. Chen, X. Chen, J. Wang, J. Chen, P. Lu and R. Chen, Rapid and label-free identification of normal spermatozoa based on image analysis and micro-Raman spectroscopy, *Journal of Biophotonics* **7**(9) (2014), 671–675.
[24] P.R.T. Jess, V. Garcés-Chávez, D. Smith, M. Mazilu, L. Paterson, A. Riches, C.S. Herrington, W. Sibbett and K. Dholakia, Dual beam fibre trap for Raman micro-spectroscopy of single cells, *Opt. Express* **14**(12) (2006), 5779–5791.
[25] L. Kong, P. Zhang, G. Wang, J. Yu, P. Setlow and Y. Li, Characterization of bacterial spore germination using phase-contrast and fluorescence microscopy, Raman spectroscopy and optical tweezers, *Nature Protocols* **6**(5) (2011), 625–639.
[26] C. Krafft and J. Popp, Raman4clinics: The prospects of Raman-based methods for clinical application, *Analytical and Bioanalytical Chemistry* **407**(27) (2015), 8263–8264.
[27] C. Krafft, G. Steiner, C. Beleites and R. Salzer, Disease recognition by infrared and Raman spectroscopy, *Journal of Biophotonics* **2**(1,2) (2009), 13–28.
[28] A. Kramida, Yu. Ralchenko, J. Reader and NIST ASD Team, NIST atomic spectra database (version 5.3), available at: http://physics.nist.gov/asd [January 13 2016], 2015.
[29] E.E. Lawson, B.W. Barry, A.C. Williams and H.G.M. Edwards, Biomedical applications of Raman spectroscopy, *J. Raman Spectrosc.* **28**(2,3) (1997), 111–117.
[30] I.R. Lewis and H. Edwards, *Handbook of Raman Spectroscopy: From the Research Laboratory to the Process Line*, CRC Press, 2001, p. 00379.
[31] H. Li, H. Wang, D. Huang, L. Liang, Y. Gu, C. Liang, S. Xu and W. Xu, Note: Raman microspectroscopy integrated with fluorescence and dark field imaging, *Review of Scientific Instruments* **85**(5) (2014), 056109.

[32] Q. Li, E. Suasnavas, L. Xiao, S. Heywood, X. Qi et al., Label-free and non-invasive monitoring of porcine trophoblast derived cells: Differentiation in serum and serum-free media, *Journal of Biophotonics* **8**(8) (2015), 638–645.
[33] D.A. Long, *The Raman Effect: A Unified Treatment of the Theory of Raman Scattering by Molecules*, Wiley, Chichester; New York, 2002.
[34] G.F. Marshall, *Handbook of Optical and Laser Scanning*, Marcel Dekker, New York, 2004.
[35] C. Matthäus, A. Kale, T. Chernenko, V. Torchilin and M. Diem, New ways of imaging uptake and intracellular fate of liposomal drug carrier systems inside individual cells, based on Raman microscopy, *Molecular Pharmaceutics* **5**(2) (2008), 287–293, PMID: 18197626.
[36] M. Miljkovic, T. Chernenko, M.J. Romeo, B. Bird, C. Matthäus and M. Diem, Label-free imaging of human cells: Algorithms for image reconstruction of Raman hyperspectral datasets, *Analyst* **135** (2010), 2002–2013.
[37] U. Neugebauer, T. Bocklitz, J.H. Clement, C. Krafft and J. Popp, Towards detection and identification of circulating tumour cells using Raman spectroscopy, *Analyst* **135**(12) (2010), 3178–3182.
[38] U. Neugebauer, J.H. Clement, T. Bocklitz, C. Krafft and J. Popp, Identification and differentiation of single cells from peripheral blood by Raman spectroscopic imaging, *Journal of Biophotonics* **3**(8,9) (2010), 579–587.
[39] K.C. Neuman, E.H. Chadd, G.F. Liou, K. Bergman and S.M. Block, Characterization of photodamage to Escherichia coli in optical traps, *Biophysical Journal* **77**(5) (1999), 2856–2863.
[40] G.J. Puppels, J.H.F. Olminkhof, G.M.J. Segers-Nolten, C. Otto, F.F.M. De Mul and J. Greve, Laser irradiation and Raman spectroscopy of single living cells and chromosomes: Sample degradation occurs with 514.5 nm but not with 660 nm laser light, *Experimental Cell Research* **195**(2) (1991), 361–367.
[41] R Core Team, *R Development Core Team. R: A Language and Environment for Statistical Computing*, R foundation for statistical computing, Vienna, Austria, 2014.
[42] I.W. Schie, L. Alber, A.L. Gryshuk and J.W. Chan, Investigating drug induced changes in single, living lymphocytes based on Raman micro-spectroscopy, *Analyst* **139**(11) (2014), 2726–2733.
[43] I.W. Schie and T. Huser, Methods and applications of Raman microspectroscopy to single-cell analysis, *Appl. Spectrosc.* **67**(8) (2013), 813–828.
[44] U. Schmid, P. Rösch, M. Krause, M. Harz, J. Popp and K. Baumann, Gaussian mixture discriminant analysis for the single-cell differentiation of bacteria using micro-Raman spectroscopy, *Chemometrics and Intelligent Laboratory Systems* **96**(2) (2009), 159–171.
[45] M. Schmitt and J. Popp, Raman spectroscopy at the beginning of the twenty-first century, *J. Raman Spectrosc.* **37** (2006), 20–28.
[46] B. Schrader, *Infrared and Raman Spectroscopy: Methods and Applications*, Wiley, 2008.
[47] N.M. Sijtsema, S.D. Wouters, C.J. De Grauw, C. Otto and J. Greve, Confocal direct imaging Raman microscope: Design and applications in biology, *Appl. Spectrosc.* **52**(3) (1998), 348–355.
[48] E. Smith and G. Dent, *Modern Raman Spectroscopy: A Practical Approach*, Wiley, Hoboken, NJ, 2005.
[49] R. Tabaksblat, R.J. Meier and B.J. Kip, Confocal Raman microspectroscopy: Theory and application to thin polymer samples, *Appl. Spectrosc.* **46**(1) (1992), 60–68.
[50] A. Taleb, J. Diamond, J.J. McGarvey, J.R. Beattie, C. Toland and P.W. Hamilton, Raman microscopy for the chemometric analysis of tumor cells, *The Journal of Physical Chemistry B* **110**(39) (2006), 19625–19631.
[51] J.M. Tedesco and K.L. Davis, Calibration of dispersive Raman process analyzers, in: *Proceedings of SPIE*, M. Fallahi, R.J. Nordstrom and T.R. Todd, eds, 1999, pp. 200–212.
[52] H. Tsuda and J. Arends, Raman spectroscopy in dental research: A short review of recent studies, *ADR* **11**(4) (1997), 539–547.
[53] N.A. Turko, I. Barnea, O. Blum, R. Korenstein and N.T. Shaked, Detection and controlled depletion of cancer cells using photothermal phase microscopy, *Journal of Biophotonics* **8**(9) (2015), 755–763.
[54] N. Uzunbajakava and C. Otto, Combined Raman and continuous-wave-excited two-photon fluorescence cell imaging, *Optics Letters* **28**(21) (2003), 2073–2075.
[55] K.P.J. Williams, G.D. Pitt, D.N. Batchelder and B.J. Kip, Confocal Raman microspectroscopy using a stigmatic spectrograph and CCD detector, *Appl. Spectrosc.* **48**(2) (1994), 232–235.
[56] M.E. Winter, N-FINDR: An algorithm for fast autonomous spectral end-member determination in hyperspectral data, in: *SPIE's International Symposium on Optical Science, Engineering, and Instrumentation*, International Society for Optics and Photonics, 1999, pp. 266–275.
[57] C. Xie, J. Mace, M.A. Dinno, Y.Q. Li, W. Tang, R.J. Newton and P.J. Gemperline, Identification of single bacterial cells in aqueous solution using confocal laser tweezers Raman spectroscopy, *Analytical Chemistry* **77**(14) (2005), 4390–4397.

Editors
V. E. Borisenko
S. V. Gaponenko
V. S. Gurin
C. H. Kam

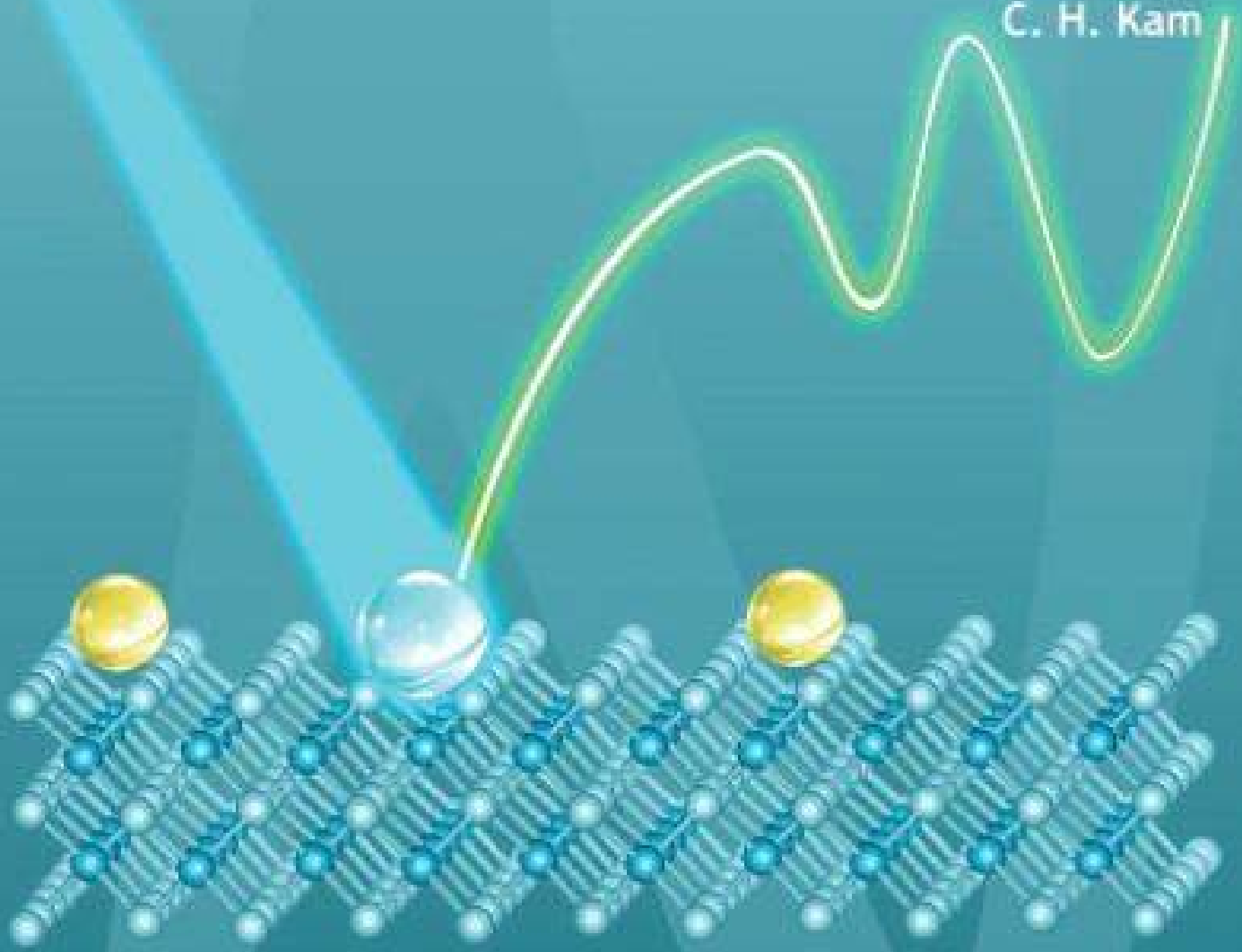

PROCEEDINGS OF INTERNATIONAL CONFERENCE
NANOMEETING - 2017

REVIEWS AND SHORT NOTES

PHYSICS, CHEMISTRY AND APPLICATIONS OF NANOSTRUCTURES

FORMATION OF MONO- AND MULTI-LAYERED FILMS OF LATERALLY ORIENTED SEMICONDUCTOR COLLOIDAL NANOPLATELETS

A. Mikhailov[1], G. Isic[2], S. Askrabic[2], A. Antanovich[1], A. Prudnikau[1], M. Artemyev[1]

[1]*Research Institute for Physical Chemical Problems, Belarusian State University*
Leningradskaya 14, 220006 Minsk, Belarus
[2]*Institute of Physics Belgrade, University of Belgrade*
Pregrevica 118, 11080 Belgrade, Serbia

We demonstrate successful utilization of the Langmuir technique for deposition of thin films of laterally oriented CdSe nanoplatelets from their colloidal solutions. We studied the morphology of the deposited films by TEM and AFM techniques, as well as their optical absorption and photoluminescence.

1. Introduction

Semiconductor nanoplatelets (NPls) are 2D nanostructures with physical properties similar to classic quantum wells, that makes them of a great fundamental interest as quantum objects with anisotropic optical properties [1]. Along with luminescent properties semiconductor NPls are perspective for practical applications, like photovoltaic or laser-gain active media. In order to investigate anisotropy-caused properties it is necessary to obtain a flat film with uniform lateral orientation of NPls. In the present paper, we utilized the Langmuir-like technique to fabricate thin films comprised of monolayer or multilayers of laterally oriented CdSe NPls and studied their morphology and optical properties.

2. Experimental

Colloidal 4.5 ML CdSe NPls were synthesized as described in [2]. NPls in the colloidal solution in chloroform were additionally treated with cadmium acetate and oleic acid according to the procedure described in [3] in order to avoid stacking of nanoplatelets into large aggregates. Afterwards, CdSe NPls were purified by precipitation with acetonitrile, washed with isopropanol and then redispersed in chloroform. Thus, the final solution contained colloidal CdSe NPls terminated by Cd atoms and capped with oleic acid. The solution was drop-cast on the water surface and dried until thin solid film of NPls formed on the water surface. These films were transferred onto quartz substrates and polymer-coated grids and dried in ambient conditions, and subsequently subjected to optical, AFM and TEM investigations. Multilayered thin films of

CdSe NPls were prepared by subsequent deposition of several monolayers by the same technique.

Room temperature optical absorption and photoluminescence (PL) spectra of thin films of CdSe NPls were measured with an OceanOptics HR-2000 spectrometer and a Jobin-Yvon Fluoromag spectrofluorimeter, respectively. Spatial arrangement of CdSe NPls in thin films was studied using a Leo 906E transmission electron microscope. AFM examination of thin NPLs films was performed using a NT-MDT Ntegra Prima SPM system in the tapping mode.

3. Results and discussion

The TEM image in Fig. 1 shows that the film consists of domains of laterally oriented CdSe NPls.

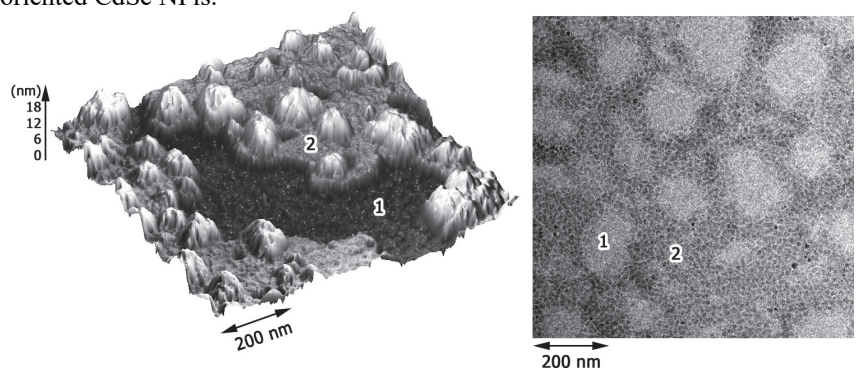

Figure 1. AFM (left) and TEM (right) images of CdSe NPls film prepared by the Langmuir technique (1 – empty area containing no NPls, 2 – area covered with a monolayer of NPls).

The NPls domains in the films are separated by empty areas free from NPls. Such domain structure forms when the thin liquid film of NPls in chloroform quickly spreads off the water surface and dries. The resulting solid film of laterally oriented NPls is rigid and cannot be compressed into a homogeneous monolayer without applying an external force. AFM measurements show a consistent height difference of around 6 nm between areas denoted by 1 and 2 in Fig. 1 indicating the substrate and the NPl monolayer, respectively. The inferred thickness of 6 nm is consistent with the thickness of a monolayer of 4.5 ML CdSe NPls (≈ 2 nm) and two monolayers of oleic acid molecules on the top and bottom surfaces of each NPl. Some hillock exceeding 10 nm in the AFM image and invisible in this TEM image (Fig. 1) are probably related to residual organic molecules crystallized from the colloidal solution during the Langmuir film formation.

Fig. 2 shows a series of optical absorption spectra of a monolayer and multilayered films of 4.5 ML CdSe NPls deposited onto quartz substrate.

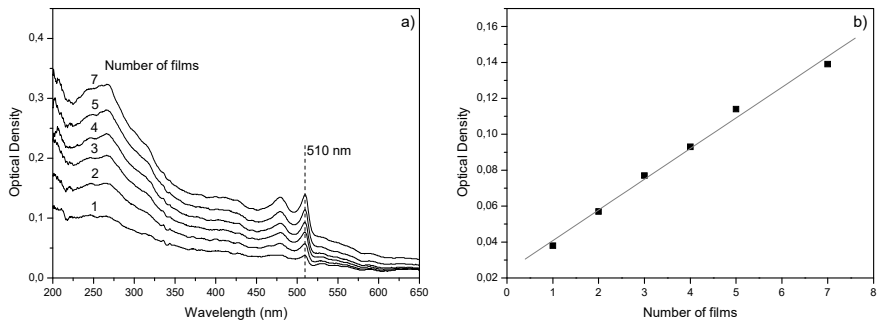

Figure 2. a) Absorption spectra of multilayered films of 4.5 ML CdSe NPls on quartz. b) Linear relationship between the first exciton (λ = 510 nm) optical density and the number of monolayers.

All spectra contain the characteristic first exciton peak at λ = 510 nm similar to that in the colloidal solution of NPls in chloroform. The optical absorption increases monotonously with the number of monolayers over the entire investigated spectral range demonstrating that the Langmuir technique can be successfully used for a reliable control of the precise amount of NPls deposited onto the substrate. Moreover, the linear relationship between the optical density at first exciton and the number of subsequently deposited layers indicates that each new layer contains a nearly constant amount of NPls.

Fig. 3 shows absorption and PL spectra of 4.5 ML CdSe NPls in the colloidal solution and in the monolayer film.

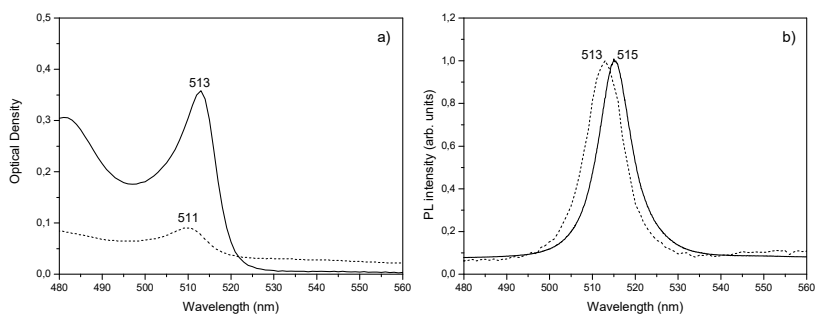

Figure 3. Absorption (a) and normalized luminescence spectra (b) of 4.5 ML CdSe NPls in the colloidal solution in chloroform (solid lines) and in the monolayer film (dashed lines).

The first exciton in the monolayer is blue-shifted by 2 nm both in the absorption and PL spectra relative to the colloidal solution spectra due to the changes in dielectric surrounding. The magnitude of the optical absorption of a

CdSe NPls monolayer is much higher as compared to that of quantum dots or nanorods of the same size, *i.e.*, the same energy of optical transitions due to the effect of giant optical oscillator (GOST) [4]. We did not observe any remarkable spectral shifts with increasing the number of monolayers which pointed to the absence of collective effects.

4. Conclusion

Uniform monolayers and multilayers of colloidal CdSe NPls were fabricated by Langmuir technique. The films consist of monolayers of laterally oriented NPls forming domains. The first exciton absorption peak of multilayered films is linearly proportional to the number of NPLs monolayers. Such structures can be utilized to study anisotropy of optical properties of oriented 2D quantum confined nanostructures.

Acknowledgements

We acknowledge financial support from BRFFR X16SRBG-001 project. This work was supported by the Science and Technology Committee of Belarus and the Ministry of Education, Science and Technological Development of Serbia through the bilateral collaboration program 2016-2018 (#451-03-00293/01).

References

1. M. Nasilowski, B. Mahler, E. Lhuillier, S. Ithurria, B. Dubertret, *Chem. Rev.***116**, 10934 (2016).
2. A. W. Achtstein *et al.*, *ACS Nano* **8**, 7678 (2014).
3. A. Antanovich, A. Prudnikau, A. Matsukovich, A. Achtstein, M. Artemyev, *J. Phys. Chem. C* **120**, 5764 (2016).
4. A. W. Achtstein, A. Antanovich, A. Prudnikau, R. Scott, U. Woggon, M. Artemyev, *J. Phys. Chem. C* **119**, 20156 (2015).

Book of abstracts

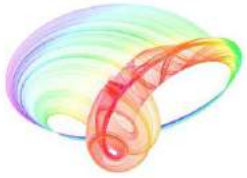

PHOTONICA2019

The Seventh International School and Conference on Photonics, 26 August – 30 August 2019, Belgrade, Serbia

& Machine Learning with Photonics Symposium (ML-Photonica 2019)

& ESUO Regional Workshop

& COST action CA16221

Editors: Milica Matijević, Marko Krstić and Petra Beličev

Belgrade, 2019

Effects of cerium-dioxide nanoparticles in cervical cancer cells studied by Raman spectroscopy

M. Miletić[1], S. Aškrabić[1], I. Schie[2], J. Rüger[2], L. Korićanac[3], A. S. Mondol[2], B. Vasić[1] and Z. Dohčević-Mitrović[1]
[1]*Institute of Physics Belgrade, University of Belgrade, Belgrade, Serbia*
[2]*Leibniz Institute of Photonic Technology, Jena, Germany*
[3]*Vinca Institute of Nuclear Sciences, University of Belgrade, Belgrade, Serbia*
e-mail: mileticjm@ipb.ac.rs

Study of the interaction between nanoparticles and human cells is usually performed using customized biochemical assays that mostly offer measurements of a single quantity/property and use labels. Raman spectroscopy on the other hand offers integral insight into complex information on biomolecular composition and molecule conformation inside cells by measuring vibrational spectra from the entire cell [1]. Furthermore, it does not require dyes nor other labels and sample preparation is very simple, which reduces time consumation and possibility of cell damage during preparation.

Cerium-dioxide (CeO_2) nanoparticles are known for their controversial dual activity in numerous studied cancer cell lines: while protecting some cell types from oxidative damage, their cytotoxic effect in other cell lines is also reported [2, 3]. Here, effects of two types of CeO_2 nanoparticles: uncoated and dextran-coated, were studied in HeLa cells, a cervical carcinoma derived cell line. Nanoparticle-treated cells were probed by routinely used biological assays for cell growth and viability, based on dying with Sulforhodamine B and Trypan Blue, respectively [3]. The tests have shown that the nanoparticles have more prominent effect on cell growth than on viability. In the light of this information Raman spectroscopy was employed in order to investigate the changes in biomolecular content of the cervical cancer cells after treatment with nanoparticles and find connection between these changes and the resulting cell status. Raman spectra of nanoparticle-treated and control (untreated) cells were obtained using 532 nm laser line as an excitation probe. From each experimental group, at least 250 cell spectra were measured. Principal component analysis (PCA) covering the spectral regions (700-1800) cm^{-1} and (2800-3200) cm^{-1} has extracted the differences between vibrational spectra features of nanoparticle-treated and control cells, but also between spectra of cells treated with uncoated and coated CeO_2 nanoparticles. These changes have been associated with induced alterations of prominent groups of biomolecules, DNA, lipids and proteins. Reduced total DNA content and/or breaking of O-P-O bonds leads to the decreased vibrational intensity of 785 cm^{-1} peak which differentiates to a large degree treated and control cells. Amide I vibrational band (1600-1670) cm^{-1}, characteristic for peptide bonds and modulated by proteins secondary structure, differentiates between cells treated with coated and uncoated nanoparticles. Correlation of the spectral information with the results of biological assays was performed.

REFERENCES

[1] R. Smith, K. L. Wright, L. Ashton, Analyst. 141, 3590 (2016).
[2] S. Das et al., Nanomedicine (Lond). 8, 1483 (2013).
[3] G. Pulido-Reyes et al., Sci. Rep. 5, 15613 (2015).
[4] S. A. G. Longo-Sorbello et al., *Cell Biology,* vol. 1, Elsevier Inc, 2006.

Chemical doping of Langmuir-Blodgett assembled few-layer graphene films with Au and Li salts aimed for optoelectronic applications

I. R. Milošević[1], B. Vasić[1], A. Matković[2], J. Vujin[1], S. Aškrabić[3], C. Teichert[2] and R. Gajić[1]
[1] *Laboratory for Graphene, other 2D materials and Ordered Nanostructures of Center for Solid State Physics and New Materials, Institute of Physics, University of Belgrade, Belgrade, Serbia*
[2]*Institute of Physics, Montanuniversität Leoben, Leoben, Austria*
[3]*Nanostructured Matter Laboratory of Center for Solid State Physics and New Materials, Institute of Physics, University of Belgrade, Belgrade, Serbia*
e-mail: novovic@ipb.ac.rs

For mass production of graphene, simple and low-cost methods are needed especially in the cases where high-quality films are not crucial for the desired purposes. Thus, liquid-phase exfoliation (LPE) is a perspective way of obtaining stable dispersion of few-layer graphene sheets (GS) in the solvent [1]. A promising pathway to achieve high degree of ordering of graphene sheets prepared via LPE-process is to utilize Langmuir-Blodgett assembly (LBA) technique. Thin-films are self-assembled from LPE dispersion by LBA technique at the water-air interface. LBA method is a suitable method for production of large-scale, transparent, thin solution-processed graphene films [2, 3]. Chemical doping of graphene films allows to tune its work function (WF) and therefore gives LPE GS films the ability to serve two different roles in electronic and optoelectronic applications, both as an anode and as a cathode.

Here, we demonstrate the method for the forming and doping of LPE graphene sheet films (LPE GS) in one-step by metal standard solutions. Doping of the graphene film occurs at the moment of its formation from the LPE graphene dispersion by LBA method at the air-metal standard solution interface. n-doping is achieved by Li standard solutions (LiCl, $LiNO_3$, Li_2CO_3), while Au standard solution ($H(AuCl_4)$) leads to p-doping. WF of the film was decreased with Li based salts, while Au based salts increase the WF of the film. The maximal doping in both directions allow a significant range of around 0.7 eV for the WF modulation. The results were obtained for 0.1 mol/dm^3 concentration of dopants. Roughness of the LPE GS films does not change by the doping, except that doped films contain occasional agglomerates. FT-IR measurements point out that the charge transfer process is enabled by physical adsorption of the metal salts and that the graphene basal planes stay chemically unchanged by metal doping. No significant shifts of any characteristic Raman peaks of graphene were detected after chemical doping. Calculated values of the intensity ratio between D and D' peak indicate that the edges are the dominant type of defects in the undoped and metal salt doped LPE GS films. Electrical properties of the films were significantly influenced by changing the dopant (Au or Li). A significant suppression of the field-effect mobility and the increase of the sheet resistivity were observed in the case of the Li standard solution doping of the film. This indicates that adsorbed Li anions act as scattering centers for the charges. Lithium nitrate provides the largest work function modulation (by 400 meV) and the least influence on the sheet resistance of the film. Therefore, it was selected as the best choice for n-type doping.

Since, the proposed one-step method for chemical doping of graphene films allows to tune WF in a large range, it extends the potential use of these materials in low-cost optoelectronic applications, as in low-power lighting, sensors, transparent heating, and de-icing applications.

REFERENCES

[1] C. Backes et al., Chem. Mater. 29, 243 (2017).
[2] Q. Zheng et al., ACS Nano. 5, 6039 (2011).
[3] A. Matković et al., 2D Mater. 3, 015002 (2016).

"Point-by-point" inversion vs. parametrized fitting of ultrathin film's dielectric function measured by rotating polarizer ellipsometry

M. M. Jakovljević[1], S. Aškrabić[1], M. Artemyev[2], A. V. Prudnikau[2], A. V. Antanovich[2], G. Isić[1], B.Vasić[1], U. Ralević[1], Z. Dohčević-Mitrović[1] and R. Gajić[1]
[1] *Center for Solid State Physics and New Materials, Institute of Physics, Belgrade, Serbia*
[2] *Research Institute for Physical Chemical Problems of the Belarusian State University, Belarus*
[3] *Texas A&M University at Qatar, Doha, Qatar*
e-mail: milka@ipb.ac.rs

With the emergence of nanotechnology, spectroscopic ellipsometry (SE) got an important role in optical characterization of ultra-thin nanostructured films [1]. Using this technique, various relevant characteristics such as film thickness, surface roughness and optical functions can be determined, but only by proper modeling of the near-surface region of multilayer samples.

In this work, we investigated the extraction of optical properties of ultrathin (~5 nm) films composed of a single layer of core-shell CdSe-CdS nanoplatelets on SiO_2(85 nm)/Si(bulk) substrate. The ellipsometric spectra were measured using SE in rotating polarizer ellipsometry (RPE) configuration. We compared two standard approaches for SE thin film analysis: "point-by-point" inversion and model based (parametrized) data fitting [2]. While the model based data fitting is quite effective in the case where the shape of film's dielectric function is easy to anticipate, one should be careful with analysis of nanometer scaled film thicknesses. Since they are very thin, reasonable goodness of fit could be misleading. On the other hand, "point-by-point" inversion suffers from the fact that the neighbouring wavelengths do not support each other, eventually leading to lack of Krammers-Kroning consistency [3]. It also strongly depends on measurement precision and sensitivity which is critical in RPE configuration in case of Δ being close to 0 or 180° [4]. For both approaches, pre-knowledge about the underlying substrate is essential. Having all this in mind, the combination of both "point-by-point" inversion and parametrized fitting should be applied.

REFERENCES

[1] M. Losurdo, K. Hingerl, *Ellipsometry at Nanoscale*, Springer, (2013).
[2] H. Fujiwara, *Spectroscopic Ellipsometry: Principles and applications*, John Wiley & Sons, Ltd, (2007).
[3] H. Tompkins, J. Hilfiker, *Spectroscopic Ellipsometry: Practical Application to Thin Film Characterization*, Momentum Press Engineering, (2016).
[4] D. E. Aspnes, J. Opt. Soc. Am. 64, 639 (1974).

3rd International Meeting

on

Materials Science for Energy Related Applications

held on September 25-26, 2018

at the University of Belgrade, Faculty of Physical Chemistry,

Belgrade, Serbia

is a satellite event of

PHYSICAL CHEMISTRY 2018

14th International Conference on Fundamental and Applied Aspects of Physical Chemistry

organized by

KTH
ROYAL INSTITUTE OF TECHNOLOGY
Stockholm, Sweden

UNIVERSITY OF BELGRADE
FACULTY OF PHYSICAL CHEMISTRY
Belgrade, Serbia

in co-operation with

THE SOCIETY OF PHYSICAL CHEMISTS OF SERBIA

Funded by

Swedish Research Council

INFLUENCE OF Co DOPING ON OPTICAL AND PHOTOCATALYTIC PERFORMANCES OF $SnO_{2-\delta}$ NANOCRYSTALS

S. Aškrabić[1], Z.D. Dohčević-Mitrović[1], V.D. Araújo[2], M. Radović[3], G.R. Costa[4], M.I.B. Bernardi[4], M.G. Nikolić[1]

[1]*Institute of Physics Belgrade, University of Belgrade, Belgrade, Serbia*
[2]*UACSA, UFRPE, BR 101 Sul, 5225, CEP 54510-000 Cabo de Santo Agostinho, PE, Brazil*
[3]*Nano and Microelectronics Group, BioSense Institute, Novi Sad, Serbia*
[4]*Instituto de Física de São Carlos, Universidade de São Paulo, USP, 13560-970, São Carlos – SP, Brasil*

Tin oxide (SnO_2) is a n-type semiconductor with large band gap (3.6 eV) at room temperature. Electronic, optical and electrochemical properties of SnO_2 promote itswide application in solar cells, catalysis, transparent conductive electrodes, solid state sensors, rechargeable Li batteries and optical electronic devices [1,2]. The mentioned properties are very much influenced by the presence of defects, particularly oxygen vacancies that introduce donor states inside the band gap, but also change optical and other properties that depend on the electronic structure [3]. These newly formed electronic states can also influence the photocatalytic activity of SnO_2. This work intends to explore how the doping with Co^{2+} ions influences the optical and photocatalytic properties of $SnO_{2-\delta}$nanopowders. It is expected that divalent Co ions would create more oxygen vacances changing the electronic structure of SnO_2 which can have a strong impact on potential applicability of these materials for organic pollutant remediation processes.

Undoped and Co-doped $SnO_{2-\delta}$ nanopowders (δ=0, 1, 3 and 5 mol%) were synthesized using microwave-assisted hydrothermal method. X-ray diffraction analysis confirmed the single phase tetragonal structure of the samples composed of very fine nanocrystals. Average crystallite size decreased with increased Co doping (from 2.5 nm in undoped sample to 2.2 nm in 5 % Co doped sample), implying that Co doping has an inhibiting effect on the crystal growth. In the Raman spectra of pure and Co-doped $SnO_{2-\delta}$, confinement effect strongly influenced the position and bandwidth of Raman modes. New modes, ascribed to defect modes, were present in undoped sample and were more intense than the Raman modes characteristic for tetragonal rutile SnO_2 [4]. The intensity of these modes decreased with Co doping.

ABSTRACTS OF TUTORIAL, KEYNOTE, INVITED LECTURES, PROGRESS REPORTS AND CONTRIBUTED PAPERS

of

The Sixth International School and Conference on Photonics PHOTONICA2017

28 August – 1 September 2017
Belgrade Serbia

Editors
Marina Lekić and Aleksandar Krmpot

Technical assistance
Marko Nikolić and Danica Pavlović

Publisher
Institute of Physics Belgrade
Pregrevica 118
11080 Belgrade, Serbia

Printed by
Serbian Academy of Sciences and Arts

Number of copies
300

ISBN 978-86-82441-46-5

Study of acute complications of diabetes mellitus type II by Raman spectroscopy

M.Miletic[1,2], S.Askrabic[1], D. Popovic[3], M.Djordjevic[3], I. Mrdovic[3] and Z. Dohcevic-Mitrovic[1]
[1]*Institute of Physics,University of Belgrade*
Belgrade, Serbia
[2]*Faculty of Biology,University of Belgrade*
Belgrade, Serbia
[3]*Emergency Centre, Clinical Centre of Serbia,*
Belgrade, Serbia
e-mail:sonask@ipb.ac.rs

Among major acute complications of diabetes are ketoacidosis and hyperglycemic hyperosmolar state. Diabetic ketoacidosis (DKA) appears due to the insulin deficiency, which causes hyperglycemia and increased lipolysis, and, as a result, increased level of ketone bodies in blood and urine. This reduces pH value of blood, leading to metabolic acidosis. Hyperglycemic hyperosmolar state (HHS) is characterized by extremely high serum glucose level and hyperosmolality without significant ketone bodies production. However, some overlapping between the characteristics of DKA and HHS may exist. Precise diagnosis, as well as clinical and biochemical hour-by-hour monitoring, is crucial for the adequate treatment of these severe and life-threatening conditions.

Raman spectroscopy, a non-invasive method which is based on the effect of inelastic light scattering and can be used for molecular fingerprinting of various biomaterials [1], was applied in order to try to discern between DKA and HHS conditions in a label-free and time efficient manner. Raman spectra of blood serum and plasma of patients diagnosed with diabetes type 2 with/without acute complications of ketoacidosis and HHS were obtained. Spectra were acquired in the range 350-3700 cm^{-1} using excitation line of 532 nm and afterwards background corrected with polynomial function of 5th order. Dominant features of the majority of spectra are positioned at 1003 cm^{-1}, 1155 cm^{-1}, 1515 cm^{-1} and belong to phenylalanine and beta carotene (resonantly enhanced) vibrations. Amide (protein) and lipid related bands were registered in the intervals (1200 -1380) cm^{-1} and (1450-1700) cm^{-1}.

Potential of Raman spectroscopy for differentiation between the two acute complications of diabetes is analyzed by use of principal component analysis (PCA). PCA was performed using different spectral intervals in order to classify spectra of serum and plasma from different patients according to the inter-spectra variations in these intervals. Most pronounced differences between the spectra of serum of patients with ketoacidosis compared to the spectra of serum of HHS patients were expressed in the high-wavenumber region containing C-H and O-H vibrations.

REFERENCES

[1] C. G. Atkins, K. Buckley, M. W. Blades and R.F.B. Turner, Applied Spectroscopy 71, 767 (2017).

The Serbian Society for Ceramic Materials
The Academy of Engineering Sciences of Serbia
Institute for Multidisciplinary Research-University of Belgrade
Institute of Physics-University of Belgrade
Vinča Institute of Nuclear Sciences-University of Belgrade

PROGRAMME AND THE BOOK OF ABSTRACTS

3rd Conference of The Serbian Society for Ceramic Materials

June 15-17, 2015
Belgrade, Serbia
3CSCS-2015

Edited by:
Branko Matović
Zorica Branković
Dušan Bućevac
Vladimir V. Srdić

P-14

EFFICIENT PHOTOCATALYTIC DEGRADATION OF AZO-DYE RO16 BY PURE AND Eu-DOPED $Pr(OH)_3$ NANOSTRUCTURES

Nataša Tomić[1], Sonja Aškrabić[1], Vinicius Dantas de Araújo[2], Marijana Milićević[1], Saša Lazović[1], Zoran Petrović[1], Zorana Dohčević-Mitrović[1]

Institute of Physics, University of Belgrade, 11080 Belgrade, Serbia
Instituto de Física, Universidade de São Paulo-USP, 13560-970, São Carlos-SP, Brasil

Mixed nanorods/nanopowders of pure $Pr(OH)_3$ and doped with Eu^{3+} (1, 3, and 5 mol %) were synthesized by microwave-assisted hydrothermal method. The oxides Pr_6O_{11} and Eu_2O_3 were dissolved in aqueous HNO_3 and used as the precursors.

Structural properties of synthesized nanomaterials were analyzed by X-ray diffraction (XRD) spectroscopy. The influence of Eu^{3+} content on structural and morphological characteristics of nanorods/nanopowders was also investigated by Raman spectroscopy and Field Emission Scanning Electron Microscopy (FESEM).

Synthesized nanostructures were tested for photocatalytic degradation of azo-dye Reactive Orange 16 since azo-dyes belong to the most toxic ones among various types of dyes. Eu-doped $Pr(OH)_3$ nanostructures showed very good photocatalytic performances, higher than pure $Pr(OH)_3$.

P-15

PREPARATION OF CARBONACEOUS MICROSPHERES BY HYDROTHERMAL TREATMENT OF FRUCTOSE WITH PHOSPHORIC ACID AND DIAMETER SIZE COMPARISON

Sanja Krstić[1], Branka Kaluđerović[1], Vladimir Dodevski[1], Anđelika Bjelajac[2]

[1]*Institute of Nuclear Sciences Vinča, Laboratory for Material Science, University of Belgrade, P.O.B. 522, Mike Alasa 14, 11001 Belgrade, Serbia*
[2]*Faculty of Technology and Metallurgy, University of Belgrade, Karnegijeva 4, P.O.B, 3503, 11001 Belgrade, Serbia*

Carbonaceous microspheres have been prepared by hydrothermal treatment of fructose. Parameters such as concentration of carbohydrate, reaction time, treatment temperature and concentration of phosphoric acid have been changed. Obtained